Universitat Autònoma de Barcelona

Doctoral Thesis

Theoretical study of the electronic properties of 2D materials

A thesis submitted to obtain the degree of
Doctor of Philosophy
in the program

Doctorat en Física

at the Departament de Física
of the Facultat de Ciències
of the Universitat Autònoma de Barcelona

Defended by:

Jose Angel Silva Guillén

Supervisors:

Pablo Ordejón Rontomé Enric Canadell Casanovas

Tutor:

J. Miguel Alonso Pruneda

Institut Català de Nanociència i Nanotecnologia, ICN2
Consejo Superior de Investigaciones Científicias, CSIC
Campus UAB-Bellaterra. Spain

2015

CSIC Consejo Superior de Investigaciones Científicas

ICN2 Institut Català de Nanociència i Nanotecnologia — Excelencia Severo Ochoa

A la máma y el pápa

La vida es una anécdota termodinámica.
J. A. Martínez-Lozano.

Día 4 que fuera y lo pasao pasao.
Dicho Villenero.

Acknowledgments

Considero que el proceso de escribir una tesis es un proceso largo y costoso. En mi caso empieza en el momento de recibir una llamada de Pablo el verano del año 2010, en la cual me informó de que podía optar a una beca.

Creo que llegar al punto final es un camino muy largo y que todo lo que he pasado en la vida me ha llevado al final a concluir en estas palabras que ando escribiendo bajo la luz de un flexo en la soledad de una habitación de una residencia universitaria (por tanto, si me dejo a alguien, que no me lo tenga en cuenta).

Ese camino, por supuesto, empieza en un colegio y, es de justicia, que agradezca al Colegio Público Ruperto Chapí y a todos los profesores que me fueron guiando por mis primeras clases. También, como todo en la vida influye, es de recibo que nombre a la Montessori School de Providence que en un año fue capaz, con sus bonitos métodos de enseñanza, de que pasara de tener una completa ignorancia en el inglés a poder hablar tranquilamente con mis compañeros de clase. Por último, agradecer al Instituto Público Antonio Navarro Santafé y a sus profesores que me empezaron a dar pinceladas de lo que sería la materia que al final tanto me fascinaría, la Física y también por formarme como persona en esos años que son tan importantes. Que conste que he remarcado públicos porque en estos tiempos que corren es importante recordar que tenemos un bonito sistema de enseñanza público y que deberíamos intentar conservarlo a toda costa.

Como es lógico, del Instituto pasamos a la Universidad (también pública), en mi caso un gran salto en que dejé atrás a amigos, familia , etc. Lo que no sabía en los primeros días cuando llegué a Valencia es que formaría una nueva familia allí. Creo que no hay forma suficiente para agradecer a esa familia: Alberto, Sara, Guillem, Ana, Loli, María Lizondo, María Gracia, Cristian, Elena, Néstor, Carlos, Javi y Laura (os pongo salteados porque en realidad el orden no importa) el tiempo que pasamos en esa facultad. Por los buenos momentos y por el apoyo en los malos. Ya sabéis que la frase célebre va por vosotros. No me puedo olvidar de mis compañeros de residencia y piso que me hicieron pasar una de las mejores épocas de mi vida (Marqués, Marcos, Nico, Edu, JuanMi, etc). Seguro que me dejo gente, pero no tenedmelo en cuenta, son las 11:30 de la noche y esto se está alargando hasta el infinito.

Llegamos al momento en que había que dar el salto de la Universidad a dar los primeros pasos en esto de escribir una tesis doctoral pasando de Valencia a Barcelona. En estos primeros pasos tengo agradecer a César y Sofia (y demás gente del grupo) por hacerme sentir como en casa y como parte de la familia. También a tod@s mis compañer@s de despacho: Carlos, Miguel Ángel, Frederico, Richard, Ermin y Dessa por los buenos momentos dentro y fuera del despacho y por la paciencia para ayudarme en la adaptación a este nuevo mundo. Especialmente a Rafa que ha sido un gran compañero y amigo en este largo camino. También a Miguel y Roberto por todos los buenos consejos, la paciencia y lo que me han enseñado. A Alberto por toda la ayuda con las cosas de Siesta. A Stephan y al resto del grupo de teoría del ICN2 e ICMAB por su amabilidad durante todos estos años. También a Eduardo, Francisco, Ruben, Bogdam y Lorenzo porque aunque no estuvieran desde el primer momento han sido de gran ayuda en estos últimos tiempos. A Marta, Raquel e Irene por amenizar las comidas, los cafés y algún que otro fin de semana en Barcelona.

Quiero agradecer especialmente a Pablo y Enric, mis directores de tesis, por toda la Física que me han enseñado durante todo este tiempo, por su comprensión y por haberme dirigido

para llevar este proyecto a su forma final.

En este tiempo de formación hubo un periodo en el que estuve en el Instituto de Ciencias de Materiales en Madrid. Allí encontré a gente increíble que no sólo me enseñó muchísimo, si no que también integró de una forma excelente en su grupo humano. Por ello, gracias a Paco, María, Belén, Alberto, Mauricio, Héctor, Ángel, Emmanuele, Rafa, Bruno y Vincenzo.

También es de agradecer el trato recibido por el PAS durante este tiempo, sobre todo al principio cuando estaba más perdido en este mundo.

Por supuesto, como he dicho antes, al final éste es un proceso muy largo y en el que, claramente, mi familia y amigos han sido de un gran apoyo.

Un especial agradecimiento a Montse por ser mi compañera, aguantando los extraños horarios que tiene este trabajo que al principio cuestan de entender. Por las risas y las experiencias vividas durante este tiempo. Por su interés en estas cosas raras que hago. En definitiva, por su apoyo y su cariño, sobre todo en esta última parte de escritura. También a su familia por haberme acogido como a uno más.

Por último (last but not least), agradecer a mis padres todo el apoyo en estos largos años, por darme siempre todo lo necesario para llegar a donde estoy hoy, por su comprensión y por educarme como lo han hecho, pero sobre todo, por no dejarme tomar estúpidas decisiones en los peores momentos.

List of Publications

- E. Cappelluti, R. Roldán, J. A. Silva-Guillén, Pablo Ordejón, F. Guinea.
  Tight-binding model and direct-gap/indirect-gap transition in single-layer and multilayer MoS_2.
  Physical Review B **88**, 075409 (2013).

- R. Roldán, M. P. López-Sancho, F. Guinea, E. Cappelluti, J. A. Silva-Guillén, P. Ordejón.
  Momentum dependence of spin-orbit interaction effects in single-layer and multi-layer transition metal dichalcogenides.
  2D materials **1**, 034003 (2014).

- R. Roldán, J. A. Silva-Guillén, M. P. López-Sancho, F. Guinea, E. Cappelluti, P. Ordejón.
  Electronic properties of single-layer and multilayer transition metal dichalcogenides MX_2 *(*M *=Mo, W and* X *= S, Se*).
  Annalen der Physik **526**, 347 (2014).

- Y. Noat, J. A. Silva-Guillén, T. Cren, V. Cherkez, C. Brun, C. Carbillet, S. Pons, F. Debontridder, D. Roditchev, W. Sacks, L. Cario, P. Ordejón, A. García, E. Canadell.
  Quasiparticle spectra of 2H-$NbSe_2$*: two-band superconductivity and the role of tunneling selectivity..*
  Physical Review B. In press.

- J. A. Silva-Guillén, Y. Noat, T. Cren, W. Sacks, and E. Canadell, P. Ordejón.
  Tunneling and electronic structure of the two-gap superconductor MgB_2.
  Physical Review B. Submitted.

- J. A. Silva-Guillén, F. Hidalgo, E. Cappelluti, R. Roldán, R. Robles, J. M. Pruneda, F. Guinea , P. Ordejón.
  Electronic structure calculations on graphene/WS_2 *hybryd structures.*
  In preparation.

- F. Hidalgo, J. A. Silva-Guillén, J. M. Pruneda, P. Ordejón.
  Optimal strictly localized basis sets for graphene adsorbated in transition metal dichalcogenides.
  In preparation.

- J. A. Silva-Guillén, P. Ordejón.
  Electronic transport between platinum contacts through graphene/nanotubes structures.
  In preparation.

Index

Chapter 1

Introduction

Layered materials are those in which a strong bonding exists in two directions of the space but there is a weaker bonding (in many cases of van der Waals type) in the third direction.[1] Due to this weaker bonding, these materials are easily exfoliable, even to the limit of truly 2D material such as graphene, which is a single layer of carbon atoms that can be created from exfoliated graphite.

2D materials have been studied for a long time, but due to the discovery of the aforementioned graphene in 2004,[2] which had promising properties that could make it useful for making technological devices and to study exotic quantum phenomena, there has been a huge boost in the investigation of this type of materials. This occured thanks to the great improvement in the creation, modification and manipulation of the experimental methods that have been developed in order to study graphene.

Although graphene is the 2D material most studied and known, there are also an immense number of 2D materials that can be found in nature with different mechanical, electronic and transport properties. In the past few years, a family of materials has brought the attention of the scientific community, the so-called transition metal dichalcogenides (TMDCs). This family has a wide variety of electronic properties, going from metallic behaviours (such as $NbSe_2$) to semiconductors or insulators (such as MoS_2). They even present, as for example $NbSe_2$, strongly correlated phenomena such as superconductivity.[3]

Despite a first pioneering work by Frindt *et al.* where they exfoliated such materials into a few and single layers,[4] not until recently, when Mak and coworkers[5] found that there was a transition from an indirect gap to a direct gap when exfoliating a sample of MoS_2 to a single layer, these materials became very interesting to the scientific community. The same happens for a variety of semiconducting materials of the type MX_2 (such as WS_2, $MoSe_2$, WSe_2, etc.). Due to the change of character in the gap, a huge variety of applications,[3] going from electronic devices[1] to optoelectronic applications[3] and even to molecular sensing applications,[6] opened with this kind of materials. Even novel field effect transistors were fabricated with hybrid structures combining graphene with MoS_2[7] or WS_2.[8] Furthermore, the strong spin-orbit coupling in these materials, which lifts the degeneracy of energy bands due to the absence of inversion symmetry, opens the possibility of controlling the coupling of the spin, the valley and the layer degrees of freedom which could be usefull in order to build future devices based in spintronics and valleytronics.[3] Moreover, due to the similarity of structure, chemical conformation and small lattice mismatch, the stacking of different TMDCs is possible and the number of different heterostructures that can be built with different electronic properties is almost infinite.[9]

On the other hand, other layered materials, such as MgB_2 or even TMDCs such as $NbSe_2$ present, as we said before, strongly correlated phenomena[3] such as superconductivity and even, in the case of $NbSe_2$, a charge density wave.

In this thesis we are going to study several aspects of the electronic properties of some of these materials.

- In Chapter 2 we briefly describe the methods used along the thesis to perform theoretical calculations of the electronic properties of the studied materials.

- In Chapter 3 we develop a tight-binding method for the family of superconducting TMDCs of the type MX_2 and we fit it to first-principles calculations. This model is the one with the minimal basis set that is able to account for the transition of the gap from direct to indirect when adding layers to the system. Afterwards, due to the strong spin-orbit coupling that this kind of materials presents, we extend the tight-binding model including this effect.

- In Chapter 4 we study a new possible family of substrates for graphene such as TMDCs. We study the structure and electronic properties such as the band structure, the charge redistribution and the dipole of these hybrid structures. Since the electronic properties of TMDCs change with the number of layers, the effect of adding more layers to the system is also studied.

- Finally, in Chapter 5 we investigate the two band gap superconductivity that arises in some layered materials such as MgB_2 and $NbSe_2$. Using first principles calculations we will give support to the assignment of the different gaps to the bands generating them. This assignment is studied from an experimental point of view by the group of Dimitri Roditchev, at Paris, with whom we have established a fruitful collaboration during the period of this thesis.

Chapter 2

Theoretical and methodological background

Along this thesis we are going to face calculations for quantum systems where we have to solve the Schrödinger equation. Therefore, we are dealing with a quantum mechanical problem that cannot be solved exactly because of the huge number of variables ($3N$, with N being the number of particles) and the complexity of the equations. As we have said, the basic equation we will solve is the Schrödinger equation, that is given by:

$$\hat{H}\Psi = E\Psi, \tag{2.1}$$

where, $\hat{H}$ is the Hamiltonian, Ψ the wavefunction and E the energy. In the particular case of condensed matter calculations the Hamiltonian is given by:

$$\begin{aligned} \hat{H} &= -\frac{\hbar^2}{2m_e}\sum_{i=1}^{n}\nabla_i^2 - \sum_{I=1}^{m}\frac{\hbar^2}{2M_I}\nabla_I^2 - \sum_{i,J=1}^{n,m}\frac{Z_J e^2}{|\mathbf{R}_J - \mathbf{r}_i|} + \qquad (2.2)\\ &+ \sum_{i<j}^{n}\frac{e^2}{|\mathbf{r}_i - \mathbf{r}_j|} + \sum_{I<J}^{m}\frac{Z_I Z_J e^2}{|\mathbf{R}_I - \mathbf{R}_J|} + V_{ext} = \\ &= \hat{T}_e + \hat{T}_N + \hat{V}_{Ne} + \hat{V}_{ee} + \hat{V}_{NN} + V_{ext}, \qquad (2.3) \end{aligned}$$

where the first two terms represent the kinetic energy of the electrons and nuclei, the third term is the interaction between the nuclei and the electrons, the fourth and fifth term are the electron-electron and nuclei-nuclei interaction, respectively and the last term is any kind of external potential, for example, resulting from electric or magnetic fields.

As we can see, this is a very complicated Hamiltonian and we must make some approximations. A widely used approximation in this field is the so-called Born-Oppenheimer approximation, which is based in the idea that the electrons move much faster than the nuclei (due to the small mass of the electron compared to the nuclei) and thus, we can decouple the total wavefunction in an electron and in a nuclear part:

$$\Psi(\mathbf{r},\mathbf{R}) = \varphi_{ni}(\mathbf{R})\,\Phi_i(\mathbf{r},\mathbf{R}), \tag{2.4}$$

where φ_{ni} is the wavefunction of the nuclei for the different nuclear states, n, and Φ_i is the electronic wavefunction in the ith stationary state of the electronic Hamiltonian, Eq. (2.5), where the atomic positions are parameters:

$$\hat{H}_e = \hat{T}_e + \hat{V}_{Ne} + \hat{V}_{ee} + V_{ext} \Longrightarrow \tag{2.5}$$

$$\Longrightarrow \hat{H}_e\Phi_i(\mathbf{r},\mathbf{R}) = E_i[\mathbf{R}]\,\Phi_i(\mathbf{r},\mathbf{R}). \tag{2.6}$$

After solving equation (2.6) for fixed nuclei positions, we would then have to solve the Schrödinger equation for the nuclei:

$$\left[\hat{T}_N + \hat{V}_{NN} + E_{e_i}\left[\mathbf{R}\right]\right]\varphi_{ni}\left(\mathbf{R}\right) = E_{ni}\varphi_{ni}\left(\mathbf{R}\right). \tag{2.7}$$

Although in this thesis we are not going to treat the dynamics of atoms, it is worh mentioning that even solving the uncoupled quantum nuclear equation (Eq. (2.7)) is difficult and another approach is usually taken: Since we can approximate the behaviour of the nuclei as if it was classical, we can treat them as classical particles in a potential $E_i\left[\mathbf{R}\right]$ generated by the electrons. Therefore, the movement of the nuclei is described by Newton's equations.

Now, if we focus on the main problem that we are going to encounter along this thesis, that is solving the many body electronic Schrödinger equation, it should be noted that for small systems we could be able to solve it, but in systems with a high number of electrons, as in this work, it is too difficult and a different approach has to be taken. Many theories have been developed during the years in order to solve in an approximate way electronic many body problems: Hartree-Fock (HF), density functional theory (DFT), etc.

In this chapter, we are just going to briefly explain the method used during the development of this thesis, DFT. Also, we will explain the tight-binding (TB) approach, which allows us to solve the resulting one electron Hamiltonian.

2.1 Density Functional Theory

DFT is a theory to handle correlated many-body systems widely used in electronic structure calculations for condensed matter.[10] The basic idea of this theory is that any property of the ground state of a system can be described as a functional of the ground state electron density. Therefore, we would transform our $3N$ variable problem (wave function of N electrons) as is the case of N interacting electrons, to a 3 variable problem with the electronic density (function of position). In the next sections, we will present the theorems that prove this statement. However, the exact expression for this functional is not known and some approximations must be made. The theory itself does not provide any guidance for constructing the functionals. However, as we will see, there are many approximations available for these functionals that work well. Also, much work is still done in the scientific community in order to find new functionals and to improve those already established.

2.1.1 Hohenberg-Kohn theorems

Hohenberg and Kohn presented two theorems that allow to transform the many-body problem in terms of the many body wave function to one in terms of the electronic density. These theorems can be applied to any system of interacting particles in an external potential:[11]

Theorem 1 *For any system of interacting particles in an external potential, the external potential is determined uniquely, except for a constant, by the ground state particle density.*

Corollary 1 *Since the Hamiltonian is thus fully determined, except for a constant shift of the energy, it follows that the many-body wavefunctions for all states (ground and excited) are determined. Therefore, all properties of the system are completely determined given only the ground state density.*

Theorem 2 *A universal functional for the energy in terms of the density can be defined, valid for any external potential. For a particular value of the latter, the exact ground state energy of the system is the global minimum value of this functional, and the density that minimizes the functional is the exact ground state density.*

Corollary 2 *The functional alone is sufficient to determine the exact ground state energy and density.*

Up to this point, we have an exact theory due to the previous theorems. However, this theory is still abstract and it is just telling us that minimizing this functional as a function of the density would show us which is the ground state. But the functional is not known. Besides, the minimization problem is a complex mathematical problem. The contributions of Kohn and Sham provided solutions to these issues.

2.1.1.1 Kohn-Sham approach

The approach that Kohn and Sham[12] propose is to group all the many-body terms which make the theory untreatable into an exchange-correlation potential (V_{xc}). This change allows us to treat the many-body interacting system as a one electron non-interacting system under the action of this potential. The accuracy is limited only by the approximations in the exchange-correlation functional:[10] If we knew the exact expression for the potential, the theory would be exact.

The Kohn-Sham ansatz is based on two assumptions:

1. The exact ground state density can be represented by the ground state density of an auxiliary system of non-interacting particles. This density can be expressed mathematically as:
$$\rho(\mathbf{r}) = \sum_i |\psi_i(\mathbf{r})|^2 , \tag{2.8}$$
with $\psi_i(\mathbf{r})$ being one electron wave functions.

2. The auxiliary one electron Hamiltonian is chosen to have the usual one electron kinetic energy operator and an effective local potential acting on the electron at each position with a defined spin.

With these two assumptions, we arrive to the Kohn-Sham equations:

$$\left(H_{KS}^{\sigma} - \epsilon_i^{\sigma}\right) \psi_i^{\sigma}(\mathbf{r}) = 0 \tag{2.9}$$

$$H_{KS}^{\sigma}(\mathbf{r}) = -\frac{1}{2}\nabla^2 + V_{KS}^{\sigma}(\mathbf{r}) \tag{2.10}$$

$$V_{KS}^{\sigma}(\mathbf{r}) = V_{ext}(\mathbf{r}) + V_{Hartree}(\mathbf{r}) + V_{xc}^{\sigma}(\mathbf{r}) \tag{2.11}$$

Exchange-Correlation Approximations

As we said before, DFT is an exact theory and no approximations are made until the actual expression for the exchange-correlation potential is written. This potential is a functional of the density and, if it were exact, the results of the calculations would also be exact, but this expression is not knwon. There are many approximations for the exchange correlation term such as the local density approximation (LDA), generalized-gradient approximation (GGA), hybrid functionals, van der Waals functionals, etc. In this thesis we will restrict to the use of LDA and GGA.

LDA is based on the idea that we can approximate a nonhomogeneous system, which exchange-correlation potential at $\mathbf{r}$ not only depends on the value of the density, but also on its value in the whole space, to a homogeneus system, which potential only depends on the

value of the density at $\mathbf{r}$, neglecting all the variations. This leads to an expression for the exchange-correlation energy that is given by:[10]

$$E_{xc}^{LDA}\left[n\left(\mathbf{r}\right)\right] = \int n(\mathbf{r})\epsilon\left[n\left(\mathbf{r}\right)\right] d\mathbf{r}, \tag{2.12}$$

where $\epsilon\left[n\left(\mathbf{r}\right)\right]$ is the exchange correlation energy density of a uniform electron gas of density $n(\mathbf{r})$.

Although it seems a quite rude approximation, it typically gives very acceptable results and therefore it is widely used. However, it has well known deficiencies like the underestimation of the bonding distances between atoms and the overestimation of binding energies.

GGA is the next step of the approximation of the potential. Instead of neglecting all possible variations of the density, it uses a gradient to modify the behaviour when its variation is important. In this case, the exchange-correlation energy is given by:[10]

$$E_{xc}^{GGA}\left[n\left(\mathbf{r}\right)\right] = \int f\left(n(\mathbf{r}), \nabla n(\mathbf{r})\right) d\mathbf{r}, \tag{2.13}$$

GGA functionals provide better binding energies than LDA but they overestimate the bonding distances.

As we said before, new exchange-correlation functionals are being developed. In particular, LDA and GGA are not able to describe weakly interacting systems, where van der Waals interactions are important. This is due to the fact that LDA and GGA are based on (quasi) local approximations to the exchange-correlation energy, whereas van der Waals interactions are intrinsecally non-local. Although some new functionals have been proposed recently to describe van der Waals interactions, they still perform questionable results in calculations of systems with metals, like those considered in this work.

2.1.2 The SIESTA method

In addition to the exchange-correlation approximation, simulation codes usually have other approximations in order to make the computations feasible. This thesis has been developed using SIESTA, which makes these basic approximations:

- Pseudopotentials are used to replace the core electrons.

It is well known that core electrons do not contribute to the chemical bonding of the materials since their wavefunctions are very localized around the nuclei. Moreover, along these thesis we will study the electronic properties related to the valence electrons of the atoms. Therefore, we could separate the core electrons from the valence electrons since the former mainly affect to the screening of the nuclear charge seen by the outer electrons. Pseudopotentials allows us to replace the core electrons by an effective potential that acts on the valence electrons. Moreover, they are not only useful in order to decrease the number of electrons needed to describe an atom but they also allow us to transform the wavefunction of the valence electrons that has nodes into a smooth function without radial nodes. These two characteristics lead to an improvement of the computational cost.[10]

- Pseudo-atomic orbitals (numerical) are used as basis sets to describe the KS orbitals.

Another of the main features of SIESTA is the type of basis set that it uses to expand the Kohn-Sham orbitals:

$$\psi_i\left(\mathbf{r}\right) = \sum_{\mu} c_{i\mu}\chi_{\mu}\left(\mathbf{r}\right), \tag{2.14}$$

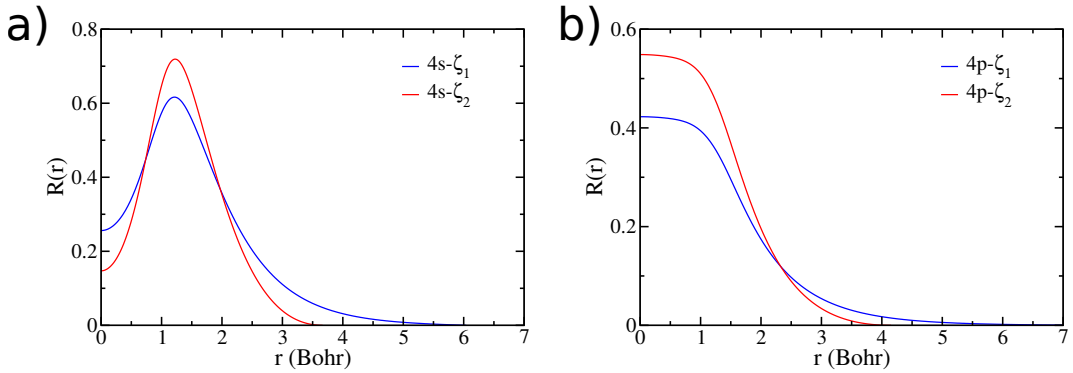

Figure 2.1: Radial part of the basis function for selenium.

where $c_{i\mu}$ are coefficients that have to be determined and $\chi_\mu(\mathbf{r})$ are the basis functions. The index μ stands for the different functions in the basis set.

In SIESTA these basis functions are numerical atomic orbitals, which are strictly localized (that is, they are zero beyond a certain radius from the nucleus). The atomic orbitals are a product of a numerical radial function (with a finite range) and a spherical harmonic:

$$\chi_\mu(\mathbf{r}) \equiv \chi_{jnlm}(\mathbf{r}) = R_{jnl}(\mathbf{r}) \cdot Y_{lm}(\theta, \phi), \tag{2.15}$$

where the index n is the principal quantum number, l the orbital angular momentum and m is the projection of the orbital angular momentum in the azimuthal axis. As we said before, SIESTA uses pseudopotentials, therefore, these basis sets only describe the valence states. j is an index that indicates that, for a given set of n and l, several radial functions with different radial shape can be included in the basis set.

Although an exact description of the Kohn-Sham orbitals can only be achieved using an infinitely large basis, this is not possible in practice, and therefore one has to attempt to achieve sufficiently converged results by using the minimum possible number of orbitals. Here, we are going to use the so-called single-ζ and double-ζ polarised basis sets (SZP and DZP, respectively). SZP means that we will have one orbital for each occupied state of the free atom (SZ) plus a polarization orbital (P). The latter is an orbital with a higher angular momentum $l_P = l + 1$. For example, for the Hydrogen atom we would have a $1s$ orbital plus a shell of $2p$ orbitals. In the case of the DZP basis set we have two orbitals (with the same angular shape but different radial function) for each occupied state of the free atom, plus a polarization shell that is defined as in the case of SZP. Therefore, in the Hydrogen case, we would have two orbitals of s symmetry with different radial dependence and a shell of $2p$ orbitals. The choice of the radial shape for the two orbitals in the same shell can be done in several ways. In SIESTA, for multiple-ζ bases, the first-ζ is generated by solving the radial Schrödinger equation for the atom. In order to obtain orbitals which are zero beyond a certain radius, the radial Schrödinger equation can be solved in the presence of a hard wall potential or in the presence of a soft confinement potential. In our case, we chose the latter scheme, with a potential of the form:[13]

$$V(r) = V_0 \frac{e^{\frac{r_c - r_i}{r - r_i}}}{r_c - r}, \tag{2.16}$$

where V_0 is a parameter, r_i is the internal radius where the potential starts and r_c the cutoff radius where the potential becomes infinite.

There are several methods to generate the second-ζ implemented in SIESTA. We chose the "split-valence" scheme.[14] This method consists in building an orbital with the same tail as the

first-ζ orbital, but changing it into a simple polynomal behaviour inside a "split radius", r_l^s:

$$R^{\mathrm{SV}}_{2\zeta,nl}(\mathbf{r}) = \begin{cases} r^l\left(a_l - b_l r^2\right) & \text{if} \quad r < r_l^s. \\ R_{1\zeta,nl}(\mathbf{r}) & \text{if} \quad r \geq r_l^s, \end{cases} \tag{2.17}$$

where a_l and b_l are parameters determined by imposing the continuity of value and slope at r_l^s. Moreover, the definition of Eq. (2.17) is not the second-ζ orbital, the actual definition is:

$$R_{2\zeta,nl}(\mathbf{r}) \equiv R_{1\zeta,nl}(\mathbf{r}) - R^{\mathrm{SV}}_{2\zeta,nl}(\mathbf{r}) \tag{2.18}$$

2.2 Tight-Binding method

The tight-binding method is an approximation that allows to solve the one electron Schrödinger equation in an efficient way that allows for large calculations. Furthermore, it allows to add many-body electron-electron effects, as well as of the dynamical effects of the electron-lattice interaction. Since we can see a solid or a molecule just as atoms arranged together, it would be a good guess that the solution to our Hamiltonian could be a linear combination of atomic orbitals. Since most of the calculations in condensed matter are crystals which, by definition, are periodic systems, we can use a basis set that satisfies the Bloch theorem:

$$\chi_{\mu\mathbf{k}}(\mathbf{r}) = \frac{1}{\sqrt{N}} \sum_{\mathbf{R}_j} e^{i\mathbf{k}\mathbf{R}_j} \phi_\mu(\mathbf{r} - \mathbf{R}_j). \tag{2.19}$$

This Bloch basis is used to expand the solutions of the one electron Schrödinger equation:

$$\psi_{i\mathbf{k}}(r) = \sum_{i\mu} C_i(\mathbf{k}) \chi_{\mu\mathbf{k}}(\mathbf{k}). \tag{2.20}$$

With this, the secular equation $H\psi = E\psi$ can be written as:

$$H_{\mu\nu}(\mathbf{k}) C_{i\mu}(\mathbf{k}) = E_{i\nu}(\mathbf{k}) S_{\mu\nu} C_{i\nu}(\mathbf{k}), \tag{2.21}$$

where $H_{\mu\nu}(\mathbf{k})$ and $S_{\mu\nu}(\mathbf{k})$ are:

$$H_{\mu\nu} = \langle \chi_{\mu\mathbf{k}} | H | \chi_{\nu\mathbf{k}} \rangle, \tag{2.22}$$

$$S_{\mu\nu} = \langle \chi_{\mu\mathbf{k}} | \chi_{\nu\mathbf{k}} \rangle, \tag{2.23}$$

or, in its integral form:

$$H_{\mu\nu} = \sum_{\mathbf{R}} e^{i\mathbf{k}\mathbf{R}} \int d\mathbf{r} \phi^*(\mathbf{r}) H \phi(\mathbf{r} - \mathbf{R}), \tag{2.24}$$

$$S_{\mu\nu} = \sum_{\mathbf{R}} e^{i\mathbf{k}\mathbf{R}} \int d\mathbf{r} \phi^*(\mathbf{r}) \phi(\mathbf{r} - \mathbf{R}), \tag{2.25}$$

One approximation that we could make is to get rid of the electron-electron interaction and, with this, we can write the independent electron Hamiltonian as:

$$\hat{H}_e = \hat{T}_e + \hat{V}_{eff}, \tag{2.26}$$

where $\hat{V}_{eff}$ is a effective potential that contains all the possible interactions that occur in the solid.

The simplest approximation that we could make is to suppose that V_{eff} is just the sum of the atomic potentials generated by all the atoms in the solid:

$$\hat{V}_{eff} = \sum_J v(\mathbf{r} - \mathbf{R_J}). \tag{2.27}$$

Introducing Eq. (2.27) to Eq. (2.24) we would find that we have four main kinds of matrix elements:

1. One center, where the two orbitals and the potential are at the same atom (see Fig. 2.2a):

$$\int d\mathbf{r}\phi^*(\mathbf{r} - \mathbf{R}_j)v(\mathbf{r} - \mathbf{R_j})\phi(\mathbf{r} - \mathbf{R}_j) \tag{2.28}$$

2. Two center, where each orbital is sitting on a different atom and the potential on one of them (see Fig. 2.2b):

$$\int d\mathbf{r}\phi^*(\mathbf{r} - \mathbf{R}_i)v(\mathbf{r} - \mathbf{R_j})\phi(\mathbf{r} - \mathbf{R}_j) \tag{2.29}$$

3. Two center, where the two orbitals are sitting on the same site but the potential is centered in another (see Fig. 2.2c):

$$\int d\mathbf{r}\phi^*(\mathbf{r} - \mathbf{R}_j)v(\mathbf{r} - \mathbf{R_i})\phi(\mathbf{r} - \mathbf{R}_j) \tag{2.30}$$

4. Three center, where all three (the two orbitals and the potential) are centered on different atoms (see Fig. 2.2d):

$$\int d\mathbf{r}\phi^*(\mathbf{r} - \mathbf{R}_i)v(\mathbf{r} - \mathbf{R_j})\phi(\mathbf{r} - \mathbf{R}_k) \tag{2.31}$$

Since calculating all the matrix elements of the Hamiltonian that involves even multi-center integrals is computationally very costly, an approximation can be made. In 1954 J. C. Slater and G. F. Koster[15] proposed that all the matrix elements could be treated in an effective way as two center integrals and then fit them to experimental or first-principles calculations data.

Along this thesis, in some chapters we will perform calculations where all the integrals in Eqs. 2.24 and 2.25 are calculated using a DFT potential using the SIESTA code. On the other hand, in other chapters, the SK approach will be used, fitting the parameters of the model to DFT calculations.

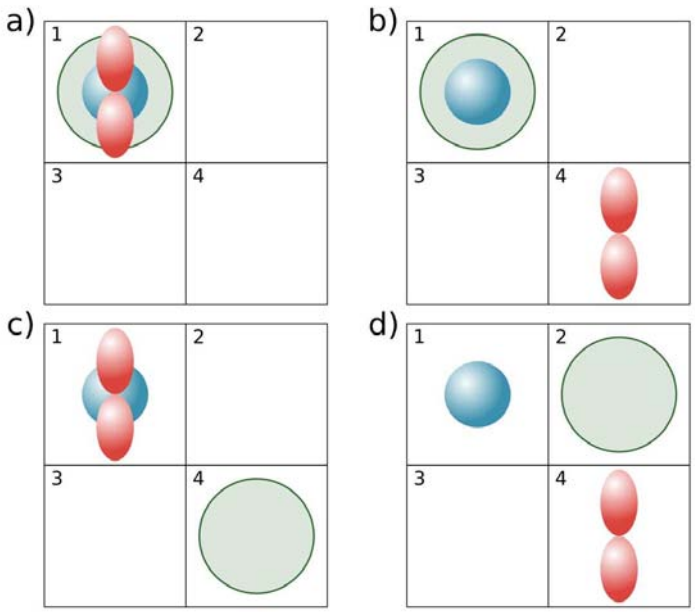

Figure 2.2: Schematic view of the one-center (a), two centers (b) and (c) and three centers integrals (d). Blue balls represent an s type orbital, red lobes represent a p orbital and the green circles represent the potential, $v(\mathbf{r})$.

Chapter 3

Minimal tight-binding model for transition metal dichalcogenides

Since the discovery of graphene in 2004[2,16,17] there has been a lot of interest in exfoliable materials due to the dramatic change of the electronic, optical and many other properties when going from 3D to 2D, that is, from having many layers to just having one layer.

In 2010 Mak and coworkers,[5] found that a single-layer of MoS_2 was a direct-gap semiconductor. Also, other transition metal dichalcogenides (TMDCs) such as WS_2 had the same property. Much work has been done concerning these materials in the past years[18] since they have an interesting property that makes them very versatile: they change from an indirect gap to a direct gap when going from a multi-layer structure to a single-layer sample (see Fig. 3.1). In addition, the electronic properties appear to be highly sensitive to the external pressure and strain, which affect the insulating gap and, under particular conditions, can also induce an insulator/metal transition.[19–29] This tunability of the gap is very interesting for optoelectronic applications.[3]

Another important feature of the TMDCs is the possibility to control quantum degrees of freedom such as the electron spin, the valley pseudospin and layer pseudospin.[30] In fact, the strong spin-orbit interaction in these compounds, and the coupling of the spin, the valley and the layer degrees of freedom open the possibility to manipulate them for future applications in spintronics and valleytronics devices.[31–38] The spin orbit coupling lifts the spin degeneracy of the energy bands in single layer samples due to the absence of inversion symmetry.[39] By time reversal symmetry the spin splitting in inequivalent valleys must be opposite, leading to the so called spin-valley coupling,[35] which has been observed experimentally[31,33,36,37,40,41] and also studied theoretically.[42–47]

On the theoretical level, while much of the work of graphenic materials has been based on simple tight-binding-like approaches, the electronic properties of single-layer and few-layer dichalcogenides have been so far mainly investigated by means of DFT calculations,[19–29,42,48–56] despite early work in nonorthogonal tight-binding (TB) models for TMDCs.[57] A few simplified low-energy Hamiltonian models have been presented for these materials, whose validity is, however, restricted to the specific case of single-layer systems. An effective low-energy model was, for instance, introduced by Xiao *et al.*[35] and Kormanyos *et al.*[58] to discuss the spin/orbital/valley

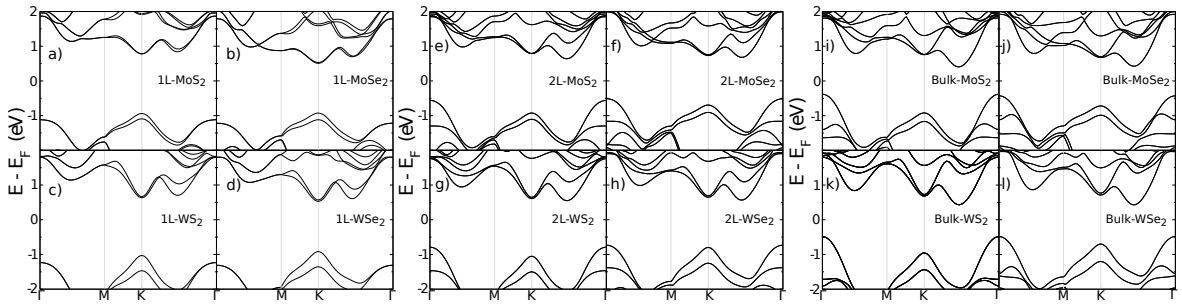

Figure 3.1: Calculated DFT band structures for different TMDCs with different number of layers. The image shows the change of character from direct to indirect of the gap when adding layers. Spin-orbit coupling is included in the calculations.

coupling at the K and/or the Γ point. Being limited to the vicinity of a specific high-symmetry point, these models cannot be easily generalized to the multilayer case where the gap is indirect with valence and conduction edges located far from the K point. An effective TB Hamiltonian was, on the other hand, proposed by Rostami and coworkers,[44] valid, in principle, in the whole Brillouin zone. This model considers the spin-orbit coupling, and it includes the effect of a quantizing magnetic field in the spectrum. However, the band structure of the single layer lacks the characteristic second minimum in the conduction band (see Fig. 3.1) that will become the effective conduction edge in multilayer systems. Therefore, also in this case, the generalization to the multilayer compounds is doubtful. Although first-principles calculations are very accurate and are currently able to handle systems with hundreds or even thousand of atoms[59,60] (for instance, they have been thoroughly applied to large-scale graphene-related problems)[61–64] they are still computationally demanding. Moreover, the further inclusion of many-body effects by means of quantum field theory methods, as well as of the dynamical effects of the electron-lattice interaction is also computationally challenging. Tight-binding models, although less accurate, allow us to tackle this kind of calculations. Therefore, a model that describes correctly the bands would be useful in order to calculate disordered and inhomogeneous systems[65–78] materials nanostructured in large scales (nanoribbons, ripples)[79–87] or in twisted multilayer materials.[88–99]

In this Chapter, we will try to build a TB model within the Slater-Koster approach[15] for the dichalcogenides valid in both the single-layer case and the multilayer one and that is able to reproduce correctly DFT bands. To do this, we first analyse the orbital character of these bands and, afterwards, we will build the model and try to fit the parameters in order to obtain the correct bands. Moreover, since the spin-orbit interaction in these compounds is strong, we will extend the TB model with the effect of the spin-orbit coupling.

We are going to focus on the most studied structure of TMDCs which is the 2H-MX_2 (M = transition metal, X = dichalcogenide) (space group: $P6_3/mmc$) (see Fig. 3.2). The monolayer is composed of an inner layer of M atoms on a triangular lattice sandwiched between two layers of X atoms lying on the triangular net of alternating hollow sites. Following standard notations,[57] we denote a as the distance between nearest neighbour in-plane M-M and X-X atoms, b as the nearest neighbour M-X distance and u as the distance between the M and X planes. The bulk structure is an $ABAB$ stacking of two of these monolayers separated by van der Waals gaps, one rotated with respect to each other by a screw axis along the z-direction.

3.1 DFT calculations and orbital character

In the construction of a reliable TB model for semiconducting dichalcogenides we will be guided by first-principles DFT calculations that will provide the reference against which to calibrate the TB model. We will focus here on 2H-MoS_2 (from now on we will refer to this structure simply as MoS_2) as a representative case, although we have performed first-principle calculations for comparison also on WS_2. The differences in the electronic structure and in the orbital character of these two compounds are, however, minimal and they do not involve any different physics.

The MoS_2 crystal forms an almost perfect trigonal prism structure with b and u very close to their ideal values $b \simeq \sqrt{7/12}a$ and $u \simeq a/2$. In our DFT calculations, we use experimental values for bulk MoS_2,[57] namely $a = 3.16$ Å, $u = 1.586$ Å, and, in bulk systems, a distance between Mo planes as $c' = 6.14$ Å, with a lattice constant in the MoS_2 structure of $c = 2c'$. The in-plane and out-of-plane S–S distances in the layer are 3.16 Å and 3.172 Å, respectively. The most important points in the Brillouin zone are the high-symmetry points which, in this case, are: $\Gamma = (0,0,0)$, K$= 4\pi/3a(1,0,0)$, and M$= 4\pi/3a(0,\sqrt{3}/2,0)$.

The electronic dispersion for the single-layer MoS_2 is nowadays well known. We will only focus on the block of bands containing the four lowest conduction bands and the seven highest

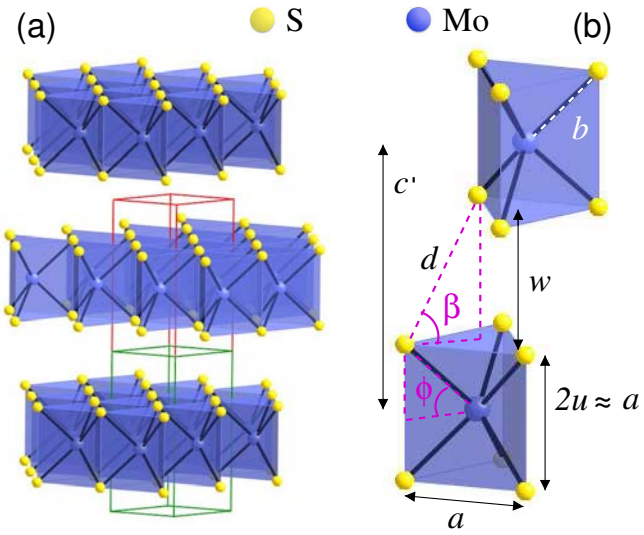

Figure 3.2: (a) Model of the atomic structure of TMDCs.The bulk compound has a 2H-MX_2 structure with two layers per unit cell, each layer being built up from a trigonal prism coordination unit. The small green rectangle represents the unit cell of a monolayer of MX_2, which is doubled (red extension) in the bulk crystal. (b) Detail of the trigonal prisms for the two layers in the bulk compound, showing the lattice constants and the definition of the structural angles used in the text.

valence bands, in an energy window of from -7 to 5 eV around the Fermi level. Our DFT calculations are shown in Fig. 3.3, where we also show the orbital character of each band. We use here the shorthand notation d_2 to denote Mo $4d_{x^2-y^2}$, $4d_{xy}$ orbitals; d_1 for the Mo $4d_{xz}$, $4d_{yz}$ orbitals; d_0 for the Mo $4d_{3z^2-r^2}$ orbital; p_{xy} (or simply p) to denote the S $3p_x$, $3p_y$ orbitals; and p_z (or simply z) for the S $3p_z$ orbital. The four conduction bands and the seven valence bands are mainly constituted by the five $4d$ orbitals of Mo and the six (three for each layer) $3p$ orbitals of S, which sum up to the 93% of the total orbital weight of these bands.

A special role in the electronic properties of these materials is played by the electronic states labeled as (A)-(D) and marked with black bullets in Fig. 3.3. A detailed analysis of the orbital character of each energy level at the main high-symmetry points of the Brillouin zone, as calculated by DFT, is provided in Table 3.1. We can notice that an accurate description of the conduction and valence band edges (A)-(B) at the K point involves at least the Mo orbitals $d_{3z^2-r^2}$, $d_{x^2-y^2}$, d_{xy}, and the S orbitals p_x, p_y. Along this perspective, a 5-band TB model, restricted to the subset of these orbitals, was presented in the work by Rostami and coworkers,[44] whereas even the S $3p$ orbitals were furthermore omitted in the work by Xiao and coworkers.[35]

The failure of this latter orbital restriction for a more comprehensive description is however pointed out when analyzing other relevant high-symmetry Brillouin points. In particular, concerning the valence band, we can notice a second maximum at the Γ point, labeled as (C) in Fig. 3.3, just 42 meV below the absolute band edge at the K point and with main d_0-p_z orbital character. The relevance of this secondary band extreme is evident in the multilayer compounds ($N \geq 2$), where such maximum at Γ increases its energy to become the absolute band edge.[48,50]

The band structure with the orbital character for the bulk ($N = \infty$) case, representative of the multilayer case, is shown in Fig. 3.4. A similar feature occurs at the band edge of the conduction band. Here a secondary minimum, labeled as (D) in Fig. 3.3, at $\mathrm{Q} = 4\pi/3a(1/2, 0, 0)$, midway along the Γ-K cut, is present in the single-layer compounds. Such minimum, however, moves down in energy in multilayer systems to become the effective conduction band edge.[48,50] Even in this case, a relevant p_z component is involved in the orbital character of this electronic

Energy DFT (eV)	Main orbital	Secondary orbital	Other orbitals	Symmetry	TB label
		Γ point			
2.0860*	68% $p_{x/y}$	29% d_2	3%	E	$E_{pd_2,+}(\Gamma)$
1.9432*	58% $p_{x/y}$	36% d_1	6%	O	$E_{pd_1,+}(\Gamma)$
-1.0341	66% d_0	28% p_z	6%	E	$E_{zd_0,+}(\Gamma)$
-2.3300*	54% d_1	42% $p_{x/y}$	4%	O	$E_{pd_1,-}(\Gamma)$
-2.6801	100% p_z	-	0%	O	$E_z(\Gamma)$
-3.4869*	65% d_2	32% $p_{x/y}$	3%	E	$E_{pd_2,-}(\Gamma)$
-6.5967	57% p_z	23% d_0	20%	E	$E_{zd_0,-}(\Gamma)$
		K point			
4.0127	60% d_1	36% p_z	4%	O	$E_{zd_1,+}(K)$
2.5269	65% d_2	29% p_z	6%	E	$E_{zd_2,+}(K)$
1.9891	50% d_1	31% $p_{x/y}$	19%	O	$E_{pd_1,+}(K)$
0.8162	82% d_0	12% $p_{x/y}$	6%	E	$E_{pd_0,+}(K)$
-0.9919	76% d_2	20% $p_{x/y}$	4%	E	$E_{pd_2,+}(K)$
-3.1975	67% p_z	27% d_1	6%	O	$E_{zd_1,-}(K)$
-3.9056	85% $p_{x/y}$	-	15%	O	$E_p(K)$
-4.5021	65% p_z	25% d_2	10%	E	$E_{zd_2,-}(K)$
-5.0782	71% $p_{x/y}$	12% d_2	17%	E	$E_{pd_2,-}(K)$
-5.5986	66% $p_{x/y}$	14% d_0	20%	E	$E_{pd_0,-}(K)$
-6.4158	60% $p_{x/y}$	37% d_1	3%	O	$E_{pd_1,-}(K)$

*Double-degenerate level

Table 3.1: Energy levels and orbital content of single-layer MoS_2 evaluated by DFT calculations. We report here the first two main orbital characters belonging to the blocks Mo-4d and S-3p, while the following column shows the remaining character not belonging to these orbital group. Also shown is the association of each level with the corresponding eigenvalue of the TB model and the symmetry with respect to the $z \to -z$ inversion (E=even, O=odd). The label $E_{\alpha\beta,\pm}$ in the last column denotes the orbital character of the TB eigenstate, with $\alpha, \beta = p, z, d_2, d_1, d_0$, where $p = p_x, p_y$, $z = p_z$, $d_2 = d_{x^2-y^2}, d_{xy}$, $d_1 = d_{xz}, d_{yz}$, $d_0 = d_{3z^2-r^2}$. The index $\pm$ denotes the higher energy [(+) = antibonding] and the lower energy [(−) = bonding].

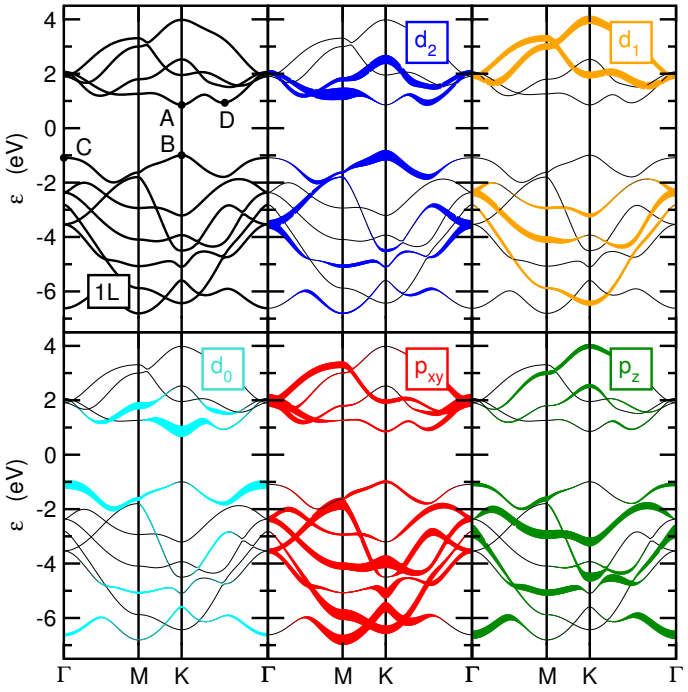

Figure 3.3: Band structure and orbital character of single-layer MoS_2. The top left panel shows the full band structure while, in the other panels, the thickness of the bands represents the orbital weight, where the d-character ($d_2 = d_{x^2-y^2}$, d_{xy}, $d_1 = d_{xz}$, d_{yz}, $d_0 = d_{3z^2-r^2}$) refers to the Mo atom $4d$ orbitals, while the p-character ($p_{xy} = p_x$, p_y) refers to $2p$ orbitals of sulfur.

state. The changes of the location of the band edges in the Brillouin zone are responsible for the observed switch from a direct to an indirect gap in multilayer samples. As we will see, thus, the inclusion of the p_z orbitals in the full TB Hamiltonian is not only desirable for a more complete description, but it is also unavoidable to understand the evolution of the band structure as a function of the number of layers.

3.2 Tight-binding description of the single-layer

The aim of this Section is to define a TB model for the single-layer which will be straightforwardly generalizable to the multilayer case by adding the appropriate interlayer hopping. We will show that, to this purpose, all the $4d$ Mo orbitals and the $3p$ S orbitals must be taken into account. Considering that the unit cell contains two S atoms, we define the Hilbert space by means of the 11-fold vector:

$$\phi_i^\dagger = (p_{i,x,t}^\dagger, p_{i,y,t}^\dagger, p_{i,z,t}^\dagger, d_{i,3z^2-r^2}^\dagger, d_{i,x^2-y^2}^\dagger, d_{i,xy}^\dagger, d_{i,xz}^\dagger, d_{i,yz}^\dagger, p_{i,x,b}^\dagger, p_{i,y,b}^\dagger, p_{i,z,b}^\dagger), \tag{3.1}$$

where $d_{i,\alpha}$ creates an electron in the orbital α of the Mo atom in the i-unit cell, $p_{i,\alpha,t}$ creates an electron in the orbital α of the top (t) layer S atom in the i-unit cell, and $p_{i,\alpha,b}$ creates an electron in the orbital α of the bottom (b) layer S atom in the i-unit cell.

Once the Hilbert space has been introduced, the TB model is defined by the hopping integrals between the different orbitals, described, in the framework of a Slater-Koster description, in terms of σ, π and δ ligands.[15] In order to provide a TB model as a suitable basis for the eventual inclusion of many-body effects by means of diagrammatic techniques, we assume that the basis orbitals are orthonormal, so that the overlap matrix is the unit matrix. A preliminary analysis based on the interatomic distance can be useful to identify the most relevant hopping

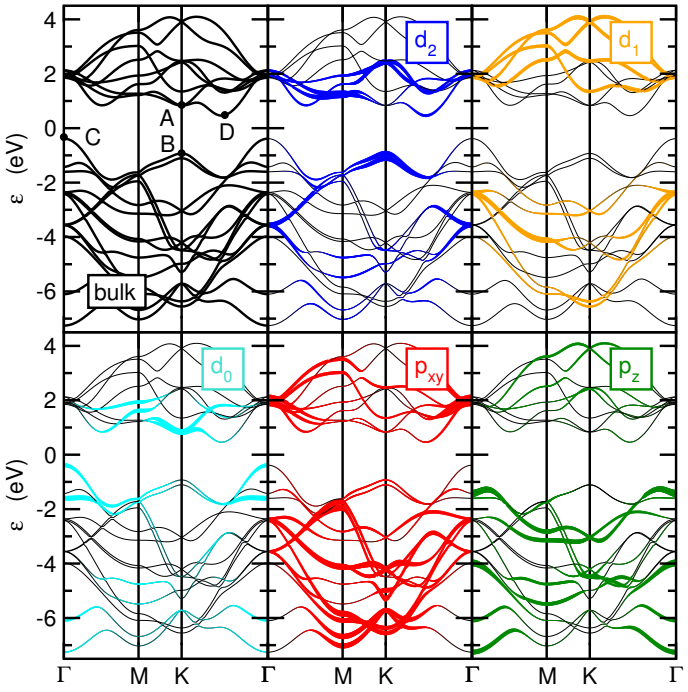

Figure 3.4: Band structure and orbital character for bulk 2H-MoS_2. Labels are as in Fig. 3.3.

processes. In particular, these are expected to be the ones between nearest neighbour Mo-S (interatomic distances $b = 2.41$ Å) and between the nearest neighbour in-plane Mo-Mo and between the nearest neighbour in-plane and out-of-plane S-S atoms. Further distant atomic bonds, in single-layer systems, start from hopping between second nearest neighbour Mo-S atoms, with interatomic distance 3.98 Å, and they will be here discarded.

All the hopping processes of the relevant pairs of neighbours are described in terms of the Slater-Koster parameters, respectively $V_{pd\sigma}$, $V_{pd\pi}$ (Mo-S bonds), $V_{dd\sigma}$, $V_{dd\pi}$, $V_{dd\delta}$ (Mo-Mo bonds), and $V_{pp\sigma}$, $V_{pp\pi}$ (S-S bonds). Additional relevant parameters are the crystal fields Δ_0, Δ_1, Δ_2, Δ_p, Δ_z, describing respectively the atomic level the $l = 0$ ($d_{3z^2-r^2}$), the $l = 1$ (d_{xz}, d_{yz}), the $l = 2$ ($d_{x^2-y^2}$, d_{xy}) Mo orbitals, the in-plane (p_x, p_y) S orbitals and of the out-of-plane p_z S orbitals. We end up with a total of 12 TB parameters to be determined, namely: Δ_0, Δ_1, Δ_2, Δ_p, Δ_z, $V_{dd\sigma}$, $V_{dd\pi}$, $V_{dd\delta}$, $V_{pp\sigma}$, $V_{pp\pi}$, $V_{pd\sigma}$, $V_{pd\pi}$.

In the orbital basis of Eq. (3.1), we can thus write the TB Hamiltonian in the form:

$$H = \sum_{\mathbf{k}} \phi^{\dagger}_{\mathbf{k}} \hat{H}_{\mathbf{k}} \phi_{\mathbf{k}}, \tag{3.2}$$

where $\phi_{\mathbf{k}}$ is the Fourier transform of ϕ_i in momentum space. The Hamiltonian matrix can be written (we drop for simplicity from now on the index $\mathbf{k}$) as:

$$\hat{H} = \begin{pmatrix} \hat{H}_{pt,pt} & \hat{H}^{\dagger}_{d,pt} & \hat{H}_{pt,pb} \\ \hat{H}_{d,pt} & \hat{H}_{d,d} & \hat{H}_{d,pb} \\ \hat{H}^{*}_{pt,pb} & \hat{H}^{\dagger}_{d,pb} & \hat{H}_{pb,pb} \end{pmatrix}, \tag{3.3}$$

where $\hat{H}_{pb,pb} = \hat{H}_{pt,pt}$ describes the in-plane hopping in the top and bottom S layer, namely,

$$\hat{H}_{pb,pb} = \hat{H}_{pt,pt} = \begin{pmatrix} H_{x/x} & H_{x/y} & 0 \\ H^{*}_{x/y} & H_{y/y} & 0 \\ 0 & 0 & H_{z/z} \end{pmatrix}, \tag{3.4}$$

$\hat{H}_{d,d}$ the in-plane hopping in the middle Mo layer, namely,

$$\hat{H}_{d,d} = \begin{pmatrix} H_{z^2/z^2} & H_{z^2/x^2} & H_{z^2/xy} & 0 & 0 \\ H^*_{z^2/x^2} & H_{x^2/x^2} & H_{x^2/xy} & 0 & 0 \\ H^*_{z^2/xy} & H^*_{x^2/xy} & H_{xy/xy} & 0 & 0 \\ 0 & 0 & 0 & H_{xz/xz} & H_{xz/yz} \\ 0 & 0 & 0 & H^*_{xz/yz} & H_{yz/yz} \end{pmatrix}, \tag{3.5}$$

$\hat{H}_{pt,pb}$ the vertical hopping between S orbitals in the top and bottom layer,

$$\hat{H}_{pt,pb} = \begin{pmatrix} V_{pp\pi} & 0 & 0 \\ 0 & V_{pp\pi} & 0 \\ 0 & 0 & V_{pp\sigma} \end{pmatrix}, \tag{3.6}$$

and $\hat{H}_{d,pt}$, $\hat{H}_{d,pb}$ the hopping between Mo and S atoms in the top and bottom planes, respectively:

$$\hat{H}_{d,pt} = \begin{pmatrix} H_{z^2/x} & H_{z^2/y} & H_{z^2/z} \\ H_{x^2/x} & H_{x^2/y} & H_{x^2/z} \\ H_{xy/x} & H_{xy/y} & H_{xy/z} \\ H_{xz/x} & H_{xz/y} & H_{xz/z} \\ H_{yz/x} & H_{yz/y} & H_{yz/x} \end{pmatrix}, \tag{3.7}$$

$$\hat{H}_{d,pb} = \begin{pmatrix} H_{z^2/x} & H_{z^2/y} & -H_{z^2/z} \\ H_{x^2/x} & H_{x^2/y} & -H_{x^2/z} \\ H_{xy/x} & H_{xy/y} & -H_{xy/z} \\ -H_{xz/x} & -H_{xz/y} & H_{xz/z} \\ -H_{yz/x} & -H_{yz/y} & H_{yz/x} \end{pmatrix}. \tag{3.8}$$

Here and in the following, for the sake of compactness, we use the shorthand notation $3z^2-r^2 \Rightarrow z^2$ and $x^2-y^2 \Rightarrow x^2$. An explicit expression for the different Hamiltonian matrix elements in terms of the Slater-Koster TB parameters can be provided following the seminal work by Doran *et al.*[100] and it is reported for completeness in Appendix B.

Eqs. (3.2)-(3.8) define our TB model in terms of an 11×11 Hamiltonian, $\hat{H}$, which can be now explicitly solved to get eigenvalues and eigenvectors in the whole Brillouin zone or along the main axes of high symmetry. It is now an appealing task to associate each DFT energy level with the Hamiltonian eigenvalues, whose eigenvectors will shed light on the properties of the electronic states. Along this line, we are helped by symmetry arguments which allow, in the monolayer compounds, to decouple the 11×11 Hamiltonian in Eq. (3.3), in two main blocks, with different symmetry with respect to the mirror inversion $z \to -z$.[100] This task is accomplished by introducing a symmetric and antisymmetric linear combination of the p orbital of the S atoms on the top/bottom layers. More explicitly, we use the basis vector

$$\tilde{\phi}^\dagger_k = (d^\dagger_{k,3z^2-r^2}, d^\dagger_{k,x^2-y^2}, d^\dagger_{k,xy}, p^\dagger_{k,x,S}, p^\dagger_{k,y,S}, p^\dagger_{k,z,A}, d^\dagger_{k,xz}, d^\dagger_{k,yz}, p^\dagger_{k,x,A}, p^\dagger_{k,y,A}, p^\dagger_{k,z,S}), \tag{3.9}$$

where $p^\dagger_{k,\alpha,S} = (p^\dagger_{k,\alpha,t} + p^\dagger_{k,\alpha,b})/\sqrt{2}$, $p^\dagger_{k,\alpha,A} = (p^\dagger_{k,\alpha,t} - p^\dagger_{k,\alpha,b})/\sqrt{2}$.

In this basis we can write

$$\hat{H} = \begin{pmatrix} \hat{H}_{\rm E} & 0 \\ 0 & \hat{H}_{\rm O} \end{pmatrix}, \tag{3.10}$$

where $\hat{H}_{\mathrm{E}}$ is a 6×6 block with even (E) symmetry with respect to the mirror inversion $z \to -z$, and $\hat{H}_{\mathrm{O}}$ a 5×5 block with odd (O) symmetry. We should remark, however, that such decoupling holds true only in the single-layer case and only in the absence of a z-axis electric field, as can be induced by substrates or under gating conditions. In the construction of a TB model that could permit a direct generalization to the multilayer case, the interaction between the band blocks with even and odd symmetry should be thus explicitly retained.

The association between DFT energy levels and TB eigenstates is now further simplified on specific high-symmetry points of the Brillouin zone. Most important are the K and the Γ points, which define the direct and indirect gap in monolayer and multilayered compounds.

3.2.1 Γ point

We present here a detailed analysis of the eigenstates and their orbital character at the Γ point. For the sake of simplicity, we discuss separately the blocks with even and odd symmetry with respect to the inversion $z \to -z$. The identification of the DFT levels with the TB eigenstates is facilitated by the possibility of decomposing the full Hamiltonian in smaller blocks, with typical size 2×2 (dimers) or 1×1 (monomers). In particular, the 6×6 block with even symmetry can be decomposed (see Appendix C for details) as:

$$\hat{H}_{\mathrm{E}}(\Gamma) \;=\; \begin{pmatrix} \hat{H}_{zd_0}(\Gamma) & 0 & 0 \\ 0 & \hat{H}_{pd_2}(\Gamma) & 0 \\ 0 & 0 & \hat{H}_{pd_2}(\Gamma) \end{pmatrix}. \tag{3.11}$$

Here, each matrix, $\hat{H}_{pd_2}$, $\hat{H}_{zd_0}$ represents a 2×2 block where the indices describe the orbital character of the dimer. In particular, $\hat{H}_{pd_2}$ involves only $d_2 = d_{x^2-y^2}, d_{xy}$ Mo-orbitals and p_x, p_y S-orbitals, whereas $\hat{H}_{zd_0}$ involves only the $d_0 = d_{3z^2-r^2}$ Mo-orbital and the p_z S-orbital. As it is evident in Eq. (3.11), the block $\hat{H}_{pd_2}$ appears twice and it is thus doubly degenerate. Similarly, we have

$$\hat{H}_{\mathrm{O}}(\Gamma) \;=\; \begin{pmatrix} \hat{H}_{pd_1}(\Gamma) & 0 & 0 \\ 0 & \hat{H}_{pd_1}(\Gamma) & 0 \\ 0 & 0 & \Gamma_z^{\mathrm{O}} \end{pmatrix}, \tag{3.12}$$

where the doubly degenerate block $\hat{H}_{pd_1}$ involves only $d_1 = d_{xz}, d_{yz}$ Mo-orbitals and p_x, p_y S-orbitals, while Γ_z^{O} is a 1×1 block (monomer) with pure character p_z.

It is also interesting to give a closer look at the inner structure of a generic Hamiltonian sub-block. Considering, for instance, $\hat{H}_{zd_0}$ as an example, we can write

$$\hat{H}_{zd_0}(\Gamma) \;=\; \begin{pmatrix} \Gamma_0 & \sqrt{2}\Gamma_{zd_0} \\ \sqrt{2}\Gamma_{zd_0} & \Gamma_z^{\mathrm{E}} \end{pmatrix}, \tag{3.13}$$

where Γ_0 is an energy level with pure Mo d_0 orbital character and Γ_z^{E} an energy level with pure S p_z orbital character. Thus, the off-diagonal term $\sqrt{2}\Gamma_{zd_0}$ acts here as a "hybridization", mixing the pure orbital character of Γ_0 and Γ_z^{E}. The suffix "E" here reminds that the level Γ_z^{E} belongs to the even symmetry block, and it is useful to distinguish this state from a similar one with odd symmetry (and different energy). Keeping $\hat{H}_{zd_0}$ as an example, the eigenvalues of a generic 2×2 block can be obtained analytically:

$$E_{zd_0,\pm}(\Gamma) \;=\; \frac{\Gamma_0 + \Gamma_z^{\mathrm{E}}}{2} \pm \sqrt{\left(\frac{\Gamma_0 - \Gamma_z^{\mathrm{E}}}{2}\right)^2 + 2\Gamma_{zd_0}^2}. \tag{3.14}$$

The explicit expressions of Γ_α and $\Gamma_{\alpha\beta}$ in terms of the Slater-Koster TB parameters is reported in Appendix B.

It is interesting to note that the diagonal terms Γ_α ($\alpha = d_0, d_1, d_2, p, z$) are purely determined by the crystal fields Δ_α and by the TB parameters $V_{dd\sigma}$, $V_{dd\pi}$, $V_{dd\delta}$, $V_{pp\sigma}$, $V_{pp\pi}$, connecting Mo-Mo and S-S atoms, whereas the hybridization off-diagonal terms $\Gamma_{\alpha\beta}$ depend exclusively on the Mo-S nearest neighbour hopping $V_{pd\sigma}$, $V_{pd\pi}$.

A careful comparison between the orbital character of each eigenvector with the DFT results permits now to identify in an unambiguous way each DFT energy level with its analytical TB counterpart. Such association is reported in Table 3.1, where also the even/odd symmetry inversion is considered.

The use of the present analysis to characterize the properties of the multilayer MoS_2 will be discussed in Section 3.3.

3.2.2 K point

The K point of the Brillouin zone plays a crucial role influencing the properties of semiconducting dichalcogenides as the direct semiconducting gap occurs at this point for the single-layer systems. The detailed analysis of the electronic spectrum is also favored here by the possibility of reducing the complex 11×11 Hamiltonian in smaller sub-blocks. This feature is, however, less evident than at the Γ point. The even and odd components of the Hamiltonian take the form:

$$\hat{H}_{\rm E}({\rm K}) = \begin{pmatrix} K_0 & 0 & 0 & -i\sqrt{2}K_{pd_0} & \sqrt{2}K_{pd_0} & 0 \\ 0 & K_2 & 0 & i\sqrt{2}K_{pd_2} & \sqrt{2}K_{pd_2} & \sqrt{2}K_{zd_2} \\ 0 & 0 & K_2 & -\sqrt{2}K_{pd_2} & i\sqrt{2}K_{pd_2} & -i\sqrt{2}K_{zd_2} \\ i\sqrt{2}K_{pd_0} & -i\sqrt{2}K_{pd_2} & -\sqrt{2}K_{pd_2} & K_p^{\rm E} & 0 & 0 \\ \sqrt{2}K_{pd_0} & \sqrt{2}K_{pd_2} & -i\sqrt{2}K_{pd_2} & 0 & K_p^{\rm E} & 0 \\ 0 & \sqrt{2}K_{zd_2} & i\sqrt{2}K_{zd_2} & 0 & 0 & K_z^{\rm E} \end{pmatrix}, \quad (3.15)$$

$$\hat{H}_{\rm O}({\rm K}) = \begin{pmatrix} K_1 & 0 & \sqrt{2}K_{pd_1} & -i\sqrt{2}K_{pd_1} & -i\sqrt{2}K_{zd_1} \\ 0 & K_1 & -i\sqrt{2}K_{pd_1} & -\sqrt{2}K_{pd_1} & \sqrt{2}K_{zd_1} \\ \sqrt{2}K_{pd_1} & i\sqrt{2}K_{pd_1} & K_p^{\rm O} & 0 & 0 \\ i\sqrt{2}K_{pd_1} & -\sqrt{2}K_{pd_1} & 0 & K_p^{\rm O} & 0 \\ i\sqrt{2}K_{zd_1} & \sqrt{2}K_{zd_1} & 0 & 0 & K_z^{\rm O} \end{pmatrix}. \quad (3.16)$$

As for the Γ point, also here the upper labels (μ = E, O) in K_α^μ (μ = E, O) express the symmetry of the state corresponding to the energy level K_α^μ with respect to the $z \to -z$ inversion. The electronic properties of the Hamiltonian at the K point look more transparent by introducing a different "chiral" base:

$$\bar{\psi}_k^\dagger = (d^\dagger_{k,3z^2-r^2}, d^\dagger_{k,L2}, d^\dagger_{k,R2}, p^\dagger_{k,L,S}, p^\dagger_{k,R,S}, p^\dagger_{k,z,A}, d^\dagger_{k,L1}, d^\dagger_{k,R1}, p^\dagger_{k,L,A}, p^\dagger_{k,R,A}, p^\dagger_{k,z,S}), \quad (3.17)$$

where $d_{k,L2} = (d_{k,x^2-y^2} - id_{k,xy})/\sqrt{2}$, $d_{k,R2} = (d_{k,x^2-y^2} + id_{k,xy})/\sqrt{2}$, $d_{k,L1} = (d_{k,xz} - id_{k,yz})/\sqrt{2}$, $d_{k,R1} = (d_{k,xz} + id_{k,yz})/\sqrt{2}$, $p_{k,L,S} = (p_{k,x,S} - ip_{k,y,S})/\sqrt{2}$, $p_{k,R,S} = (p_{k,x,S} + ip_{k,y,S})/\sqrt{2}$, $p_{k,L,A} = (p_{k,x,A} - ip_{k,y,A})/\sqrt{2}$, $p_{k,R,A} = (p_{k,x,A} + ip_{k,y,A})/\sqrt{2}$.

In this basis, the Hamiltonian matrix can be also divided in smaller sub-blocks (see Appendix C) as:

$$\hat{H}_{\rm E}({\rm K}) = \begin{pmatrix} \hat{H}_{pd_0}({\rm K}) & 0 & 0 \\ 0 & \hat{H}_{zd_2}({\rm K}) & 0 \\ 0 & 0 & \hat{H}_{pd_2}({\rm K}) \end{pmatrix}, \quad (3.18)$$

and

$$\hat{H}_{\mathrm{O}} = \begin{pmatrix} \hat{H}_{pd_1}(\mathrm{K}) & 0 & 0 \\ 0 & \hat{H}_{zd_1}(\mathrm{K}) & 0 \\ 0 & 0 & K_p^{\mathrm{O}} \end{pmatrix}. \tag{3.19}$$

As it is evident from the labels, each sub-block is also here a 2×2 dimer, apart from the term K_p^O which is a 1×1 block (monomer) with pure p_x, p_y character. The association between the DFT energy levels and the TB eigenstates is reported also for the K point in Table 3.1.

3.2.3 Q point

As discussed above, another special point determining the electronic properties of MoS_2 is the Q point, halfway between the Γ and K points in the Brillouin zone, where the conduction band, in the single-layer system, has a secondary minimum in addition to the absolute one at the K point. Unfortunately, not being a point of high-symmetry, the TB Hamiltonian cannot be decomposed in this case in simpler smaller blocks. Each energy eigenvalue will contain, thus, a finite component of all the Mo and S orbitals. In particular, focusing on the secondary minimum in Q, DFT calculations give 46 % d_2, 24 % $p_{x/y}$, 11 % p_z and 9 % d_0. The orbital content of this level will play a crucial role in determining the band structure of multilayer compounds.

3.2.4 Orbital constraints for a tight-binding model

After having investigated in detail the orbital contents of each eigenstate at the high-symmetry points and having identified them with the corresponding DFT energy levels, we can now employ such analysis to assess the basic conditions that a TB model must fulfill and to elucidate the physical consequences.

A first interesting issue is about the minimum number of orbitals needed to be taken into account in a TB model for a robust description of the electronic properties of these materials. A proper answer to such issue is, of course, different if referred to single-layer or multilayer compounds. For the moment we focus only on the single-layer case but we will emphasize the way the relevant features that will be needed to take into account in multi-layer systems.

In the single-layer case, focusing only on the band edges determined by the states (A) and (B) at the K point, we can identify them with the eigenstates $E_{pd_0,+}(K)$, $E_{pd_2,+}(K)$, respectively, with a dominant Mo $4d$ character and a marginal S $p_{x/y}$ component, as we show below. It is thus tempting to define a reduced 3-band TB model, keeping only the Mo $4d_{3z^2-r^2}$, $4d_{x^2-y^2}$, $4d_{xy}$ orbitals with dominant character and disregarding the S p_x, p_y orbitals, with a small marginal weight. A similar phenomenological model was proposed in the work by Xiao *et al.*[35] However, the full microscopic description here exposed permits to point out the inconsistency of such a model. This can be shown by looking at Eq. (3.18). The band gap at K in the full TB model including S p_x, p_y orbitals is determined by the upper eigenstate of $\hat{H}_{pd_0}$,

$$E_{pd_0,+}(K) = \frac{K_0 + K_p^{\mathrm{E}}}{2} + \sqrt{\left(\frac{K_0 - K_p^{\mathrm{E}}}{2}\right)^2 + 4K_{pd_0}^2}, \tag{3.20}$$

and the upper eigenstate of $\hat{H}_{pd_2}$,

$$E_{pd_2,+}(K) = \frac{K_2 + K_p^{\mathrm{E}}}{2} + \sqrt{\left(\frac{K_2 - K_p^{\mathrm{E}}}{2}\right)^2 + 8K_{pd_2}^2}, \tag{3.21}$$

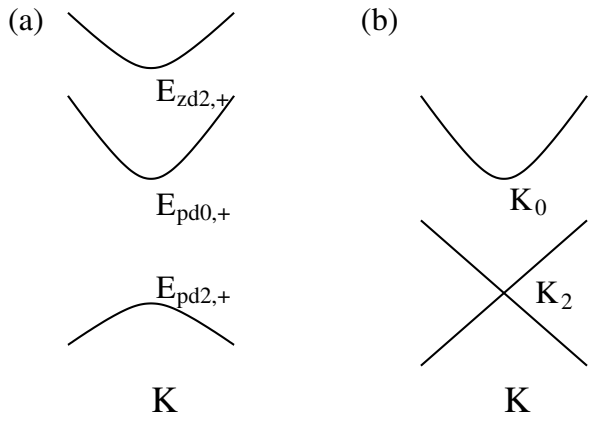

Figure 3.5: Schematic band structure close to the K point for the valence and conduction bands: (a) including S p_x, p_y orbitals; (b) omitting S p_x, p_y orbitals.

both with main Mo 4*d* character, while the eigenstate

$$E_{zd_2,+}(K) = \frac{K_2 + K_z^{\mathrm{E}}}{2} + \sqrt{\left(\frac{K_2 - K_z^{\mathrm{E}}}{2}\right)^2 + 4K_{zd_2}^2}, \tag{3.22}$$

also with dominant Mo 4*d* character, but belonging to the block $\hat{H}_{zd_2}$, lies at higher energy (see Table 3.1). The 3-band model retaining only the d_0, d_2 orbitals is equivalent to switch off the hybridization terms K_{pd_0}, K_{pd_2}, K_{zd_2}, ruled by $V_{pd\sigma}$, $V_{pd\pi}$, so that $E_{pd_0,+}(K) = K_0$, $E_{pd_2,+}(K) = E_{zd_2,+}(K) = K_2$. In this context, the level $E_{zd_2,+}(K)$ becomes degenerate with $E_{pd_2,+}(K)$. This degeneracy is not accidental but it reflects the fact that the elementary excitations of the d_2 states, in this simplified model, are described by a Dirac spectrum, as sketched in Fig. 3.5. As a consequence, no direct gap can be possibly established in this framework. It is worth mentioning that a spin-orbit coupling can certainly split the Dirac cone to produce a direct gap at the K point, but it would not explain in any case the direct gap observed in the DFT calculations without spin-orbit coupling.

We should also mention that, in the same reduced 3-band model keeping only the d_0 and d_2 Mo orbitals, the secondary maximum (C) of the valence band would have a pure d_0 orbital character. As we are going to see in the discussion concerning the multilayer samples, this would have important consequences on the construction of a proper TB model.

A final consideration concerns the orbital character of the valence band edge, $E_{pd_2,+}(K)$. This state is associated with the third 2×2 block of Eq. (3.18) and it results from the hybridization of the chiral state $d_{k,R2} = (d_{k,x^2-y^2} + id_{k,xy})/\sqrt{2}$ of the Mo d orbitals with the chiral state $p_{k,R,S} = (p_{k,x,S} + ip_{k,y,S})/\sqrt{2}$ of the S p orbitals. The role of the chirality associated with the d orbitals, in the presence of a finite spin-orbit coupling, has been discussed in detail in relation with spin/valley selective probes.[31–37] What results from a careful TB description is that such d-orbital chirality is indeed entangled with a corresponding chirality associated with the S p orbitals. The possibility of such entanglement, dictated by group theory, was pointed out in the work by Ochoa *et al.*[38]

A similar feature is found for the conduction band edge, $E_{pd_0,+}(K)$. So far, this state has been assumed to be mainly characterized by the $d_{3z^2-r^2}$ character, and hence without an orbital moment. However, as we can see, this is true only for the Mo d part, whereas the S p component does contain a finite chiral moment. On the other hand, the spin-orbit coupling associated with the S atoms as well as with other chalcogenides (e. g., Se) is quite small, and taking into account also the small orbital S weight, the possibility of a direct probe of such orbital moment is still to be explored.

3.3 Tight-binding description of the bulk system

In the previous Section we have examined in detail the content of the orbital character in the main high-symmetry points of the Brillouin zone of the single-layer MoS_2, to provide theoretical constraints on the construction of a suitable TB model. Focusing on the low-energy excitations close to the direct gap at the K point, we have seen that a proper model must take into account at least the three Mo orbitals $d_{3z^2-r^2}$, $d_{x^2-y^2}$, d_{xy} and the two S orbitals p_x, p_y. On the other hand, our wider aim is to introduce a TB model for the single-layer that would be the basic ingredient for a TB model in *multilayer* systems, simply adding the interlayer coupling.

For the sake of simplicity, as in the previous Section, we focus here on the bulk MoS_2 structure as a representative case that contains already all the ingredients of the physics of multilayer compounds. The band structure for the bulk compound is shown in Fig. 3.4. As it is known, the secondary maximum (C) of the valence band at the Γ point is shifted to higher energies in multilayer systems with respect to the single-layer case, becoming the valence band maximum. At the same time, also the secondary minimum (D) of the conduction band, roughly at the Q point, is lowered in energy, becoming the conduction band minimum. All these changes result in a transition between a direct gap material in single-layer compounds to indirect gap systems in the multilayer case. Although such an intriguing feature has been discussed extensively and experimentally observed, the underlying mechanism has not been so far elucidated. We show here that such transition can be naturally explained within the context of a TB model as a result of an orbital selective (and hence momentum dependent) band splitting induced by the interlayer hopping.

The orbital content of the bulk band structure along the same high-symmetry lines as in the single-layer case is shown in Fig. 3.4. We focus first on the K point, where the single-layer system has a direct gap. We note that the direct gap at K is hardly affected. The interlayer coupling produces just a very tiny splitting of the valence band edge $E_{pd_2,+}(K)$, while the conduction band edge $E_{pd_0,+}(K)$ at K becomes doubly degenerate.

Things are radically different at the Γ point. The analysis of the orbital weight $d_{3z^2-r^2}$ in Fig. 3.4 shows indeed that there is a sizable splitting of the $E_{zd_0,+}(\Gamma)$ level, of the order of 1 eV. A bit more difficult to discern, because of the multi-orbital component, but still visible, is the splitting of the secondary minimum (D) of the conduction band in Q. This is clearly detected by looking in Fig. 3.4 at the d_2 and d_0 characters, which belong only to the E block. One can thus estimate from DFT a splitting of this level at the Q point of ~ 1.36 eV.

We are now going to see that all these features are consistent with a TB construction where the interlayer hopping acts as an additional parameter with respect to the single-layer TB model. From the TB point of view, it is clear that the main processes to be included are the interlayer hoppings between the external S planes of each MoS_2 block. This shows once more the importance of including the S p orbital in a reliable TB model. Moreover, for geometric reasons, one could expect that the interlayer hopping between the p_z orbitals, pointing directly out-of-plane, would be dominant with respect to the interlayer hopping between p_x and p_y. This qualitative argument is supported by the DFT results, which indeed report a large splitting of the $E_{zd_0,+}(\Gamma)$ level at the Γ point, with 27% of the p_z component, but almost no splitting of the degenerate $E_{pd_2,+}(\Gamma)$ at ~ 2 eV, with 68% component of p_x, p_y.

We can quantify this situation within the TB description by including explicitly the interlayer hopping between the p orbitals of the S atoms in the outer planes of each MoS_2 layer, with interatomic distance $d = 3.49$ Å (see Fig. 3.2). These processes will be parametrized in terms of the interlayer Slater-Koster ligands $U_{pp\sigma}$, $U_{pp\pi}$. The Hilbert space is now determined by a 22-fold vector, defined as:

$$\tilde{\Phi}_k^\dagger = (\tilde{\phi}_{k,1}^\dagger, \tilde{\phi}_{k,2}^\dagger), \tag{3.23}$$

where $\tilde{\phi}^{\dagger}_{k,1}$ represents the basis (Eq. (3.9)) for the layer 1, and $\tilde{\phi}^{\dagger}_{k,2}$ the same quantity for the layer 2. The corresponding Hamiltonian, in the absence of interlayer hopping, would read thus:

$$\hat{H}_{\text{bulk}} = \begin{pmatrix} \hat{H}_1 & \hat{0} \\ \hat{0} & \hat{H}_2 \end{pmatrix}, \tag{3.24}$$

where $\hat{H}_1$, $\hat{H}_2$ refer to the intralayer Hamiltonian for the layer 1 and 2, respectively.

Note that the Hamiltonian of layer 2 in the MoS_2 structure is different with respect to the one of layer 1. From a direct inspection we can see that the elements $H_{2,\alpha,\beta}(\xi,\eta)$ of layer 2 are related to the corresponding elements of layer 1 as:

$$H_{2,\alpha,\beta}(\xi,\eta) = P_\alpha P_\beta H_{1,\alpha,\beta}(\xi,-\eta), \tag{3.25}$$

where $\xi = k_x a/2$, $\eta = \sqrt{3}k_y a/2$, and $P_\alpha = 1$ if the orbital α has even symmetry for $y \to -y$, and $P_\alpha = -1$ if it has odd symmetry. We note that both effects can be re-absorbed in a different definition of the orbital basis so that the eigenvalues of $\hat{H}_2$ are of course the same as the eigenvalues of $\hat{H}_1$.

Taking into account the inter-layer S-S hopping terms, we can write thus:

$$\hat{H}_{\text{bulk}} = \begin{pmatrix} \hat{H}_1 & \hat{H}_\perp \\ \hat{H}^{\dagger}_\perp & \hat{H}_2 \end{pmatrix}, \tag{3.26}$$

where $\hat{H}_\perp$ is here the interlayer hopping Hamiltonian, namely:

$$\hat{H}_\perp = \begin{pmatrix} \hat{I}_{\text{E}} \cos\zeta & \hat{I}_{\text{EO}} \sin\zeta \\ -\hat{I}^{\text{T}}_{\text{EO}} \sin\zeta & \hat{I}_{\text{O}} \cos\zeta \end{pmatrix}, \tag{3.27}$$

where $\zeta = k_z c/2$ and

$$\hat{I}_{\text{E}} = \begin{pmatrix} \hat{0}_{3\times3} & \hat{0}_{3\times3} \\ \hat{0}_{3\times3} & \hat{I} \end{pmatrix}, \tag{3.28}$$

$$\hat{I}_{\text{O}} = \begin{pmatrix} \hat{0}_{2\times2} & \hat{0}_{2\times3} \\ \hat{0}_{3\times2} & \hat{I} \end{pmatrix}, \tag{3.29}$$

$$\hat{I}_{\text{EO}} = \begin{pmatrix} \hat{0}_{3\times2} & \hat{0}_{3\times3} \\ \hat{0}_{3\times2} & i\hat{I} \end{pmatrix}, \tag{3.30}$$

$$\hat{I} = \begin{pmatrix} I_{x/x} & I_{x/y} & I_{x/z} \\ I_{x/y} & I_{y/y} & I_{y/z} \\ I_{x/z} & I_{y/z} & I_{z/z} \end{pmatrix}. \tag{3.31}$$

The analytical expression of the elements $I_{\alpha/\beta}$ as functions of the Slater-Koster interlayer parameters $U_{pp\sigma}$, $U_{pp\pi}$ is provided in Appendix B. Note that, in the presence of interlayer hopping in the bulk MoS_2, we cannot divide anymore, for generic momentum $\mathbf{k}$, the 22×22 Hamiltonian in smaller blocks with even and odd symmetry with respect to the change $z \to -z$. The analysis is however simplified at specific high-symmetry points of the Brillouin zone. In particular, for $k_z = 0$ ($\zeta = 0$), we can easily see from Eq. (3.27) that the block 12×12 ($6\times6 + 6\times6$) with even symmetry and the block 10×10 ($5\times5 + 5\times5$) with odd symmetry are still decoupled.

Exploiting this feature, we can now give a closer look at the high-symmetry points.

3.3.1 Γ point

In Section 3.2 we have seen that at the Γ point the Hamiltonian can be decomposed in 2×2 blocks. Particularly important here is the block H_{zd_0} whose upper eigenvalue $E_{zd_0,+}(\Gamma)$, with main orbital character $d_{3z^2-r^2}$ and a small p_z component, represents the secondary maximum (C) of the valence band. A first important property to be stressed in bulk systems is that, within this (Mo $4d$)+(S $3p$) TB model, the interlayer coupling at the Γ point does not mix any additional orbital character. This can be seen by noticing that the interlayer matrix $\hat{I}$ is diagonal at the Γ point. Focusing on the $E_{zd_0}(\Gamma)$ levels, we can write thus a 4×4 reduced Hamiltonian (see Appendix C):

$$\hat{H}_{zd_0} = \begin{pmatrix} \Gamma_0 & \sqrt{2}\Gamma_{zd_0} & 0 & 0 \\ \sqrt{2}\Gamma_{zd_0} & \Gamma_z^{\mathrm{E}} & 0 & \Gamma_{zz} \\ 0 & 0 & \Gamma_0 & \sqrt{2}\Gamma_{zd_0} \\ 0 & \Gamma_{zz} & \sqrt{2}\Gamma_{zd_0} & \Gamma_z^{\mathrm{E}} \end{pmatrix}, \tag{3.32}$$

where Γ_{zz} represents the interlayer hopping mediated by $U_{pp\sigma}$, $U_{pp\pi}$ between p_z orbitals belonging to the outer S planes on different layers. Eq. (3.32) is important because it shows the correctness of the qualitative idea that each energy level in the bulk system is just split by the interlayer hopping. In particular, under the reasonable hypothesis that the interlayer hopping is much smaller than intralayer processes, denoting $E_{zd_0,+a}(\Gamma)$, $E_{zd_0,+b}(\Gamma)$ the two eigenvalues with primary d_0 components, we get:

$$\begin{aligned} \Delta E_{zd_0,+}(\Gamma) &= E_{zd_0,+a}(\Gamma) - E_{zd_0,+b}(\Gamma) \\ &\approx \Gamma_{zz} \left[\frac{\Gamma_0 - \Gamma_z^{\mathrm{E}}}{2\sqrt{\left(\frac{\Gamma_0 - \Gamma_z^{\mathrm{E}}}{2}\right)^2 + 2\Gamma_{zd_0}}} - 1 \right] \\ &= \Gamma_{zz} \left[\frac{\Gamma_0 - \Gamma_z^{\mathrm{E}}}{E_{zd_0,+}(\Gamma) - E_{zd_0,-}(\Gamma)} - 1 \right]. \end{aligned} \tag{3.33}$$

A similar situation is found for the other 2×2 blocks $\hat{H}_{pd_2}(\Gamma)$, $\hat{H}_{pd_1}(\Gamma)$, and the 1×1 block $\hat{H}_z(\Gamma)$. Most important, tracking the DFT levels by means of their orbital content, we can note that both levels $E_{zd0,+}(\Gamma)$ and $E_{zd0,-}(\Gamma)$ undergo a quite large splitting ≈ 1.2 eV, and the level $E_z(\Gamma)$ a splitting ≈ 2.6 eV, whereas the levels $\hat{H}_{pd_2}(\Gamma)$, $\hat{H}_{pd_1}(\Gamma)$ are almost unsplit. This observation strongly suggest that, as expected, the interlayer hopping between p_x, p_y orbitals is much less effective than the interlayer hopping between p_z.

3.3.2 K point

A similar conclusion can be drawn from the investigation of the energy levels at the K point, although the analysis is a bit more complicated.

The properties of the bulk system at the K point are dictated by the structure of the interlayer matrix $\hat{I}$ which, in the basis defined in Eq. (3.23), at the K point reads:

$$\hat{I}_{66}(K) = \begin{pmatrix} K_{pp} & iK_{pp} & iK_{pz} \\ iK_{pp} & -K_{pp} & K_{pz} \\ iK_{pz} & K_{pz} & 0 \end{pmatrix}. \tag{3.34}$$

As discussed in detail in Appendix C, the electronic structure is made more transparent by using an appropriate chiral basis, which is a direct generalization of the one for the single-layer.

We can thus write the even and odd parts of the resulting Hamiltonian in the form:

$$\hat{H}_{\mathrm{E}}(K) = \begin{pmatrix} \hat{H}_{pzd_{02}}(K) & 0 & 0 \\ 0 & \hat{H}_{pzd_{02}}(K) & 0 \\ 0 & 0 & \hat{H}_{pd_2,\mathrm{E}}(K) \end{pmatrix}, \tag{3.35}$$

$$\hat{H}_{\mathrm{O}}(K) = \begin{pmatrix} \hat{H}_{pzd_1}(K) & 0 & 0 \\ 0 & \hat{H}_{pzd_1}(K) & 0 \\ 0 & 0 & \hat{H}_{pd_1,\mathrm{O}}(K) \end{pmatrix}, \tag{3.36}$$

where

$$\hat{H}_{pzd_{02}}(K) = \begin{pmatrix} K_0 & -2iK_{pd_0} & 0 & 0 \\ 2iK_{pd_0} & K_p^{\mathrm{E}} & 0 & i\sqrt{2}K_{pz} \\ 0 & 0 & K_2 & 2K_{zd_2} \\ 0 & -i\sqrt{2}K_{pz} & 2K_{zd_2} & K_z^{\mathrm{E}} \end{pmatrix}, \tag{3.37}$$

$$\hat{H}_{pd_2,\mathrm{E}}(K) = \begin{pmatrix} K_2 & i\sqrt{8}K_{pd_2} & 0 & 0 \\ -i\sqrt{8}K_{pd_2} & K_p^{\mathrm{E}} & 0 & 2K_{pp} \\ 0 & 0 & K_2 & i\sqrt{8}K_{pd_2} \\ 0 & 2K_{pp} & -i\sqrt{8}K_{pd_2} & K_p^{\mathrm{E}} \end{pmatrix}, \tag{3.38}$$

$$\hat{H}_{pzd_1}(K) = \begin{pmatrix} K_1 & -2iK_{zd_1} & 0 \\ 2iK_{zd_1} & K_z^{\mathrm{O}} & 0 \\ 0 & 0 & K_p^{\mathrm{O}} \end{pmatrix}, \tag{3.39}$$

$$\hat{H}_{pd_1,\mathrm{O}}(K) = \begin{pmatrix} K_1 & \sqrt{8}K_{pd_1} & 0 & 0 \\ \sqrt{8}K_{pd_1} & K_p^{\mathrm{O}} & 0 & 2K_{pp} \\ 0 & 0 & K_1 & \sqrt{8}K_{pd_1} \\ 0 & 2K_{pp} & \sqrt{8}K_{pd_1} & K_p^{\mathrm{O}} \end{pmatrix}. \tag{3.40}$$

We can notice that Eq. (3.38) has the same structure as Eq. (3.32), with two 2×2 degenerate sub-blocks hybridized by a nondiagonal element (K_{pp} in this case). This results in a splitting of the single-layer levels $E_{pd_2,+}(K) \rightarrow E_{pd_2,+a}(K), E_{pd_2,+b}(K)$, $E_{pd_2,-}(K) \rightarrow E_{pd_2,-a}(K), E_{pd_2,-b}(K)$. The two levels $E_{pd_2,+a}(K)$, $E_{pd_2,+b}(K)$, by looking at their orbital character, can be identified in DFT results in the small splitting of the (B) $E_{pd_2,+}(K)$ level, confirming once more the smallness of the interlayer $p_{x/y}$-$p_{x/y}$ hopping.

Less straightforward is the case of the 4×4 block $\hat{H}_{pzd_{02}}(K)$ where the hybridization term $\sqrt{2}K_{pz}$ mixes two different 2×2 sub-blocks, $\hat{H}_{pd_0}$ and $\hat{H}_{zd_2}$. In this case, a mixing of the orbital character will result. We note, however, that the block $\hat{H}_{pzd_{02}}(K)$ appears twice in Eq. (3.35), so that each energy level will result doubly degenerate, in particular the minimum (A) of the conduction band at K. Note, however, that the negligible shift of such energy level in the DFT calculations with respect to the single-layer case is an indication that also the interlayer hopping element K_{pz}, between p_z on one layer and p_x, p_y on the other one, is negligible.

3.3.3 Q point

An analytical insight on the electronic structure at the Q point was not available in single-layer systems and it would be thus even more complicated in the bulk case. A few important considerations, concerning the minimum (D) can, however, be drawn from the DFT results. In particular, we note that in the single-layer case this energy level had a non-vanishing p_z component. As we have seen above, the interlayer hopping between p_z orbitals appears to be

dominant with respect to the interlayer hopping between $p_{x/y}$ and $p_{x/y}$ and with respect to the mixed interlayer hopping p_z-$p_{x/y}$. We can thus expect a finite sizable splitting of the (D) level, containing a finite p_z component, with respect to the negligible energy shift of $E_{pd_0,+}$ (A), which depends on the mixed interlayer process K_{pz}.

3.4 Fitting of the tight-binding model to DFT calculations

In the previous Sections we elucidated, using a TB model, the orbital character of the band structure of MoS_2 on the main high-symmetry points of the Brillouin zone. We have shown how a reliable minimal model for the single-layer case needs to take into account at least the p_x, p_y orbitals of the S atoms in addition to the $4d$ orbitals of Mo. A careful inspection of the electronic structure shows also that the band edges at the K point defining the direct band gap in the single-layer case are characterized not only by a chiral order of the d Mo orbitals, as experimentally observed, but also by an entangled chiral order of the minor component of the $p_{x/y}$ S orbitals.

An important role is also played by the p_z orbitals of the S atoms. In single-layer systems, the p_z orbital character is particularly relevant in the (C) state, characterizing a secondary maximum in the valence band at the Γ point, and in the (D) state, which instead provides a secondary minimum in the conduction band at the Q point.

The p_z component becomes crucial in multilayer compounds, where a comparison with DFT results shows that the interlayer coupling is mainly driven by the p_z-p_z hopping whereas $p_{x/y}$-$p_{x/y}$, p_z-$p_{x/y}$ are negligible. This results in an orbital-selective and momentum-dependent interlayer splitting of the energy levels, being larger for the (C) and (D) states and negligible for (A) and (B). This splitting is thus the fundamental mechanism responsible for the transition from a direct (A)-(B) gap in single-layer compounds to an indirect (C)-(D) gap in multilayer systems. Controlling these processes is therefore of the highest importance for electronic applications. Note that such direct/indirect gap switch is discussed in terms of the number of layers. On the other hand, the microscopic identification of such mechanism, which is essentially driven by the interlayer coupling, makes it possible to understand on physical grounds the high sensitivity to pressure/strain effects, as well as to the temperature, via the lattice expansion.

Therefore, we have developed a tight-binding model with the minimal basis in order to be able to describe TMDCs systems with variable number of layers. As in graphene and other graphenic materials, it is interesting to have this kind of simple TB model since then you can apply it in order to, for example, study and perform transport calculations in large systems. Although in the case of graphene the model is much simpler, we have shown that this is a model in which we can rely eventually to study the aforementioned properties.

Finally, in order to make the TB useful, we have performed a fitting procedure to determine the TB parameters that best reproduce the DFT bands within the model defined here. The task was divided in two steps: *i*) we first focus on the single-layer case to determine the relevant Slater-Koster intra-layer parameters in this case; *ii*) afterwards, keeping the intralayer parameters fixed, we determine the interlayer parameters. To this purpose we employ a simplex method[101] to minimize a weighted mean square error between the TB and DFT band energies, that is:

$$f_{wMSE} = \sum_{i=1}^{N} \sum_{\mathbf{k}} w_i(\mathbf{k}) \left[\epsilon_i^{TB}(\mathbf{k}) - \epsilon_i^{DFT}(\mathbf{k})\right]^2, \tag{3.41}$$

where $\epsilon_i^{DFT}(\mathbf{k})$ is the dispersion on the ith band of the 11-band block under consideration, $\epsilon_i^{TB}(\mathbf{k})$ is the corresponding TB description and $w_i(\mathbf{k})$ is a band/momentum resolved weight factor which can be used to give more weight to particular $\mathbf{k}$ regions or over selected bands. In

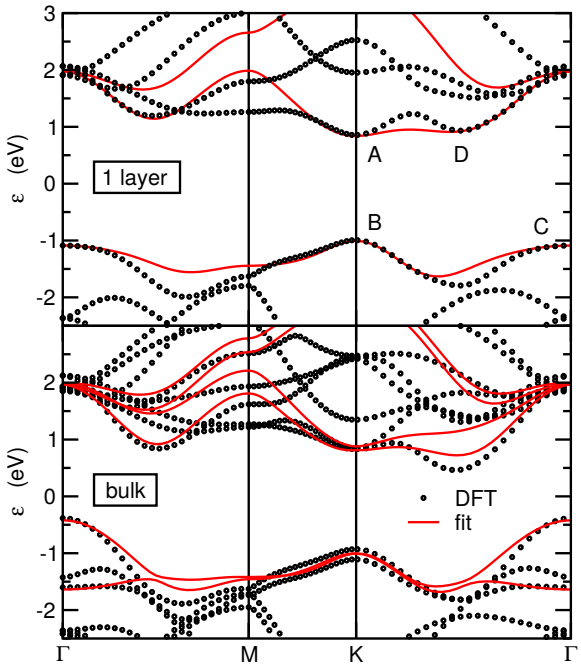

Figure 3.6: Comparison between the DFT band structure (black dots) and the best fit TB model (red solid lines) for single-layer (top panel) and bulk MoS_2 (bottom panel).

spite of many efforts, we could not find a reliable fit for the whole electronic structure including the seven valence bands and the four lowest conduction bands.[1] As our analysis and our main objective concerns the description of the valence and conduction bands that define the band gap of these systems, we focus on finding a set of parameters that describe properly these bands. Since both the lowest conduction and highest valence band belong to the electronic states with even $z \to -z$ symmetry, the fit was performed in the 6×6 orbital space defined by this symmetry. In addition, due to the degeneracy at the Γ point and to the band crossing along the Γ-M direction, the two conduction bands with even symmetry for $z \to -z$ were considered in the fit. Additionally, we give a larger weight to the (A)-(D) band edges in order to obtain a better description of the most important features of the band structure.

Our best fit for the single-layer case is shown in the top panel of Fig. 3.6 (where only the TB bands with even symmetry $z \to -z$ are shown), compared with the DFT bands. The corresponding TB parameters are listed in Table 3.2. Note that, due to the restriction of our fitting procedure to only some bands belonging to the block with even symmetry, the atomic crystal field Δ_1 for the Mo orbitals d_{xz}, d_{yz} (not involved in the fitting procedure) results undetermined. The fit reported in Fig. 3.6 agrees in a qualitative way with the DFT results, showing, in particular, a direct gap at the K point ((A) and (B) band edges) and secondary band edges for the valence and conduction bands lying at the Γ (C) and the Q point (D), respectively. Finally, we also generalize these results by including also the crystal field Δ_1, obtained by fixing the minimum of the conduction band at K of the electronic bands belonging to the *odd* block to the same energy of the DFT calculations.

Turning now to the bulk system, the further step of determining the interlayer hopping parameters $U_{pp\sigma}$, $U_{pp\pi}$, is facilitated by the strong indication, from the DFT analysis, of a dominant role of the interlayer hopping between the p_z orbitals and a negligible role of the interlayer hopping between the $p_{x/y}$ orbitals. Focusing on the Γ point, these two different

[1] A good fitting agreement with DFT data was shown in the work by Zahid and coworkers,[102] but using a larger, non-orthogonal basis set, and involving up to 96 fitting parameters.

		MoS_2	WS_2
Crystal Fields	Δ_0	-1.512	-1.550
	Δ_1	0.419	0.851
	Δ_2	-3.025	-3.090
	Δ_p	-1.276	-1.176
	Δ_z	-8.236	-7.836
Intralayer Mo-S	$V_{pd\sigma}$	-2.619	-2.619
	$V_{pd\pi}$	-1.396	-1.396
Intralayer Mo-Mo	$V_{dd\sigma}$	-0.933	-0.983
	$V_{dd\pi}$	-0.478	-0.478
	$V_{dd\delta}$	-0.442	-0.442
Intralayer S-S	$V_{pp\sigma}$	0.696	0.696
	$V_{pp\pi}$	0.278	0.278
Interlayer S-S	$U_{pp\sigma}$	-0.774	-0.774
	$U_{pp\pi}$	0.123	0.123

Table 3.2: TB parameters for single-layer MoS_2 (Δ_α, V_α) as obtained by fitting the low energy conduction and valence bands. Also shown are the inter-layer hopping parameters U_α relevant for bulk MoS_2. All hopping terms V_α, U_α and crystal fields Δ_α are in units of eV. The parameters for WS_2 are also shown for completeness.

hopping processes are parametrized in terms of the corresponding interlayer parameters Γ_{zz} and Γ_{pp}, as discussed in Appendix C. We can thus approximate $\Gamma_{pp} = 0$, providing a constraint between $U_{pp\sigma}$ and $U_{pp\pi}$, and leaving thus only one effective independent fitting parameter: Γ_{zz}. We determine it, and hence $U_{pp\sigma}$ and $U_{pp\pi}$, by fixing the effective splitting of the $E_{zd_0,+}(\Gamma)$ level as in the DFT data. The values of $U_{pp\sigma}$ and $U_{pp\pi}$ found in this way are also reported in Table 3.2, and the resulting band structure in the lower panel of Fig. 3.6, where only the TB bands with even symmetry $z \to -z$ are shown. We stress that the intralayer hoppings are taken from the fitting of the single-layer case. The agreement between the DFT and the TB bands is also qualitatively good in this case. In particular, we would like to stress the momentum/orbital selective interlayer splitting of the bands, which is mainly concentrated at the Γ point for the valence band and at the Q point for the conduction band. This yields to the crucial transition between a direct gap in single-layer MoS_2, located at the K point, to an indirect gap Γ-Q in multilayer systems.

On more quantitative grounds, we can see that, while the interlayer splitting of the conduction level $E_{zd_0,+}(\Gamma)$ is easily reproduced, the corresponding splitting of the conduction band at the Q point is considerably underestimated in the TB model (0.20 eV) as compared to the DFT data (1.36 eV). This discrepancy is probably due to the underestimation, in the TB model, of the p_z character of the conduction band at the Q point. As a matter of fact, the set of TB parameters reported in Table 3.2 gives at the Q point of the conduction band, for the single-layer case, only a 3.8% of p_z orbital character, in comparison with the 11% found by the DFT calculations. It should be kept in mind, however, that the optimization of the TB fitting parameters in such a large phase space (12 free parameters) is a quite complex and not unambiguous procedure, and other solutions are possible. In particular, a simple algebraic analysis suggests that an alternative solution predicting 11% of p_z character at the Q point would yield to a corre-

sponding splitting of the order of 1.2 eV, in quantitative agreement with the DFT data. A more refined numerical search in the optimization of the TB parameters, using global minimization techniques, might result in better comparison with the DFT results and further work along this line should be of great interest.

3.5 Spin-orbit interaction and the tight-binding Hamiltonian

In this Section we present the analytical structure of the TB Hamiltonians for single-layer and bulk TMD MX_2 compounds including the spin-orbit (SO) interaction. Specific parameters for realistic materials will be provided in the next Section, as well as a discussion of the physical consequences of the spin-orbit coupling (SOC).

3.5.1 Single-layer case

In the context of the TB model introduced in the previous Sections, we include the spin-orbit coupling term in the Hamiltonian by means of a pure atomic spin-orbit interaction acting on both the metal and chalcogen atoms. Explicitly we consider here the SOC given by:

$$\hat{H}^{\mathrm{SO}} = \sum_a \frac{\lambda_a}{\hbar} \hat{\mathbf{L}}_a \cdot \hat{\mathbf{S}}_a, \tag{3.42}$$

where λ_a, the intra-atomic SOC constant, depends on the specific atom ($a = M, X$). $\hat{\mathbf{L}}_a$ is the atomic orbital angular momentum operator and $\hat{\mathbf{S}}_a$ is the electronic spin operator.[103–105] It is convenient to use the representation

$$\hat{H}^{\mathrm{SO}} = \sum_a \frac{\lambda_a}{\hbar} \left(\frac{\hat{L}_a^+ \hat{S}_a^- + \hat{L}_a^- \hat{S}_a^+}{2} + \hat{L}_a^z \hat{S}_a^z \right), \tag{3.43}$$

where (omitting now for simplicity the atomic index a):

$$\hat{S}^+ = \begin{pmatrix} 0 & 1 \\ 0 & 0 \end{pmatrix}, \quad \hat{S}^- = \begin{pmatrix} 0 & 0 \\ 1 & 0 \end{pmatrix}, \quad \hat{S}^z = \frac{1}{2} \begin{pmatrix} 1 & 0 \\ 0 & -1 \end{pmatrix}. \tag{3.44}$$

In a similar way, the orbital angular momentum operator $\hat{\mathbf{L}}$ acts on the states $|l, m\rangle$ as

$$\begin{aligned} \hat{L}^{\pm}|l,m\rangle &= \hbar\sqrt{l(l+1) - m(m\pm 1)}\, |l, m\pm 1\rangle, \\ \hat{L}^{z}|l,m\rangle &= \hbar m\, |l,m\rangle, \end{aligned} \tag{3.45}$$

where l refers to the orbital momentum quantum number and m to its z component.

We choose the orbital basis set in the following manner:

$$\begin{aligned} |p_z\rangle &= |1,0\rangle \\ |p_x\rangle &= -\frac{1}{\sqrt{2}}[|1,1\rangle - |1,-1\rangle] \\ |p_y\rangle &= \frac{i}{\sqrt{2}}[|1,1\rangle + |1,-1\rangle] \\ |d_{3z^2-r^2}\rangle &= |2,0\rangle \\ |d_{xz}\rangle &= -\frac{1}{\sqrt{2}}[|2,1\rangle - |2,-1\rangle] \\ |d_{yz}\rangle &= \frac{i}{\sqrt{2}}[|2,1\rangle + |2,-1\rangle] \\ |d_{x^2-y^2}\rangle &= \frac{1}{\sqrt{2}}[|2,2\rangle + |2,-2\rangle] \\ |d_{xy}\rangle &= -\frac{i}{\sqrt{2}}[|2,2\rangle - |2,-2\rangle] \end{aligned} \tag{3.46}$$

As in the case without SOC, we further simplify the problem by introducing the aforementioned symmetric (S) and antisymmetric (A) combination of the p orbitals of the top (t) and bottom (b) X layers:

$$\begin{aligned} |p_{\alpha,S}\rangle &= \frac{1}{\sqrt{2}}[|p_{\alpha,t}\rangle + |p_{\alpha,b}\rangle], \\ |p_{\alpha,A}\rangle &= \frac{1}{\sqrt{2}}[|p_{\alpha,t}\rangle - |p_{\alpha,b}\rangle]. \end{aligned} \tag{3.47}$$

The total Hamiltonian, including the SO interaction for the single-layer, can be now written as

$$\hat{H}_{1\mathrm{L}}(\mathbf{k}) = \hat{H}^{\mathrm{sl}}_{1\mathrm{L}}(\mathbf{k}) \otimes \mathbb{1}_2 + \hat{H}^{\mathrm{SO}}_{1\mathrm{L}}, \tag{3.48}$$

where the SOC term $\hat{H}^{\mathrm{SO}}_{1\mathrm{L}}$ is

$$\hat{H}^{\mathrm{SO}}_{1\mathrm{L}} = \begin{pmatrix} \hat{M}^{\uparrow\uparrow} & \hat{M}^{\uparrow\downarrow} \\ \hat{M}^{\downarrow\uparrow} & \hat{M}^{\downarrow\downarrow} \end{pmatrix}, \tag{3.49}$$

and where

$$\hat{M}^{\sigma\sigma} = \begin{pmatrix} \hat{M}^{\sigma\sigma}_{\mathrm{EE}} & \hat{0}_{6\times5} \\ \hat{0}_{5\times6} & \hat{M}^{\sigma\sigma}_{\mathrm{OO}} \end{pmatrix}, \tag{3.50}$$

and

$$\hat{M}^{\sigma\bar{\sigma}} = \begin{pmatrix} \hat{0}_{6\times6} & \hat{M}^{\sigma\bar{\sigma}}_{\mathrm{EO}} \\ \hat{M}^{\sigma\bar{\sigma}}_{\mathrm{OE}} & \hat{0}_{5\times5} \end{pmatrix}. \tag{3.51}$$

Here we have chosen the spin notation $\bar{\sigma} = \downarrow$ ($\bar{\sigma} = \uparrow$) when $\sigma = \uparrow$ ($\sigma = \downarrow$).

The different blocks $\hat{M}^{\sigma\sigma}_{\mathrm{EE}}$, $\hat{M}^{\sigma\sigma}_{\mathrm{OO}}$, $\hat{M}^{\sigma\bar{\sigma}}_{\mathrm{EO}}$, $\hat{M}^{\sigma\bar{\sigma}}_{\mathrm{OE}}$, that constitute the above 22×22 matrix, are explicitly reported in Appendix D. We notice here that, in the most general case, the SO interaction couples the E and O sectors of the 22×22 TB matrix. Such mixing arises in particular from the spin-flip/spin-orbital processes associated with the transverse quantum fluctuation described by the first two terms of Eq. (3.43). The effective relevance of these terms can now be directly investigated in a simple way. The explicit analysis of this issue is discussed in Section 3.5.4. We anticipate here that the effects of the off-diagonal spin-flip terms result to be negligible for all the cases of interest here. This is essentially due to the fact that such processes involve virtual transitions towards high-order energy states.[38] At a very high degree of accuracy, we are thus justified in neglecting the spin-flip terms and retaining in Eq. (3.43) only the spin-conserving terms $\propto \lambda_a \hat{L}^z_a \hat{S}^z_a$. An immediate consequence of that is that the even and odd sectors of the Hamiltonian remain uncoupled, allowing us to restrict our analysis, for the low-energy states of the valence and conduction bands, only to the E sector.

3.5.2 Bulk case

Once introduced the TB model for a single-layer in the presence of SOC, as in the case without it (Section 3.3), it is quite straightforward to construct a corresponding theory for the bulk and bilayer systems by including the relevant inter-layer hopping terms in the Hamiltonian.

Considering that the unit cell is now doubled, we can thus write the Hamiltonian for bulk MX_2 in the presence of SOC in the matrix form:

$$\hat{H}_{\mathrm{Bulk}}(\mathbf{k}) = \hat{H}^{\mathrm{sl}}_{\mathrm{Bulk}}(\mathbf{k}) \otimes \mathbb{1}_2 + \hat{H}^{\mathrm{SO}}_{\mathrm{Bulk}}, \tag{3.52}$$

which is a 44×44 matrix due to the doubling of the unit cell with respect to the single-layer case discussed in Sec. 3.5.1.

Here $\hat{H}^{\rm sl}_{\rm Bulk}(\mathbf{k})$, which is given by Eq. 3.26, represents the spinless Hamiltonian for the bulk system. We refer to Section 3.3 for further details of this matrix.

On the other hand, $\hat{H}^{\rm SO}_{\rm Bulk}$ in Eq. (3.52) accounts for the SOC in the bulk system, and it can be written as:

$$\hat{H}^{\rm SO}_{\rm Bulk} = \begin{pmatrix} \hat{M}^{\uparrow\uparrow} & 0 & \hat{M}^{\uparrow\downarrow} & 0 \\ 0 & \hat{M}^{\uparrow\uparrow} & 0 & \hat{M}^{\uparrow\downarrow} \\ \hat{M}^{\downarrow\uparrow} & 0 & \hat{M}^{\downarrow\downarrow} & 0 \\ 0 & \hat{M}^{\downarrow\uparrow} & 0 & \hat{M}^{\downarrow\downarrow} \end{pmatrix}, \tag{3.53}$$

where we can recognize both the spin-diagonal ($\hat{M}^{\sigma\sigma}$) and spin-flip ($\hat{M}^{\sigma\bar{\sigma}}$) processes induced by the atomic spin-orbit interaction.

Eqs. (3.52) and (3.53) provide the general basic framework for a deeper analysis in more specific cases. In particular, as already mentioned above, the spin-flip terms triggered by SOC can be substantially neglected for all the cases of interest. The total Hamiltonian (Eq. (3.52)) can thus be divided in two 22×22 blocks $\hat{H}^{\sigma\sigma}_{\rm Bulk}(\mathbf{k})$ related by the symmetry $\hat{H}^{\uparrow\uparrow}_{\rm Bulk}(\mathbf{k}) = \hat{H}^{\downarrow\downarrow}_{\rm Bulk}(-\mathbf{k})$. Further simplifications are available at specific symmetry points of the Brillouin zone (BZ). More specifically, we can notice that for $k_z = 0$ the E and O sectors remain uncoupled. Focusing, at low-energies for the conduction and valence bands, only on the E sector, we can write:

$$\hat{H}_{\rm Bulk,E}(\mathbf{k}, k_z = 0) = \hat{H}^{\rm sl}_{\rm Bulk,E}(\mathbf{k}) + \hat{H}^{\rm SO}_{\rm Bulk,E}, \tag{3.54}$$

where

$$\hat{H}^{\rm sl}_{\rm Bulk,E}(\mathbf{k}) = \begin{pmatrix} \hat{H}_{\rm E,1} & \hat{I}_{\rm E} & 0 & 0 \\ \hat{I}^{\dagger}_{\rm E} & \hat{H}_{\rm E,2} & 0 & 0 \\ 0 & 0 & \hat{H}_{\rm E,1} & \hat{I}_{\rm E} \\ 0 & 0 & \hat{I}^{\dagger}_{\rm E} & \hat{H}_{\rm E,2} \end{pmatrix}, \tag{3.55}$$

and

$$\hat{H}^{\rm SO}_{\rm Bulk,E} = \begin{pmatrix} \hat{M}^{\uparrow\uparrow}_{\rm EE} & 0 & 0 & 0 \\ 0 & \hat{M}^{\uparrow\uparrow}_{\rm EE} & 0 & 0 \\ 0 & 0 & \hat{M}^{\downarrow\downarrow}_{\rm EE} & 0 \\ 0 & 0 & 0 & \hat{M}^{\downarrow\downarrow}_{\rm EE} \end{pmatrix}, \tag{3.56}$$

where the explicit expression of each block Hamiltonian is also reported in Appendix D.

3.5.3 Bilayer

The Hamiltonian for the bilayer can also be derived in a very similar form as in the bulk case. In particular, we can write:

$$\hat{H}_{\rm 2L}(\mathbf{k}) = \hat{H}^{\rm sl}_{\rm 2L}(\mathbf{k}) + \hat{H}^{\rm SO}_{\rm 2L}. \tag{3.57}$$

Since we are considering intrinsic SOC (purely local), $\hat{H}^{\rm SO}_{\rm 2L}$ is not affected by the interlayer coupling. Therefore, we have $\hat{H}^{\rm SO}_{\rm 2L} = \hat{H}^{\rm SO}_{\rm Bulk}$, where $\hat{H}^{\rm SO}_{\rm Bulk}$ is defined in Eq. (3.56).

On the other hand, similarly to the bulk case, the spinless TB term $\hat{H}^{\rm sl}_{\rm 2L}(\mathbf{k})$ for the bilayer case can be written as:

$$\hat{H}^{\rm sl}_{\rm 2L}(\mathbf{k}) = \begin{pmatrix} \hat{H}^{\rm sl}_{1} & \hat{H}_{\perp,\rm 2L} \\ \hat{H}^{\dagger}_{\perp,\rm 2L} & \hat{H}^{\rm sl}_{2} \end{pmatrix}, \tag{3.58}$$

	MoS_2	WS_2
λ_M	0.075	0.215
λ_X	0.052	0.057

Table 3.3: Spin-orbit coupling λ_α for single-layer MoS_2 and WS_2 taken from the work by Liu *et al.*[39] and Komider *et al.*[106] Units are given in eV.

where now

$$\hat{H}_{\perp,2\mathrm{L}}(\mathbf{k}) \;=\; \frac{1}{2}\begin{pmatrix} \hat{I}_{\mathrm{E}} & \hat{I}_{\mathrm{EO}} \\ -\hat{I}_{\mathrm{EO}}^{\mathrm{T}} & \hat{I}_{\mathrm{O}} \end{pmatrix}. \tag{3.59}$$

Note that Eq. (3.59) can be obtained as a limiting case of Eq. (3.27) by setting $\zeta = \pi/4$, corresponding to the effective uncoupling of bilayer blocks.

3.5.4 TB parameters and comparison with DFT calculations

After having developed a suitable TB model with SOC for single and multi-layer MX_2 compounds, we compare here, as in the case without SOC (Section 3.4) the band structure obtained by the TB model to the corresponding band structure obtained from DFT methods. We are guided along this task by the set of Slater-Koster TB parameters already presented in Section 3.4. Here, we also compare the case of WS_2 since W is a heavier atom and, therefore, the effect of the SOC will be more noticeable. The only left unknown parameters are thus the atomic spin-orbit constants λ_M and λ_X for the transition metal and for the chalcogen atom, respectively. We take the corresponding values from the works by Liu *et al.*[39] and Komider *et al.*[106] (see Table 3.3), and we recall Table 3.2 for the full set of TB parameters for the case without SOC for MoS_2 and WS_2. Therefore, we can compare the resulting band structure for the full TB model in the presence of SOC, with corresponding first-principles results including also SO interaction.

The representative band structure for monolayer MoS_2 and WS_2, as well as for the bulk counterpart, are shown in Fig. 3.7, for both DFT (dashed red lines) and TB calculations (solid blue lines). We observe that the TB model with the set of Slater-Koster parameters provided in Tables 3.2 and 3.3 leads to a reasonable fitting of the DFT band structure. In particular we see that, for single layer samples (Figs. 3.7a and 3.7b) the edges of the valence band at K and Γ, as well as the edges of the conduction band at K and Q (marked by a dot in Fig. 3.7a), are properly captured by the TB model. The TB valence bands are less dispersive than the DFT bands in the intermediate regions between high symmetry points.

As in Section 3.4, the TB band structure for bulk samples, shown in Fig. 3.7c and 3.7d, have been obtained by adding only two extra Slater-Koster parameters, $U_{pp\sigma}$ and $U_{pp\pi}$, which account for inter-layer hopping between p orbitals of the adjacent chalcogen atoms of different layers. The obtained band structure for the valence band reproduce reasonably well the DFT band structure, as well as the experimental band structure measured by ARPES,[107] and accounts for the direct- to indirect-gap transition when going from single layer to bulk materials. As for the conduction band, the minimum at K is also captured by the TB model, but the position of the minimum at Q does not agree with DFT results. The inclusion of hopping terms between M orbitals of different layers, as well as next nearest neighbour hopping terms, could improve such fitting.[2] However, we notice that no experimental measurements of the conduction band

[2]We notice that the TB parameters used in this work lead to a trigonal warping of the conduction band which is rotated $\pi/3$ with respect to the DFT bands. This fact does not affect the results discussed here.

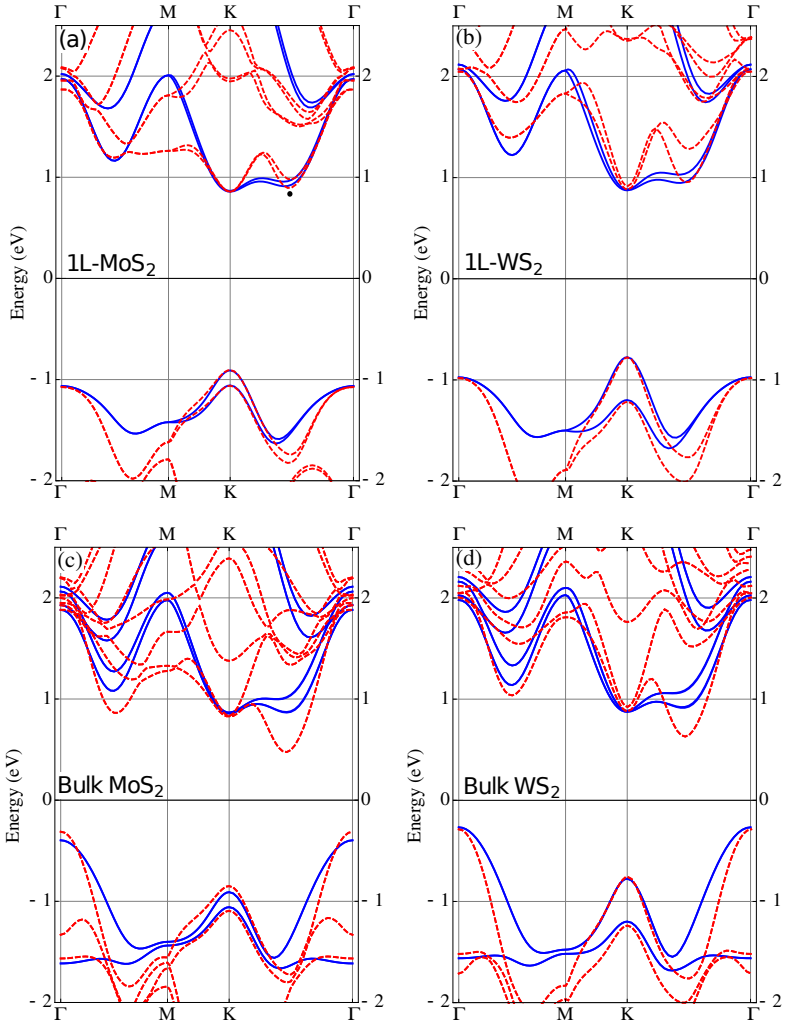

Figure 3.7: Band structure of single-layer and bulk MoS_2 and WS_2 including SO interaction. Red dashed lines correspond to DFT calculations and solid blue lines to TB calculations using the sets of parameters given in Tables 3.2 and 3.3. The dot in panel (a) indicates the position of the minimum of the conduction band, referred in the text as Q.

dispersion are available so far in the literature that could serve to validate the DFT and the TB results presented here.

In addition to the above remarks, a fundamental advantage of the TB model with respect to first-principles calculations is that it allows to investigate, in an analytical way, the relevance of the microscopic underlying processes. We have already mentioned above how transverse spin-flip fluctuations play here a marginal role and they can be disregarded, making the overall modeling of the SO interaction extremely direct and simple. We can now explicitly address and quantify this issue by comparing in the TB model the band structure obtained by using the full SOC as described by Eq. (Eq. (3.43)) and the one obtained considering only the last spin-diagonal terms $\hat{L}_a^z \hat{S}_a^z$. The results are shown in Fig. 3.8, where we compare, for single-layer MoS_2, the total band structure (red dashed lines) obtained by considering the full spin-orbit interaction (3.43) with the one obtained using the spin-conserving part (third term in Eq. (3.43)). As we can see in Fig. 3.8a, there is an almost perfect agreement of the band structures for MoS_2 obtained including and neglecting the spin-flip terms, demonstrating the negligible role of these processes. The effect is still weak but more noticeable for the case of WS_2 (Fig. 3.8b), due to the larger intra-atomic SOC associated to the heavier W atoms, as compared to Mo.

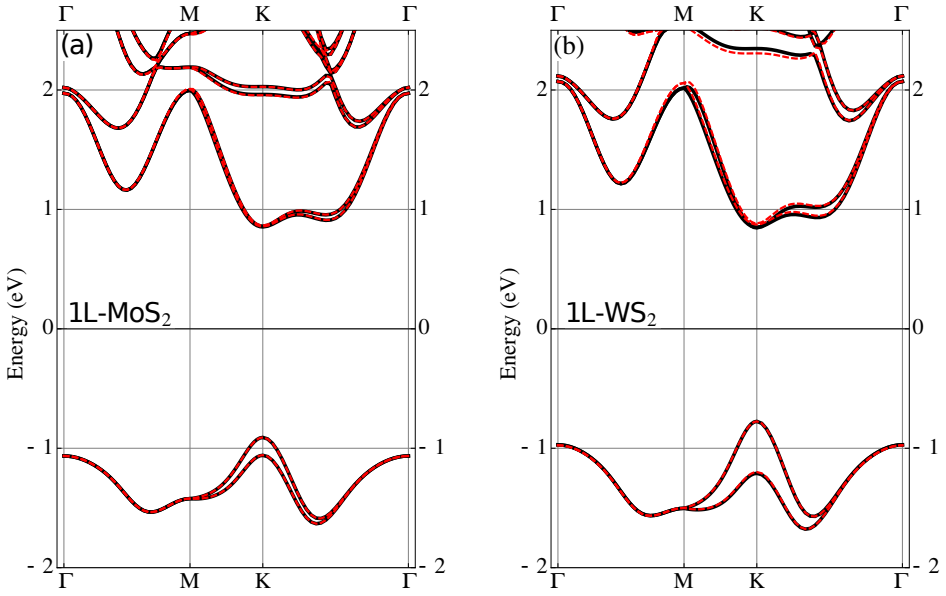

Figure 3.8: TB band structure of single-layer MoS_2 (a) and WS_2 (b) including SO interaction. Red dashed lines corresponds to the TB bands including the whole SO coupling terms. Black solid lines correspond to the TB band structure including only the spin-conserving terms of the SO coupling.

Of special interest is the minimum of the conduction band at the K point of the BZ: here, as discussed in the works by Liu *et al.*[46], Kosmider *et al.*[108] and Kormanyos *et al.*,[106] the competition between second order spin-flip processes associated with the transition metal atom M and first order (spin-conserving) processes of the chalcogen atom X, are responsible for the crossing/non crossing of the conduction bands in a very narrow region close to this K point.

3.5.5 Discussion

The TB model introduced in Sec. 3.5, for single-layer and multi-layer compounds, and the specific Slater-Koster parameter discussed in Sec. 3.5.4 provide a comprehensive tool for the study of the electronic properties and the entanglement between different degrees of freedom (spin, orbital, valley, layer, lattice) in these compounds in the presence of a relevant spin-orbit coupling acting both on the chalcogen X and on the transition metal atoms M. As we summarize in the present Section, such physics results to be relevant not only for the valence bands, whose band edge in the single layer materials is mainly built by the M orbitals d_{xy}, $d_{x^2-y^2}$ and d_{z^2}, but also for the conduction band and for the secondary extrema of both conduction and valence bands, whose energy can be effectively tuned by the interlayer coupling and by the SO interaction itself.

3.5.5.1 Spin-polarized pockets in the Fermi surfaces

The role of the spin-orbit coupling on the spin-orbital-valley entanglement at the band edge at K of the single-layer and bilayer compounds has been widely discussed in literature, using mainly low-energy effective Hamiltonians focused on the role of the transition metal M d-orbitals and of their corresponding spin-orbit coupling.[35,44,109–113] Such scenario can be now well reproduced by the present TB model and generalized to the whole BZ.

The SOC, in particular, is expected to be most relevant for the band edges of the valence band at the K point, whose orbital content is mainly associated with the d_{xy} and $d_{x^2-y^2}$ orbitals of the transition metal. A large band splitting induced by the SOC is thus predicted in this case. Such feature is indeed well captured by the TB model. In Figs. 3.9a and 3.9b we show the

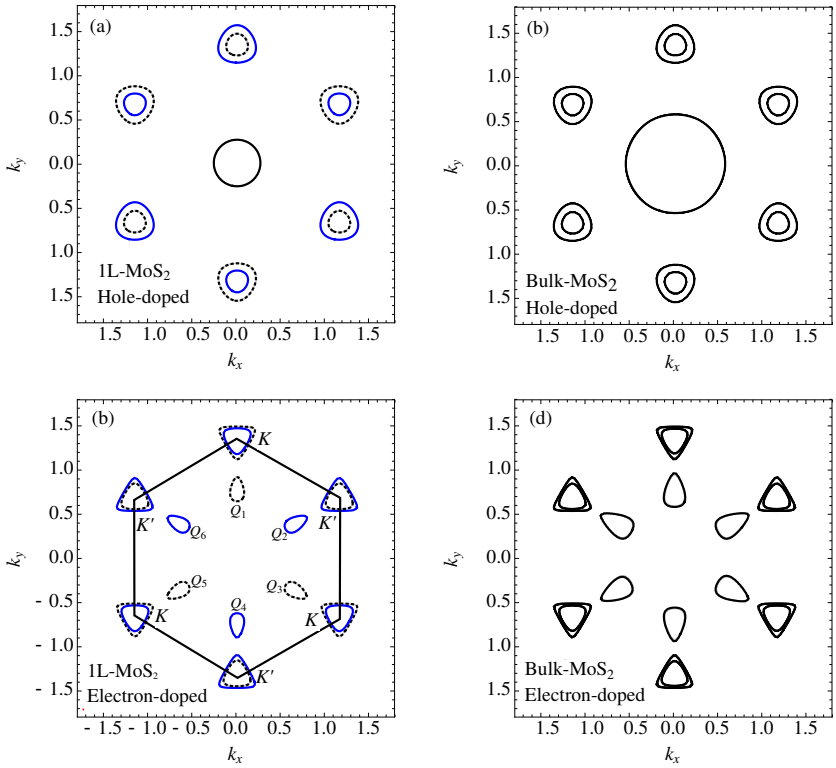

Figure 3.9: Fermi surfaces of MoS_2, obtained from the TB band structure. Panels (a) and (c) correspond to single-layer and panels (b) and (d) to the bulk. Top panels represent hole-doped systems, with the Fermi energy in the valence band (at $E_F = -1.134$ eV), whereas bottom panels represent electron-doped systems, with the Fermi energy in the conduction band ($E_F = 0.95$ eV). Energies are measured with respect to the zero of the TB Hamiltonian. The hexagonal 2D BZ is shown in (c) by the black solid lines. In the plots for single-layer systems, (a) and (c), solid blue and dashed black lines correspond to Fermi surfaces with main $S_z =\uparrow$ and $S_z =\downarrow$ polarization, respectively. All the Fermi surfaces of the bulk system (panels (b) and (d)) are degenerate in spin.

Fermi surfaces obtained with the present TB model, including atomic spin-orbit coupling, for a finite hole-doping probing the valence band of both single-layer and bulk compounds. In order to point out the different physics occurring close to the different band edges at K and Γ points, we show here Fermi surfaces corresponding to a sizable negative Fermi energy cutting both edges at K and Γ. In particular, the central Fermi pocket located around Γ is spin degenerate, for both single-layer and bulk systems since its orbital character is mainly due to the $d_{3z^2-r^2}$ orbitals of M and to the p_z orbitals of X, both of them with $L_z = 0$ (see Section 3.1). On the other hand, as discussed in Section 3.1, the pockets around K and K' are mainly due to the $d_{x^2-y^2}$ and d_{xy} orbitals of the metal M (with $|m| = 2$), plus a minor component of p_x and p_y orbitals of the chalcogen X (with $|m| = 1$). This results in a finite SOC splitting of the valence band at the K and K' points, due mainly to first order spin-orbit coupling on the d orbitals of M. Furthermore, because of the lack of inversion symmetry in single layer samples (or in multi-layer samples with an odd number of layers), the spin degeneracy is lifted, presenting an opposite spin polarization on different valleys.[35] This feature is well reproduced by our model and shown in Fig. 3.9a, where Fermi surfaces with main $S_z =\uparrow$ character are denoted by solid blue lines, while Fermi surfaces with main $S_z =\downarrow$ character are denoted by dashed black lines. On the other hand, the Fermi surfaces of hole-doped bulk MoS_2, for the same E_F, are shown in Fig. 3.9b. Since the maximum of the valence band for the bulk compound, because of the interlayer coupling, is located at the Γ point (see the band structure of Fig. 3.7c), the central pocket in Fig. 3.9b is considerably larger than in Fig. 3.9a for single layer samples. The double Fermi surfaces

around the K and K' points in Fig. 3.9b are spin degenerate, as imposed by inversion symmetry. A recent set of ARPES measurements for MoS_2 and $MoSe_2$[114] have shown the importance of the SOC in the band structure, obtaining experimental constant energy contours in very much agreement with those presented in Fig. 3.9a and 3.9b.

Although smaller and less noticed,[38,54,58,106,108,115] a spin-valley coupling is present also for the conduction band edge of the single-layer systems at the K and K' points. It is important to remind here that the orbital character in these points of the BZ is mainly associated with the $d_{3z^2-r^2}$ orbital (with $m = 0$) of the transition metal M, but with a finite contribution from the p_x and p_y orbitals of the chalcogen (with $m = \pm 1$) (see Section 3.1). The spin-orbit coupling of the chalcogen atom X, mainly through the diagonal term $L_X^z S_X^z$, results thus in a smaller but finite splitting of the conduction band edge, as it can be also inferred by the Fermi surfaces for electron-doped single-layer compounds, as shown in Fig. 3.9c. It is worth to stress that, although the resulting spin-induced splitting can be quite small, the entanglement between band splitting, spin and valley degrees appears to be quite strong, so that the lower band is $\uparrow$ polarized and the upper band $\downarrow$ polarized (or viceversa, depending on the valley). Note also that, although the atomic spin-orbit coupling due to the sulfur in MoS_2 or WS_2 is not very large, it can be of importance for Se compounds (with a larger atomic mass than sulfur), as $MoSe_2$ or WSe_2. The role of the SOC on the chalcogen atom will be analyzed in more detail in Section 3.5.5.2.

Finally, we can note that, as previously discussed in the work by Zhu and coworkers[39] using first principles calculations, the SOC induces a finite band splitting in single-layer systems also at the Q point, with a corresponding spin-polarization. Also, this feature is nicely captured by our TB model in the presence of atomic SOC on both chalcogen and transition metal atoms, as shown in Fig. 3.9c, where we plot the Fermi surfaces of an electron-doped system with a Fermi level cutting only the lower conduction band at Q. As we can see, the TB model is able not only to reproduce the band splitting, but also to point out a strong degree of entanglement in this point of the BZ, with Fermi pockets with a strong spin polarization, and with an alternating polarization of the entangled spin/valley/orbital degrees of freedom along the six inequivalent valleys[116]. On the microscopic ground, we can notice that the main orbital character of the conduction bands at the Q point is due to a roughly equal distribution of the $d_{x^2-y^2}$ and d_{xy} orbitals of the transition metal M, and of the p_x and p_y orbitals of the chalcogen atom X. Given the presence of a large contribution from both p and d orbitals, we expect these states to stem from a strong hybridization between X and M atoms, and hence to be highly sensitive to uniform and local strains and lattice distortions.[117] In addition, it should be kept in mind that the minimum of the conduction band at Q becomes the absolute band edge in bilayer and multilayer compounds (as well as in strained single-layer systems). These considerations thus suggest that the minima of the conduction band at the Q point as the most promising states for tuning the spin/orbital/valley entanglement in these materials by means of strain engineering[117] or (in multilayer systems) by means of electric fields.[36]

3.5.5.2 Effects of the SOC at the chalcogen atom on the band structure

Most of the existing theoretical works have focused on the effects of the spin-orbit interaction associated with the transition metal atom. Less attention has been paid, in general, to the SOC induced by the chalcogen atom. As we have seen in the previous Section, however, the role of the SOC can be remarkably relevant also at the Q point of the BZ, resulting in a strong spin/orbital/valley entanglement also in this point, with the advantage to be extremely sensitive to the M-X hybridization and hence to the lattice effects. In addition, since the orbital content in this point is a mixture of d and p orbitals of the metal and the chalcogen atoms, the spin-orbit coupling is expected to be significantly driven not only by the d-orbital of

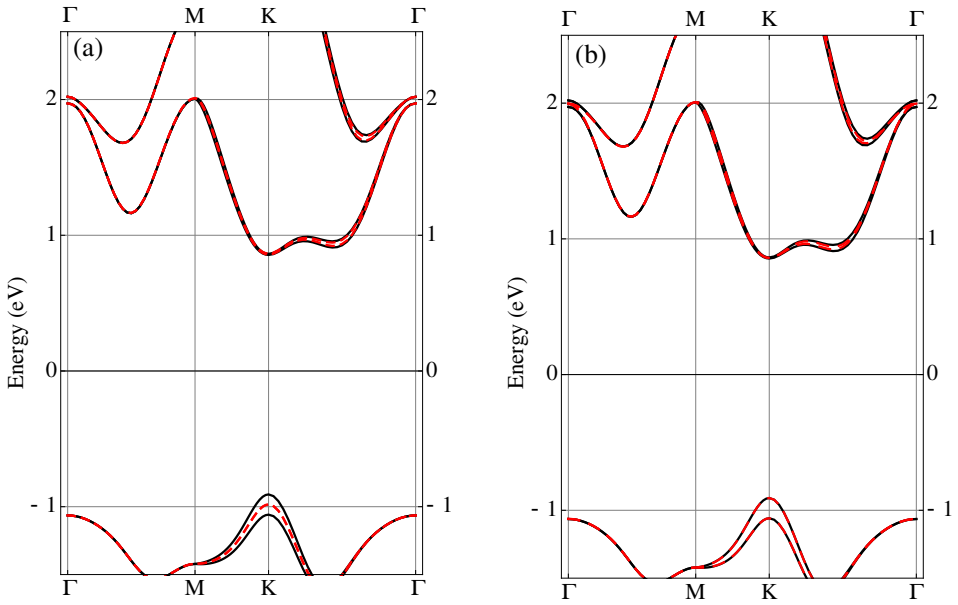

Figure 3.10: TB band structure of MoS_2 including SOC. Solid black lines corresponds to the TB bands using λ_{Mo} and λ_S as given in Table 3.3. Red dashed lines in (a) corresponds to $\lambda_S = 0.052$ eV and $\lambda_{Mo} = 0$. Red dashed lines in (b) correspond to $\lambda_{Mo} = 0.075$ eV and $\lambda_S = 0$.

the transition metal M, but also by the p orbitals of the chalcogen X atom. TB models can be quite useful to investigate this issue since we can easily tune the atomic SOC, keeping all the remaining Hamiltonian (Slater-Koster) parameters fixed, which permits to isolate the effects of the modified SOC without involving other structural and electronic changes. Figure 3.10 shows the effect of removing the SOC on either the Mo or the S atoms for the case of the single-layer of MoS_2. While the splitting of the valence band at the K point is fully caused by the SOC on the transition metal, the contributions to the splitting of the conduction band at Q from Mo and S are comparable.

We can validate these findings by performing DFT calculations on the four compounds MX_2 with M = Mo, W and X = S, Se (all of them done using the experimental structure). In the DFT calculation, we can also turn on and off the SOC in a particular species, by removing the SO component of the pseudopotential.[118] Fig. 3.11 shows the DFT results for the four compounds, including the SOC on all the atoms, and removing this coupling on either the chalcogen or the transition metal. In particular, the DFT results for MoS_2 shown in Fig. 3.11a agree reasonably well with those of Fig. 3.10, signaling that the SOC splitting of the bands in the sulfur compounds is dominated by the contribution due to the transition metal atom.

The importance of the SOC of the chalcogen atom is expected to be even more remarkable for heavier atoms, such as selenium, instead of sulfur. In Figs. 3.11c and 3.11d we show the DFT band structure for $MoSe_2$ and WSe_2, isolating the contribution of the SOC due to the metal and to the chalcogen atoms. As expected, we observe that a relevant contribution to the SOC splitting of the bands is due to the Se atom. This can be seen by a noticeable splitting of the blue lines in Figs. 3.11c and 3.11d (for which the SOC due to the metal M has been switched off) which is governed by the SO interaction of the Se atoms. Interestingly, this effect is not relevant only at the Q point of the conduction band, but also at the K point of the valence band, for which the orbital weight of the p_x and p_y orbitals of Se is only $\approx 20\%$ (see Section 3.1). We conclude that, although for the MoS_2 and WS_2 the effect of the SOC of the chalcogenides does not have much effect on the band structure, when S is changed by Se, the effects is much more noticeable.

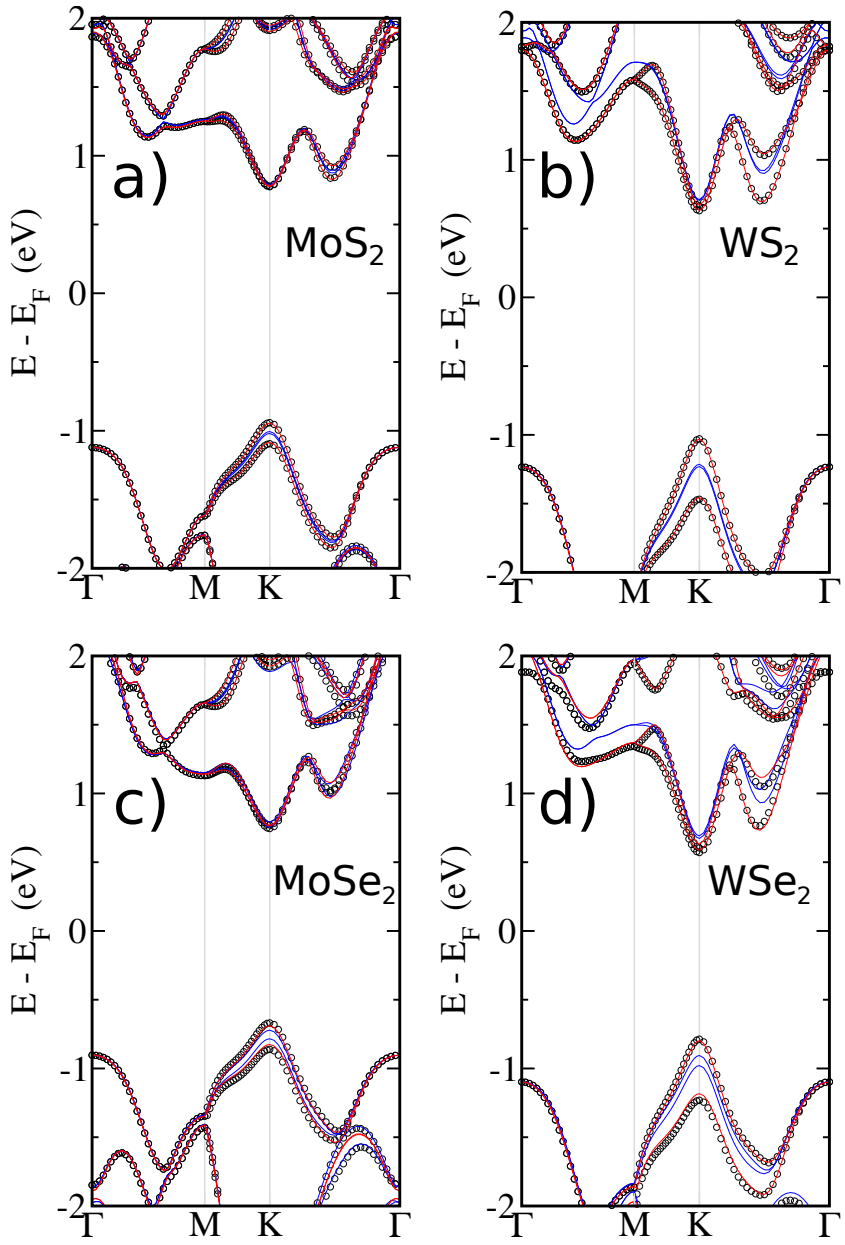

Figure 3.11: DFT band structure of the four compounds MoS_2, WS_2, $MoSe_2$ and WSe_2. Black circles show the results when the SOC on all the atoms are included. Red (blue) lines correspond to the removal of the SOC on the chalcogen (transition metal) atoms.

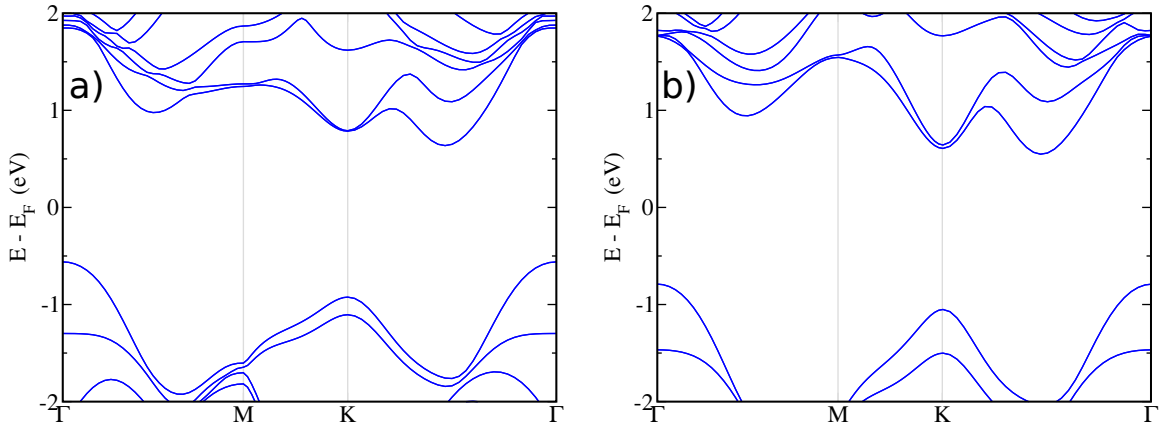

Figure 3.12: Band structure of bilayer MoS_2 and WS_2 obtained from DFT calculations. The combined effect of inter-layer hopping and spin-orbit interaction drives the minimum of the conduction band to the Q point, and the maximum of the valence band to the Γ point (see text)

3.5.5.3 Spin-Valley-Layer coupling in Bilayer MX_2

Of special interest is the case of bilayer TMDCs, corresponding to a stack of two single layers in-plane rotated by 180° with respect to each other, such that the transition metal atoms of one layer are above the chalcogen atoms of the other layer. The two layers are bound by means of weak van der Waals interactions. The inter-layer hopping of electrons between different layers leads to a strong modification of the band structure, driving a transition from a direct gap semiconductor in single-layer systems to an indirect gap semiconductor in bilayer and multi-layer compounds (see Section 3.3). The inter-layer hopping links mainly the p orbitals of the chalcogen atoms X of different layers. The result of this hopping is a splitting of the maximum of the valence band at the Γ point, which becomes the absolute valence band edge, as well as a splitting of the minimum of the conduction band at the Q point which becomes the absolute minimum of the conduction band. This situation is shown in Fig. 3.12, where we report the band structure of bilayer MoS_2 and WS_2 calculated by DFT methods. A qualitative similar feature is observed also in other bilayer compounds, as $MoSe_2$ or WSe_2.

Contrary to single-layer MX_2, the bilayer presents point-center inversion symmetry.[36,41,119] Therefore, as we have discussed for the bulk case, the corresponding band structure remains spin degenerate even in the presence of SOC. However, since the SOC Hamiltonian does not couple orbitals of different layers, each single band preserves a finite entanglement between spin, valley and the layer index. Such spin-valley-layer coupling has been discussed in the work by Gong and coworkers,[119] where the authors focused on the relevance of this effect at the K point of the valence band. Here we notice that the same effect occurs also for the conduction band, and it can be thus relevant for electron-doped samples. Indeed for slightly electron-doped bilayer MoS_2 and WS_2 the Fermi surface presents six pockets centered at the inequivalent Q valleys of the BZ, and no pockets at the K and K' valleys. Interestingly, the SOC for the TMDC families with stronger spin-orbit interaction, like WS_2 and WSe_2, can be larger than the inter-layer hopping, enhancing the spin/layer/valley entanglement. Then, although inversion symmetry forces each Fermi pocket to be spin degenerate, the layer polarization makes that each layer contributes with opposite spin in alternating valleys. This property can be of interest for *valleytronics* devices: by partially filling only one of the two subbands at the Q point of the conduction band, one would have a situation in which the upper layer contributes to three of the six valleys with spin-↑, and with spin-↓ to the other three valleys, whereas the opposite contribution is inferred from the bottom layer. This spin-valley coupling scenario resembles that of single-layer and bilayer

MX_2 discussed in the literature,[35,36,41,119] but for electron-doped samples, which is the kind of doping most commonly reported for those materials. Although we have focused in this Section in the most simple multi-layer compound, which is the bilayer MX_2, the physics discussed above applies also to any multi-layer TMDCs with an even number of layers, because they contain the same symmetry properties as that of bilayer MX_2 discussed here.

3.6 Conclusions

In this Chapter we have provided an analytic and reliable description of the electronic properties of single-layer and multi-layer semiconduting transition-metal dichalcogenides in terms of a suitable tight-binding model. We have shown that the band structure of the multilayer compounds can be generated from the TB model for the single-layer system by adding the few relevant interlayer hopping terms. The microscopic mechanism for the transition between a direct-gap to an indirect-gap from single-layer to multi-layer compounds is thus explained in terms of a momentum/orbital selective interlayer band splitting, where the orbital p_z component of the S atoms plays a central role. After developing the model, we found a set of tight-binding parameters that fits our previously calculated DFT band structure. Therefore, the present work provides a suitable basis for the inclusion of many-body effects within the context of Quantum Field Theory, for the analysis of local strain effects related to the modulation of the M-X, M-M and X-X ligands as well as the possibility of performing transport calculations of large samples. It is worth mentioning that this TB model is the minimal one that can reproduce the change of character of the gap from direct to indirect when changing the number of layers and, although more complicated, it should be as useful as the TB models developed for other 2D materials such as graphene.

Also, we have studied the effect of SOC in the band structure of TMDCs. We have extended the TB model including the SO interaction for both single-layer samples and multi-layer samples. The band structure obtained from the TB model has been, as in the case without SOC, compared to DFT calculations for MoS_2 and WS_2. Based on the orbital character at each relevant point of the Brilloin zone, we have discussed the origin and main features of the SOC at the different band edges. In particular we have found that, for the cases of interest here, spin-flip processes are negligible in the SOC Hamiltonian. This allows to highly simplify the model, making possible to construct a reduced TB Hamiltonian which contains the orbital character and SOC which is relevant for the description of the system around the gap. Special attention has been paid to the role of the SOC associated to the chalcogen atom. In fact, whereas most of the previous works have focused on the SOC associated to the metal atom (which is indeed the responsible for the large splitting of the valence band at the K point), here we have shown that the SOC associated to the chalcogen atom may be important at the Q point of the conduction band, especially for $MoSe_2$ and WSe_2. Furthermore, we have considered the effect of SOC in bilayer TMDCs. Whereas for single-layer MX_2 inversion asymmetry leads to spin-valley coupling, the band edges of bilayer TMDCs are spin degenerate. However, since inter-layer hopping conserves the spin, the spin physics can be exploited in bilayer MX_2 due to spin-valley-layer coupling. Whereas this issue has been recently studied in detail for hole-doped samples,[119] here we have argued that a similar effect can be expected for slightly electron-doped samples.

Chapter 4

Transition metal dichalcogenides as substrates for graphene

As stated in Chapter 1, the discovery of graphene and its promising properties for electronics (high mobility, stability, surface area, etc.), made a huge boost in the community towards the creation and manipulation of 2D materials. Furthermore, building devices that contain such materials emerged as an important topic in the scientific community.

One of the most interesting devices are the field effect transistors (FETs). Due to the high mobility and extreme atomic thickness, graphene seemed as a perfect candidate in order to replace "old"-Silicon-based technology. But, due to the fact that it is a semimetal (does not have a band gap) and that it has a linear dispersion around the K-point, we cannot make an efficient on/off switch. Therefore, a trend towards the opening of a band gap in graphene emerged in the graphene community. One of the first approaches was to put graphene on top of a substrate to see whether the electronic properties changed or not and, therefore, the study of graphene interacting with a substrate became very important.

SiO_2 is one of the first and most commonly used substrates, but the inhomogeneties make this material not very suitable for this purpose.[120] As we said, due to the huge improvement in the characterization and the manipulation of graphene, these techniques could be used in other materials. One of them was BN, an hexagonal lattice of B and N that was first isolated in 1997 by Suenaga *et al.*[121] The huge gap (5.97 eV[122]) and small lattice mismatch between graphene and BN (2%)[123] made it a suitable material to be combined with graphene. Although first theoretical studies found that the gap of graphene deposited on BN was of about 53 meV,[123] it was found later that this gap was due to the commensurability of the system. When building a Moirè lattice, the gap became much smaller. If the system is incommensurable the gap will disappear.[120] This issue was addressed recently by Jung and coworkers[124] were they found that an actual gap appears in systems with graphene on top of a BN layer and they were able to explain the experimental results obtained in this kind of systems.

As we said in Chapter 1, in 2010 Mak and coworkers[5] found that a single-layer of MoS_2 was a direct-gap semiconductor. Also, other transition metal dichalcogenides (TMDCs) such as WS_2 presented the same property. Since then, much work has been done concerning these materials in the past years.[18] Even new FET architectures such as the ones used in the works by Britnell *et al.*[7] and Georgiou *et al.*,[8] show that actual transistors could be implemented with BN, MoS_2 and WS_2. In fact, they showed that a better performance of the devices was achieved when having four or five layers. Therefore, a theoretical study of graphene on these materials could be interesting. Since there are many studies from the past few years about BN as a substrate for graphene, we will focus in the TMDCs.

In this Chapter, we will study the structure and electronic properties of devices where TMDCs are used as substrates for graphene. Since TMDCs present a change in the band structure from an indirect gap to a direct gap when changing the number of layers (from n layers to 1 layer) it is also interesting to see whether the properties of the system change with the number of layers.

We will focus on the case of WS_2, but the main conclusions should be general for other

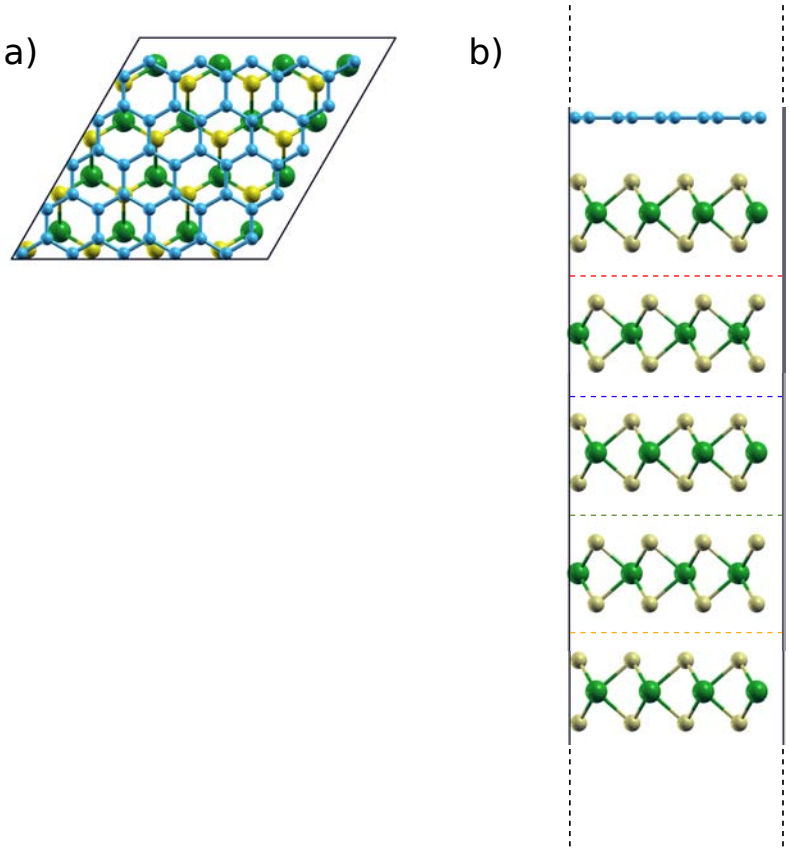

Figure 4.1: (a) Top view of the 1G/nWS$_2$ structures. (b) Side view of the 1G/5WS$_2$, to build the different studied cases we just need to "cut" the sytem by the red ($n = 1$), blue ($n = 2$), green ($n = 3$) and orange ($n = 4$) line.

dichalcogenides of the type MX_2 (M=Mo, W, X=S, Se).

4.1 WS$_2$/graphene structure

In this Section, we describe the WS$_2$/graphene structures that we will study. We build a supercell of 5×5 unit cells of graphene on top of a supercell of 4×4 unit cells of n-WS$_2$ layers (n being the number of layers, see Fig. 4.1). Graphene is scaled to the experimental lattice parameter of WS$_2$ (3.153 Å[125]) and both layers are aligned with respect to each other. Although other Moirè patterns could have been chosen, with this structure we already have a small lattice missmatch (2.5%) and the systems are computationally manageable. We change the number of WS$_2$ layers to study how it affects the electronic structure properties of the interface using the usual stacking for these materials (that is, $ABABAB$, see Fig. 4.1b). We also see how the relaxation of the system affects the properties that we want to study. This is interesting since we could save a lot of computational time if there were no appreciable changes between the relaxed and initial structure. If there are no differences, as we will see in the following Sections, we can avoid the relaxation process when we add more layers to the system.

First of all, we have to find the optimal distance between graphene and WS$_2$. To do so we plot the energy vs. interlayer distance which is shown in Fig. 4.2a. In this Figure we can see that bringing the two surfaces together increases the energy due to the repulsive forces between them. If we start separating them we find that the energy starts to decrease until it reaches a shallow minimum (which will be the optimal distance) and finally further separating both surfaces will increase a little bit the energy until it stabilizes. To do these calculations, we use

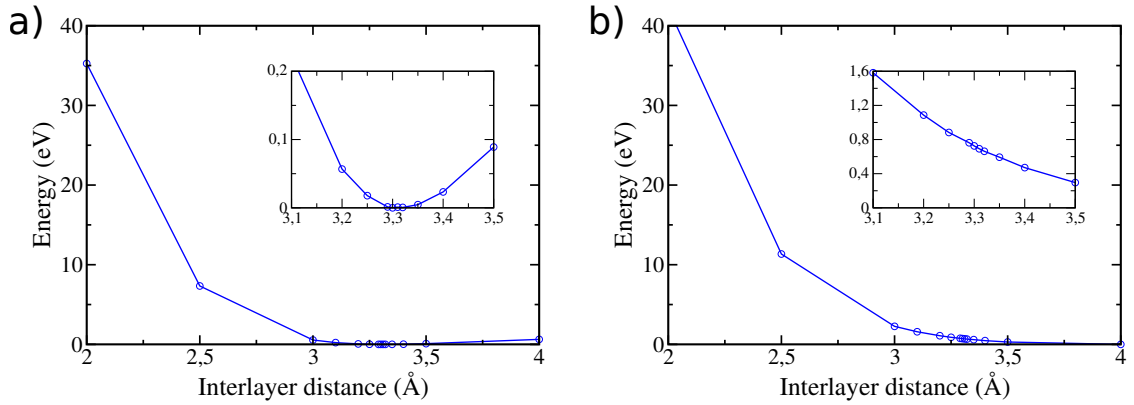

Figure 4.2: LDA (a) and GGA (b) calculations of the energy vs. interlayer distance.

the system with a monolayer of graphene on top of one layer of WS_2 and we do a calculation changing each time the distance from the last plane of sulphur atoms to the graphene layer. From this graph we obtain a value of 3.30 Å which is in good agreement to other TMDCs hybrid structures such as graphene on MoS_2[126] and $MoSe_2$.[127] This distance will be used for all the systems that we build in the following Sections. It is important to note that we are using LDA in a system in which the bonding between layers is supposed to be of van der Waals character. Previous experience with this kind of layered systems indicates that LDA provides a reasonable description of the distance between layers and even the bonding energy. However, this result is not due to the right reason (the non-local correlation that yields the dispersion interaction, which is missing in LDA functionals), but to the tendency of LDA to overestimate the binding from the superposition of the charge densities of the two layers. This can be easily checked if one performs the same calculation using GGA functionals. These do not show this tendency to overestimate the tendency to overbind, but also lacks the dispersion interactions, and therefore GGA results typically do not show any binding for van der Waals systems. This is actually shown in our case, as we can see in Figure 4.2b, where we see that the interaction between graphene and WS_2 obtained with GGA is purely repulsive (there is no minimum in the energy versus distance curve). Although other schemes exist to add the dispersion energies on top of the GGA results (like the so-called Grimme functional[128]), or specific DFT functionals that include the van der Waals interaction[129] (which are usually based on further corrections to a GGA calculation), all these typically do not change significantly the description of the electronic structure (band structure) and chemical bonding provided by GGA, but only provide the missing non-local correlation energies to provide a minimum of the energy versus distance curves, and the corresponding binding between the layers. Here, as in many other works in this topic, we take a more pragmatic approach, and use the LDA results (which provide a good description of the binding curve), but taking care of checking that the resulting electronic structure, charge redistribution, dipole moments, etc. are not an artifact of the LDA functional, but that they are robust and hold when the calculations are done using GGA (for the same distance between the graphene and WS_2 layers). We will show this in Section 4.2. Therefore, we can be confident that our results are qualitatively correct.

Going back to the results obtained with LDA, we can calculate the adsorption energy, E_{ads}, with the total energy obtained in the calculation at the optimised distance, as:

$$E_{ads} = E_{nWS_2-G} - E_{nWS_2} - E_G, \tag{4.1}$$

where E_{nWS_2-G}, E_{nWS_2} and E_G are the total energies of the total system with n-WS_2 layers, the isolated n-WS_2 layers and graphene monolayer, respectively.

In the case of $n = 1$ we have that $E_{ads} = 31$ meV per carbon atom which is also similar to previous works of other TMDCs as graphene on MoS_2[126] and $MoSe_2$.[127]

All these calculations were made with the atoms with fixed positions, using the experimental lattice constant of WS_2, adapting graphene to that lattice constant and also, the interlayer distance was fixed to its calculated optimal value. Therefore, it is important to study whether the properties of such structures vary when relaxing the system because, if they are the same, we can save a lot of computational effort just by fixing their positions to the aforementioned ones. In the initial structure, the WS_2 layer will break the symmetry of the graphene layer and all the carbon atoms will no longer be equivalent, inducing local electrostatic forces over each carbon atom. Therefore, the relaxation process could result in a displacement of the atoms. The result of such relaxation is that there is a small corrugation of the graphene layer of about 0.065 Å. Therefore, the distance between graphene and the top sulphur layer changes from 3.30 to 3.327 Å. It is important to note that the adsorption energy does not change qualitatively due to this relaxation. This is also in good agreements with previous works.[126,127]

Adding more WS_2 layers to the system ($n = 2$ to 5), with the distance between graphene and WS_2 taken from the optimised value in the case $n = 1$, does not change significantly the adsorption energies per carbon atom. Furthermore, doing the same relaxation procedure as in the $n = 1$ case for the $n = 2$ case, we find again that the adsorption energies, corrugation and interlayer distance also do not change notably. Moreover, as we will see in the following Section, when comparing the electronic properties such as the band structure of the systems before and after the relaxation, we find that no change is noticeable.

Therefore, after all these results, we can be confident that the calculations will not change quantitatively with relaxation and we can avoid this procedure for the case of $n > 2$, which otherwise would be very expensive computationally.

4.2 Electronic properties of the n-WS_2/graphene hybrid structures

In this Section we are going to study the electronic properties such as the band structure and how the charge redistributes in such system, creating a dipole moment in the interlayer of the hybrid structure of one graphene layer on top of a WS_2 monolayer. Afterwards, we will see how these properties are affected by the variation of the number of WS_2 layers.

4.2.1 Band structure

As in the case of the structural description, we will start studying the case of $n = 1$, that is, we will have a layer of graphene on top a WS_2 monolayer (see Fig. 4.1).

In Fig. 4.3c, we show the band structure for the $1G/1WS_2$. We can see that the characteristic Dirac cone of graphene and the lineal dispersion around that point are preserved (for clarity, the band structure for the case of the isolated graphene is shown in Fig. 4.3a). This is in accordance with the work on G/BN structures by Bokdam *et al.*[120] and in the case of graphene on metal substrates with low interaction between them, as in the case of the work by Khomyakov *et al.*[130] where they find that the interaction with the substrate does not change essentially the electronic properties of graphene. Also, it is worth noting that the band structure of the WS_2 layer does not change appreciably from the isolated case, just as in the case of graphene (see Fig. 4.3b for the band structure of a WS_2 monolayer). On the other hand, a zoom at the region around the Dirac point of Fig. 4.3c (which we do not plot), would show that a small gap of about 0.1 meV opens at the Dirac point. A similar gap has been reported previously in studies with other materials used a substrate such as the works by Bokdam *et al.*[120] and Ma and coworkers.[126,127]

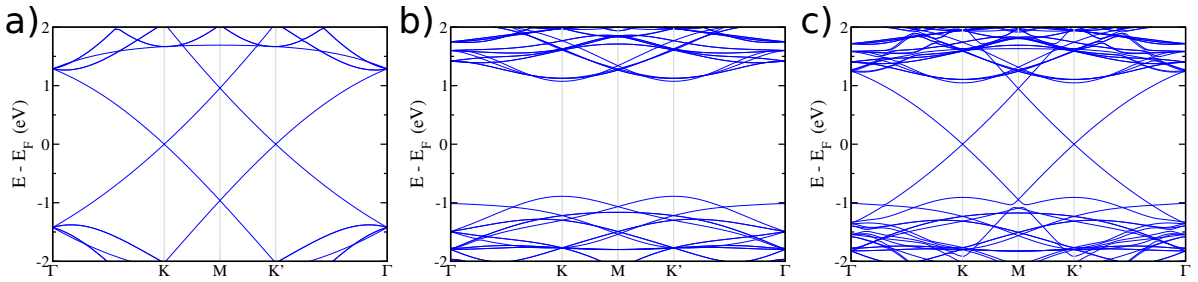

Figure 4.3: Band structures of the isolated graphene layer (a), of the WS_2 isolated layer (b) and the $1G/1WS_2$ structure (c).

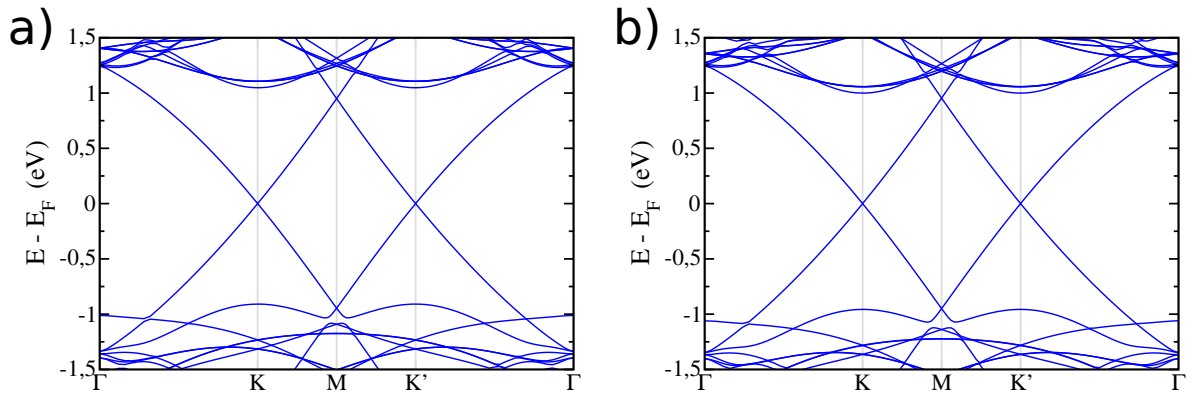

Figure 4.4: Band structure for the $1G/1WS_2$ structure before the relaxation process (a) and after the relaxation process (b).

As in the previous Section, it is important to compare with the case where we relax the system, which we show in Fig. 4.4, where we can see that there is no appreciable change between both band structures. Furthermore, no appreciable change is observed when calculating with GGA the same system at the optimised distance between layers obtained with LDA.

In Fig. 4.5 the band structure for the cases $n = 1$ to $n = 5$ are shown. In this Figure, we can see that the linear dispersion of the graphene bands is still preserved and, if we zoomed in (which, as before, we do not show), we would see that the small gap of 0.1 meV at the Dirac point is also preserved. Interestingly, there is a change near the Γ-point of the WS_2 band. We can see this more clearly in Fig. 4.6, where we show the highest valence and lowest conduction bands with increasing number of WS_2 layers. Although the lowest conduction band does not change notably except for a small shift towards lower energies, we can see that the valence band approaches the Fermi level with increasing number of layers. For instance, while the valence band at the Γ-point is 1.30 eV below the Fermi level for the case of isolated graphene, for the system with one WS_2 layer we have that the separation is 1.0 eV, with a decrease occuring when having two (0.5 eV) or more layers. In this Figure we can also see that for $n = 4, 5$ the distance to the Fermi level remains almost constant, approaching the bulk limit. Concerning the K-point, we can see that the appreciable change occurs now in the conduction band, where there is a shift towards lower energies.

4.2.2 Charge distribution

We now focus on how the charge distributes in space in these systems and how it varies with increasing number of layers.

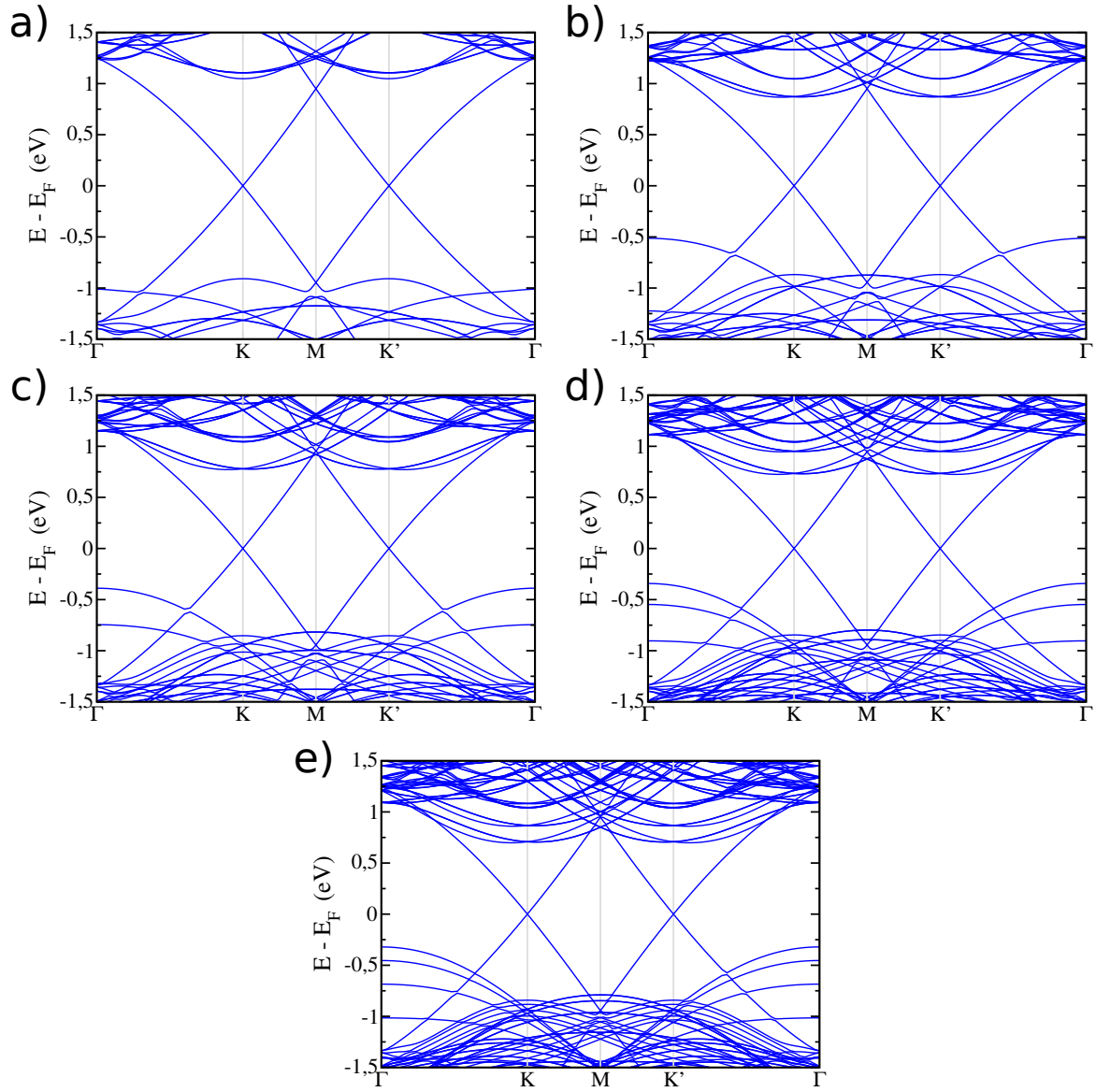

Figure 4.5: Band structure for the $1G/1WS_2$ (a), $1G/2WS_2$ (b), $1G/3WS_2$ (c), $1G/4WS_2$ (d) and $1G/5WS_2$ (e).

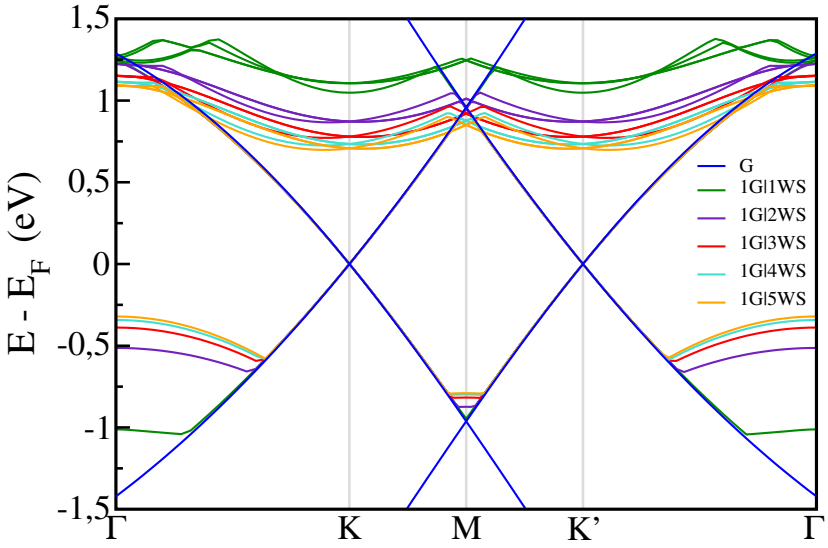

Figure 4.6: Comparison of the band structure for the systems with varying number of layers from 1 to 5.

We calculate the induced charge density in real space, that is defined as:

$$\rho_{ind}(x,y,z) = \rho(x,y,z) - \sum_{i}^{N} \rho_i(x,y,z), \tag{4.2}$$

where ρ is the charge density of the total system and i runs over all the subsystems that conform the total system when calculated separately. This quantity is an indication of how the charge redistributes due the interaction between graphene and WS_2.

As we can see in this Fig. 4.7, there is a formation of "patches" of charge in different positions of the cells. The redistribution of charge occurs mainly in the graphene/top S layer interface. Although we are not showing the results for the case of the relaxated structure, all these properties are mantained.

Furthermore, in Fig. 4.8 we show how the number of layers modifies the charge density in real space. As we see, all the charge redistribution occurs mainly between the graphene and the top layer S interface, as in the case of $n = 1$, and little is distributed in the lower layers, disappearing almost completely in the third layer of the WS_2.

For a more detailed and quantitative analysis, we will also study quantities such as charge densities and dipole moments only as a function of the direction perpendicular to our slab (z in our case). To do so we will compute these quantities as planar averages over the xy-plane parallel to the surface.

The z-dependent charge density will be defined as:

$$\rho(z) = \int_A \rho(x,y,z)dxdy, \tag{4.3}$$

where A is the area of the supercell in the xy-plane. As before, we study the induced charge densities, which is the modification in the charge density due to the formation of the bond between the substrate and graphene and it is defined in Eq. (4.2).[131]

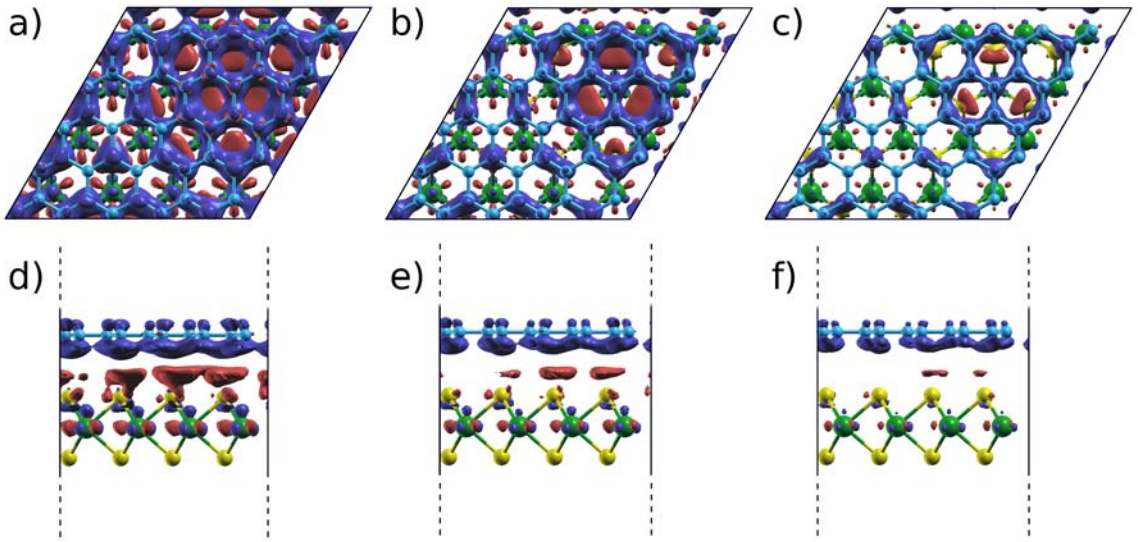

Figure 4.7: (a), (b) and (c) Top view of ρ_{ind} for the $1G/1WS_2$ structure for three different isovalues: 0.00015, 0.0002 and 0.00025 $e^-/Å^3$. (d), (e) and (f) Side view. Blue and red color represent a reduction (holes) and accumulation (electrons) of charge, respectively.

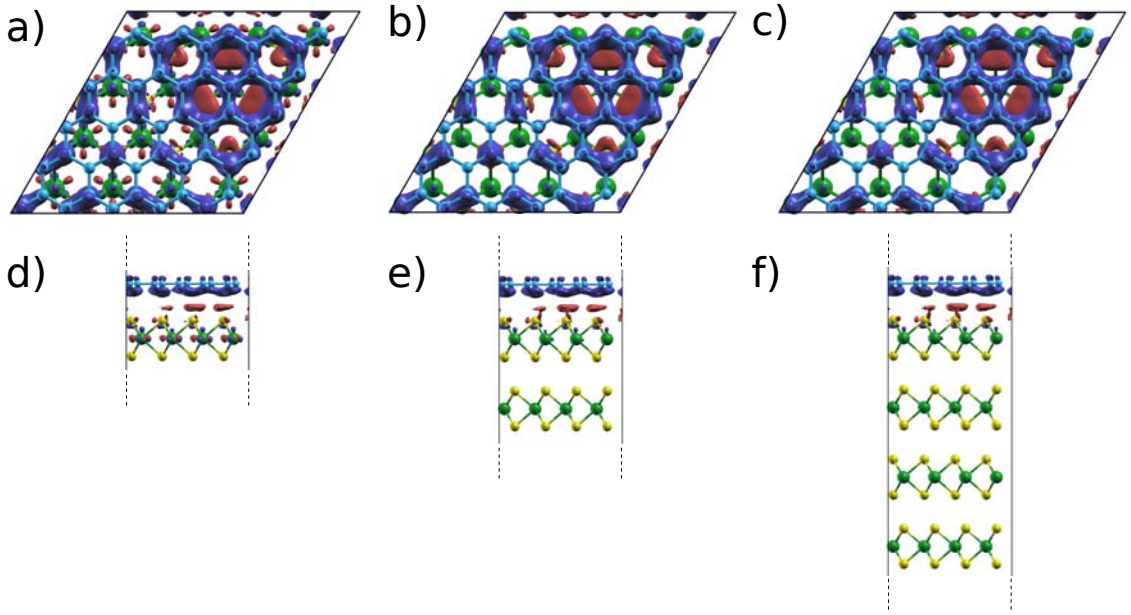

Figure 4.8: (a), (b) and (c) Top view of ρ_{ind} for the $1G/1WS_2$, $1G/2WS_2$ and $1G/4WS_2$ structures. (d), (e) and (f) Side view. All images were taken with an isovalue of 0.0002 $e^-/Å^3$. Blue and red color represent a reduction (holes) and accumulation (electrons) of charge, respectively.

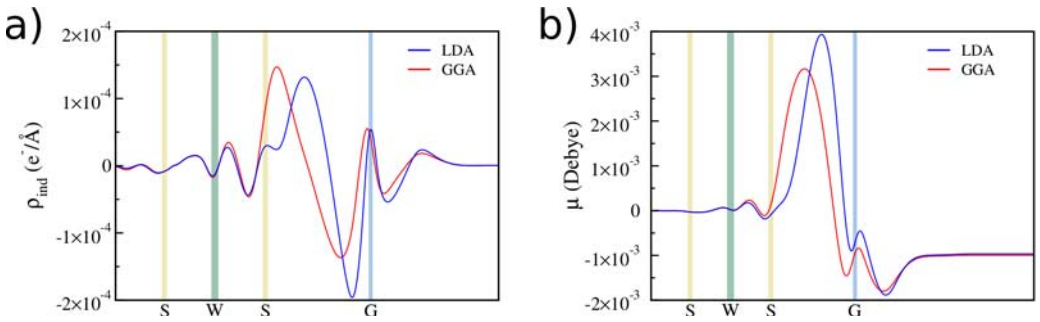

Figure 4.9: Comparison of the $\rho_{ind}(z)$ and $\mu(z)$ for different functionals. Blue (red) line corresponds to the LDA (GGA) calculation.

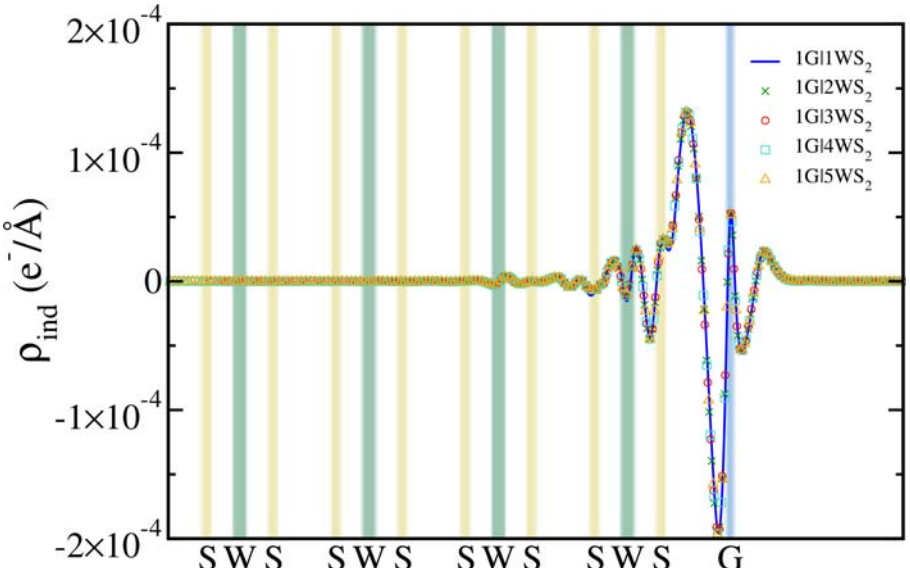

Figure 4.10: Comparison of $\rho_{ind}(z)$ for different numbers of layers. Blue line, green crosses, red circles, blue squares and orange triangles correspond to the case of $n = 1, 2, 3, 4$ and 5-WS_2, respectively.

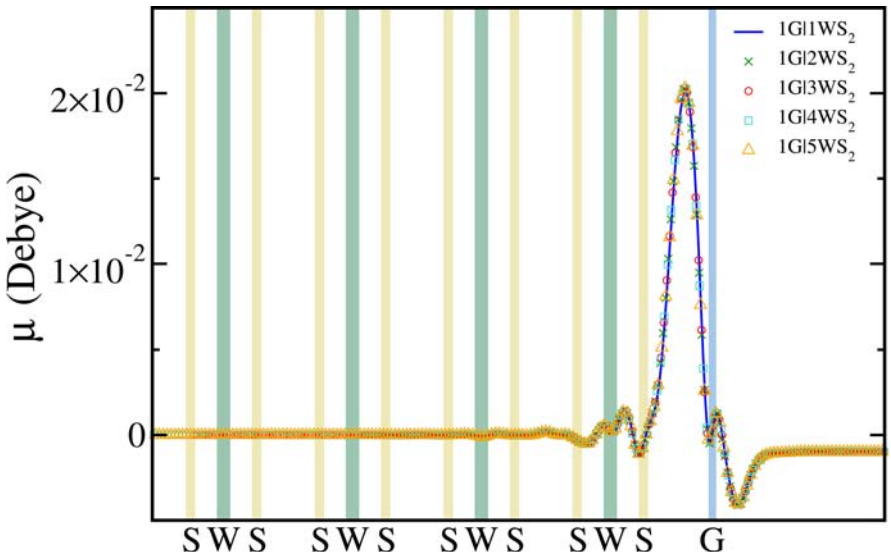

Figure 4.11: Comparison of $\mu(z)$ for different numbers of layers. Blue line, green crosses, red circles, blue squares and orange triangles correspond to the case of $n = 1, 2, 3, 4$ and 5-WS_2, respectively.

In a similar way, we will define the dipole moments associated with each of these charges. We define the dipoles as z-dependent quantities:

$$\mu(z) = \int_{z_0}^{z} z' \rho_{ind}(z') dz', \tag{4.4}$$

where z_0 is taken in the middle of the slab (where the perturbation due to the presence of the interface has been screened and $\rho_{ind}(z)$ tends to zero). The total dipoles of the surface are obtained for z well inside the vacuum away from the surface. These quantities will be denoted removing the dependence on z, as μ.

First, as we said in Section 4.1, it is important to test whether the electronic properties change qualitatively when changing from an LDA functional to a GGA functional. We show this study in Fig. 4.9, where we show the charge density for the 1G/1WS_2 system and we can see that there is no qualitatively change between both calculations and that the redistribution of charge occurs in both cases in the interlayer.

In Fig. 4.10 we plot the charge density for the systems going from 1 to 5 layers. As we saw before, most of the charge is accumulated between the graphene/WS_2 interface. It is interesting to note that there is almost no change when we increase the number of layers and that beyond the second layer there is almost no charge redistribution.

In Fig. 4.11 we plot the dipole that is formed due to the charge distribution for the systems with different number of layers. As we can see, the dipole is localized, as expected from what we saw in the study of the charge density distribution, between the graphene/WS_2 interface. The actual value of the dipole for the area of the supercell considered is of $\approx 10^{-3}$ Debyes and does not change with the number of layers.

4.3 Conclusions

In this Chapter we have studied the properties of a new family of substrates for graphene. Despite the fact that we just focus in the case of WS_2, the results should be qualitatively similar for other TMDCs of the type MX_2 (M = Mo, W; X = S, Se). We have seen that, although the linear behaviour of the surroundings of the Dirac cone is preserved, a small gap is opened in the band structure. On the other hand, adding more layers approaches the highest valence band in the surroundings of the Γ point to the Dirac cone. This change becomes more or less constant for $n > 3$, when the bulk limit is reached.

We also study the charge distribution in the different systems, finding that the charge is redistributed in the Graphene/WS_2 interface, where a small dipole is formed. Adding more layers to the systems does not affect this characteristic and, actually, there is no significant charge redistribution beyond the second layer.

Chapter 5

Two band gap superconductivity in layered materials

Metals have an electrical resistivity that depends on temperature. This resistivity comes, in the majority of the cases, from the interaction of electrons with phonons, defects, surface effects and other electrons. Although intuitively we could think that lowering the temperature we could reduce the resistivity to zero, this is not the case and, actually, there is always some residual resistivity (see Fig. 5.1a).

Some materials, below some critical temperature (T_c), lower their resistivity to values that are essentially zero. This phenomenon is called *superconductivity*, and was discovered in 1911 by Heike Kammerlingh Onnes when he saw a reduction of the resistivity when he cooled an Hg sample below 4.2 K (see Fig. 5.1b). Additionally to the low resistivity, there are other properties such as the one discovered by Meissner and Ochsenfeld in 1933 that shows that, inside a superconductor (SC) there is no magnetic field. This effect is called the Meissner effect, and it holds for SC called of type 1. For SC of type 2, from a certain value of the magnetic field, inside the SC some *vortices* are formed where the magnetic flux can penetrate inside the sample. As we will see later in the Chapter, both materials studied here are of type 2.

Many theories were initially developed in order to explain these new physical phenomena, but all of them were phenomenological, such as the ones by London and Ginzburg-Landau. It was not until 1957 that a breakthrough in the understanding of superconductivity was achieved due to the microscopic theory developed by Bardeen, Cooper and Schrieffer[132] (BCS) where, with the introduction of Cooper pairs, they were able to give a microscopic explanation of the phenomenon.

BCS theory shows that, due to electron-phonon coupling, below T_c, an attractive electron-electron interaction leads to the ground state of the system which is the one with paired electrons that form the so called Cooper pairs.[133] In a simple way, we can see this interaction as if one moving electron changes the position of some ions of the lattice, leaving an electric local density charge that attracts another electron[134] (see Fig. 5.2a). In a quantum-mechanical point of view,

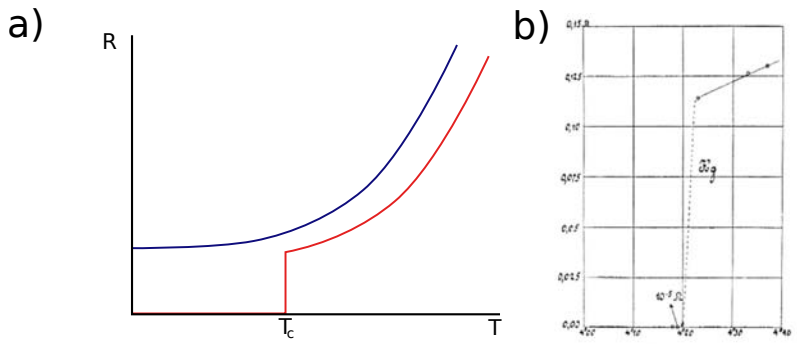

Figure 5.1: (a) Schematics of the resistance vs. temperature for a normal metal (blue line) and a superconductor (red line). (b) Original measurement by Kammerlingh Onnes when he discovered superconductivity in cooled Hg.

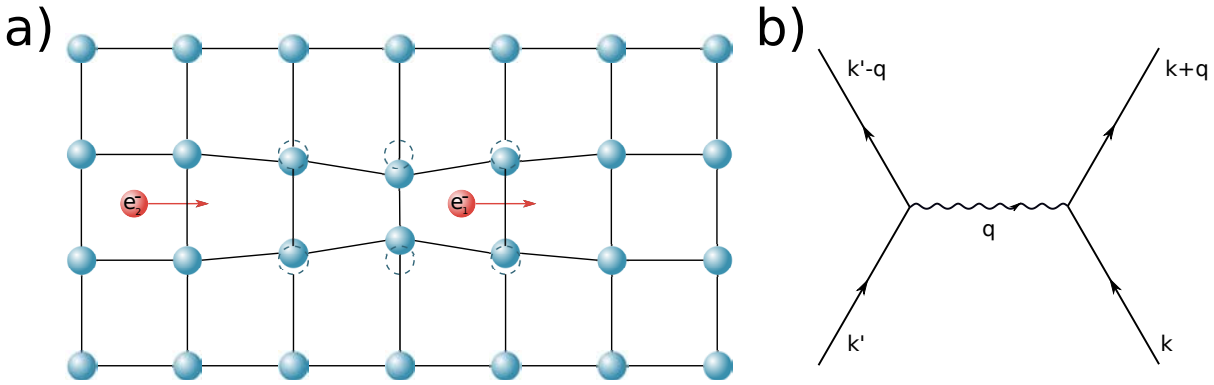

Figure 5.2: (a) Schematic drawing of the classical view of a Cooper pair formation. Electron (red) #1 attracts two ions (blue) of the crystal lattice creating a local density charge that attracts electron #2. (b) Feynman diagram of an e^--e^- interaction mediated by a virtual phonon.

we could see this as if two electrons interact by an exchange of a virtual phonon (see Fig. 5.2b).

The BCS theory takes into account electrons in a single band, but in many superconductors there can be two contributing bands, for example: in SCs with transition elements, there are $s-d$ bands at the Fermi level, so one of the natural improvements to the BCS model would be to extend it to these cases. This issue was addressed by Suhl *et al.*[135] They found that each band had a different superconducting gap and that, if there was no interband coupling, each of them would have a different T_c.

For a long time, the BCS description for superconductivity was very successful in the explanation of the properties of conventional superconductors.[136] When the experimental methods improved, a close look at the details of the results showed that there were some deviations from this theory. In 1977 Schopohl and Scharnberg[137] (SS) improved Suhl's model adding a quasiparticle scattering from one band to the other which gives two coupled equations for the two gaps that arise in these materials.[136] The interband coupling can even induce superconductivity in an non-superconducting band.[138] The equations that are given by the SS formalism are equivalent to those of McMillan which applies to the case where a SC is in contact to a metal[139] (therefore, in the literature, as in the following, the formalism is either called SS, McMillan or SSM). On the other hand, though they are mathematically equivalent, both approaches have a different physical origin: while in the one by SS the proximity effect is in the reciprocal space, the later originates in real space.[136] An important result that we obtain from the SSM approach, as we will see further in the development of the Chapter, is that the scattering rates are related to the partial normal-state density of states which can be computed within standard DFT.[136]

Experimentally, though there was some possible evidence of multi band superconductivity, it was not clear until 1980 when Binnig and coworkers[140] found this effect in Nb-doped $SrTiO_3$. The low transition temperature of this material and the quite difficult experimental methods made, at that time, a rather challenging experiment to carry out and the topic was not further pursued.

However, in 2001 superconductivity at 39 K in MgB2 was discovered.[141] Soon later two band superconductivity was confirmed for this system and the topic became quite popular.

There are many experimental methods to study the value of the superconducting gaps, such as specific heat measurements, low-temperature Raman-scattering, scanning tunneling microscopy (STM) and spectroscopy (STS) (in the superconductor-insulator-normal-metal (SIN) configuration or in the superconductor-insulator-superconductor (SIS) configuration).

Theoretically, there are several ways to study the existence of two SC gaps by first-principles

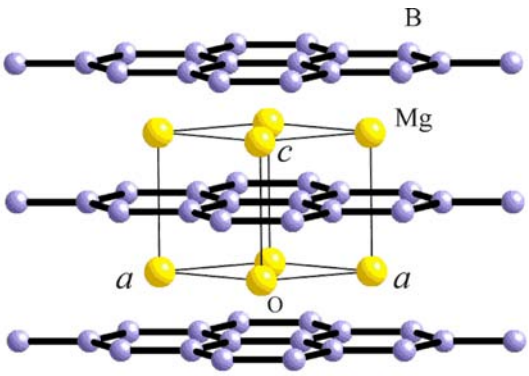

Figure 5.3: Crystal structure of MgB_2.

calculations such as the calculation of the electron-phonon coupling for using it for the Eliashberg theory and the density functional theory for the superconducting state.[142,143] Though they do not need experimental parameters in order to obtain predictions, the calculations are quite challenging.

In this Chapter, we will develop another approach to study the electronic properties of two band gap SCs like MgB_2 and $NbSe_2$. During the development of this thesis, we stablished a collaboration with the group leaded by Dimitri Roditchev[1] which had experimental SIS data without a clear interpretation in both materials in the superconducting state. With the help of DFT calculations of the normal state of these materials, we were able to study properties that are correlated with the characteristics of the superconducting state. As we will see, studying the theoretical electronic properties and STM images of these systems we are able to give support to the assignment of the different superconducting gaps to the bands that generate them.

5.1 Multi band superconductivity in MgB_2

As stated in the introduction of this Chapter, MgB_2 has been known for a long time[144,145] but interest in this material was boosted by the discovery of superconductivity with a relatively high critical temperature (T_c = 39 K).[141] MgB_2 exhibits the AlB_2-type crystal structure,[146] where graphene-like hexagonal layers of boron atoms alternate with hexagonal layers of magnesium atoms sitting on top of the center of the boron hexagons (see Fig. 5.3). The simplicity of the structure made possible very detailed theoretical studies. An and Pickett[147] proposed that superconductivity originates in the boron (p_x,p_y) bands and Liu *et al.*[148] suggested the possibility of two-gap superconductivity for this compound.

The two-band superconductivity scenario for MgB_2 soon received support from different experimental studies using STM tunneling spectroscopy[149], point-contact spectroscopy,[150–152] specific heat measurements[153] and Raman spectroscopy.[154] Iavarone *et al.*[155] reported tunneling studies on both *c*-axis oriented films and compact pellets and provided evidence for directional tunneling with respect to the crystallographic orientation of the grains in the pellets. It is now well established that there are two distinct superconductivity energy gaps, Δ_1 = 2.3 meV and Δ_2 = 7.1 meV.[155,156]

Although there have been several first principles theoretical studies[147,148,157–159] of the electronic structure of MgB_2, to the best of our knowledge there is no study of the tunneling images and it was noted by Schmidt *et al.*[150] that the calculated contributions of the two different types of bands to the bulk density of states at the Fermi level are insufficient to account for

[1]Spectroscopie des Nouveaux Etats Quantiques group at the Institut des Nanosciences de Paris.

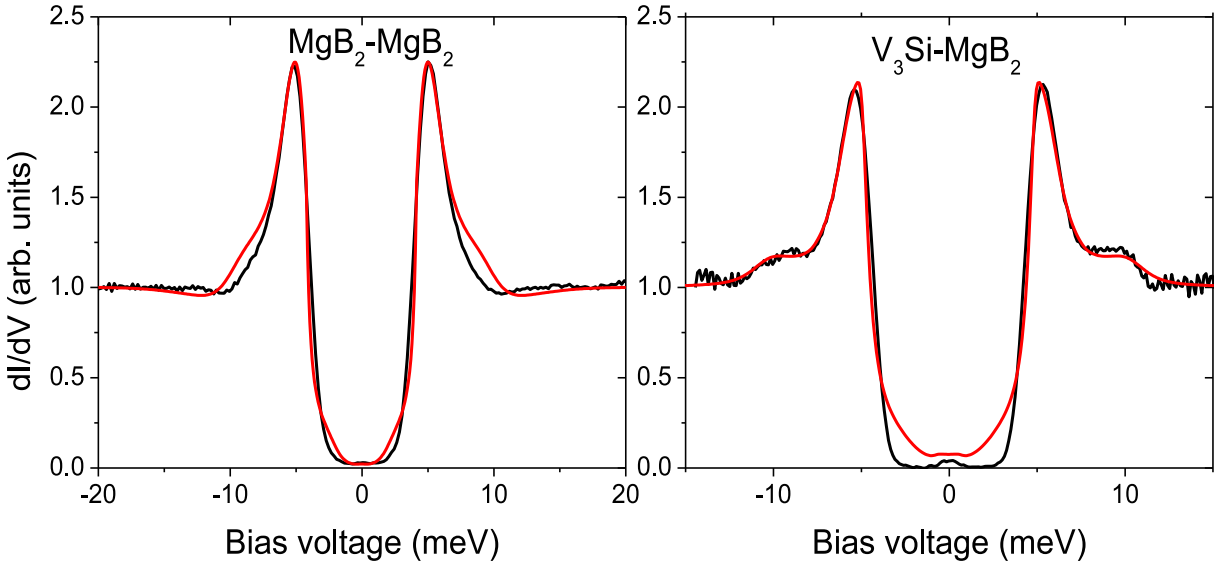

Figure 5.4: (a) SIS tunneling spectrum by Roditchev *et al.* measured with an MgB_2 tip and a MgB_2 'c' axis oriented film. The experimental data (black line) is fitted (red line) using the SSM model (Eq. 5.3). The parameters used for the fit are $\Gamma_S = 2.6$ meV; $\Gamma_L = 2.6$ meV; $\Delta_S^0 = 1.1$ meV, $\Delta_L^0 = 7.4$; $T_S = 1$; $T_L = 0$; (b) SIS tunneling spectrum measured with an MgB_2 tip and a V_3Si 'c' axis oriented surface. The parameters used for the fit are $\Gamma_S = 2.6$ meV; $\Gamma_L = 2.6$ meV; $\Delta_S^0 = 1.1$ meV, $\Delta_L^0 = 7.5$; $T_S = 0.9$; $T_L = 0.1$.

the tunneling experiments. In the following we show a first-principles density functional theory (DFT) study of the electronic properties and tunneling images of the normal state of MgB_2 and provide theoretical support for the assignement of the different superconducting gaps to the corresponding band that generates them.

5.1.1 Experimental results

In this Section, we are going to show the experimental results obtained in Roditchev's group. In Figure 5.4, we show two experimental tunneling spectra in SIS geometry with a SC MgB_2 tip and a MgB_2 or V_3Si surface, measured using their home built STM/STS setup at low temperature (most of the experiments were done at $T = 4.2$ K).

As we said before, these experimental data can be fitted using the SSM model, in which a multiband superconductor is described by intrinsic gaps, Δ_i^0, resulting from electron-phonon coupling in each band i and by the quasiparticle coupling between bands i and j, characterized by a coupling parameter Γ_{ij}, which represents the inverse lifetime of a quasiparticle in band i due to its coupling to band j. Such a coupling could result from the presence of impurities electron–electron interaction, as other effects.[137]

The interband coupling leads to energy-dependent gaps, $\Delta_i(E)$, which can be calculated by the self-consistent equations:[139]

$$\Delta_i(E) = \frac{\Delta_i^0 + \Gamma_{ij}\Delta_j(E)/\sqrt{\Delta_j^2(E) - E^2}}{1 + \Gamma_{ij}/\sqrt{\Delta_j^2(E) - E^2}} \tag{5.1}$$

with $i = 1, 2$. The density of states $N_S(E) = \sum_i N_S^i(E)$ is expressed as a sum over the partial density of states $N_S^i(E)$ in each band i:

$$N_S^i(E) = N_i(E_F)\mathrm{Re}\left[\frac{|E|}{\sqrt{E^2 - \Delta_i(E)^2}}\right] \tag{5.2}$$

where $N_i(E_F)$ is the partial density of states at the Fermi level of the i band in the normal state.

Taking into account selectivity effects, the tunneling DOS probed by STS for a two gap superconductor can be written in the general way:

$$\begin{aligned} N_S(E) &= \sum_{i=1,2} T_i N_i(E_F) \mathrm{Re}\left[\frac{|E|}{\sqrt{E^2-\Delta_i(E)^2}}\right] \\ &= \sum_{i=1,2} N_i^{eff} \mathrm{Re}\left[\frac{|E|}{\sqrt{E^2-\Delta_i(E)^2}}\right], \end{aligned} \tag{5.3}$$

where T_i accounts for the k-averaged tunneling probability towards a given band i and $N_i^{eff} = T_i N_i(E_F)$ is the effective DOS in band i as measured by STS taking into account the tunneling selectivity.

The parameters that they deduced from the fits are very similar for the two types of junctions MgB_2-MgB_2 and MgB_2-V_3Si. In both cases, it is found that T_S is close to one, meaning that the contribution of the small gap band strongly dominates in the tunneling process.

It is important to note that the interband quasiparticle coupling leads to characteristic signatures in the excitation spectra which deviate from the standard BCS form.[136] This is at odds with the case of interband pair coupling as considered by Suhl *et al.*[135] which gives rise to a standard BCS DOS for each band. Thus, from the tunneling conductance fit, we can deduce the values of the intrinsic gaps in each band Δ_0^i, as well as the interband coupling parameters Γ_{ij}. Note that the ratio of the partial DOS of the two bands is directly related to the interband coupling between them:

$$\frac{\Gamma_{ij}}{\Gamma_{ji}} = \frac{N(E_F^j)}{N(E_F^i)} \tag{5.4}$$

This property is very useful and will allow us to compare this ratio with the result of bulk measurements such as specific heat and our DFT calculations.

As expected, from the fit, Roditchev and coworkers find a ratio close to 1, in striking agreement with the value that can be inferred from specific heat and penetration depth measurements. [160]

Therefore, from the experiment done by Roditchev *et al.* we obtain two main conclusions:

1. The tunneling probability of the small gap is close to 1, which means that it will dominate the tunneling process.

2. The ratio between the interband coupling parameters is close to 1.

In the following Sections, we will use calculations of the normal state of MgB_2 in order to give support to the experimental results. For example, calculating the DOS at the Fermi level of the bands in the normal state, could help us understand the ratio of the interband coupling parameters and give theoretical support to the experimental results showed in this Section.

5.1.2 Electronic structure

The electronic structure of MgB_2 has been discussed a number of times in the literature as in the works by An *et al.*,[147] Li *et al.*,[157] Kortus *et al.*,[158] Nuñez *et al.*[159] and Satta *et al.*,[161] here we just highlight the aspects which are important in understanding the signatures of multigap superconductivity in tunneling spectroscopy. The calculated band structure is shown in Fig. 5.5a. There are three partially filled bands, two of them are based on the boron p_x and p_y orbitals (bands shown with blue circles in Fig. 5.5a) and have a two-dimensional (2D) character because of the lack of interaction with the magnesium orbitals (see the Γ to A line in Fig. 5.5a).

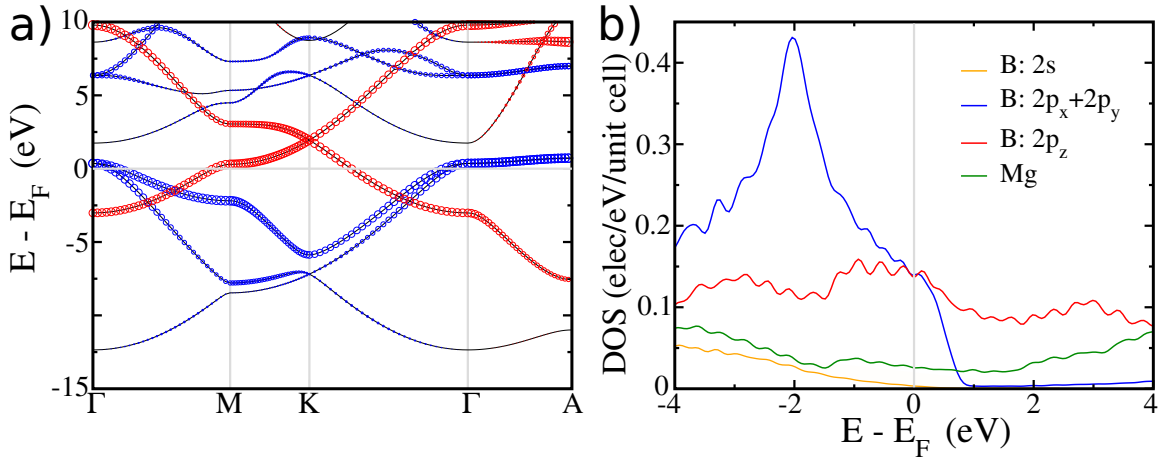

Figure 5.5: (a) Band structure for MgB_2 where the blue circles correspond to the boron p_x, p_y character and the red circles to the boron p_z character. $\Gamma = (0, 0, 0)$, $M = (1/2, 0, 0)$, $K = (1/3, 1/3, 0)$ and $A = (0, 0, 1/2)$ correspond to high symmetry points in units of the reciprocal hexagonal lattice vectors; (b) Density of states near the Fermi level where the contributions of the boron s, the boron (p_x, p_y), boron p_z and magnesium orbitals are separately shown.

They are associated with the σ bonds of the boron layers. In contrast, the other partially filled band (shown with red circles in Fig. 5.5a), which is built from the boron p_z orbitals, exhibits dispersion along both the plane of the boron layers (because of their π-type interactions along the boron layers) and the interlayer direction (because of the good overlap between the out-of-plane pointing boron p_z and magnesium orbitals). Consequently, the Fermi surface (see Fig. 5.6) is made of two cylinders parallel to the c-direction centered around Γ, associated with the boron p_x and p_y orbitals, and a complex three-dimensional network, mostly associated with the boron p_z orbitals. Note that despite the very different Fermi surfaces, the densities of states at the Fermi level for the boron (p_x,p_y) and boron p_z orbitals (see Fig. 5.5b) are practically the same because the Fermi velocity of the cylinders is very low along the c^* direction. The actual ratio is ≈ 0.99, which is in agreement with the experimental results of Section 5.1.1 which shows that the ratio of the interband coupling (Eq. 5.4) is close to 1. If we project the contribution of the different bands, that of the cylinders is of 44% and that of the 3D network is 56%. It is worth noting that the wavefunctions are of e-type symmetry with respect to the threefold symmetry axis parallel to the c direction and going through one boron atom and, consequently, the boron s orbitals can not mix in. Thus, the boron s content of the Fermi surface cylinders will be quite small.

5.1.3 Tunneling Images

Once we have given support to the experimental result that the interband coupling parameters is close to 1, we study now the other experimental result: the tunneling probability of the small gap is close to one, that is, in the experimental SIS measurements, we probe the small gap since it is coupling almost perfectly with the tip. To do so, we have done several simulations of STM images, which we present in this Section. The calculations were done using the Tersoff-Hamann approximation,[162] where the current at a given tip position is proportional to the integral of the local density of states of the sample at that point (integrated in an energy window (± 0.1 eV) given by the tip-surface potential difference). The images correspond to constant current images, showing the maps of heights that produce a constant tip-surface current. Instead of specifying the value of the current (which is what would be done in the experiment), we choose a particular value of the density of sates and plot the corresponding isosurface, which would

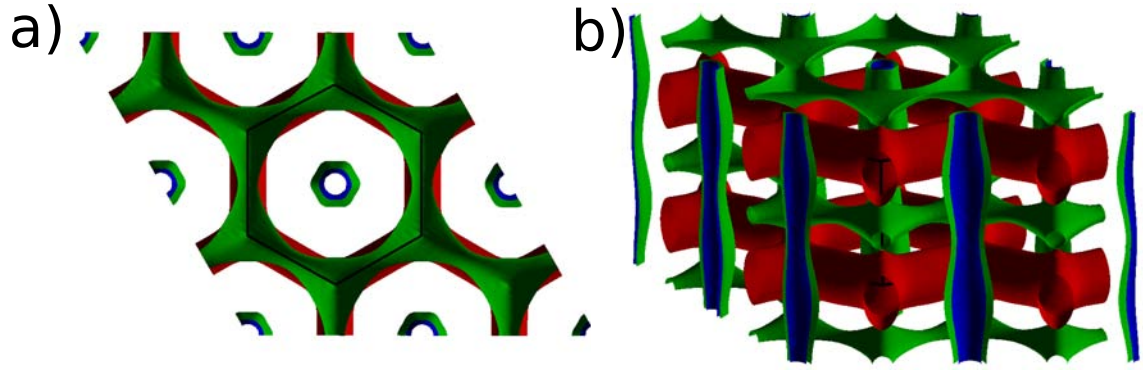

Figure 5.6: Top (a) and side (b) views of the calculated Fermi surface for MgB_2. The red and green tubular structure come from the boron p_z contribution while the cylinders in green and blue come from the p_x, p_y bands from the boron.

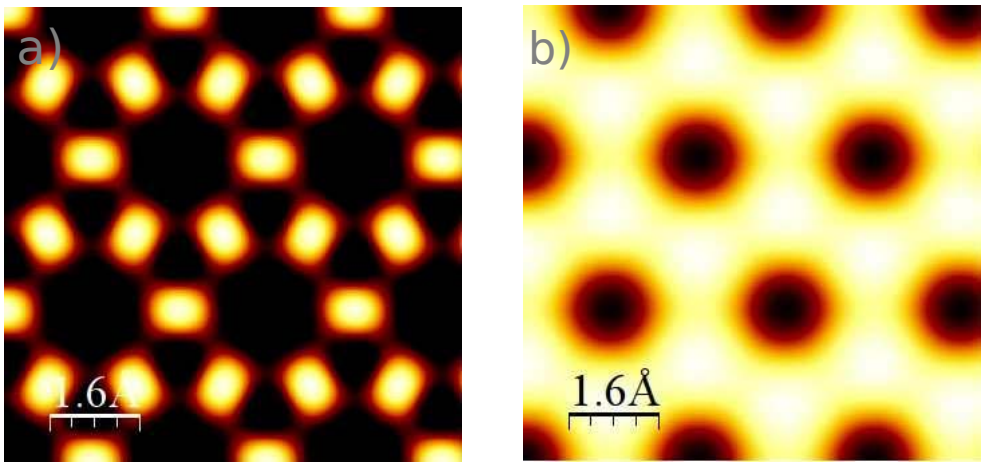

Figure 5.7: STM images for the p_x, p_y (a) and for the p_z (b) contribution. The maxima in (b) correspond to the position of the B atoms and those in (a) to the B-B bonds.

correspond to different values of the current. In our images, we have separated the contribution of the different bands at the Fermi surface: the (p_x, p_y) based bands (from now on we will refer to them as (p_x, p_y) bands) that generate the blue and green cylinders and the p_z based band (from now on we will refer to them as (p_z) bands) that generates the green and red tubular network (see Fig. 5.6). We did this by calculating separately the STM image for each band (taking into account in which region of k-space they are located). The results are shown in Fig. 5.7.

The (p_x, p_y) states lay on the (xy)-plane and they do not extend much along the z-direction, unlike the p_z states. Besides, these states form σ bonds between the B atoms at the surface, whereas the p_z bands form π states pointing out of the surface. Therefore, in the STM images generated from the (p_x, p_y) bands (see Fig. 5.7a), the brightest positions are the center of the bonds between surface B atoms. On the other hand, for the p_z states, the brightest positions are on top of the positions of the surface B atoms (see Fig. 5.7b).

We have studied the decay of the current (I) with the height (z) in different positions of the (x, y)-plane. To do this we draw the I vs. z curve at different (x, y)-plane positions. At sufficiently large distances, the current I should be roughly related to z exponentially:

$$I = Ae^{-\alpha z}, \tag{5.5}$$

thus, we can obtain α easily by plotting $ln(I)$ vs. z and doing a linear fit of the data (see Fig.

Bands	Position	Fit exp 1	Fit exp 2
	At atom	1.312	2.33
(p_x, p_y) bands	At bond	1.317	2.693
	At center of hexagon	1.307	1.93
	At atom	1.321	-
p_z band	At bond	1.319	-
	At center of hexagon	1.313	-

Table 5.1: Summary of the I vs z fits. "Fit exp 1" and "Fit exp 2" refer to the value of the slope (α) for the two possible decaying ratios that can occur (far and near to the surface). Values are given in Bohr^{-1}.

5.8).

The fitting parameters obtained for lines passing through a surface atom, a surface bond and the middle of a surface hexagon are reported in Table 5.1. In all cases we show the contribution of the (p_x, p_y) and p_z bands separately. In the case of the bands with (p_x, p_y) character, the curves do not correspond to a single exponential as in Eq. 5.5. We actually have two exponential regimes (two different slopes at the curve). This can be explained if we look into the formulas that describe the decay of the wave functions of the crystal into vacuum (which we use to generate the STM images). Far from the surface (where the potential is constant and equal to the vacuum potential), the wave functions can be expressed as:

$$\psi_{\mathbf{k}}(x, y, z) = \sum_{G_x} \sum_{G_y} C_{\mathbf{k}}(\mathbf{G}) e^{i(\mathbf{G}+\mathbf{k})\cdot\mathbf{r}} e^{-\alpha_{\mathbf{k}+\mathbf{G}} z}, \tag{5.6}$$

where $C_{\mathbf{k}}(\mathbf{G})$ is the Fourier component of the wavefunction at a reference plane (taken as $z = 0$), $\mathbf{G} = (G_x, G_y)$ is the surface reciprocal lattice vectors and $\mathbf{r} = (x, y)$ is the in-plane position. The decay of the corresponding Fourier component with z is thus given by

$$\alpha_{\mathbf{k}+\mathbf{G}} = \sqrt{\kappa^2 + (\mathbf{k} + \mathbf{G})^2}, \tag{5.7}$$

where κ^{-1} is the standard decay length determined by the work function, ϕ, (i.e. $\kappa = \frac{\sqrt{2m\phi}}{\hbar}$ where m is the electron mass).

From this formula, it is apparent that the wave functions have different components with different decay into vacuum. The decay depends on the work function ϕ (which is the same for all the states), the $\mathbf{G}$ vector of that component, and on the surface momentum $\mathbf{k}$ of the electronic state. For a given wavefunction, at large distances from the surface, only the $\mathbf{G} = 0$ component will survive, with a decay $\alpha = \sqrt{2\phi + \mathbf{k}^2}$. In that case, the decay of the wave function is determined by the work function and the wave vector of the states at the Fermi surface. For distances close to the surface, several $\mathbf{G}$ will contribute leading to different decay rates. If we are close to Γ (where the cylinder generated by the (p_x, p_y) bands in the Fermi surface is placed (see Figure 5.6)), we have that $\mathbf{k} \simeq \mathbf{0}$. For the states from the p_z bands, the wave vectors are far from the Γ point. Consequently, reasoning on the basis of this k-selectivity would let us expect that the decay into vacuum will be faster for them. This is what we find when looking at the results in Table 5.1, where we see that the slopes for the p_z bands is slightly larger than the corresponding ones of the (p_x, p_y) bands.

Although these results clearly show that the contribution of the (p_x, p_y) bands decays faster than that of the p_z bands relatively close to the surface, the intensity of the images coming from the p_z contribution is approximately three orders of magnitude than the (p_x, p_y) contribution (see Fig. 5.8). For larger distances, the decay rates do not significantly change with the position in

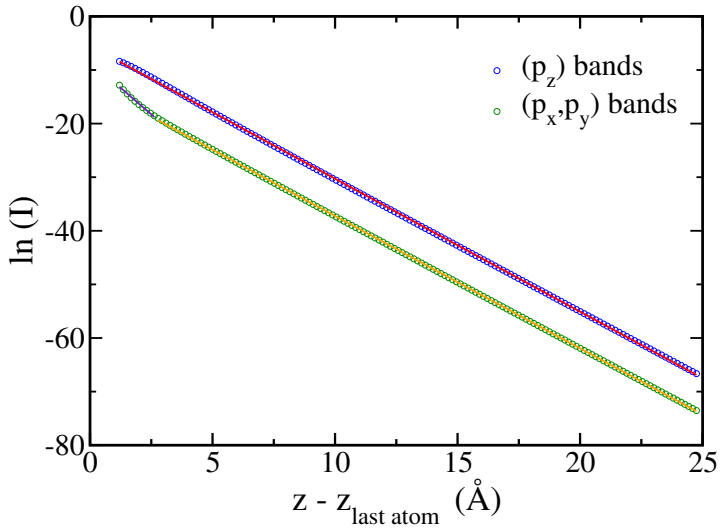

Figure 5.8: $ln(I)$ vs. z fits at a center of an hexagon. Blue and green circles represent the data for the p_z bands ($k > 0$) and (p_x, p_y) bands ($k \simeq 0$). The lines represent the different fits for this data. The data for the (p_x, p_y) bands have two fits for the two different regimes of decay.

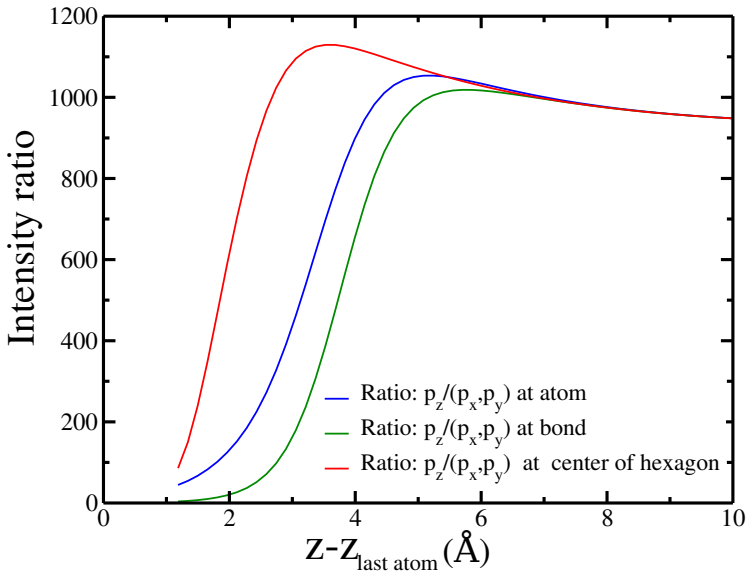

Figure 5.9: Ratio of intensities for different positions.

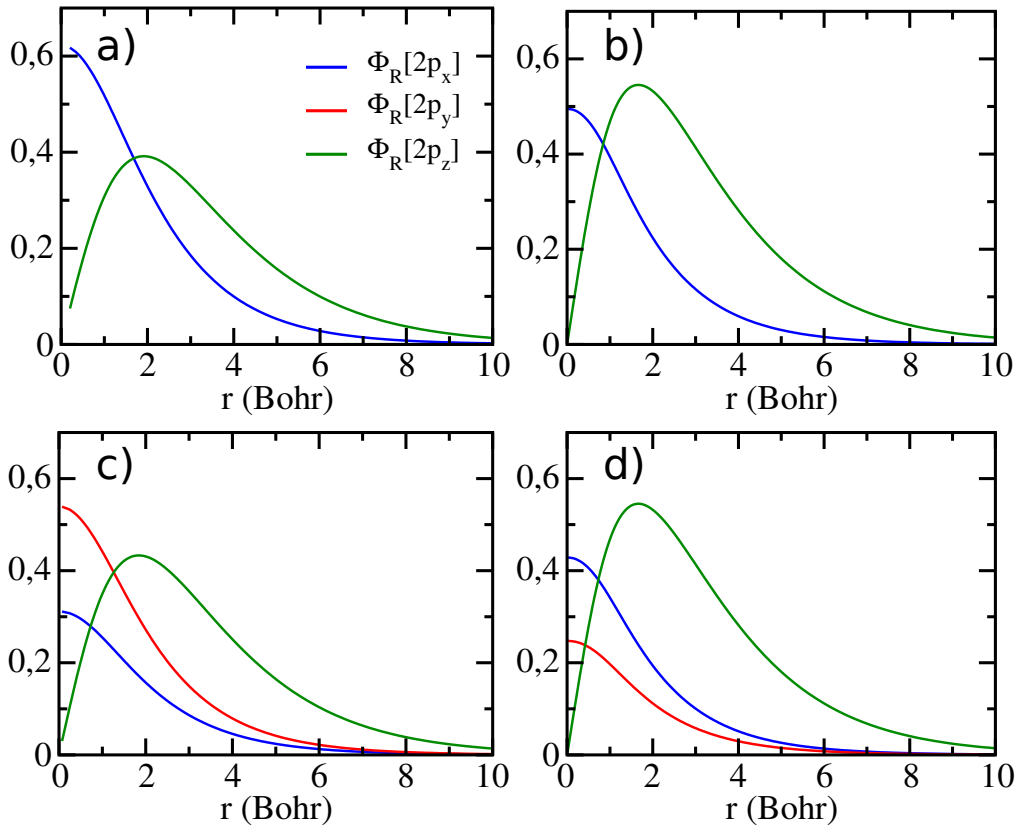

Figure 5.10: Comparison of the decay of the boron (p_x, p_y) and p_z orbitals along the c axis for different positions of the surface ((a) at mid distance between two B atoms, (b) at a quarter distance between two B atoms, (c) at a Mg position and (d) at mid distance between a Mg and B atom), which is taken as the origin.

the (x,y) plane. The ratio of the STM image intensity associated with the p_z and (p_x, p_y) bands as a function of the distance from the surface is shown in Figure 5.9. Except for unreasonably short tip to surface distances the curves for different positions in the (x,y) plane evolve to very similar values. It is clear from these results that for any reasonable distance from the surface the tunneling images will be completely controlled by the p_z band.

Which is the main factor leading to this result? As mentioned above, the **k** selectivity of the tunneling current would let us predict that the contribution of the p_z orbitals would decay faster that of the (p_x, p_y). However, the results of Fig. 5.9 and the experimental evidence from Section 5.1.1 that showed that $T_s = 1$ and, therefore, the tunneling conductance should be dominated by the small gap which is known to be generated from the p_z band. Note that the two types of bands have a not very different contribution to the density of states at the Fermi level (see above). Consequently, the most likely explanation for the almost complete control of the tunneling images along c must lie in the shape of the different orbitals.

The different decays of the atomic p_x (or p_y) and the p_z orbitals along c for different in-plane positions are shown in Fig. 5.10. To do this, we just calculate the wave function of a free Boron atom along the c axis at different positions of the (x, y)-plane. It is clear that the p_z orbitals decay considerably slower than the $(p_x,\ p_y)$ orbitals and must dominate the tunneling at reasonable tip to surface distances. As a matter of fact, there are also strong symmetry reasons behind the results of Fig. 5.9. As mentioned before, the wavefunctions of the Fermi surface cylinders have a pseudo e-type symmetry. Such e-type functions have a nil value along the threefold symmetry axis parallel to the c direction and going through one boron atom. Consequently, these wavefunctions must have quite small values along this axis and the

region around. This is in contrast with the large and slowly decaying values of the boron p_z orbitals in the same region. A similar symmetry argument applies for the axis perpendicular to the layer and passing through the center of the boron hexagons, predicting also very small values of the Fermi surface cylinders wavefunctions around this axis. Of course, the symmetry restrictions become less stringent outside the regions around these axes but it is clear that there are large areas where these wavefunction are forced to have small values for symmetry reasons. In contrast, this kind of symmetry restrictions have no detectable influence on the wavefunctions based on the boron p_z orbitals. These features are already clear from the STM images in Fig. 5.7. Altogether, the faster decay of the (p_x, p_y) orbitals and the confinement due to symmetry reasons leads to quite small values of the wavefunction for reasonable tip to surface distances.

We thus conclude that, both the directional shape of the boron p_z orbital and the symmetry properties of the lattice lie behind the fact that only the small superconductivity gap, which is associated with the 3D component of the Fermi surface and originates from the boron p_z states, may be directly probed in the SIS experiments along the c direction.

Therefore, with this calculation and the one shown in Section 5.1.2 we have tested the two experimental results obtained in Section 5.1.1: the ratio between the interband coupling parameters is close to 1 and the small gap is dominating the tunneling process. Moreover, we have shown that the small gap is generated by the p_z character band.

5.2 Multi band superconductivity in $NbSe_2$

Superconductivity in niobium diselenide (2H-$NbSe_2$), $T_c \sim 7$ K was discovered about fifty years ago.[163,164] In spite of numerous experimental and theoretical studies of the material, the precise nature of its superconducting (SC) state remains controversial. In particular, the relation between the SC transition[163,164] and the charge density wave order[165] is still debated.

The possibility of some anisotropy in the SC gap was already noted in the 1970's by Morris *et al.*[166] Clear deviations from the standard BCS density of states (DOS) were then observed by Hess *et al.*[167] using scanning tunneling spectroscopy (STS) on a c-axis oriented sample, but were not given much attention at the time. This is surprising since the two-branch Fermi surface (FS), with a set of Nb-derived cylinders around the central Γ point of the hexagonal Brillouin zone and another set of cylinders around the corner K points, had been well established.[168–170] A few years after, the gap anisotropy was modeled by Rodrigo *et al.*[171] using a continuous gap distribution.

More recently, a two-gap scenario was proposed by several groups based on photoemission (ARPES),[172] heat conductivity,[173] specific heat[174,175] and penetration length measurements.[176] In all these works, the system is described by the early model of Suhl, Matthias and Walker,[135] which assumes a pair coupling between the two bands, giving rise to a BCS-like density of states.[132] A particular feature of the Fermi surface of 2H-$NbSe_2$ is the existence of a selenium-based pocket near the Brillouin zone center. This was first revealed by a combined de Haas-van Alphen and density functional theory (DFT) study[177] and later confirmed by ARPES Fermi surface mappings.[172,178] Its role in the multigap scenario has not been determined yet.

The room temperature crystal structure of 2H-$NbSe_2$[179,180] (see Fig. 5.11) is built from hexagonal $NbSe_2$ layers containing Nb atoms in a trigonal prismatic coordination. The six Nb–Se bonds within these layers are identical (2.598 Å). As shown in Fig. 5.11, the repeat unit of the solid contains two symmetry equivalent layers related by a screw axis along c. Successive layers are separated by van der Waals coupling through which there are relatively short Se–Se contacts, i.e. every Se atom makes three Se–Se contacts (3.537 Å) shorter than the sum of the van der Waals radii with the Se atoms of the adjacent layer. The Se–Se contacts along the c-direction within the hexagonal layers are even shorter, 3.347 Å. These two structural features

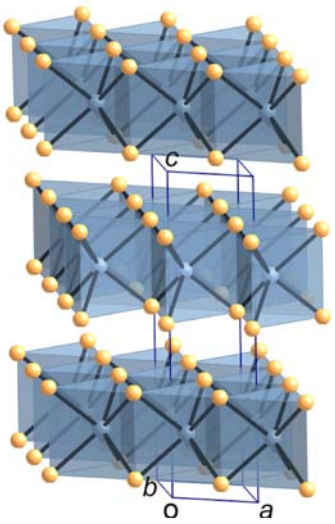

Figure 5.11: Crystal structure of $2H$-$NbSe_2$. The Nb and Se atoms are represented with blue and yellow spheres, respectively.

give a considerable three-dimensional character to this layered material.

At 30 K 2H-$NbSe_2$ undergoes a distortion leading to a $(3a\times3a\times c)$ superstructure.[165] Its origin has been attributed to a Fermi surface nesting driven charge density wave (CDW)[181] although this explanation has been challenged.[169,170,178,182–184] Recently, it has been shown both experimentally and theoretically that a strong electron-phonon coupling occurs in this material.[185,186] Although several models of the distorted phase have been discussed,[187,188] only recently in the course of our work the detailed structure of this phase has been reported.[189]

Along the following Sections, the question of multigap superconductivity in 2H-$NbSe_2$ (from now on we will refer to 2H-$NbSe_2$ simply as $NbSe_2$) will be adressed. First, we will study the experimental results in the literature and show the ones obtained by Roditchev and coworkers of tunneling measurements along different crystal orientations and show how the measurements can be described using the two-band model of McMillan. Then, we explain why the 'large gap' is dominantly observed along the c-axis. We will be able to explain these results using tunneling selectivity arguments and DFT band structure calculations of the material together with the CDW state coexisting at low temperature.

5.2.1 One or two gaps? Survey of available experimental results

5.2.1.1 Gap anisotropy vs two-gap superconductivity

Clear deviations from conventional BCS behavior were observed in the tunneling spectra[167] and in the field dependence of the γ coefficient in the specific heat.[173,175,191,192] The origin of these deviations was addressed by means of many experimental techniques: specific heat,[174,175] heat transport,[173] penetration length[176] and scanning tunneling spectroscopy.[136,171] The results are summarized in Table 5.2. They can be sorted into two groups, either concluding that $NbSe_2$ is a two-gap superconductor,[136,173,174] including a possible gap distribution,[171] or that the gap is anisotropic in k-space.[190] Some works[175,176] suggest that the experimental results could be interpreted in both ways.

It is important to note that, in order to fit the specific heat or penetration depth data,[174–176] it was implicitly assumed that the DOS is a weighted sum of BCS DOS with two different gap values. This assumption is equivalent to the pioneering model of Suhl, Matthias, Walker[135] for a two-gap superconductor, where the two corresponding bands are coupled by an interband

Work	Exp.	Model	Gap value(s) (meV)
Huang *et al.*[174]	SH	Two isotropic gaps (fit)	Δ_S =0.73, Δ_L =1.26 Weights: 20%; 80%
Ying *et al.*[175]	SH	Two isotropic gaps (fit)	Δ_S =0.85, Δ_L =1.5 Weights: 36%; 64%
Ying *et al.*[175]	SH	Anisotropic gap (fit) $\Delta = \Delta_0 [0.4 + 0.6\lvert\cos(3\theta)\rvert]$	Δ_0=1.62
Rodrigo *et al.*[171]	STS	Gap distribution (fit) $N(E) = \frac{1}{\alpha_i}\sum \alpha_i N_{BCS}(\Delta_i, E)$	Gap values in the range $[0.4 - 1.4]$
Fletcher *et al.*[176]	PL	Two isotropic gaps (fit)	Δ_S =0.62-0.67, Δ_L =0.98-1.27 Weights: 0.43-0.5%; 0.57-0.57%
Fletcher *et al.*[176]	PL	Six fold gap $\Delta(\phi, T) = \Delta_{min}(T)\frac{[1+\epsilon\cos(6\phi)]}{1-\epsilon}$	Δ_{min} =0.56-0.58 $\frac{1+\epsilon}{1-\epsilon}$=1.74-2.33
Boaknin *et al.*[173]	HC	Two gaps (Deduced from two length scales)	$\frac{\Delta_L}{\Delta_S}$ ~3
Sanchez *et al.*[190]	SH	Anisotropic gap (fit) $\Delta_k(T) = \Delta_0(T)(1 - \epsilon_2 \cos^2\theta)$	$\Delta_0(0)$ =1.55; ϵ_2=0.6

Table 5.2: Survey of the experimental results for $NbSe_2$ addressing the issue of gap anisotropy vs. two-gap superconductivity. SH, PL and HC stand for specific heat, penetration length and heat conductivity, respectively

pair coupling term. While penetration depth and specific heat measurements do not allow to conclude which model describes best the SC properties in $NbSe_2$, we show in section 5.2.2 that a different mechanism for the band coupling has to be considered to precisely reproduce the shape of the tunneling spectra. The model developed in this work should also describe properly specific heat and penetration depth measurements.

5.2.1.2 Photoemission results

ARPES results measured for $NbSe_2$ are often contradictory.[172,193–197] The resolution of the photoemission, at best of the order of twice the superconducting gap, and the low critical temperature of this material makes the data difficult to analyze. Moreover, the transition to the CDW state, whose origin and consequences on the spectral weight and superconducting state are still debated, complicates the determination of the spectral modification at the Fermi energy E_F near the SC critical temperature. Yet, some general features emerge from the analysis of the more recent fine ARPES experiments (see Table 5.3 for a comparison of reported photoemission results): a 'large gap' is shown to open in the Nb cylinders around K while a smaller gap is found associated with the Nb Γ-cylinders. There is no indication of the existence of a gap in the small Se pocket around Γ. However, these results should be taken with care since the ARPES data for the Se p_z pocket are affected by the very strong k_z dispersion (see the band diagram calculations in section 5.2.3.1) and possibly also by surface defects. The selenium p_z states appear strongly blurred in photoemission images and a quantitative analysis of this band is questionable. Indeed, the finding of non-gapped states at the Fermi energy in the Se pocket contradicts the existence of a superconducting state and is most probably due to a lack of sufficient energy resolution. In contrast, STS experiments, as well as specific heat measurements, clearly imply a fully gapped DOS at E_F.

Work	Gap (meV)		
	Se pocket	Nb (Γ)	Nb (*K*)
Kiss *et al.*[193]	-	0.65±0.05	-
Yokoya *et al.*[172]	0	1 ± 0.1	0.9 ±0.1
Kiss *et al.*[195]	0	0.9-1.1	0.3-1.1
Borisenko *et al.*[196]	-	0-0.5	0.8
Rahn *et al.*[197]	0 ±0.2	0.1 ±0.3	2.3-2.6 ±0.2

Table 5.3: Comparison of gap values (in meV) deduced from photoemission experiments for $NbSe_2$ in the Se pocket around Γ as well as in the Nb cylinders around Γ and K.

5.2.2 Experimental results: Scanning tunneling spectroscopy experiment

5.2.2.1 Tunneling along the *c*-axis

Fig. 5.12 shows a typical tunneling conductance spectrum measured at low temperature with a PtIr tip. As reported previously by Hess *et al.*[167] and Rodrigo *et al.*,[171] a well-pronounced gap is observed. However, as shown in the following, this does not mean that only a single gap parameter is present. In this case the tunneling conductance shape deviates from a conventional single-gap BCS superconductor.

As shown in a previous report by Noat and coworkers,[136] the tunneling conductance can be fitted by the McMillan equations[139] (Eq. 5.1), in agreement with this two band scenario.[198,199]

To describe the scanning tunneling experiment, we take into account an additional tunneling selectivity. Depending on the configuration in k-space and symmetries of the bands relevant to the surface plane probed by STS, one particular band or the other can be probed. This effect was clearly demonstrated in magnesium diboride. Indeed, it has been shown that for c-axis oriented samples of MgB_2, only the small gap is observed in the tunneling density of states,[200,201] while two gaps are clearly seen for an a/b-axis oriented sample in grains with arbitrary orientations.[202] As we saw in Section 5.1, this is due to the particular symmetries of the bands in MgB_2: the 'large gap' develops in the σ band, with high electron phonon coupling and having a rather 2D nature, while a small gap is induced in the π band having 3D character.[203,204] This explains why the small gap is preferentially observed in a nominal c-axis oriented sample by scanning tunneling spectroscopy.

Recalling the formulas from the McMillan model of Section 5.1.1 we get from the fits (see Fig. 5.12a): $\Delta_L^0 = 1.4 \pm 0.1$ meV and $\Delta_S^0 = 0.00 \pm 0.1$ meV. In order to confirm the fine structure of the gap, additional measurements were also done at $T = 300$ mK. The tunneling conductance and the corresponding fit with the two-gap model is plotted in Fig. 5.13a.[2] In Fig. 5.13b we show the partial DOS of $NbSe_2$ deduced from these fits. Each curve is clearly different from the usual BCS DOS. In particular, a distinctive kink is noticeable at the 'small gap' energy (see arrows in Fig. 5.13b) in the partial DOS corresponding to the 'large gap' band.

With this analysis one finds that superconductivity preferentially develops in one band while Cooper pairs arise in the other band by the proximity effect, since $\Delta_S^0 = 0$. This is analogous to the case of MgB_2 where superconductivity develops in the σ band and is induced in the π band.[203] The values found in $NbSe_2$ for the interband coupling parameters are: $\Gamma_{SL} = 3 \pm 0.3$ and $\frac{\Gamma_{LS}}{\Gamma_{SL}} = 1/3 \pm 0.03$. Let us recall that, since the ratio of the partial DOS at the Fermi energy is related to the coupling parameters (see Eq. (5.4)), the first could help us identify in which

[2]The parameters used for the fit are in good agreement but are slightly different from those deduced at $T = 2K$. This might come from different surface conditions. One also notes that the fit deviates from the data inside the gap for bias voltages close to the excitation gap. This could further be explained in terms of a three band model, which would take into account the effect of the Se pocket, as explained in section 5.2.5.2.

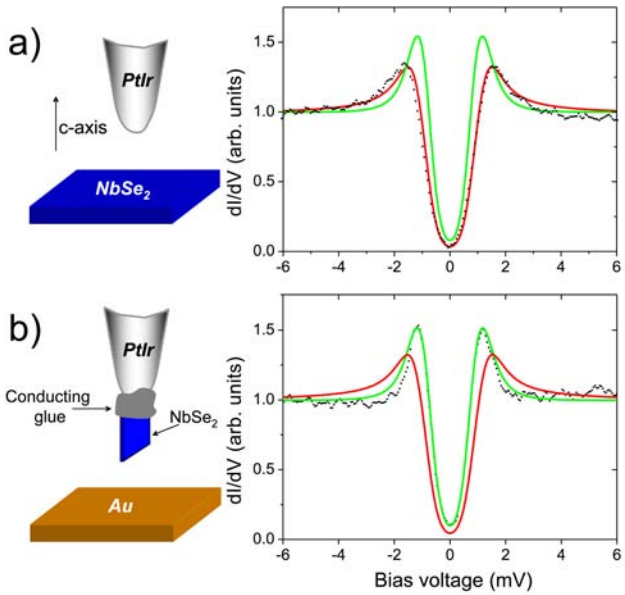

Figure 5.12: a) Tunneling conductance obtained by Roditchev *et al.* with a metallic (platinum-iridium) tip in a *c*-axis oriented $NbSe_2$ sample. The data (black dots) are fitted by a two gap model (McMillan equations) assuming a full tunneling selectivity towards the 'large gap' band ($T_L = 1$, in red). It is compared to the situation where the tunneling arises towards the band with a small gap ($T_S = 1$, in green). b) Tunneling conductance obtained with a $NbSe_2$ tip oriented along the a/b axis. The tip is obtained by gluing a $NbSe_2$ sample on the side to a platinum-iridium tip. The data are fitted by a two gap model (McMillan equations) assuming a tunneling selectivity towards the small gap band ($T_S = 1$, in green). It is compared (red curve) to the situation where the tunneling arises towards the band with a large gap ($T_L = 1$). The parameters used for the fit in both cases are the following: $T_{fit} = 2.2$K; $\Delta_L^0 = 1.4$ meV; $\Delta_S^0 = 0$ meV; $\Gamma_{SL} = 3$ meV; $\frac{\Gamma_{LS}}{\Gamma_{SL}} = 1/3$.

band superconductivity develops preferentially (i. e. the band with a large SC gap).

The relative weights in the DOS found for the 'small' and 'large gap' bands are in qualitative agreement with the values deduced from the temperature and magnetic field dependence of the specific heat measurements.[174] Indeed, fitting these data with a simple two-band model (i.e. the model of Suhl *et al.*[135]), Huang *et al.*[174] found a ratio close to 1/4 with gap values $\Delta_S = 0.73$ meV and $\Delta_L = 1.26$ meV while Ying *et al.*[175] found a ratio 0.56 with gap values $\Delta_S = 0.85$ meV and $\Delta_L = 1.5$meV.

The tunneling selectivity that appears in the STS experiment on $NbSe_2$ is very sensitive to the cleavage conditions. When the cleavage was done under UHV conditions, the 'large gap' DOS dominates in the tunneling current, i.e. $T_L \approx 1$. On the other hand, when the sample is cleaved in air, the tunneling selectivity varies and a combination of the small and 'large gap' DOS is necessary to fit the data properly ($0 \leq T_S \leq 0.5$). We propose that this effect is related to some modifications in the Se pocket arising with surface contamination when the sample is cleaved in air.

5.2.2.2 Tunneling along the a/b axis

In a second step, Roditchev *et al.* measured the tunneling conductance for a $NbSe_2$ sample with a different orientation (see schematics in Fig. 5.12b). A typical conductance spectrum is shown in Fig. 5.12b, with a fit using the two-gap proximity effect model as described previously, with the tunneling selectivity fully towards the 'small gap' band (green) and, for comparison, towards the 'large gap' band (red). The other parameters are unchanged in the fits within the uncertainty mentioned above. For this orientation, it is clear from the fit that the 'small gap' is

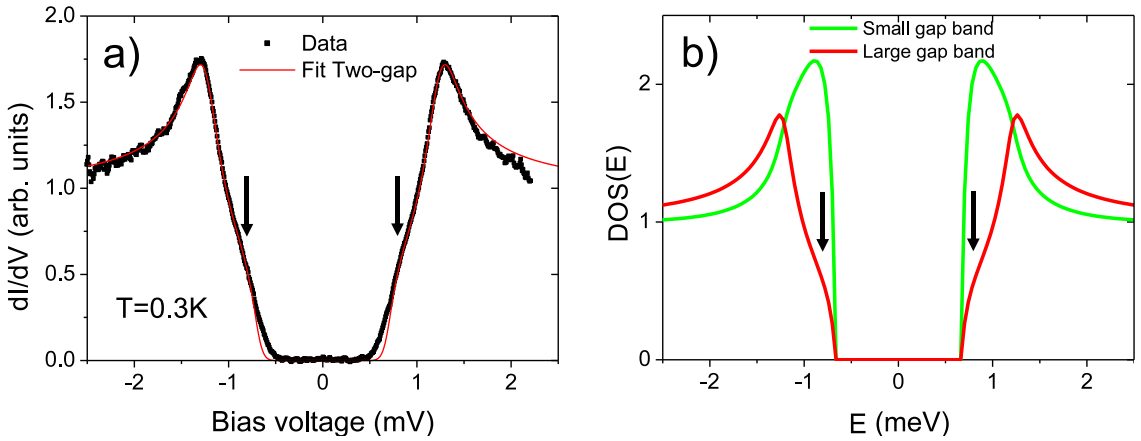

Figure 5.13: (a) Tunneling conductance obtained by Roditchev *et al.* at 2.3 K with a metallic (platinum-iridium) tip in a *c*-axis oriented $NbSe_2$ sample at T=300 mK. The data are fitted by a two-gap model (McMillan equations) assuming a full tunneling selectivity towards the 'large gap' ($T_L = 1$, in red). The parameters used for the fit are the following: $T_{fit} = 0.4$K; $\Delta_L^0 = 1.32$ meV; $\Delta_S^0 = 0$ meV; $\Gamma_{SL} = 2.5$ meV; $\frac{\Gamma_{LS}}{\Gamma_{SL}} = 1/4$. (b) Partial DOS for the small (in green) and 'large gap' (in red) obtained with the parameters deduced from the fits (shown in Fig. 5.12). $\Delta_L^0 = 1.3$ meV; $\Delta_S^0 = 0$ meV; $\Gamma_{SL} = 2.5$ meV; $\frac{\Gamma_{LS}}{\Gamma_{SL}} = 1/4$.

dominantly probed, as opposed to the nominal *c*-axis experiment. This demonstrates that the tunneling selectivity clearly depends upon the sample orientation as in the case of MgB_2.

This important point is further checked by using a SIS junction with a $NbSe_2$ tip and a *c*-axis oriented sample. For a SIS junction, the tunneling current is given by

$$I(V,z) = I_0 e^{-2\,\alpha_k\, z} \int_E N_{tip}(E) N_{sample}(E+eV)\,[f(E) - f(E+eV)]\,dE, \tag{5.8}$$

where $f(E)$ is the Fermi-Dirac function, $N_{tip}(E)$ and $N_{Sample}(E)$ are, respectively, the DOS of the tip and the sample. As shown in Fig. 5.14, the SIS tunneling conductance is well fitted assuming that a full tunneling selectivity towards the 'small gap' band for the tip (i.e. T_S =1 and T_L =0) and towards the 'large gap' band for the sample (i.e. T_S =0 and T_L =1), therefore confirming the previous results.

We should note that there are some small deviations of the fit from the experimental curve inside the gap, which could result from a small contribution of a third band (see section 5.2.5.2). In some of the SIS spectra, small dips are also visible outside the gap and could be related to particular surface conditions.[3]

5.2.2.3 Temperature dependence of the tunneling conductance

The tunneling spectra for a SIS junction (see Fig. 5.15b, $NbSe_2$ tip-$NbSe_2$ sample) as well as for SIN (superconductor-vacuum-normal) junction (see Fig. 5.15a, $NbSe_2$ tip-gold sample) were measured by Roditchev *et al.* as a function of temperature. The conductance curves were fitted at each temperature with the McMillan model for a two-gap superconductor as described in section 5.2.2.1. The same parameters were used for both SIS and SIN junctions.

[3] A small dip outside the gap is also present in some of the SIS spectra. This feature could be attributed to a small contribution of the 'small gap' band due to some surface conditions. As a matter of fact, it has been shown by Noat *et al.*[136] that such dips can arise in the SIS spectra of a two-band superconductor when tunneling takes place toward the 'small gap' band. One needs that one of the two electrode is either a conventional superconductor or the same two-gap superconductor with a tunneling towards the 'small gap' band.

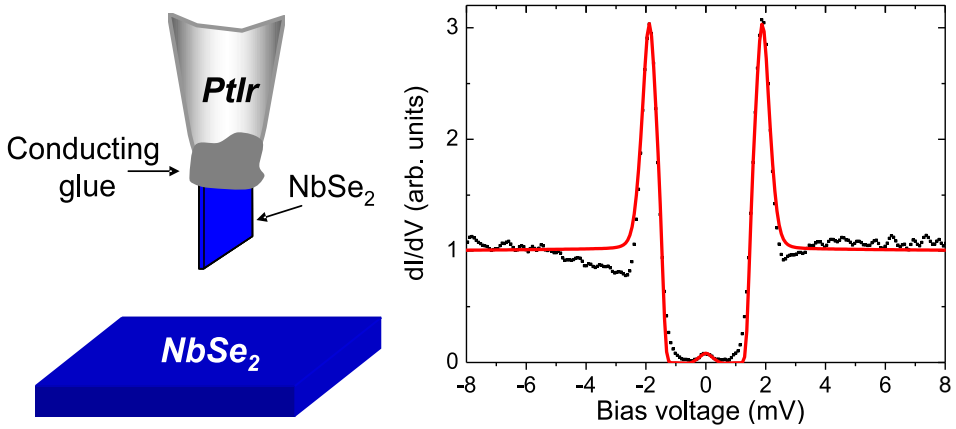

Figure 5.14: Left: Scheme of the tunneling junction used by Roditchev *et al.* The tip is oriented in the a/b axis while the sample is c-axis oriented. Right: Tunneling conductance of the SIS junction at $T = 2.3$ K. The spectrum is fitted with the McMillan model, assuming a tunneling selectivity towards the 'small gap' band for the tip ($T_S = 1$; $T_L = 0$) and the 'large gap' band for the sample ($T_S = 0$; $T_L = 1$). The tip and sample are described by the same other parameters as before.

From the fits we can deduce the temperature dependence of the intrinsic gaps $\Delta_L^0(T)$ and $\Delta_S^0(T)$. Note that $\Delta_S^0(T)$ is close to zero for all temperatures. In addition, the theoretical dependence of the intrinsic gaps with temperature can be obtained from the self-consistent equations:

$$\begin{aligned}\Delta_i^0 \;=\; & \lambda_{ii}\int_0^{\hbar\omega_i} \mathrm{d}E \tanh\left[\frac{E}{2k_BT}\right] \mathrm{Re}\left[\frac{\Delta_i(E)}{\sqrt{E^2-\Delta_i^2(E)}}\right] + \\ & +\lambda_{ij}\sqrt{\tfrac{N_j}{N_i}}\int_0^{\hbar\omega_{ij}} \mathrm{d}E \tanh\left[\frac{E}{2k_BT}\right] \mathrm{Re}\left[\frac{\Delta_i(E)}{\sqrt{E^2-\Delta_i^2(E)}}\right],\end{aligned} \tag{5.9}$$

where $\lambda_{ii} = V_{ii}N_i$ are the intraband electron-phonon coupling constants of each band, while $\lambda_{ij} = V_{ij}\sqrt{N_iN_j}$ is the interband electron-phonon coupling constant of the Suhl-Matthias-Walker model.[135]

While in the most general case, the intrinsic gaps result from both intraband and interband pair coupling, for $NbSe_2$, interband pair coupling can be neglected, but not interband quasiparticle scattering. Fitting Eq. 5.3 and Eq. 5.9 to the SIN and SIS spectra (Fig. 5.15), we find $\lambda_{12} = 0$ and that only the large intrinsic gap is not zero: $\lambda_{22} \approx 0.5$ and $\lambda_{11} = 0$. The corresponding phonon frequency extracted from the fit is $\hbar\omega_2 \approx 6.55$ meV. This shows unambiguously that the small gap is induced by proximity effects as a result of quasiparticle interband coupling, similarly to the case of MgB_2.[199]

The temperature dependence of the intrinsic 'large gap', $\Delta_L^0(T)$, deduced from the fits of the tunneling spectra at each temperature is shown in Fig. 5.16a (squares). This dependence is compared to the theoretical expectation $\Delta_L^{0,th}(T)$, shown as a continuous curve in Fig. 5.16a, obtained using Eq. (5.9) and the low temperature gap value, together with the critical temperature of $NbSe_2$. A reasonably good agreement is found between the extracted $\Delta_L^0(T)$ and the theoretical dependence $\Delta_L^{0,th}(T)$. From the calculation, we also deduce the theoretical temperature dependence of the peak to peak gap $\Delta_{S,L}^{pp,th}(T)$ in the small/large partial DOS $N_{S,L}(E)$ as well as that of the excitation gap $\Delta^{ex,th}(T)$ (Fig. 5.16b), which can also be compared to the corresponding value deduced from the fit at each temperature. Such plots are often found in the literature of multigap superconductors. Nevertheless, our analysis clearly shows that, despite

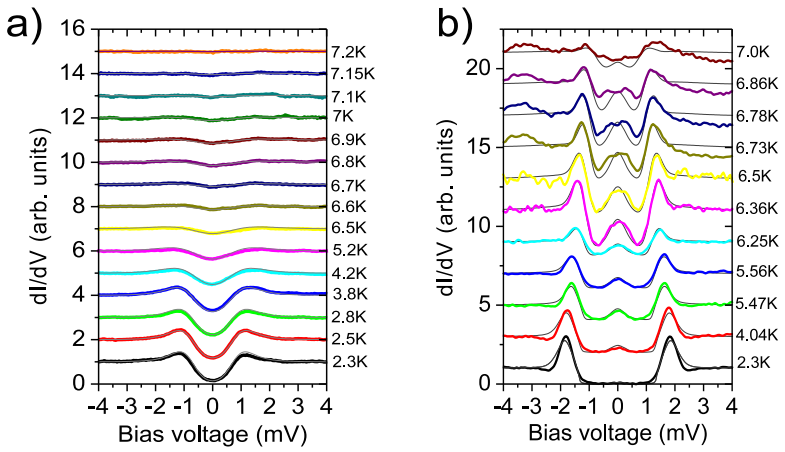

Figure 5.15: (a) Temperature dependence of the tunneling conductance by Roditchev *et al.* obtained for a SIN junction with a $NbSe_2$ tip oriented along the a/b axis and a gold sample and corresponding McMillan fit (thin lines). (b) Temperature dependence of the tunneling conductance obtained for a SIS junction with a $NbSe_2$ tip oriented along the a/b axis and a c-axis oriented sample, and corresponding McMillan fit (thin lines). The data are fitted with the McMillan model for a two gap superconductor with the same parameters for the tip and sample: Δ_S^0 =0 meV; Γ_{SL} =3 meV; $\Gamma_{LS} = \frac{N_S(E_F)}{N_L(E_F)} = \Gamma_{SL}/3$. The intrinsic 'large gap' Δ_L^0 is the adjustable parameter. In the SIS case, the spectra are fitted with the McMillan model, assuming a tunneling selectivity towards the 'small gap' band for the tip ($T_S = 1$; $T_L = 0$) and towards the 'large gap' band for the sample ($T_S = 0$; $T_L = 1$). In the SIN case, we assume a full tunneling towards the 'small gap' band ($T_S = 1$; $T_L = 0$). At each temperature, the fit gives the value of the intrinsic 'large gap' $\Delta_L^0(T)$, with $\Delta_S^0(T)$ =0.

the fact that $NbSe_2$ shows two different SC gaps, only one intrinsic gap is necessary to describe well the tunneling conductance spectra and their evolution as a function of temperature.

5.2.2.4 Two band model vs distribution of gaps

As already mentioned, the tunneling conductance in $NbSe_2$ was interpreted previously in terms of a continuous gap distribution.[171] In this phenomenological model, the tunneling DOS is described by a weighted sum of BCS DOS: $N(E) = \sum_i g(\Delta_i) N_{BCS}(E, \Delta_i)$, where $g(\Delta_i)$ is a distribution function describing the probability of having a gap value Δ_i. Following the model of Rodrigo *et al.*,[171] Roditchev *et al.* determined the two gap distributions $g(\Delta_i)$ needed to reproduce the DOS of the 'large' and 'small gap' bands shown in Figs. 5.16c and 5.16c which were calculated by solving the self-consistent equations in the McMillan model. These distributions are shown in Fig. 5.17.

At low temperature, the distribution function found for the 'large gap' DOS exhibits two well-defined peaks around 0.77 meV and 1.16 meV. One notes that their positions are close to the peak-to-peak "gaps" in the McMillan DOS shown in Fig. 5.16b. The distribution function found for the 'small gap' is strikingly different from that of the 'large gap'. In particular, it exhibits a single peak at 0.76 meV. More importantly, one notices that in some energy ranges, the distribution function has negative values. This demonstrates that it is not possible to properly reproduce the DOS of the 'small gap' band with a gap distribution having only positive weights. This is due to the very peculiar shape of the peaks of the 'small gap' DOS (Fig. 5.16c), whose amplitude decreases more rapidly than $\sim 1/\sqrt{E-\Delta}$ close to the gap edge. The same conclusion would of course have been obtained by directly fitting the conductance curve obtained in the tunneling experiment with the tip oriented in the a/b-axis. Thus, while the DOS of the 'large gap' band can be fitted by a gap distribution, this is not the case for the DOS of the 'small gap' band.

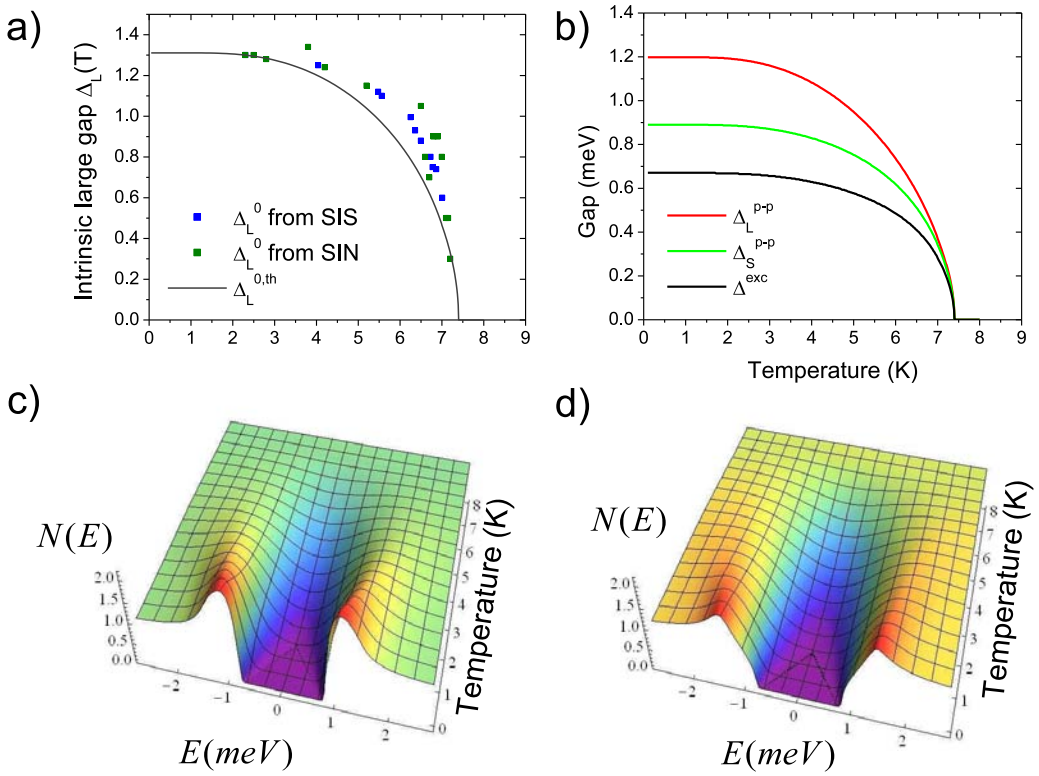

Figure 5.16: (a) Temperature dependence of the intrinsic 'large gap' $\Delta_L^0(T)$ deduced from the fits for the SIN ($NbSe_2$ tip-gold sample) (green squares) and SIS junction ($NbSe_2$ tip-$NbSe_2$ sample) (blue squares) compared to the theoretical value $\Delta_L^{0,th}(T)$ calculated by the resolution of the self-consistent equations (5.9) (black line). (b) Theoretical temperature dependence of the excitation gap $\Delta^{ex,th}$ (in black) and of the peak to peak small and large gaps (in red and green respectively) $\Delta_{S,L}^{pp,th}$ which are defined as the peak to peak value in the calculated partial DOS for the 'small' and 'large gap' $N_S(E)$ and $N_L(E)$. (c) Temperature dependence of the partial DOS for the 'small gap' band $N_S(E)$ calculated by the resolution of the self-consistent equation. (d) Temperature dependence of the partial DOS for the 'large gap' band $N_L(E)$.

At higher temperature, the 'large gap' distribution function evolves towards a distribution with a single peak. In addition, for both the 'small' and 'large gap', the distribution becomes more and more peaked as the temperature increases and gets very close to BCS, with the same gap value for both bands near the critical temperature. This behavior is in fact very different from that expected in the Suhl, Matthias and Walker model, which in the work by Rodrigo and coworkers[171] is believed to explain the temperature evolution of the two gap distributions. Indeed in this model, the ratio between the two gaps should first increase when the temperature increases. This behavior is at variance with what is observed in Fig. 5.17, where the energy of the maxima of both distribution functions decrease continuously with increasing temperature. Moreover, the observation of the collapse of the two gaps towards a single BCS like signature close to T_C (see curves in Fig. 5.17 close to T =7 K) is opposite to the model of Shul *et al.*[135], which predicts two very different gaps very close to T_c. On the other hand, such a behavior is a remarkable feature of the quasiparticle mediated interband coupling (as in Schopohl and Scharnberg's model[137]).

5.2.2.5 General conclusions of the experiment

These series of experiments and analyses that Roditchev *et al.* performed leads us to three major conclusions:

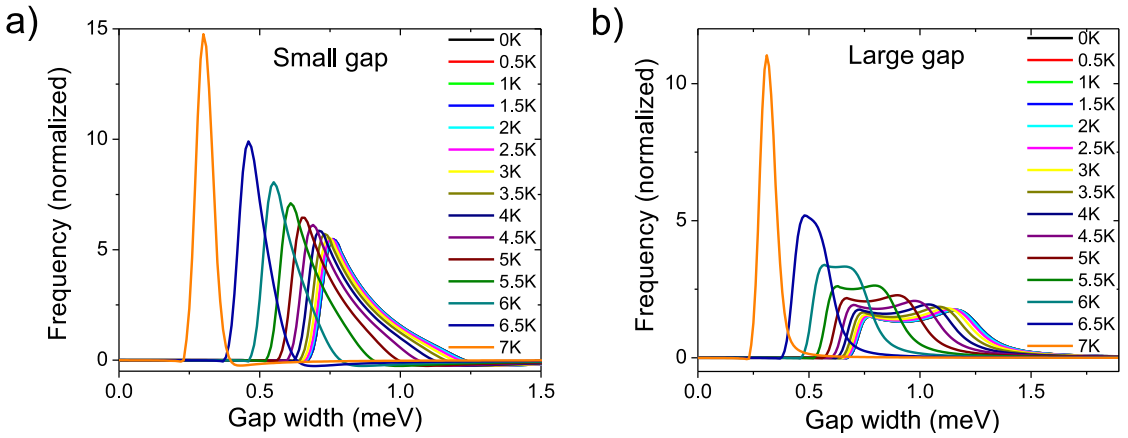

Figure 5.17: Small (a) and large (b) gaps distributions obtained by fitting the DOS shown in Fig. 5.16c and Fig. 5.16d, calculated self-consistently as a function of temperature, with a weighted sum of BCS DOS, following the empirical model of Rodrigo *et al.*[171].

1. Tunneling data of $NbSe_2$ can be explained in terms of a two-band proximity effect within the McMillan model. Superconductivity arises in one band, where the electron-phonon coupling constant is large, and is induced in a second band by quasiparticle interband scattering.

2. The tunneling selectivity has to be taken into account in order to reproduce the different tunneling spectra measured along various crystal orientations.

3. Tunneling towards the c-axis (a/b-axis) leads to the coupling with band of the large (small) gap.

However, two points remain to be elucidated:

1. With respect to the band structure, which band corresponds to which gap?

2. As it is now well established,[177] the Se bands contribute an additional branch to the Fermi surface (i.e. the Se based pancake), so its role must be elucidated with respect to the SC properties.

To clarify these aspects, in the following we first discuss the electronic structure of $NbSe_2$ and its implication for the tunneling results on the basis of first-principles DFT calculations. We then consider the possible role of the low temperature CDW transition occurring in this material below 33 K on the superconductivity.

5.2.3 DFT calculations

5.2.3.1 Electronic structure of $NbSe_2$

The electronic structure of $NbSe_2$ has been calculated a number of times in the literature;[182,183,177,178,185,205,206] here we just highlight some aspects which are relevant in order to understand the signatures of multigap superconductivity in the tunneling spectroscopy of $NbSe_2$. The calculated band structure is shown in Fig. 5.18. There are three partially filled bands, the two upper ones having niobium $4d$ as the dominant character (except around Γ), whereas the lower is mostly based on selenium orbitals. From now on these bands will be referred to as band 3, 2, and 1, respectively. This is in contrast with the situation for a single $NbSe_2$ layer where only the two niobium $4d$ based bands are partially filled.

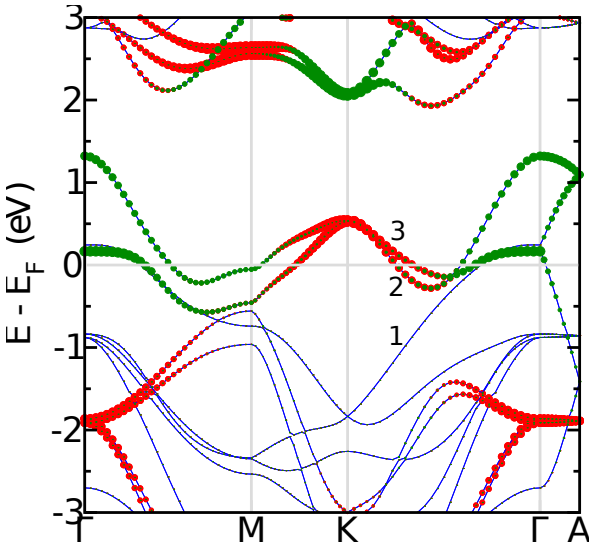

Figure 5.18: Calculated band structure for $NbSe_2$ where the size of the green and the red circles is proportional to the niobium d_{z^2} and $d_{xy}/d_{x^2-y^2}$ character, respectively. $\Gamma = (0, 0, 0)$, $M = (1/2, 0, 0)$, $K = (1/3, 1/3, 0)$, $A = (0, 0, 1/2)$ in units of the reciprocal hexagonal lattice vectors.

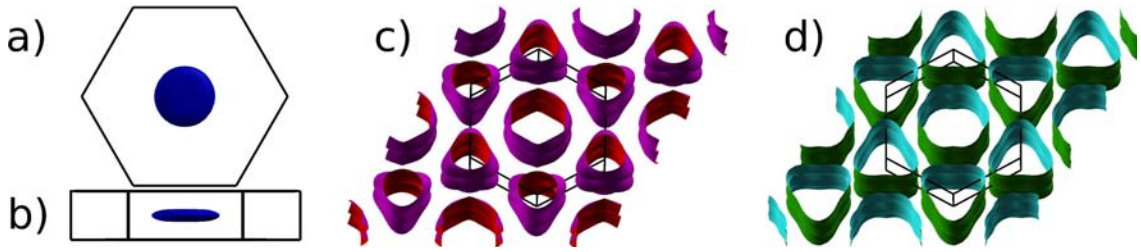

Figure 5.19: Contribution of band 1 (a and b), band 2 (c) and band 3 (d) to the Fermi surface for $NbSe_2$.

The calculated Fermi surface (see Fig. 5.19) contains three different contributions. First, a pancake-like contribution centered at the Γ point arising from the selenium based bands. Second, a pair of warped cylinders centered at Γ arising from the two partially filled niobium $4d$ bands. Third, a pair of warped cylinders centered at K arising also from the two partially filled niobium $4d$ bands. The cylinders occur in pairs because there are two layers per repeat unit and thus there are in-phase and out-of-phase combinations of the single-plane niobium bands. The two cylinders around Γ, as well as those around K, merge at the border of the Brillouin zone because there the phase factors are such that the interlayer interactions vanish. Although both pairs of cylinders around Γ and K originate from the same bands, their character strongly changes from one region to the other : whereas the niobium character is mostly d_{z^2} around Γ it is $d_{xy}/d_{x^2-y^2}$ around K (see Fig. 5.18).

For simplicity, from now on we will refer to the cylinders centered at the Γ point (K point) of the Brillouin zone as the 'Nb Γ-cylinders' ('Nb K-cylinders') since they mostly arise from the Nb bands.

5.2.3.2 Contribution of the different orbitals to the partially filled bands

In order to correlate the partially filled bands states to the STM images it is essential to have a clear idea of what is the relative weight of the different orbital contributions, i.e. niobium d_{z^2}, niobium $d_{xy}/d_{x^2-y^2}$ and selenium, for the different parts of the Fermi surface (i.e. in

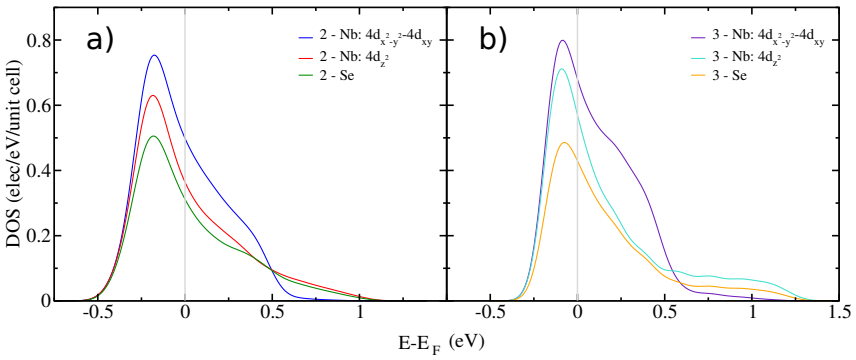

Figure 5.20: Contributions of the selenium, niobium d_{z^2} and niobium $d_{xy}/d_{x^2-y^2}$ orbitals to the density of states associated with the (a) middle -2- and (b) upper -3- partially filled bands.

the two different pairs of cylinders and in the pancake around Γ). The pancake is strongly based on the selenium orbitals. Of particular interest are the middle and upper partially filled bands. Their orbital contributions are shown in Fig. 5.20. An important observation is that the selenium contribution to these formally niobium bands is comparable to the individual niobium contributions. As shown in Fig. 5.21, almost half of this selenium contribution is p_z, i.e., the selenium orbitals perpendicular to the layers. This means that, although globally the metal character prevails in these two bands, there is a very important hybridization with the selenium orbitals, and particularly with the selenium p_z orbitals. Consequently, these p_z states are expected to dominate the tunneling along the c-axis (see the calculation of the tunneling current in section 5.2.3.6), and the Se atoms will be seen in the tunneling images, at least at large distances from the surface.

5.2.3.3 Partial DOS associated with the different portions of the Fermi surface

We report in Table 5.4 the partitioning of the bulk total density of states at the Fermi level into niobium and selenium contributions for each of the three partially filled bands. In addition, for the two niobium based bands (i.e., bands 2 and 3) we also separate the contributions into those associated with the cylinders around Γ and the cylinders around K. Since both bands contribute to the two types of cylinders, we define the contribution to the 'Nb Γ/K-cylinders' as the sum of the contributions of bands 2 and 3 around Γ/K. The most salient features of the second and third columns of this table are:

i) The total contributions to the DOS at the Fermi level of the upper niobium-based band (i.e., band 3) are considerably larger than those of the lower niobium-based band (i.e., band 2).

ii) For both niobium-based bands the contribution of the 'Nb K-cylinders' is always larger than that of the 'Nb Γ-cylinders'.

iii) The contribution of the lower selenium band (i.e., band 1) is small.

iv) The ratio between the contribution of the 'Nb K-cylinders' vs. 'Nb Γ-cylinders' to the total DOS at the Fermi level is 2.7.

The origin of these values is developed in detail in Section 5.2.3.4. From the inspection of the values of the second and third columns of this table (Nb and Se contributions), one could naively expect that the local DOS probed by STS spectroscopy will be dominated by a large contribution from the 'Nb K-cylinders', a lesser contribution from the 'Nb Γ-cylinders', and finally an even smaller contribution from the selenium based pancake. Surprisingly, this is not what is found in the calculation, as shown in the following.

	DOS (Total)	DOS (Nb contribution)	DOS (Se contribution)	DOS (Se_{p_z} contribution)
Band 1 Γ	0.117	0.035	0.080	0.062
Band 2 Γ	0.359	0.239	0.121	0.066
Band 2 K	0.731	0.528	0.203	0.052
Band 3 Γ	0.337	0.260	0.080	0.032
Band 3 K	1.175	0.848	0.331	0.117

Table 5.4: Bulk total and partial DOS for the different bands at the Fermi level around Γ and K (in electrons/eV/unit cell).

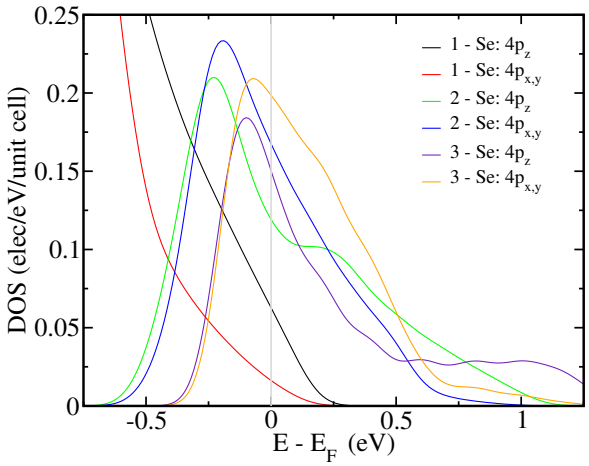

Figure 5.21: Contributions of the selenium p_z and selenium $p_{x,y}$ orbitals to the density of states associated with the lower (1), middle (2) and upper (3) partially filled bands.

5.2.3.4 Qualitative understanding of the density of states

The features of the density of states at the Fermi level can be understood on the basis of the analysis of the wave functions. The two partially filled niobium-based bands, though more heavily based on the metal atoms, contain substantial niobium-selenium antibonding character. The dispersion of these bands results from a subtle equilibrium between direct in plane niobium-niobium interactions (ultimately responsible for the 30 K structural distortion)[182] and niobium-selenium antibonding interactions.

Increasing the niobium d_{z^2} participation in the wave function is accompanied by an increase of the participation of the selenium p_z orbitals. Roughly speaking, increasing the weight of d_{z^2} in the wave function makes the Fermi surface more isotropic within the layer plane and shifts the electron density from antibonding levels to the interlayer direction so that the mixing of niobium d_{z^2} orbitals will be less favorable for the subband associated with the interlayer antibonding interactions. Increasing the niobium d_{z^2} participation (and thus the selenium p_z orbitals) increases the interlayer dispersion and reduces the density of states. Thus, keeping in mind the results of Fig. 5.18, it is easy to understand that the density of states at the Fermi level for both bands is larger for the cylinder around K and that the effect is larger for the upper, interlayer antibonding band.

5.2.3.5 Effect of the CDW on the band structure

Since our analysis is based on the room temperature crystal structure whereas the tunneling images are obtained at temperatures below the 30 K transition we must consider if the structural

Atom	Position		Experimental LC		Optimised LC	
			Model 1	Model 2	Model 1	Model 2
Nb	12j	x	0.334075	0.331592	0.335403	0.330972
		y	0.337869	0.329487	0.339518	0.327408
Se_1	12k	x_1	0.111108	0.111019	0.111198	0.111025
		z_1	0.113204	0.112344	0.116252	0.114852
Se_2	12k	x_2	0.443859	0.444995	0.443619	0.445294
		z_2	0.111032	0.114528	0.112950	0.117735
Se_3	12k	x_3	0.778434	0.777340	0.778591	0.777009
		z_3	0.114712	0.111915	0.117377	0.113985

Table 5.5: Results for the $P6_3/mmc$ model relaxation for $NbSe_2$. Six additional Nb atoms occupy positions 2b, 2c and 2d. LC stands for lattice constant.

distortion may noticeably affect the results. Therefore, though it is a bit off-topic, it is interesting to study the structure after this transition. To those not interested in the structural relaxation we can say in advance that this transition does not affect to the images and general conclusions of the work so you can happily skip this Section.

The experimental structure of the low temperature phase was not experimentally known until recently, when Malliakas and coworkers[189] did an study of such structure, so we carried out a structural optimization using a ($3a \times 3a \times c$) supercell with fixed cell parameters for the experimental and optimised lattice cell constants (because of the well known problem of DFT with van der Waals interaction, we have carried out all the optimizations keeping the experimental value for the interlayer cell constant, c). We studied two different structures exhibiting a niobium clustering pattern closely related to those proposed by Moncton, Axe and DiSalvo[187] (see Fig. 5.22a) and Brouwer and Jellinek[188] (see Fig. 5.22b) (from now on we will refer ot it as 'model 1' and 'model 2', respectively). For this, we made a modification of the relaxation SIESTA subroutine in order to take into account the symmetries of the system in its final structure using generalized coordinates. The calculated room temperature non-modulated structures ($P6_3/mmc$) using the experimental lattice constants ($a = b = 3.4425$ Å and $c = 12.547$ Å) or the optimised lattice constants ($a = b = 3.5425$ Å and $c = 12.547$ Å) are in position 4f with $z_{Se} = 0.11661$ and 0.115431, respectively with the Nb in position 2b (see Appendix E).

Since the experimental structure was not known at the beginning of the study, we first used a $P6_3/mmc$ symmetry to describe the final structure as in the work by Moncton *et al.*[187] and Brouwer *et al.*[188] On the other hand, from the work by Malliakas, it can be extracted that the system has a slight distorsion towards the $P6_3/m$ symmetry, so we also carried out the optimization of the structure for this case. It is worth noting that it is important to not break the symmetry since, due to the small energy differences between the structures at T>30 K and T<30 K, it could hide the effect of the transition. We started our calculations from different initial structures, but on Table 5.5 and 5.6 we show only the two final structures for the $P6_3/mmc$ and $P6_3/m$, respectively. This is because all the starting points took us to one model or the other. We can transform the generalized coordinates to cartesian coordinates using the crystallographic data tables (see Appendix E). Since the atoms' displacement is very small and, in order to see which structure corresponds to which model, we show in Fig. 5.22 an schematic drawing of the movement of the Nb atoms. The movement of the Se atoms is much smaller.

As it can be seen from Table 5.7, when the experimental lattice constant is kept fixed, model 1 is found to be slightly more stable. Whereas the opposite result is found when the optimised lattice constant is used. The same result is obtained when the relaxation is carried out within

Atom	Position		Experimental LC		Optimised LC	
			Model 1	Model 2	Model 1	Model 2
Nb_1	6h	x_a	0.333934	0.331651	0.336012	0.330845
		y_a	0.337690	0.329573	0.333958	0.327187
Nb_2	6h	x_b	0.662308	0.670433	0.666065	0.672851
		y_b	0.666078	0.668364	0.664004	0.669205
Se_1	12i	x_1	0.111073	0.111037	0.111463	0.111029
		y_1	0.222161	0.222098	0.222911	0.222004
		z_1	0.113111	0.112373	0.116482	0.114799
Se_2	12i	x_2	0.443883	0.445021	0.444248	0.445313
		y_2	0.887789	0.889986	0.888511	0.890667
		z_2	0.111066	0.114485	0.115257	0.117800
Se_3	12i	x_3	0.778414	0.777339	0.777625	0.776975
		y_3	0.556858	0.554695	0.555249	0.553975
		z_3	0.114624	0.111910	0.114757	0.113945

Table 5.6: Results for the $P6_3/m$ model relaxation for $NbSe_2$. Six additional Nb atoms occupy positions 2a, 2c and 2d. LC stands for lattice constant.

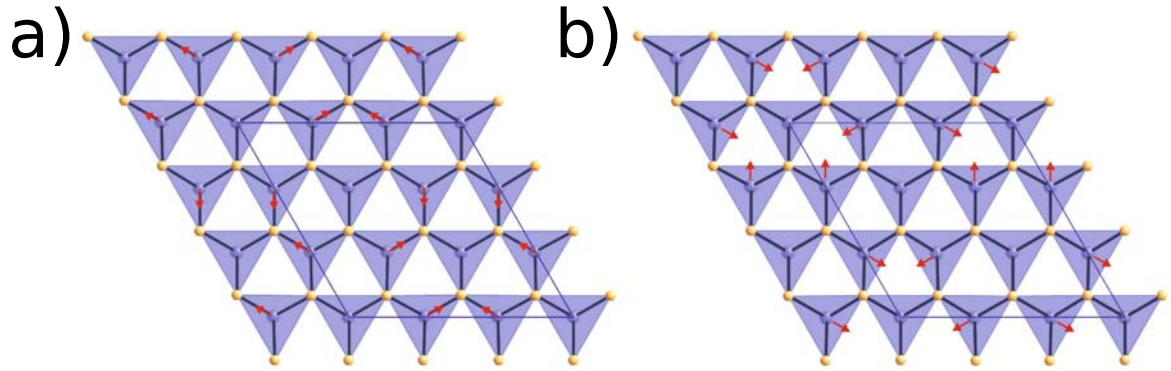

Figure 5.22: (a) and (b) Schematic view of the two possible modulations (model one and two, respectively) discussed in the text. Arrows indicate the direction of the movement of the atoms.

the $P6_3/m$ group (see Table 5.8). However, the energy difference is so small that the different 'preference' cannot be taken as indicative. Since the largest change is due to the Nb atoms, we studied the change in the total Nb-Nb overlap populations for the two structures and we found no difference. Moreover, as we will show later, from the electronic view point, both are practically equivalent. Because of the tiny difference in energy, the final adoption of one or another modulation most certainly depends of possible impurities, defects, etc. Let us note that the passage from the high temperature to the low temperature structure is not an abrupt process but a series of successive incommensurate modulations[181] most likely because of the local appearance of these two modulations.

In order to be confident with our results, it is also interesting to study the case of NbS_2 that has the same structure of $NbSe_2$ and it is also a superconductor, but it does not suffer the structural transition at 30 K. Therefore, we did an analogous study of the structure relaxation for this material. In Table 5.9, we show the generalized coordinates that resulted from the relaxation. As in the case of $NbSe_2$, the structures are relaxed but, in contrast, the difference of energy between the modulated and non-modulated structure is even smaller than before. Therefore, we can conclude that, although in nature we will not see the modulation, there is

	Experimental LC		Optimised LC	
	Model 1	**Model 2**	**Model 1**	**Model 2**
(E_{Mod}-E_{noMod}) (meV)	-11.55	-9.43	-38.66	-39.2
(E_{Mod}-E_{noMod}) (K)	-134.17	-109.54	-448.49	-456.17
(E_{Mod}-E_{noMod}) per Nb (meV)	-0.64	-0.52	-2.15	-2.18
(E_{Mod}-E_{noMod}) per Nb (K)	-7.45	-6.08	-24.92	-25.34

Table 5.7: Energy and temperature differences for the $P6_3/mmc$ modulated structures for $NbSe2_2$.

	Experimental LC		Optimised LC	
	Model 1	**Model 2**	**Model 1**	**Model 2**
(E_{Mod}-E_{noMod}) (meV)	-11.488	-9.21	-2.39	-40.16
(E_{Mod}-E_{noMod}) (K)	-133.24	-106.77	-27.79	-465.79
(E_{Mod}-E_{noMod}) per Nb (meV)	-0.64	-0.51	-0.13	-2.23
(E_{Mod}-E_{noMod}) per Nb (K)	-7.40	-5.93	-1.54	-25.88

Table 5.8: Energy and temperature differences for the $P6_3/m$ modulated structures for $NbSe_2$.

always a tendency towards it.

Finally, a good and simple way to analyze if something changes in the electronic properties after the structural transition is to study the projected densities of states. We are interested in the niobium d_{z^2}, niobium $d_{xy}/d_{x^2-y^2}$ and selenium orbitals, which are compared in Figure 5.23 for the the distorted (noted 3×3) and undistorted (noted 1×1) structures. There is a very small decrease of the DOS at the Fermi level but definitely there is no gap opening. In what concerns to the Se contribution, the difference is again very small so that the modulation should only weakly affect the tunneling. The relative weight of the Nb d contributions exhibits only small changes, therefore, the main conclusions of the previous analysis should still hold after the 30 K transition. This is in keeping with early resistivity and heat-capacity measurements[207,208] suggesting that the decrease in the density of states at the Fermi level should be of the order of only 1%. It is also in agreement with an independent theoretical study by Calandra *et al.*[185] The lack of a gap opening at the Fermi level is in agreement with a very recent atomic-scale scanning tunneling microscopy study[209] which, together with another recent work on the temperature dependence of phonon dispersion,[186] provide clear experimental evidence to exclude a Fermi surface nesting mechanism for the 30 K transition.

The main effect of the CDW is a slight rehybridization of the niobium d orbitals. As shown

Atom	**Position**		**Model 1**	**Model 2**
Nb	12j	x	0.334963	0.331697
		y	0.337549	0.329260
S_1	12k	x_1	0.111032	0.111187
		z_1	0.116565	0.115521
S_2	12k	x_2	0.443864	0.444985
		z_2	0.114283	0.117537
S_3	12k	x_3	0.778450	0.777108
		z_3	0.117230	0.114942

Table 5.9: Results for the $P6_3/mmc$ model relaxation for NbS_2. Six additional Nb atoms occupy positions 2b, 2c and 2d.

	Model 1	Model 2
(E_{Mod}-E_{noMod}) (meV)	-17.379	-16.117
(E_{Mod}-E_{noMod}) (K)	-201.612	-186.972
(E_{Mod}-E_{noMod}) per Nb (meV)	-0.9655	-0.895
(E_{Mod}-E_{noMod}) per Nb (K)	-11.2	-10.39

Table 5.10: Energy and temperature differences for the relaxed structures for NbS_2.

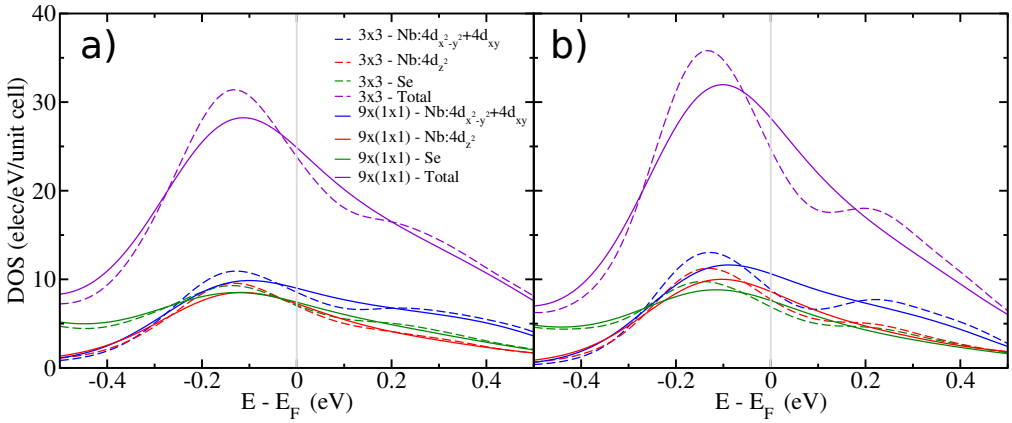

Figure 5.23: Comparison of the niobium d_{z^2}, niobium $d_{xy}/d_{x^2-y^2}$ and selenium contributions for the normal (noted as $9\times(1\times1)$) and CDW (noted (3×3)) states for $NbSe_2$ for model 1 (a) and model 2 (b).

in Fig. 5.23a for model 1, there is a small but definite decrease of both the niobium d_{z^2} and niobium $d_{xy}/d_{x^2-y^2}$ orbital contributions when the CDW occurs. Since the total DOS and the selenium contributions hardly change, the difference is due to a small additional participation of the other niobium orbitals needed to describe the small rehybridization brought about by the CDW. The same conclusion is reached when model 2 is analysed (see Fig. 5.23b).

As before, it is also interesting to analyse what happens to the PDOS of NbS_2 after the transition to the modulated structure. Therefore, we do an analog study of this quantity, which is shown in Fig. 5.24. As we can see, in contrast to $NbSe_2$, there is no such rehybridation of the Nb d orbitals.

5.2.3.6 Calculated tunneling STM images

Similarly as in the case of MgB_2 (see Section 5.1.3), we now consider STM imaging within the Tersoff-Hamman approximation,[162] where the current at a given tip position is proportional to the LDOS at that point, integrated over the standard energy window given by the tip-surface potential difference $(E_F, E_F + eV)$. Our images correspond to constant current images, showing the maps of heights that produce a constant tip-surface current. Instead of specifying the value of the current (which is the situation encountered in an experiment), we choose a particular value of the density of states and plot the corresponding constant DOS surface.

In Fig. 5.25 we show the calculated STM image for a specific DOS isovalue ($5{\cdot}10^{-5}$ elect$\cdot$ $\cdot$eV$^{-1}\cdot$ unit cell^{-1}). The image presents bright spots centered at the selenium atom positions. When the different contributions of the pancake, the 'Nb Γ-cylinders' and 'Nb K-cylinders' to this image are separated, the three calculated images have practically the same shape, although with different DOS contribution. Thus, tunneling in the three portions of the Fermi surface is dominated by the electronic states originated from the selenium atoms, whereas the niobium atoms are not visible in standard tunneling conditions.

As shown in Fig. 5.25, these calculations are in agreement with experimental results showing

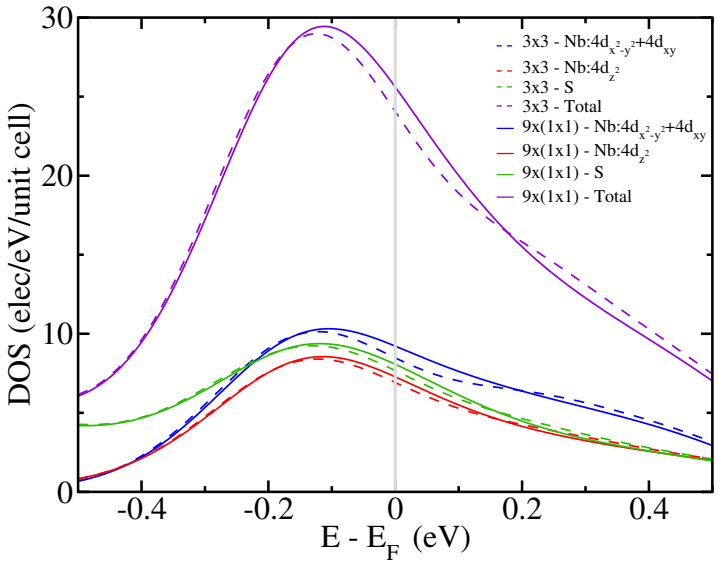

Figure 5.24: Comparison of the niobium d_{z^2}, niobium $d_{xy}/d_{x^2-y^2}$ and selenium contributions for the normal (noted as $9\times(1\times 1)$) and CDW (noted (3×3)) states for NbS_2.

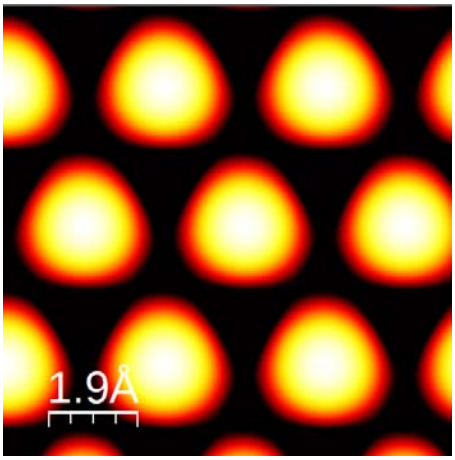

Figure 5.25: Calculated STM image for $NbSe_2$ (obtained for an iso-DOS value of $5{\cdot}10^{-5}$ elect·$\cdot eV^{-1}\cdot$ unit $cell^{-1}$).

the hexagonal atomic selenium lattice (note that for small tip-surface distances, the underlying Nb atoms have been also experimentally seen in the tunneling images[210]). We thus conclude that the Se contribution for each of the three different Fermi surface portions plays a crucial role in the tunneling process.

At this point it is important to note that actual calculations for the $(3a\times3a\times c)$ CDW modulated structure below 30 K (see the discussion in Section 5.2.3.5) show that the CDW has only a minor effect on the Se orbitals as well as in the relative weight of the Nb orbitals in the Fermi level region so that the main conclusions of our analysis should still hold after the CDW transition.

5.2.3.7 Tunneling selectivity

The key aspect when trying to use the calculated images in understanding the origin of the proposed two-gap superconductivity in this material lies in evaluating the relative weight of the tunneling current due to each of the three components of the Fermi surface. From the Tersoff

Contribution	Position	α-exp 1 (Bohr^{-1})	α-exp 2 (Bohr^{-1})
Pancake	At atom	1.3049 ± 0.0011	-
	At hollow	1.3016 ± 0.0004	-
Cylinder at Γ	At atom	1.3144 ± 0.0016	-
	At hollow	1.3093 ± 0.0007	-
Cylinder at K	At atom	1.3066 ± 0.0006	1.66 ± 0.04
	At hollow	1.3064 ± 0.0006	-

Table 5.11: Inverse decay length extracted from exponential fits of I vs z.

and Hamman analysis,[162] it is expected that the contribution of the states with small wave vector parallel to the surface will decay slower in vacuum and thus give a dominant contribution to the current for large tip-surface distance. Tersoff and Hamman also stressed that, even if it is not the dominant term, the states near the Brillouin zone boundary also give a significant contribution.

A precise analysis requires the calculation of the tunneling current as a function of the height of the tip, which reflects how the different contributions in the DOS decrease in vacuum. We have studied the decay of the current $I(z)$ with the tip height z at different positions of the (x, y)-plane for the three different components of the Fermi surface. A quick reminder from Section 5.1.3: $I(z)$ is expected to roughly vary exponentially $I \approx Ae^{-\alpha z}$. If the exponential dependence holds, we can easily obtain α by fitting the calculated $I(z)$.

As we also explained in Section 5.1.3, in some cases, the $I(z)$ curves do not correspond to a single exponential, but rather display two exponential regimes (with two different slopes). As in the case of MgB_2 we can fit the $I(z)$. The results of the fits to $I(z)$ are shown in Table 5.11. For each component of the Fermi surface, a similar inverse decay length is found (~ 1.31 Bohr^{-1}) corresponding to a typical decay length of 0.4 Å. A second exponential is needed for the component of the cylinders around K, indicating a faster decay of one contribution of the local DOS relatively close to the surface.

5.2.3.8 Contribution of the different portions of the Fermi surface to the tunneling current

The ratio of the local DOS in vacuum associated with the 'Nb Γ-cylinders' and 'Nb K-cylinders' plotted as a function of the distance from the surface is shown in Fig. 5.26. For most values of the tip-surface distance in the STM experiment (5-10 Å), the local DOS due to the 'Nb Γ-cylinders' is around twice as large as that originating from the 'Nb K-cylinders'. In view of the calculated local DOS values for the bulk (see Table 5.4), this is a surprising result. However, it can be explained by taking into account the larger weight of the Se p_z orbitals around Γ than around K and the signs of the mixing coefficients of the orbitals for a given wave vector (see the discussion in Section 5.2.4).

Let us now turn the attention to the possible role of the Se based pancake of the Fermi surface in understanding the origin of the different superconductivity gaps as probed by the tunneling experiments. Three-quarters of the local density of states at the Fermi level associated with this Se based pancake originate from the Se p_z orbitals so that some degree of interband coupling with the 'Nb Γ-cylinders' and/or the 'Nb K-cylinders' might be expected. If the contributions to tunneling of the 'Nb Γ-cylinders' and the Se based pancake are taken together, it becomes the dominant contribution to the tunneling process when compared with the contribution of the 'Nb K-cylinders' (Fig. 5.26, red curve). Recall that this occurs despite the dominant contribution of the 'Nb K-cylinders' over that of the 'Nb Γ-cylinders' to the total DOS at the Fermi level for

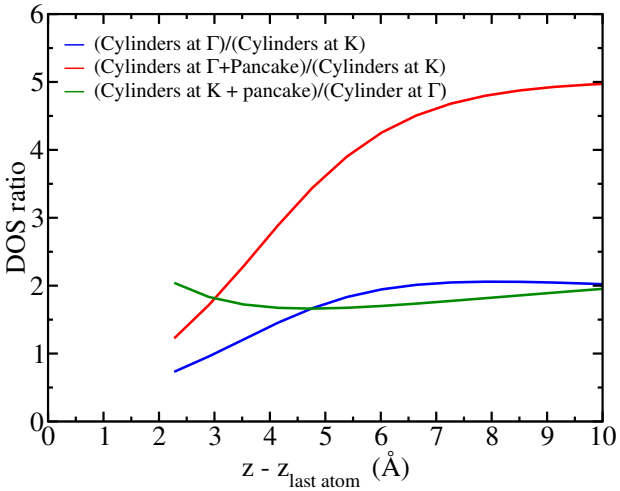

Figure 5.26: Ratios of the calculated DOS for the various portions of the Fermi surface as a function of the distance from the surface.

the bulk (see Table 5.4). However, if the contribution to tunneling of the Se based pancake is added to the contribution of the 'Nb K-cylinders', it also becomes the dominant contribution to the tunneling process when compared to the contribution of the 'Nb Γ-cylinders' (Fig. 5.26, green curve).

Consequently, our calculations show that, assuming that there is some coupling between the cylinders and the pancake portions of the Fermi surface, the Se based pancake can either reinforce or reverse the noted predominance of the 'Nb Γ-cylinders' over the 'Nb K-cylinders' in the tunneling. Thus, in order to make the link between the tunneling selectivity and the identification of the two bands associated with the McMillan model it is crucial to focus on the role of the Se based pancake. This issue is further elaborated in Section 5.2.5.

5.2.4 Discussion on the contribution of the Γ and K cylinders to the tunneling current

For most values of the tip-to-surface distance, the contribution of the cylinders around Γ to the tunneling intensity is around twice larger than that of the cylinders around K (Fig. 5.26). This may seem a bit surprising if we recall that the respective contributions to the density of states at the Fermi level were found to be just the opposite. However, this is in line with the results for the inverse decay length in Table 5.11.

One can think about two possible origins for this fact. First, the faster decaying of the contribution of the cylinders around K is due to the **k**-selectivity of the tunneling current.[162] It follows from eq. 5.7 that the contribution to the tunneling of Fermi surface states with wave vectors near the Brillouin zone center ($\mathbf{k} = 0$) should be larger. Consequently, the contribution of the cylinders around Γ should become larger because of this effect and maybe could overcome the initial difference in density of states at the Fermi level. However, in the present case, we evaluate the effect of this **k**-selectivity as leading at most to an increase of about 10% of the calculated value. Consequently, this should not be the main factor behind the dominance of the contribution of the cylinders around Γ. Second, one should be aware that the decay of the Se p_z orbitals is slower than the decay of the Se (p_x,p_y) orbitals. As discussed in detail in Sections 5.2.3.1 and 5.2.3.4, the nature of the niobium orbitals for the Fermi surface states associated with the cylinders around Γ and those around K is different and this will induce a different hybridization of the selenium orbitals in the respective wave functions. As shown in Table 5.4,

the relative weight of the Se p_z vs. Se (p_x,p_y) orbitals is larger for the cylinders around Γ. This means that the hybridization between the Se orbitals is more strongly dominated by the p_z orbitals for the states associated with the cylinders around Γ thus leading to a slower decay of these states.

A complementary aspect one must consider is that the plots of the density of states lack an important ingredient in order to understand a directional effect like the tunneling current along a certain direction: the signs of the mixing coefficients of the orbitals for a given wave vector. Of course these signs are directly related to the directionality of the electronic states and consequently strongly influence the tunneling in a given direction. Briefly speaking, the different nature of the niobium orbitals for the states around Γ and around K lead to different Se orbitals hybridizations with a stronger control of the p_z orbitals for the cylinder states around Γ. Actual calculation of the wave functions for points of the Fermi surface associated with the cylinders around Γ and around K show that the former exhibit a slower decaying along c.

5.2.5 Discussion

5.2.5.1 Linking the small and large gaps bands to the Fermi surface sheets

The study of the band structure of $NbSe_2$ by means of DFT calculations gives us the respective contributions of the different Fermi surface sheets to the DOS at the Fermi level (see Table 5.4). Moreover, from the analysis of our experimental tunneling data, we have deduced the ratio of the partial DOS corresponding to the 'small' and the 'large gap' bands: $N_S(E_F)/N_L(E_F) \sim 1/3$. This information should enable the identification in k-space of the Fermi sheets corresponding to the small and large gap bands, or at least to propose a reasonable scenario.

The two 'Nb Γ-cylinders' (as well as the two 'Nb K-cylinders') nearly touch and are of the same electronic nature. If one adds together the theoretical DOS contribution of both 'Nb Γ-cylinders' (corresponding to the portions around Γ of bands 2 and 3), one obtains 0.7 elect·eV^{-1}·unit cell^{-1} (i.e. 26% of the total DOS at E_F) while the contribution of the 'Nb K-cylinders' (bands 2 and 3 around K) gives 1.9 elect·eV^{-1}·unit cell^{-1} (i.e. 70% of the total DOS). Thus, the ratio between these two partial DOS (that around Γ divided by that around K) is 0.37, a value which is very close to the one inferred from our tunneling data: 0.33 (see Section 5.2.2.1). The immediate conclusion is that the small gap DOS is associated with the 'Nb Γ-cylinders' and the 'large gap' DOS with the 'Nb K-cylinders'. However, as shown in Fig. 5.26 (blue line), the contribution of the 'Nb Γ-cylinders' to tunneling should dominate over that of the 'Nb K-cylinders'. This is not what is observed in the measured tunneling spectra.[136,167,171]

To resolve this apparent paradox, there are two important aspects that must be taken into account. First, the existence of the Se pocket around Γ, and second, the charge density wave state present at low temperature. Both have strong implications for the tunneling selectivity and the interband coupling, as we discuss below. The existence of the Se-based pancake (Figs. 5.19 and 5.27a) has been confirmed experimentally, for instance using ARPES[172,178] or magnetoresistance measurements.[177] As mentioned before, it is strongly based on the Se p_z orbitals. Thus, as established by our calculations (see Fig. 5.26), the Se-based states should strongly contribute to the tunneling current and a question arises regarding their possible coupling to the Nb bands.

The second aspect to consider is that the low temperature Fermi surface is more complex than indicated in Fig. 5.27a due to the CDW state existing below the transition temperature $T_{CDW} \approx 30$K.[165] In the CDW state the system exhibits a nearly commensurate ($3a\times3a\times c$) superstructure.[165,181,188] This may play a significant role in both the interband coupling mechanism as well as in the tunneling selectivity. In fact, taking into account the CDW state leads to a qualitative model in good agreement with the tunneling measurements.

Assuming a commensurate ($3a\times3a\times c$) superstructure after the transition, the CDW leads

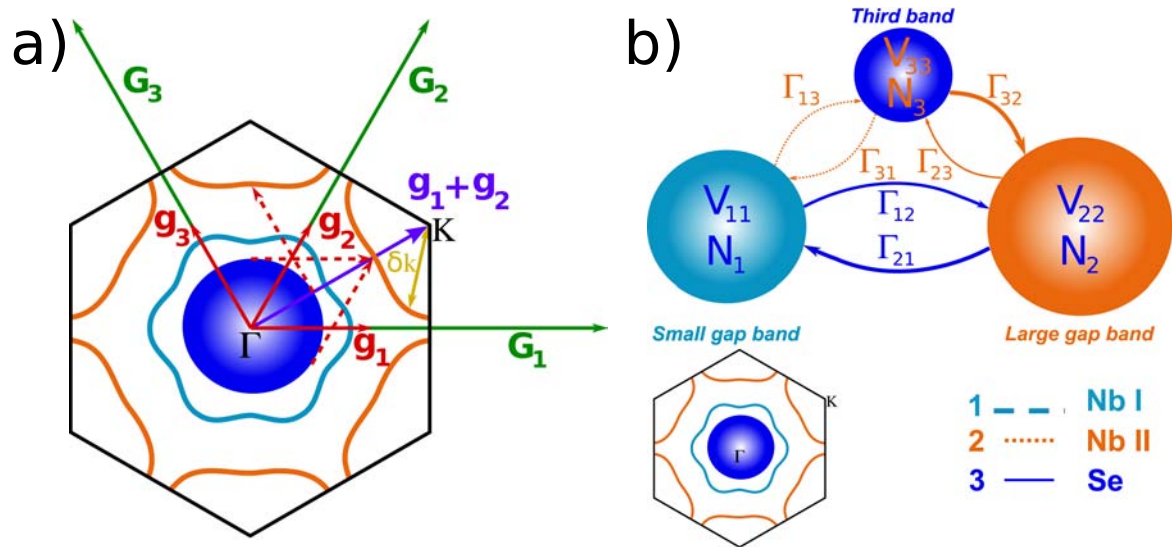

Figure 5.27: (a) Schematic view of the Fermi surface of $NbSe_2$. The wave vectors of the charge density wave $\vec{g_i} = \frac{1}{3}\vec{G_i}$ (where G_i are the basis vectors of the reciprocal space of $NbSe_2$ above the CDW phase transition temperature) link the selenium pocket around Γ (dark blue area) to the cylinders around K (orange lines) at different points of the first Brillouin zone. (b) Schematic view of the possible interband couplings between those bands associated with the three different Fermi surface components. Band 1 (2) corresponds to the Nb cylinders around Γ (K), while band 3 corresponds to the Se pocket around Γ.

to a reduced hexagonal Brillouin zone with 1/9th of the parent area. It is instructive to consider the extended zone scheme and to look for equivalent k points in the non-reduced (parent) Brillouin zone. In particular, as a result of the new periodicity, the center of the first Brillouin zone, Γ, becomes equivalent to the parent K point since $\Gamma\vec{K} = \vec{g_1} + \vec{g_2}$, with $\vec{g_1} = \frac{1}{3}\vec{G_1}$ and $\vec{g_2} = \frac{1}{3}\vec{G_2}$ (see Fig. 5.27a where $\vec{G_i}$ are the basis vectors of the parent reciprocal lattice of $NbSe_2$). Consequently, the tunneling probability to electronic states belonging to a pocket around K, will involve new wave functions with an inverse decay length given by $\alpha_k = \sqrt{\delta k^2 + \kappa^2}$ (instead of the former $\alpha_k = \sqrt{(\vec{K} - \delta\vec{K})^2 + \kappa^2}$) where $\delta\vec{k}$ is a vector joining the K point to the nearest FS sheet (see Fig. 5.27a). Clearly, due to the CDW state, the tunneling coming from the 'Nb K-cylinders' states gets considerably enhanced.

The CDW state might also play a role in the interband coupling. Indeed, as seen in Fig. 5.27a, the two wave vectors of the charge density wave $\vec{g_1} = \frac{1}{3}\vec{G_1}$ and $\vec{g_2} = \frac{1}{3}\vec{G_2}$ precisely link the small selenium pocket around Γ to the portions of the cylinders around K having high DOS. For this reason, we expect a strong coupling mediated by the charge density wave between those two areas of the Fermi surface. As will be shown in the following section, when the coupling is sufficiently strong ($\geq$ 10 meV), the Se Γ-pocket and the 'Nb K-cylinders' behave as one single band, explaining thereby why the tunneling spectra along the c-axis reflect the 'large gap' band.

5.2.5.2 Three bands model calculation

The strong coupling effect may be further illustrated by a three-band model calculation. Let us consider three bands (see Fig. 5.27b) with intrinsic gaps $\Delta_1^0 = 0$ meV, $\Delta_3^0 = 0$ meV, and $\Delta_2^0 = 1.4$ meV. The parameters of bands 1 and 2 correspond to the values found for the 'small gap' (band 1) and 'large gap' (band 2) bands of $NbSe_2$. Band 1 is thus weakly coupled to band 2 and very weakly coupled to band 3. We then studied the evolution of the partial DOS as a function of the interband coupling parameter Γ_{32} between bands 2 and 3. The ratios of the interband scattering parameters have been chosen such that they correspond to the calculated

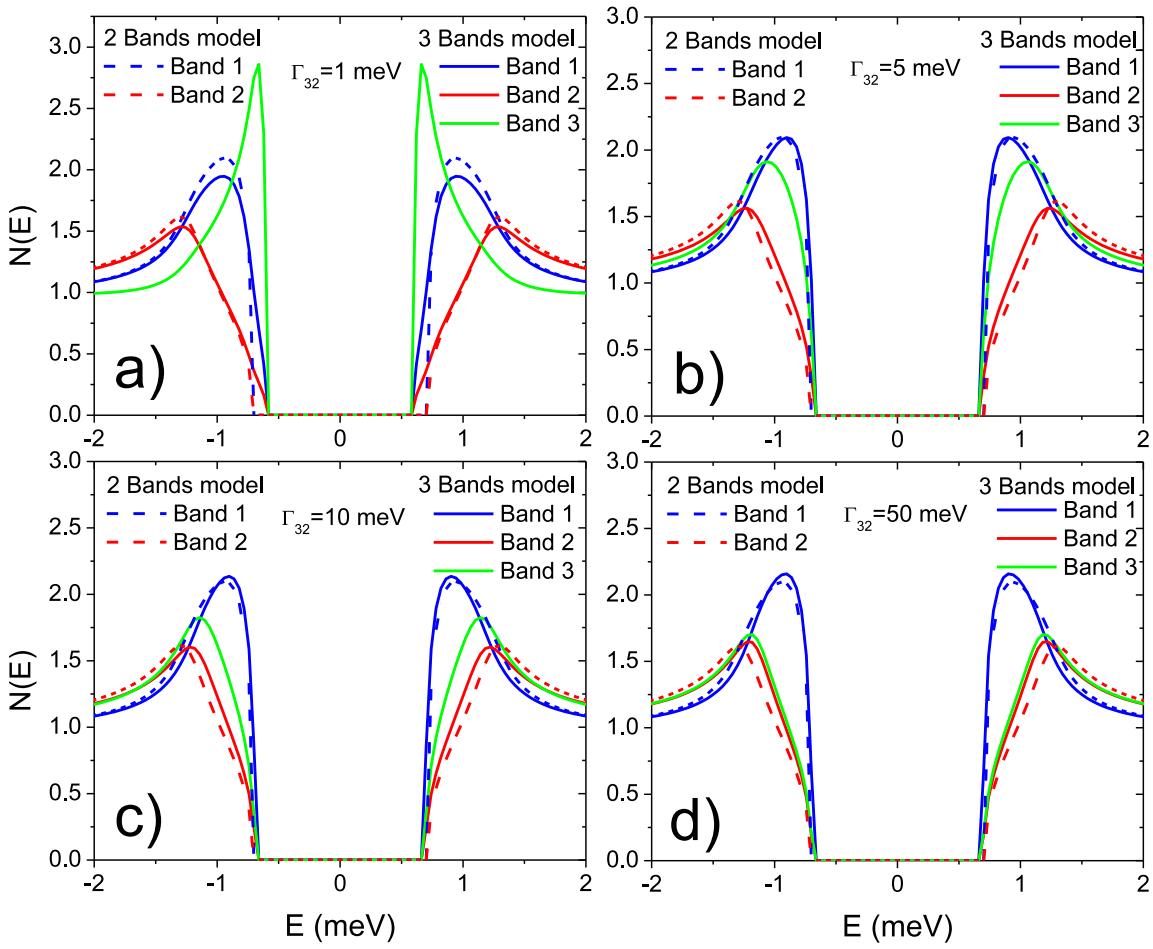

Figure 5.28: Partial DOS calculated by Roditchev *et al.* for a three bands model for different values of the interband coupling parameter between band 2 and band 3: (a) $\Gamma_{32} = 1$ meV; (b) $\Gamma_{32} = 5$ meV; (c) $\Gamma_{32} = 10$ meV; (d) $\Gamma_{32} = 50$ meV. The intrinsic gaps are $\Delta_1^0 = 0$ meV, $\Delta_2^0 = 1.4$ meV, and $\Delta_3^0 = 0$ meV. The ratio of the partial DOS at the Fermi energy are related to the ratio of quasiparticle scattering between the corresponding bands $\frac{N_1(E_F)}{N_2(E_F)} = \frac{\Gamma_{21}}{\Gamma_{12}} = 1/3$; $\frac{N_3(E_F)}{N_2(E_F)} = \frac{\Gamma_{23}}{\Gamma_{32}} = 1/16$; $\frac{N_3(E_F)}{N_1(E_F)} = \frac{\Gamma_{13}}{\Gamma_{31}} = 1/6$; The quasiparticle scattering parameters are: $\Gamma_{12} = 3$ meV; $\Gamma_{21} = 1$ meV.

DFT ratios of the partial DOS: $\frac{N_1(E_F)}{N_2(E_F)} = 1/3$; $\frac{N_3(E_F)}{N_2(E_F)} = 1/16$; $\frac{N_3(E_F)}{N_1(E_F)} = 1/6$; (we recall that band 1 is associated with the 'Nb Γ-cylinders', band 2 with the 'Nb K-cylinders'and band 3 with the Se pocket around Γ).

The interband coupling between bands 2 and 3 leads to an induced gap in band 3. As seen in Fig. 5.28, when Γ_{32} increases, the DOS of band 3 gets close to that of band 2. For very large $\Gamma_{32} \geq 50$ meV, one recovers a situation very similar to an effective two-band model with a new effective band constituted by bands 2 and 3. Thus, for a large coupling strength the model shows that bands 2 and 3 are indistinguishable from one single band. In Fig. 5.29, we plot the corresponding tunneling conductance assuming a complete tunneling selectivity towards band 3 (i.e. with tunneling weights $T_1 = 0$; $T_2 = 0$; $T_3 = 1$). For a large coupling $\Gamma_{32} \geq 50$ meV, the tunneling conductance is very close to the one predicted in the two-band model, with a complete selectivity towards the band with the 'large gap', corresponding well to the experimental observation.

In summary, we propose that the CDW state has strong implications for both the interband coupling between the Se-based pancake and the K-cylinders as well as for the probability to tunnel towards electronic states around the K point, due to the first Brillouin zone reconstruction. As a result, this gives rise to a strong contribution to the tunneling conductance of the

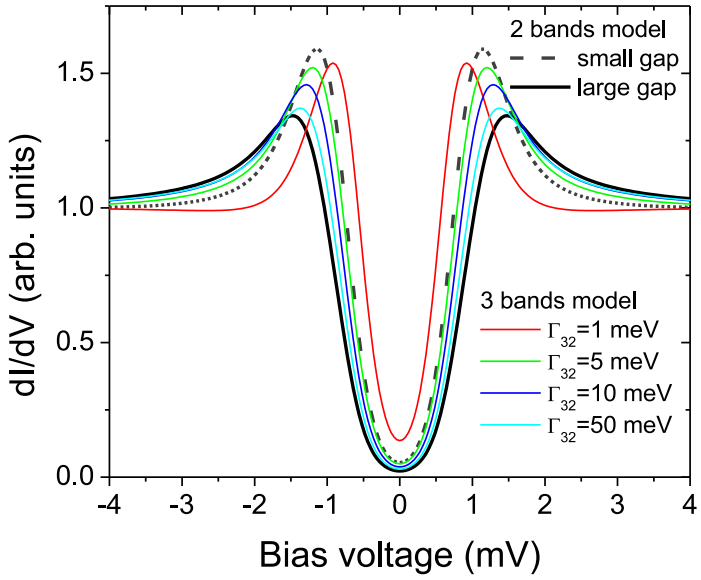

Figure 5.29: Tunneling conductance dI/dV calculated by Roditchev *et al.* in the three band model for different values of the interband coupling parameter between bands 2 and 3: Γ_{32} = 1, 5, 10, 50 meV; Dashed line: Tunneling conductance expected for the small and 'large gap' in the two band model.

states around K, an essential ingredient for the observation of the 'large gap' in c-axis tunneling spectra. The analysis above suggests that the band where the 'large gap' develops is constituted of both the K-cylinders and the Se pancake, strongly coupled together through quasiparticle scattering. Moreover, the quasiparticule coupling described in the McMillan model between the Γ and the K-cylinders, is likely to be associated to the reduced lattice reciprocal vectors $\vec{g_1}$ and $\vec{g_2}$ of the CDW state.

5.2.5.3 Comparison with 2H-NbS_2

It is also interesting to compare the tunneling conductance spectra measured on $NbSe_2$ to that reported by Guillamón *et al.* for 2H-NbS_2.[211] This material is close to $NbSe_2$, with a superconducting transition temperature of T_c= 5.7 K but does not exhibit any charge density wave instability.[212] Roditchev *et al.* fit their data with their two-band model obtaining parameters close to those of $NbSe_2$. The intrinsic gaps are: $\Delta_S^0 = 0 \pm 0.05$meV and $\Delta_L^0 = 1.15 \pm 0.05$meV, Γ_{SL}=1.5 meV and a ratio $\frac{\Gamma_{LS}}{\Gamma_{SL}} = 1/3 \pm 0.3$. The selectivity weights corresponding to the tunneling towards the two different effective bands are: $T_S = 0.4$ and $T_L = 0.6$ (see Fig. 5.30).

We thus find that, as for $NbSe_2$, our approach enables to reproduce the experimental spectra with a very good agreement. This implies that superconductivity develops in one band (or more precisely in one Fermi surface sheet) whereas it is induced in the other band by means of interband coupling mediated by quasiparticle scattering from one band to the other. The ratio found for the coupling parameters Γ_{ij} is very close to the value found for $NbSe_2$. This is in agreement with the similar density of states expected at the Fermi level for the K and Γ-cylinders in both materials. On the other hand, it is clear from the fits that the tunneling selectivity differs from $NbSe_2$ ($T_S = 0$; $T_L = 1$). This means that in 2H-NbS_2 there is a more important contribution of the band with the 'small gap' DOS to the tunneling current than in $NbSe_2$.

In principle, this feature could be explained in two different ways. First, although there is no CDW transition in 2H-NbS_2,[212] our calculations show that the Fermi surface is very similar to that of $NbSe_2$. In particular the S-based pancake around Γ is also present. This result is quite

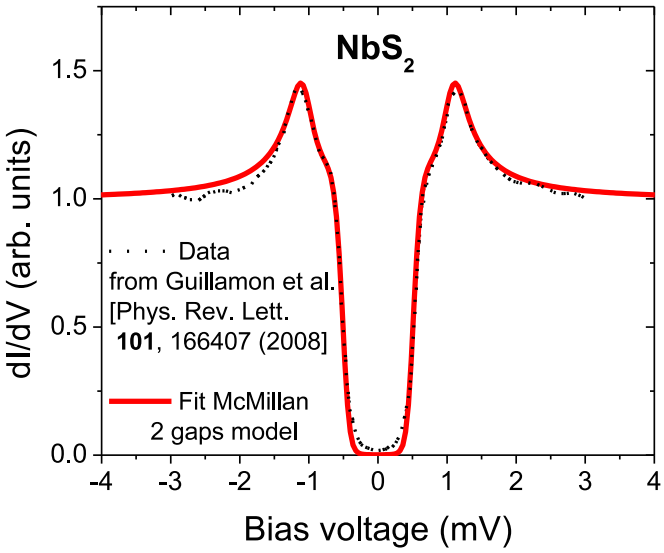

Figure 5.30: Tunneling conductance dI/dV spectrum from Guillamón *et al.*[211] and fit obtained with Roditchev's *et al.* two bands McMillan equations. The parameters for the fit are the following. The intrinsic gaps are: $\Delta_S^0 = 0 \pm 0.05$meV and $\Delta_L^0 = 1.15 \pm 0.05$meV, Γ_{SL}=1.5 meV and $\frac{\Gamma_{LS}}{\Gamma_{SL}} = 1/3 \pm 0.3$. The selectivity weights corresponding to the tunneling towards the two different effective bands are $T_S = 0.4$ and $T_L = 0.6$. Note that we have used a temperature for the fit ($T_{fit} = 0.5$K) which is significantly higher than the experimental temperature ($T_{exp} = 0.1$K).

robust since calculations for reasonable changes in the cell constants lead only to small changes in the FS shape. As for $NbSe_2$, a similar mechanism for the coupling to the 'K-cylinders' could take place through dynamical coupling,[186] although a static CDW modulation does not occur in this material. As a result the S based pocket could be strongly coupled to the 'K-cylinders'.

The change in the tunneling selectivity coefficients of the two bands (T_S and T_L), would originate from the absence of a real band structure reconstruction due to the absence of the CDW in this material. In addition, the scenario pointed out here to explain the observed differences between the experimental tunneling spectra of $NbSe_2$ and 2H-NbS_2, is in agreement with the observation that vortices in the first material where the CDW is present have a star shape, while they are circular in the other material, where the CDW is absent.[211]

5.3 Conclusions

In this Chapter, we have studied the two band gap superconductivity of two materials: MgB_2 and $NbSe_2$.

Although the two materials present the same physical phenomena, they are quite different: While in MgB_2 there are two bands crossing the Fermi level and is a quite known case of two band gap superconductivity the case of $NbSe_2$ there are three bands crossing the Fermi level and is still nowadays discussed in the literature.

In the case of MgB_2 we first studied the experimental results obtained by Roditchev *et al.*, finding that the ratio between interband coupling parameters is close to 1 and that the small gap was probed when doing STS measurements in the c-axis orientation. Using DFT calculations of the normal state we gave support to the experimental measurements.

Studying the DOS, we found that the ratio of both bands (which is directly related to the ratio of the coupling parameters) is also close to one.

Also, using STM images we studied why we preferentially see the small gap when doing STS experiments in the c-axis, finding that it is because both the directional shape of the boron p_z

orbital and the symmetry properties of the lattice.

For $NbSe_2$ we first did a survey of the experimental results that we could find in the literature. After, we studied the experimental data obtained by Roditchev *et al.* in dI/dV tunneling conductance spectra of $NbSe_2$ by scanning tunneling spectroscopy for two different crystal orientations. We found that the tunneling conductance is properly reproduced by the McMillan two-band model. In this framework, superconductivity develops in one band (with gap value $\Delta_L^0 = 1.4$ meV) and is induced in the second band by proximity effect in reciprocal space ($\Delta_S^0 = 0$ meV) through inter-band coupling provided by the scattering of quasiparticles. The data showed evidence of a strong tunneling selectivity which also depends on the crystal orientation: a DOS with a 'large gap' is mainly probed along the c-axis while a 'small gap' DOS is measured along the a/b-axis.

To interpret these results, and to link the two gaps to respective bands, a realistic band structure of $NbSe_2$ was calculated using first-principles DFT. The Fermi surface contains three components: a pancake-like Se based contribution around Γ, and two pairs of Nb-based cylinders parallel to c around Γ and K, respectively. The calculated values of the partial DOS at the Fermi energy associated with each of these three components show that the 'large gap' should be associated with the cylinders around K, while the 'small gap' should correspond to the Γ-cylinders.

In addition, our simulations of the tunneling current in the Tersoff-Hamman approximation show that the local DOS probed by STS is dominated by the p_z character of the Se orbitals. Considering that the 'large gap' DOS should originate from the K-cylinders, these results imply that a strong quasiparticle coupling should exist between the Se-based pancake and the K-cylinder Fermi surfaces. Such an interband coupling could be adequately provided by the CDW wave vectors existing in the superconducting phase of $NbSe_2$. The latter mechanism also explains the tunneling spectra measured on the related compound 2H-NbS_2 although in this case there is not a real CDW transition. This work thus brings a new light on the possible interaction between superconducting and CDW states in $NbSe_2$.

Chapter 6

Conclusions

Two-dimensional materials have been studied since long time ago. Recently, since the discovery of graphene in 2004 by the Nobel prizes A. Geim and K. Novoselov, a renewed interest in this kind of materials arose in the scientific community. Due to the excellent properties that graphene presents in order to make devices and study exotic quantum effects, there has been much development in the fabrication and manipulation of this material. This fact has led to an improvement of the techniques for 2D materials as a side effect. Nevertheless, not only 2D materials are interesting in the electronic properties/device building sense: also, the strongly correlated properties such as two band gap superconductivity that arises in some of them are also interesting. In this thesis we have studied the electronic properties of some of these materials:

- In Chapter 3 we studied the electronic properties of transition metal dichalcogenides (TMDCs) that, due to the change of gap character from direct to indirect when the sample has one layer or two or more layers, has become of great interest in the past years. Using DFT calculations we were able to identify the minimum set of orbitals to construct an analytic and trustworthy tight-binding (TB) model for these materials. Furthermore, we showed how, by just adding some interlayer hopping terms, we were able to correctly describe the aforementioned band gap transition. After building this TB model we adjusted the parameters to the previously obtained DFT band structure, finding that a qualitatively agreement was obtained. Moreover, we found that the mechanism that drives the transition from a direct to an indirect gap is due to an interlayer band splitting, where the S p_z orbitals play an essential role. Since some of these materials could present strong spin-orbit coupling (SOC) we generalized our TB model to include the SO interaction. This time, taking the already optimised parameters, we used the SOC constant obtained from the literature and found, as in the case without SOC, that there is a qualitative agreement with our DFT calculations. Due to the analyticity of these TB models, they are suitable for the inclusion of many-body effects and for the analysis of local strain effects. Furthermore, they can be used in order to perform theoretical transport calculations in real-size samples.

- In Chapter 4 we studied the properties of a new family of substrates for graphene: the transition metal dichalcogenides. After building the different structures and finding the optimised value for the distance between graphene and WS_2 we saw that, although the linear behaviour of the bands around the Dirac cone is preserved, a small gap is opened at the Dirac point. We found that when adding more WS_2 layers to the system, the valence (conduction) band approaches to the Dirac point at the vicinity of the Γ-point (K-point). The positions of these bands converge to the bulk limit when having three or more layers of WS_2. We also studied the charge redistribution for these structures, and we found that it is mostly localized at the graphene/WS_2 interface. This redistribution creates a small dipole at the interface. We also saw that adding more layers does not change neither the distribution of charge nor the interface dipole.

- In Chapter 5 we studied the two band gap superconductivity that arises in MgB_2 and $NbSe_2$.

- In the case of MgB_2 we have only two bands crossing the Fermi level. The experimental results obtained by Roditchev and coworkers at the Spectroscopie des Nouveoux etats quantiques group at the Institut des Nanociences de Paris show the well known result that that the small gap is probed when doing STS experiments in the c-axis. Combining calculations of bulk properties and simulating the STM images at the surface, we found that this is due to the directional shape of the boron p_z orbital and the symmetry properties of the lattice.
- The case of $NbSe_2$ is more complicated since we have three bands crossing the Fermi level and, furthermore, this material undergoes a charge density wave at low temperatures (before the superconducting state has occurred). Roditchev's group performed dI/dV tunneling conductance measurements in two crystal orientations. They found that the 'large gap' was probed in the c-direction while the 'small gap' was measured in the a/b-direction. To understand all the results and link, as in the case of MgB_2, the superconducting gaps to each of the bands that cross the Fermi level, we perform first-principles calculations. As we said before, $NbSe_2$ has three bands crossing at the Fermi level, which gives us three contributions to the Fermi surface which are: a pancake-like Se based contribution around Γ, and two pairs of Nb-based cylinders parallel to c around Γ and K, respectively. With this, we can show that the 'large gap' should be associated with the cylinders around K, while the 'small gap' should correspond to the Γ-cylinders. Moreover, with the theoretical STM images, we show that the tunneling current in the experiment is dominated by the p_z character of the Se orbitals. The participation of the remaining band (giving the Se based pancake Fermi surface) is less clear, and we tried to solve it. This association implied that a strong quasiparticle coupling should exist between both Fermi surfaces contributions. We showed that, since the 'large gap'originates from the K-cylinders, the Se-pancake should couple with this. Furthermore, this mechanism also allowed us to understand the tunneling spectra from 2H-NbS_2, a similar compound to $NbSe_2$, which does not undergoe a CDW transition.

Appendix A

Computational details

In this Appendix, we describe the details of the calculations for each Chapter. All DFT calculations carried out along the thesis were carried out using the Siesta code.[59,60]

A.1 DFT calculations for the TB model of TMDC

A.1.1 Without spin-orbit coupling

We use the local density approximation (LDA) to DFT and, in particular, the exchange-correlation potential of Ceperly-Alder[213] as parametrized by Perdew and Zunger.[214] The non-linear core-valence exchange-correlation scheme[215] was used for all elements. We have used a split-valence double-ζ basis set including polarization functions.[14] The energy cutoff of the real space integration mesh was chosen to converge the total energy (300 Ry). The Brillouin zone was chosen to converge the total energy and was sampled using 30×30×1 and 30×30×30 k-points in the Monkhorst-Pack scheme[216] for the single-layer and bulk systems, respectively.

Lattice parameters for MoS_2, $MoSe_2$, WS_2 and WSe_2 were chosen according to their experimental values, as reported in the works by Bromley *et al.*,[57] Schutte *et al.*,[125] and Kumar *et al.*[217] and they are listed in Table A.1.

A.1.2 With spin-orbit coupling

The spin-orbit interaction is treated as in the work by Fernández-Seivane *et al.*[218] We use the local density approximation (LDA) to DFT and, in particular, the exchange-correlation potential of Ceperly-Alder[213] as parametrized by Perdew and Zunger.[214] The non-linear core-valence exchange-correlation scheme[215] was used for all elements. We have used a split-valence double-ζ basis set including polarization functions.[14] The energy cutoff of the real space integration mesh was 300 Ry. The Brillouin zone was sampled using 30×30×1 and 30×30×30 k-points in the Monkhorst-Pack scheme[216] for the slab (single-layer and bilayer) and bulk systems, respectively.

	a	u	c'
MoS_2 1L	3.16	1.586	–
MoS_2 Bulk	3.16	1.586	6.14
$MoSe_2$ 1L	3.288	1.664	–
$MoSe_2$ Bulk	3.288	1.664	6.451
WS_2 1L	3.153	1.571	–
WS_2 Bulk	3.153	1.571	6.1615
WSe_2 1L	3.260	1.657	–
WSe_2 Bulk	3.260	1.657	6.422

Table A.1: Lattice parameters used for DFT calculation for MX_2 systems, as taken from the works by Bromley *et al.*[57], Schutte *et al.*,[125] and Kumar *et al.*[217] a represents the M-M atomic distance, u the internal vertical distance between the M plane and the X plane, and c' the distance between the M layers. In bulk systems the z-axis lattice parameter is given by $c = 2c'$. All values are in Å units.

A.2 Transition metal dichalcogenides as substrates for graphene

We use the local density approximation (LDA) to DFT and, in particular, the exchange-correlation potential of Ceperly-Alder[213] as parametrized by Perdew and Zunger.[214] The non-linear core-valence exchange-correlation scheme[215] was used for all elements. We have used a split-valence double-ζ basis set including polarization functions.[14] The energy cutoff of the real space integration mesh was chosen to converge the total energy (300 Ry). The Brillouin zone was chosen to converge the total energy and was sampled using $20\times20\times1$ k-points in the Monkhorst-Pack scheme.[216]

A.3 Two band gap superconductivity in 2D materials

A.3.1 MgB_2

We use the local density approximation (LDA) to DFT and, in particular, the functional of Ceperly-Alder.[213] Only the valence electrons are considered in the calculation, with the core being replaced by norm-conserving scalar relativistic pseudopotentials[219] factorized in the Kleinman-Bylander form.[220] The non-linear core-valence exchange-correlation scheme[215] was used for all elements. We have used a split-valence double-ζ basis set including polarization functions.[14] The energy cutoff of the real space integration mesh was 300 Ry. The experimental crystal structure was used for the bulk calculations. A symmetrical nine unit cells thick slab based on the experimental bulk structure plus an extra boron layer to compensate charge was used for the calculation of the STM images. The reason is that as Li *et al.*[157] have also shown the Mg terminated samples should exhibit the same type of STM images as the B terminated samples for any experimentally reasonable height ($>$ 4 Å). The only difference lies in the actual value of the DOS, i.e., the images for the case of an Mg terminated sample are the same as those for a B terminated surface when the probe is around 4 Å further away. Only at small distances (around 3 Å) of a Mg terminated surface the Mg atoms are visible and dominate the image. The Brillouin zone was sampled using $30\times30\times30$ and $30\times30\times1$ k-points in the Monkhorst-Pack scheme[216] for the bulk and slab calculations, respectively.

A.3.2 $NbSe_2$

We use the generalized gradient approximation (GGA) to DFT and, in particular, the functional of Perdew, Burke and Ernzerhof.[221] Only the valence electrons are considered in the calculation, with the core being replaced by norm-conserving scalar relativistic pseudopotentials[219] factorized in the Kleinman-Bylander form.[220] The non-linear core-valence exchange-correlation scheme[215] was used for all elements. We use a split-valence double-ζ basis set including polarization functions, optimized for the bulk structure of $NbSe_2$[14]. The energy cutoff of the real space integration mesh was 300 Ry. The Brillouin zone was sampled using a grid of $(30\times30\times30)$ k-points within the Monkhorst-Pack scheme[216]. The experimental crystal structure was used in the bulk calculations for $2H$-$NbSe_2$[179] and $2H$-NbS_2.[222] A symmetrical slab of ten and a half unit cells thick based on the experimental bulk structure was used for the calculation of the STM images. In that case we also used an extra diffuse orbital in the basis set so as to take into account the slab nature of the system[223] and the Brillouin zone was sampled using a mesh of $(30\times30\times1)$ k-points.

Appendix B

Tight-binding Hamiltonian elements

In this Appendix we provide an analyical expression, in terms of the Slater-Koster parameters, for the several intra-layer and inter-layer matrix elements that appear in the Hamiltonian of the tight-binding model. Following the work by Doran *et al.*,[100] it is convenient to introduce few quantities that account for the moment dispersion within the Brillouin zone, as functions of the reduced momentum variables $\xi = k_x a/2$, $\eta = \sqrt{3}k_y a/2$.

We define thus:

$$C_1(\xi,\eta) = 2\cos(\xi)\cos(\eta/3) + \cos(2\eta/3) + i[2\cos(\xi)\sin(\eta/3) - \sin(2\eta/3)], \quad \text{(B.1)}$$

$$C_2(\xi,\eta) = \cos(\xi)\cos(\eta/3) - \cos(2\eta/3) + i[\cos(\xi)\sin(\eta/3) + \sin(2\eta/3)], \quad \text{(B.2)}$$

$$C_3(\xi,\eta) = \cos(\xi)\cos(\eta/3) + 2\cos(2\eta/3) + i[\cos(\xi)\sin(\eta/3) - 2\sin(2\eta/3)], \quad \text{(B.3)}$$

$$d_1(\xi,\eta) = \sin(\eta/3) - i\cos(\eta/3), \quad \text{(B.4)}$$

$$l_1(\xi,\eta) = \cos(2\xi) + 2\cos(\xi)\cos(\eta), \quad \text{(B.5)}$$

$$l_2(\xi,\eta) = \cos(2\xi) - \cos(\xi)\cos(\eta), \quad \text{(B.6)}$$

$$l_3(\xi,\eta) = 2\cos(2\xi) + \cos(\xi)\cos(\eta). \quad \text{(B.7)}$$

B.1 Intra-layer hopping terms

Following the work by Doran *et al.*,[100] the intralayer hopping terms $H_{\alpha,\beta}$ appearing in Eqs. (3.4)-(3.8) can be written as:

$$H_{x/x}(\xi,\eta) = \Delta_p + E_{15} l_3(\xi,\eta) + 3E_{16}\cos(\xi)\cos(\eta), \quad \text{(B.8)}$$

$$H_{y/y}(\xi,\eta) = \Delta_p + E_{16} l_3(\xi,\eta) + 3E_{15}\cos(\xi)\cos(\eta), \quad \text{(B.9)}$$

$$H_{z/z}(\xi,\eta) = \Delta_z + 2E_{16} l_1(\xi,\eta), \quad \text{(B.10)}$$

$$H_{z^2/z^2}(\xi,\eta) = \Delta_0 + 2E_9 l_1(\xi,\eta), \quad \text{(B.11)}$$

$$H_{x^2/x^2}(\xi,\eta) = \Delta_2 + E_{11} l_3(\xi,\eta) + 3E_{12}\cos(\xi)\cos(\eta), \quad \text{(B.12)}$$

$$H_{xy/xy}(\xi,\eta) = \Delta_2 + E_{12}l_3(\xi,\eta) + 3E_{11}\cos(\xi)\cos(\eta), \tag{B.13}$$

$$H_{xz/xz}(\xi,\eta) = \Delta_1 + E_{13}l_3(\xi,\eta) + 3E_{14}\cos(\xi)\cos(\eta), \tag{B.14}$$

$$H_{yz/yz}(\xi,\eta) = \Delta_1 + E_{14}l_3(\xi,\eta) + 3E_{13}\cos(\xi)\cos(\eta), \tag{B.15}$$

$$H_{x/y}(\xi,\eta) = -\sqrt{3}(E_{15} - E_{16})\sin(\xi)\sin(\eta), \tag{B.16}$$

$$H_{z^2/x^2}(\xi,\eta) = 2E_{10}l_2(\xi,\eta), \tag{B.17}$$

$$H_{z^2/xy}(\xi,\eta) = -2\sqrt{3}E_{10}\sin(\xi)\sin(\eta), \tag{B.18}$$

$$H_{x^2/xy}(\xi,\eta) = \sqrt{3}(E_{11} - E_{12})\sin(\xi)\sin(\eta), \tag{B.19}$$

$$H_{xz/yz}(\xi,\eta) = \sqrt{3}(E_{14} - E_{13})\sin(\xi)\sin(\eta), \tag{B.20}$$

$$H_{z^2/x}(\xi,\eta) = -2\sqrt{3}E_1\sin(\xi)d_1(\xi,\eta), \tag{B.21}$$

$$H_{z^2/y}(\xi,\eta) = 2E_1C_2(\xi,\eta), \tag{B.22}$$

$$H_{z^2/z}(\xi,\eta) = E_2C_1(\xi,\eta), \tag{B.23}$$

$$H_{x^2/x}(\xi,\eta) = -2\sqrt{3}(\frac{1}{3}E_5 - E_3)\sin(\xi)d_1(\xi,\eta), \tag{B.24}$$

$$H_{x^2/y}(\xi,\eta) = -2E_3C_3(\xi,\eta) - 2iE_5\cos(\xi)d_1(\xi,\eta), \tag{B.25}$$

$$H_{x^2/z}(\xi,\eta) = -2E_4C_2(\xi,\eta), \tag{B.26}$$

$$H_{xy/x}(\xi,\eta) = -\frac{2}{3}E_5C_3(\xi,\eta) - 6iE_3\cos(\xi)d_1(\xi,\eta), \tag{B.27}$$

$$H_{xy/y}(\xi,\eta) = H_{x^2/x}(\xi,\eta), \tag{B.28}$$

$$H_{xy/z}(\xi,\eta) = 2\sqrt{3}E_4\sin(\xi)d_1(\xi,\eta), \tag{B.29}$$

$$H_{xz/x}(\xi,\eta) = \frac{2}{3}E_6C_3(\xi,\eta) + 6iE_7\cos(\xi)d_1(\xi,\eta), \tag{B.30}$$

$$H_{xz/y}(\xi,\eta) = 2\sqrt{3}(\frac{1}{3}E_6 - E_7)\sin(\xi)d_1(\xi,\eta), \tag{B.31}$$

$$H_{xz/z}(\xi,\eta) = -2\sqrt{3}E_8\sin(\xi)d_1(\xi,\eta), \tag{B.32}$$

$$H_{yz/x}(\xi,\eta) = H_{xz/y}(\xi,\eta), \tag{B.33}$$

$$H_{yz/y}(\xi,\eta) = 2E_7C_3(\xi,\eta) + 2iE_6\cos(\xi)d_1(\xi,\eta), \tag{B.34}$$

$$H_{yz/z}(\xi,\eta) = 2E_8C_2(\xi,\eta), \tag{B.35}$$

where

$$E_1 = \frac{1}{2}\left[-V_{pd\sigma}\left(\sin^2\phi - \frac{1}{2}\cos^2\phi\right) + \sqrt{3}V_{pd\pi}\sin^2\phi\right]\cos\phi, \tag{B.36}$$

$$E_2 = \left[-V_{pd\sigma}\left(\sin^2\phi - \frac{1}{2}\cos^2\phi\right) - \sqrt{3}V_{pd\pi}\cos^2\phi\right]\sin\phi, \tag{B.37}$$

$$E_3 = \frac{1}{4}\left[\frac{\sqrt{3}}{2}V_{pd\sigma}\cos^3\phi + V_{pd\pi}\cos\phi\sin^2\phi\right], \tag{B.38}$$

$$E_4 = \frac{1}{2}\left[\frac{\sqrt{3}}{2}V_{pd\sigma}\sin\phi\cos^2\phi - V_{pd\pi}\sin\phi\cos^2\phi\right], \tag{B.39}$$

$$E_5 = -\frac{3}{4}V_{pd\pi}\cos\phi, \tag{B.40}$$

$$E_6 = -\frac{3}{4}V_{pd\pi}\sin\phi, \tag{B.41}$$

$$E_7 = \frac{1}{4}\left[-\sqrt{3}V_{pd\sigma}\cos^2\phi - V_{pd\pi}(1-2\cos^2\phi)\right]\sin\phi, \tag{B.42}$$

$$E_8 = \frac{1}{2}\left[-\sqrt{3}V_{pd\sigma}\sin^2\phi - V_{pd\pi}(1-2\sin^2\phi)\right]\cos\phi, \tag{B.43}$$

$$E_9 = \frac{1}{4}V_{dd\sigma} + \frac{3}{4}V_{dd\delta}, \tag{B.44}$$

$$E_{10} = -\frac{\sqrt{3}}{4}\left[V_{dd\sigma} - V_{dd\delta}\right], \tag{B.45}$$

$$E_{11} = \frac{3}{4}V_{dd\sigma} + \frac{1}{4}V_{dd\delta}, \tag{B.46}$$

$$E_{12} = V_{dd\pi}, \tag{B.47}$$

$$E_{13} = V_{dd\pi}, \tag{B.48}$$

$$E_{14} = V_{dd\delta}, \tag{B.49}$$

$$E_{15} = V_{pp\sigma}, \tag{B.50}$$

$$E_{16} = V_{pp\pi}. \tag{B.51}$$

Here the angle ϕ characterize the structure of the unit cell of the compound and it is determined by purely geometric reasons (see Fig. 3.2). For the ideal trigonal prism structure, neglecting the marginal deviations from it in real systems, we have $\phi = \arccos[\sqrt{4/7}]$, so that $\cos\phi = \sqrt{4/7}$ and $\sin\phi = \sqrt{3/7}$.

With these expressions, taking into account also the further changes of basis, the Hamiltonian at the Γ point can be divided in sub-blocks as:

$$\hat{H}_{\mathrm{E}}(\Gamma) = \begin{pmatrix} \hat{H}_{zd_0}(\Gamma) & 0 & 0 \\ 0 & \hat{H}_{pd_2}(\Gamma) & 0 \\ 0 & 0 & \hat{H}_{pd_2}(\Gamma) \end{pmatrix}, \tag{B.52}$$

$$\hat{H}_{\mathrm{O}}(\Gamma) = \begin{pmatrix} \hat{H}_{pd_1}(\Gamma) & 0 & 0 \\ 0 & \hat{H}_{pd_1}(\Gamma) & 0 \\ 0 & 0 & \Gamma_z \end{pmatrix}, \tag{B.53}$$

where

$$\hat{H}_{zd_0}(\Gamma) = \begin{pmatrix} \Gamma_0 & \sqrt{2}\Gamma_{zd_0} \\ \sqrt{2}\Gamma_{zd_0} & \Gamma_z^{\mathrm{E}} \end{pmatrix}, \tag{B.54}$$

$$\hat{H}_{pd_2}(\Gamma) = \begin{pmatrix} \Gamma_2 & \sqrt{2}\Gamma_{pd_2} \\ \sqrt{2}\Gamma_{pd_2} & \Gamma_p^{\mathrm{E}} \end{pmatrix}, \tag{B.55}$$

$$\hat{H}_{pd_1}(\Gamma) = \begin{pmatrix} \Gamma_1 & \sqrt{2}\Gamma_{pd_2} \\ \sqrt{2}\Gamma_{pd_2} & \Gamma_p^{\mathrm{O}} \end{pmatrix}. \tag{B.56}$$

The parameters Γ_α can be viewed as "molecular" energy levels, and the quantities $\Gamma_{\alpha,\beta}$ as hybridization parameters. Their explicit expressions read:

$$\Gamma_0 = H_{z^2/z^2}(\Gamma) = \Delta_0 + 6E_9, \tag{B.57}$$

$$\begin{aligned} \Gamma_1 &= H_{xz/xz}(\Gamma) = H_{yz/yz}(\Gamma) \\ &= \Delta_1 + 3[E_{13} + E_{14}], \end{aligned} \tag{B.58}$$

$$\begin{aligned} \Gamma_2 &= H_{xy/xy}(\Gamma) = H_{x^2/x^2}(\Gamma) \\ &= \Delta_2 + 3[E_{11} + E_{12}], \end{aligned} \tag{B.59}$$

$$\Gamma_p^{\mathrm{E}} = \Gamma_p + V_{pp\pi}, \tag{B.60}$$

$$\Gamma_p^{\mathrm{O}} = \Gamma_p - V_{pp\pi}, \tag{B.61}$$

$$\Gamma_z^{\mathrm{E}} = \Gamma_z - V_{pp\sigma}, \tag{B.62}$$

$$\Gamma_z^{\mathrm{O}} = \Gamma_z + V_{pp\sigma}, \tag{B.63}$$

$$\begin{aligned}\Gamma_p &= H_{x/x}(\Gamma) = H_{y/y}(\Gamma)\\ &= \Delta_p + 3[E_{15} + E_{16}],\end{aligned} \tag{B.64}$$

$$\Gamma_z = H_{z/z}(\Gamma) = \Delta_z + 6E_{16}, \tag{B.65}$$

$$\Gamma_{zd_0} = H_{3z^2-r^2/z}(\Gamma) = 3E_2, \tag{B.66}$$

$$\begin{aligned}\Gamma_{pd_2} &= H_{x^2-y^2/y}(\Gamma) = H_{xy/x}(\Gamma)\\ &= -2[3E_3 + E_5],\end{aligned} \tag{B.67}$$

$$\begin{aligned}\Gamma_{pd_1} &= H_{xz/x}(\Gamma) = H_{yz/y}(\Gamma)\\ &= 2[3E_7 + E_6].\end{aligned} \tag{B.68}$$

At the K point, in the proper basis described in the main text, we can write the even and odd blocks of the Hamiltonian as:

$$\hat{H}_{\mathrm{E}}(K) = \begin{pmatrix} \hat{H}_{pd_0}(K) & 0 & 0 \\ 0 & \hat{H}_{zd_2}(K) & 0 \\ 0 & 0 & \hat{H}_{pd_2}(K) \end{pmatrix}, \tag{B.69}$$

$$\hat{H}_{\mathrm{O}} = \begin{pmatrix} \hat{H}_{pd_1}(K) & 0 & 0 \\ 0 & \hat{H}_{zd_1}(K) & 0 \\ 0 & 0 & K_p^{\mathrm{O}} \end{pmatrix}, \tag{B.70}$$

where

$$\hat{H}_{pd_0}(K) = \begin{pmatrix} K_0 & -2iK_{pd_0} \\ 2iK_{pd_0} & K_p^{\mathrm{E}} \end{pmatrix}, \tag{B.71}$$

$$\hat{H}_{zd_2}(K) = \begin{pmatrix} K_2 & 2K_{zd_2} \\ 2K_{zd_2} & K_z^{\mathrm{E}} \end{pmatrix}, \tag{B.72}$$

$$\hat{H}_{pd_2}(K) = \begin{pmatrix} K_2 & i\sqrt{8}K_{pd_2} \\ -i\sqrt{8}K_{pd_2} & K_p^{\mathrm{E}} \end{pmatrix}, \tag{B.73}$$

$$\hat{H}_{pd_1}(K) = \begin{pmatrix} K_1 & \sqrt{8}K_{pd_1} \\ \sqrt{8}K_{pd_1} & K_p^{\mathrm{O}} \end{pmatrix}, \tag{B.74}$$

$$\hat{H}_{zd_1}(K) = \begin{pmatrix} K_1 & -2iK_{zd_1} \\ 2iK_{zd_1} & K_z^{\mathrm{O}} \end{pmatrix}. \tag{B.75}$$

The parameters K_α, $K_{\alpha,\beta}$ read here:

$$K_0 = H_{z^2/z^2}(K) = \Delta_0 - 3E_9, \tag{B.76}$$

$$\begin{aligned} K_1 &= H_{xz/xz}(K) = H_{yz/yz}(K) \\ &= \Delta_1 - \frac{3}{2}[E_{13} + E_{14}], \end{aligned} \tag{B.77}$$

$$\begin{aligned} K_2 &= H_{xy/xy}(K) = H_{x^2/x^2}(K) \\ &= \Delta_2 - \frac{3}{2}[E_{11} + E_{12}], \end{aligned} \tag{B.78}$$

$$K_p^{\mathrm{E}} = K_p + V_{pp\pi}, \tag{B.79}$$

$$K_p^{\mathrm{O}} = K_p - V_{pp\pi}, \tag{B.80}$$

$$K_z^{\mathrm{E}} = K_z - V_{pp\sigma}, \tag{B.81}$$

$$K_z^{\mathrm{O}} = K_z + V_{pp\sigma}, \tag{B.82}$$

$$\begin{aligned} K_p &= H_{x/x}(K) = H_{y/y}(K) \\ &= \Delta_p - \frac{3}{2}[E_{15} + E_{16}], \end{aligned} \tag{B.83}$$

$$K_z = H_{z/z}(K) = \Delta_z - 3E_{16}, \tag{B.84}$$

$$\begin{aligned} K_{pd_0} &= H_{3z^2-r^2/y}(K) = iH_{3z^2-r^2/x}(K) \\ &= -3E_1, \end{aligned} \tag{B.85}$$

$$\begin{aligned} K_{zd_2} &= H_{x^2-y^2/z}(K) = iH_{xy/z}(K) \\ &= 3E_4, \end{aligned} \tag{B.86}$$

$$\begin{aligned} K_{pd_2} &= H_{x^2-y^2/y}(K) = -H_{xy/x}(K) \\ &= -iH_{x^2-y^2/x}(K) = -iH_{xy/y}(K) \\ &= \left[E_5 - 3E_3\right], \end{aligned} \tag{B.87}$$

$$\begin{aligned} K_{pd_1} &= H_{xz/x}(K) = -H_{yz/y}(K) \\ &= iH_{xz/y}(K) = iH_{yz/x}(K) \\ &= [E_6 - 3E_7], \end{aligned} \tag{B.88}$$

$$\begin{aligned} K_{zd_1} &= H_{yz/z}(K) = iH_{xz/z}(K) \\ &= -3E_8. \end{aligned} \tag{B.89}$$

B.2 Inter-layer hopping terms

Inter-layer hopping is ruled by the Slater-Koster parameters $U_{pp\sigma}$, $U_{pp\pi}$ describing hopping between S-3p orbitals belonging to different layers.

In terms of the reduced momentum variables $\xi = k_x a/2$, $\eta = \sqrt{3}k_y a/2$, we have thus:

$$
\begin{aligned}
I_{x/x}(\xi,\eta) &= \frac{1}{2}\left[E_{19}C_3(\xi,-\eta) + i3E_{17}\cos\xi d_1(\xi,-\eta)\right], && \text{(B.90)}\\
I_{y/y}(\xi,\eta) &= \frac{1}{2}\left[E_{17}C_3(\xi,-\eta) + i3E_{19}\cos\xi d_1(\xi,-\eta)\right], && \text{(B.91)}\\
I_{z/z}(\xi,\eta) &= E_{18}C_1(\xi,-\eta), && \text{(B.92)}\\
I_{x/y}(\xi,\eta) &= \frac{\sqrt{3}}{2}\left[E_{17}-E_{19}\right]\sin\xi d_1(\xi,-\eta), && \text{(B.93)}\\
I_{x/z}(\xi,\eta) &= -\sqrt{3}E_{20}\sin\xi d_1(\xi,\eta), && \text{(B.94)}\\
I_{y/z}(\xi,\eta) &= -E_{20}C_2(\xi,-\eta), && \text{(B.95)}\\
I_{z/z}(\xi,\eta) &= E_{18}C_1(\xi,-\eta), && \text{(B.96)}
\end{aligned}
$$

where

$$
\begin{aligned}
E_{17} &= U_{pp\sigma}\cos^2\beta + U_{pp\pi}\sin^2\beta, && \text{(B.97)}\\
E_{18} &= U_{pp\sigma}\sin^2\beta + U_{pp\pi}\cos^2\beta, && \text{(B.98)}\\
E_{19} &= U_{pp\pi}, && \text{(B.99)}\\
E_{20} &= \left[U_{pp\sigma} - U_{pp\pi}\right]\cos\beta\sin\beta. && \text{(B.100)}
\end{aligned}
$$

Here β is the angle between the line connecting the two S atoms with respect to the S planes (see Fig. 3.2). Denoting w the distance between the two S-planes, we have:

$$
\begin{aligned}
\cos\beta &= \frac{a}{\sqrt{a^2+3w^2}}, && \text{(B.101)}\\
\sin\beta &= \frac{\sqrt{3}w}{\sqrt{a^2+3w^2}}. && \text{(B.102)}
\end{aligned}
$$

Using typical values for bulk MoS_2, $a = 3.16$ Å, and $w = 2.975$ Å, we get $\cos\beta = 0.523$ and $\sin\beta = 0.852$.

At the high-symmetry points Γ, K, we have thus:

$$
\begin{aligned}
\Gamma_{pp} &= I_{x/x}(\Gamma) = I_{y/y}(\Gamma)\\
&= \frac{3}{2}\left[E_{19}+E_{17}\right], && \text{(B.103)}\\
\Gamma_{zz} &= I_{z/z}(\Gamma)\\
&= 3E_{18}, && \text{(B.104)}\\
K_{pp} &= I_{x/x}(K) = -I_{y/y}(K)\\
&= -iI_{x/y}(K) = -iI_{y/x}(K)\\
&= \frac{3}{4}\left[E_{19}-E_{17}\right], && \text{(B.105)}\\
K_{pz} &= I_{y/z}(K) = I_{z/y}(K)\\
&= -iI_{x/z}(K) = -iI_{z/x}(K)\\
&= \frac{3}{2}E_{20}. && \text{(B.106)}
\end{aligned}
$$

Appendix C

Decomposition of the Hamiltonian in sub-blocks at high-symmetry points

In this Appenddix we summarize the different unitary transformations that permit to decomposed at special high-symmetry points the higher rank Hamiltonian matrix in smaller sub-locks. In all the cases we treat in a separate way the "even" and "odd" blocks, namely electronix states with even and odd symmetry with respect to the $z \to -z$ inversion.

C.1 Single-layer

C.1.1 Γ point

In the Hilbert space defined by the vector basis $\tilde{\phi}_k^\dagger$ in Eq. (3.9), the even and odd blocks of the Hamiltonian can be written respectively as:

$$\hat{H}_{\rm E}(\Gamma) = \begin{pmatrix} \Gamma_0 & 0 & 0 & 0 & 0 & \sqrt{2}\Gamma_{zd_0} \\ 0 & \Gamma_2 & 0 & 0 & \sqrt{2}\Gamma_{pd_2} & 0 \\ 0 & 0 & \Gamma_2 & \sqrt{2}\Gamma_{pd_2} & 0 & 0 \\ 0 & 0 & \sqrt{2}\Gamma_{pd_2} & \Gamma_p^{\rm E} & 0 & 0 \\ 0 & \sqrt{2}\Gamma_{pd_2} & 0 & 0 & \Gamma_p^{\rm E} & 0 \\ \sqrt{2}\Gamma_{zd_0} & 0 & 0 & 0 & 0 & \Gamma_z^{\rm E} \end{pmatrix}, \tag{C.1}$$

and

$$\hat{H}_{\rm O}(\Gamma) = \begin{pmatrix} \Gamma_1 & 0 & \sqrt{2}\Gamma_{pd_1} & 0 & 0 \\ 0 & \Gamma_1 & 0 & \sqrt{2}\Gamma_{pd_1} & 0 \\ \sqrt{2}\Gamma_{pd_1} & 0 & \Gamma_p^{\rm O} & 0 & 0 \\ 0 & \sqrt{2}\Gamma_{pd_1} & 0 & \Gamma_p^{\rm O} & 0 \\ 0 & 0 & 0 & 0 & \Gamma_z^{\rm O} \end{pmatrix}. \tag{C.2}$$

The division in sub-blocks is already evident in Eqs. (C.1)-(C.2). They can be further ordered using the basis

$$\bar{\phi}_k^\dagger = (\bar{\phi}_{k,zd_0}^\dagger, \bar{\phi}_{k,pd_2,y}^\dagger, \bar{\phi}_{k,pd_2,x}^\dagger, \bar{\phi}_{k,pd_1,x}^\dagger, \bar{\phi}_{k,pd_1,y}^\dagger, \bar{\phi}_{k,z}^\dagger,), \tag{C.3}$$

where

$$\bar{\phi}_{k,zd_0}^\dagger = (d_{k,3z^2-r^2}^\dagger, p_{k,z,A}^\dagger,), \tag{C.4}$$
$$\bar{\phi}_{k,pd_2,y}^\dagger = (d_{k,x^2-y^2}^\dagger, p_{k,y,S}^\dagger), \tag{C.5}$$
$$\bar{\phi}_{k,pd_2,x}^\dagger = (d_{k,xy}^\dagger, p_{k,x,S}^\dagger), \tag{C.6}$$
$$\bar{\phi}_{k,pd_1,x}^\dagger = (d_{k,xz}^\dagger, p_{k,x,A}^\dagger), \tag{C.7}$$
$$\bar{\phi}_{k,pd_1,y}^\dagger = (d_{k,yz}^\dagger, p_{k,y,A}^\dagger), \tag{C.8}$$
$$\bar{\phi}_{k,z}^\dagger = (p_{k,z,S}^\dagger). \tag{C.9}$$

In this basis we get Eqs. (3.11)-(3.12), where

$$\hat{H}_{zd_0}(\Gamma) = \begin{pmatrix} \Gamma_0 & \sqrt{2}\Gamma_{zd_0} \\ \sqrt{2}\Gamma_{zd_0} & \Gamma_z^{\mathrm{E}} \end{pmatrix}, \tag{C.10}$$

$$\hat{H}_{pd_2}(\Gamma) = \begin{pmatrix} \Gamma_2 & \sqrt{2}\Gamma_{pd_2} \\ \sqrt{2}\Gamma_{pd_2} & \Gamma_p^{\mathrm{E}} \end{pmatrix}, \tag{C.11}$$

$$\hat{H}_{pd_1}(\Gamma) = \begin{pmatrix} \Gamma_1 & \sqrt{2}\Gamma_{pd_1} \\ \sqrt{2}\Gamma_{pd_1} & \Gamma_p^{\mathrm{O}} \end{pmatrix}. \tag{C.12}$$

C.1.2 K point

In the basis defined by the Hilbert vector $\tilde{\phi}_k^\dagger$, the Hamiltonian at the K point reads, for the even and odd blocks, respectively:

$$\hat{H}_{\mathrm{E}}(K) = \begin{pmatrix} K_0 & 0 & 0 & -i\sqrt{2}K_{pd_0} & \sqrt{2}K_{pd_0} & 0 \\ 0 & K_2 & 0 & i\sqrt{2}K_{pd_2} & \sqrt{2}K_{pd_2} & \sqrt{2}K_{zd_2} \\ 0 & 0 & K_2 & -\sqrt{2}K_{pd_2} & i\sqrt{2}K_{pd_2} & -i\sqrt{2}K_{zd_2} \\ i\sqrt{2}K_{pd_0} & -i\sqrt{2}K_{pd_2} & -\sqrt{2}K_{pd_2} & K_p^{\mathrm{E}} & 0 & 0 \\ \sqrt{2}K_{pd_0} & \sqrt{2}K_{pd_2} & -i\sqrt{2}K_{pd_2} & 0 & K_p^{\mathrm{E}} & 0 \\ 0 & \sqrt{2}K_{zd_2} & i\sqrt{2}K_{zd_2} & 0 & 0 & K_z^{\mathrm{E}} \end{pmatrix} \tag{C.13}$$

$$\hat{H}_{\mathrm{O}}(K) = \begin{pmatrix} K_1 & 0 & \sqrt{2}K_{pd_1} & -i\sqrt{2}K_{pd_1} & -i\sqrt{2}K_{zd_1} \\ 0 & K_1 & -i\sqrt{2}K_{pd_1} & -\sqrt{2}K_{pd_1} & \sqrt{2}K_{zd_1} \\ \sqrt{2}K_{pd_1} & i\sqrt{2}K_{pd_1} & K_p^{\mathrm{O}} & 0 & 0 \\ i\sqrt{2}K_{pd_1} & -\sqrt{2}K_{pd_1} & 0 & K_p^{\mathrm{O}} & 0 \\ i\sqrt{2}K_{zd_1} & \sqrt{2}K_{zd_1} & 0 & 0 & K_z^{\mathrm{O}} \end{pmatrix}. \tag{C.14}$$

In order to decopled the Hamiltoniam, it is convenient to introduce the chiral basis defined by the vector $\bar{\psi}_k^\dagger$ in Eq. (3.17). In this Hilbert space we have thus:

$$\hat{H}_{\mathrm{E}}(K) = \begin{pmatrix} \hat{H}_{pd_0}(K) & 0 & 0 \\ 0 & \hat{H}_{zd_2}(K) & 0 \\ 0 & 0 & \hat{H}_{pd_2}(K) \end{pmatrix}, \tag{C.15}$$

$$\hat{H}_{\mathrm{O}} = \begin{pmatrix} \hat{H}_{pd_1}(K) & 0 & 0 \\ 0 & \hat{H}_{zd_1}(K) & 0 \\ 0 & 0 & K_p^{\mathrm{O}} \end{pmatrix}, \tag{C.16}$$

where

$$\hat{H}_{pd_0}(K) = \begin{pmatrix} K_0 & -i2K_{pd_0} \\ i2K_{pd_0} & K_p^{\mathrm{E}} \end{pmatrix}, \tag{C.17}$$

$$\hat{H}_{zd_2}(K) = \begin{pmatrix} K_2 & 2K_{pd_2} \\ 2K_{pd_2} & K_z^{\mathrm{E}} \end{pmatrix}, \tag{C.18}$$

$$\hat{H}_{pd_2}(K) = \begin{pmatrix} K_2 & i\sqrt{8}K_{pd_2} \\ -i\sqrt{8}K_{pd_2} & K_p^{\mathrm{E}} \end{pmatrix}, \tag{C.19}$$

$$\hat{H}_{pd_1}(K) = \begin{pmatrix} K_1 & \sqrt{8}K_{pd_1} \\ \sqrt{8}K_{pd_1} & K_p^{\mathrm{O}} \end{pmatrix}, \tag{C.20}$$

$$\hat{H}_{zd_1}(K) = \begin{pmatrix} K_1 & -i2K_{pd_1} \\ i2K_{pd_1} & K_z^{\mathrm{O}} \end{pmatrix}. \tag{C.21}$$

C.2 Bulk system

The general structure of the tight-binding Hamiltonian $\hat{H}_{\rm bulk}$ for the bulk system, using the basis defined in Eq. (3.23), is provided in Eqs. (3.26)-(3.31), where we also remind the symmetry property (Eq. (3.25)) that related the matrix elements of $\hat{H}_2$ to $\hat{H}_1$.

As mentioned in the main text, for $k_z = 0$ the band structure can be still divided in two independent blocks with even and odd symmetry with respect to the transformation $z \to -z$.[100] Further simplicication are encountered at the high-symmetry points Γ and K.

C.2.1 Γ point

We first notice that at the Γ point the relation in Eq. (3.25) does not play any role, i.e. $\hat{H}_2(\Gamma) = \hat{H}_1(\Gamma)$, where $\hat{H}_1(\Gamma)$ is defined by Eqs. (3.10)-(3.12) in the main text.

The Hamiltonian is thus completely determined by the interlayer hopping matrix $\hat{I}$ that at the Γ point reads:

$$\hat{I}(\Gamma) = \begin{pmatrix} \Gamma_{pp} & 0 & 0 \\ 0 & \Gamma_{pp} & 0 \\ 0 & 0 & \Gamma_{zz} \end{pmatrix}. \tag{C.22}$$

A convenient basis to decoupled the Hamiltonian in smaller subblocks is thus:

$$\bar{\Phi}^\dagger_k = (\bar{\Phi}^\dagger_{k,zd_0}, \bar{\Phi}^\dagger_{k,pd_2,y}, \bar{\Phi}^\dagger_{k,pd_2,x}, \bar{\Phi}^\dagger_{k,pd_1,x}, \bar{\Phi}^\dagger_{k,pd_1,y}, \bar{\Phi}^\dagger_{k,z},), \tag{C.23}$$

where

$$\bar{\Phi}^\dagger_{k,zd_0} = (d^\dagger_{k,3z^2-r^2,1}, p^\dagger_{k,z,A,1}, d^\dagger_{k,3z^2-r^2,2}, p^\dagger_{k,z,A,2}), \tag{C.24}$$
$$\bar{\Phi}^\dagger_{k,pd_2,y} = (d^\dagger_{k,x^2-y^2,1}, p^\dagger_{k,y,S,1}, d^\dagger_{k,x^2-y^2,2}, p^\dagger_{k,y,S,2}), \tag{C.25}$$
$$\bar{\Phi}^\dagger_{k,pd_2,x} = (d^\dagger_{k,xy,1}, p^\dagger_{k,x,S,1}, d^\dagger_{k,xy,2}, p^\dagger_{k,x,S,2}), \tag{C.26}$$
$$\bar{\Phi}^\dagger_{k,pd_1,x} = (d^\dagger_{k,xz,1}, p^\dagger_{k,x,A,1}, d^\dagger_{k,xz,2}, p^\dagger_{k,x,A,2}), \tag{C.27}$$
$$\bar{\Phi}^\dagger_{k,pd_1,y} = (d^\dagger_{k,yz,1}, p^\dagger_{k,y,A,1}, d^\dagger_{k,yz,2}, p^\dagger_{k,y,A,2}), \tag{C.28}$$
$$\bar{\Phi}^\dagger_{k,z} = (p^\dagger_{k,z,S,1}, p^\dagger_{k,z,S,1},). \tag{C.29}$$

The resulting total Hamiltonian can be written as:

$$\hat{H}_{\rm bulk}(\Gamma) = \begin{pmatrix} \hat{H}_{\rm E,bulk}(\Gamma) & 0 \\ 0 & \hat{H}_{\rm O,bulk}(\Gamma) \end{pmatrix}, \tag{C.30}$$

where

$$\hat{H}_{\rm E,bulk}(\Gamma) = \begin{pmatrix} \hat{H}_{zd_0,\rm bulk}(\Gamma) & 0 & 0 \\ 0 & \hat{H}_{pd_2,\rm bulk}(\Gamma) & 0 \\ 0 & 0 & \hat{H}_{pd_2,\rm bulk}(\Gamma) \end{pmatrix}, \tag{C.31}$$

$$\hat{H}_{\rm O,bulk}(\Gamma) = \begin{pmatrix} \hat{H}_{pd_1,\rm bulk}(\Gamma) & 0 & 0 \\ 0 & \hat{H}_{pd_1,\rm bulk}(\Gamma) & 0 \\ 0 & 0 & \hat{H}_{z,\rm bulk}(\Gamma) \end{pmatrix}, \tag{C.32}$$

and where

$$\hat{H}_{zd_0,\text{bulk}} = \begin{pmatrix} \Gamma_0 & \sqrt{2}\Gamma_{zd_0} & 0 & 0 \\ \sqrt{2}\Gamma_{zd_0} & \Gamma_z^{\text{E}} & 0 & \Gamma_{zz} \\ 0 & 0 & \Gamma_0 & \sqrt{2}\Gamma_{zd_0} \\ 0 & \Gamma_{zz} & \sqrt{2}\Gamma_{zd_0} & \Gamma_z^{\text{E}} \end{pmatrix}, \tag{C.33}$$

$$\hat{H}_{pd_2,\text{bulk}} = \begin{pmatrix} \Gamma_2 & \sqrt{2}\Gamma_{pd_2} & 0 & 0 \\ \sqrt{2}\Gamma_{pd_2} & \Gamma_p^{\text{E}} & 0 & \Gamma_{pp} \\ 0 & 0 & \Gamma_2 & \sqrt{2}\Gamma_{pd_2} \\ 0 & \Gamma_{pp} & \sqrt{2}\Gamma_{pd_2} & \Gamma_p^{\text{E}} \end{pmatrix}, \tag{C.34}$$

$$\hat{H}_{pd_1,\text{bulk}} = \begin{pmatrix} \Gamma_1 & \sqrt{2}\Gamma_{pd_1} & 0 & 0 \\ \sqrt{2}\Gamma_{pd_1} & \Gamma_p^{\text{O}} & 0 & \Gamma_{pp} \\ 0 & 0 & \Gamma_1 & \sqrt{2}\Gamma_{pd_1} \\ 0 & \Gamma_{pp} & \sqrt{2}\Gamma_{pd_1} & \Gamma_p^{\text{O}} \end{pmatrix}, \tag{C.35}$$

$$\hat{H}_{z,\text{bulk}} = \begin{pmatrix} \Gamma_z^{\text{O}} & \Gamma_{zz} \\ \Gamma_{zz} & \Gamma_z^{\text{O}} \end{pmatrix}. \tag{C.36}$$

C.2.2 K point

The treatment of the bulk Hamiltonian at the K point, in order to get a matrix clearly divided in blocks, is a bit less straighforward than at the Γ point.

We first notice that the interlayer matrix, in the basis $\tilde{\Phi}_k^\dagger$, reads:

$$\hat{I}(K) = \begin{pmatrix} K_{pp} & iK_{pp} & iK_{pz} \\ iK_{pp} & -K_{pp} & K_{pz} \\ iK_{pz} & K_{pz} & 0 \end{pmatrix}. \tag{C.37}$$

We then ridefine the orbitals $d^\dagger_{k,yz,2} \to \bar{d}^\dagger_{k,yz,2} = -d^\dagger_{k,yz,2}$, $p^\dagger_{k,y,\alpha,2} \to \bar{p}^\dagger_{k,y,\alpha,2} = -p^\dagger_{k,y,\alpha,2}$ (α =A,S), in order to get, according with (3.25), $\hat{H}_2(\Gamma) = \hat{H}_1(\Gamma)$.

Following what done for the single layer, we can also introduce here a chiral basis. After a further rearrangement of the vector elements, we define thus the convenient Hilbert space as:

$$\bar{\Psi}_k^\dagger = (\bar{\Psi}^\dagger_{k,pzd_02,L}, \bar{\Psi}^\dagger_{k,pzd_02,R}, \bar{\Psi}^\dagger_{k,pd_2,\text{E}}, \bar{\Psi}^\dagger_{k,pzd_1,R}, \bar{\Psi}^\dagger_{k,pzd_1,L}, \bar{\Psi}^\dagger_{k,pd_1,\text{O}}), \tag{C.38}$$

where

$$\bar{\Psi}^\dagger_{k,pzd_02,L} = (d^\dagger_{k,3z^2-r^2,1}, p^\dagger_{k,L,S,1}, d^\dagger_{k,R,2}, p^\dagger_{k,z,A,2},), \tag{C.39}$$

$$\bar{\Psi}^\dagger_{k,pzd_02,R} = (d^\dagger_{k,3z^2-r^2,2}, p^\dagger_{k,R,S,2}, d^\dagger_{k,L,1}, p^\dagger_{k,z,A,1},), \tag{C.40}$$

$$\bar{\Psi}^\dagger_{k,pd_2,\text{E}} = (d^\dagger_{k,R,1}, p^\dagger_{k,R,S,1}, d^\dagger_{k,L,1}, p^\dagger_{k,L,S,1},), \tag{C.41}$$

$$\bar{\Psi}^\dagger_{k,pzd_1,R} = (d^\dagger_{k,R,1}, p^\dagger_{k,z,S,1}, p^\dagger_{k,R,A,2}), \tag{C.42}$$

$$\bar{\Psi}^\dagger_{k,pzd_1,R} = (d^\dagger_{k,L,2}, p^\dagger_{k,z,S,2}, p^\dagger_{k,L,A,1}), \tag{C.43}$$

$$\bar{\Psi}^\dagger_{k,pd_1,\text{O}} = (d^\dagger_{k,L,1}, p^\dagger_{k,R,A,1}, d^\dagger_{k,R,2}, p^\dagger_{k,L,A,2},). \tag{C.44}$$

In this basis, the Hamiltonian can be once more written as:

$$\hat{H}_{\text{bulk}}(K) = \begin{pmatrix} \hat{H}_{\text{E}}(K) & 0 \\ 0 & \hat{H}_{\text{O}}(K) \end{pmatrix}, \tag{C.45}$$

where $\hat{H}_{\text{E}}(K)$, $\hat{H}_{\text{O}}(K)$ are defined in Eqs. (3.35)-(3.40) of the main text.

Appendix D

SOC Hamiltonian

In this Appendix we provide the explicit expression of the matrices $\hat{M}^{\sigma\sigma}_{\rm EE}$, $\hat{M}^{\sigma\sigma}_{\rm OO}$, $\hat{M}^{\sigma\bar{\sigma}}_{\rm EO}$, $\hat{M}^{\sigma\bar{\sigma}}_{\rm OE}$, describing the local atomic spin-orbit interaction on both M and X atoms. We have:

$$\hat{M}^{\uparrow\uparrow}_{\rm EE} = \begin{pmatrix} 0 & 0 & 0 & 0 & 0 & 0 \\ 0 & 0 & -i\lambda_M & 0 & 0 & 0 \\ 0 & i\lambda_M & 0 & 0 & 0 & 0 \\ 0 & 0 & 0 & 0 & -i\lambda_X/2 & 0 \\ 0 & 0 & 0 & i\lambda_X/2 & 0 & 0 \\ 0 & 0 & 0 & 0 & 0 & 0 \end{pmatrix}, \tag{D.1}$$

$$\hat{M}^{\downarrow\downarrow}_{\rm EE} = -\hat{M}^{\uparrow\uparrow}_{\rm EE}, \tag{D.2}$$

$$\hat{M}^{\uparrow\uparrow}_{\rm OO} = \frac{1}{2}\begin{pmatrix} 0 & -i\lambda_M & 0 & 0 & 0 \\ i\lambda_M & 0 & 0 & 0 & 0 \\ 0 & 0 & 0 & -i\lambda_X & 0 \\ 0 & 0 & i\lambda_X & 0 & 0 \\ 0 & 0 & 0 & 0 & 0 \end{pmatrix}, \tag{D.3}$$

$$\hat{M}^{\downarrow\downarrow}_{\rm OO} = -\hat{M}^{\uparrow\uparrow}_{\rm OO}, \tag{D.4}$$

$$\hat{M}^{\uparrow\downarrow}_{\rm EO} = \frac{1}{2}\begin{pmatrix} -\sqrt{3}\lambda_M & i\sqrt{3}\lambda_M & 0 & 0 & 0 \\ \lambda_M & i\lambda_M & 0 & 0 & 0 \\ -i\lambda_M & \lambda_M & 0 & 0 & 0 \\ 0 & 0 & 0 & 0 & \lambda_X \\ 0 & 0 & 0 & 0 & -i\lambda_X \\ 0 & 0 & -\lambda_X & i\lambda_X & 0 \end{pmatrix}, \tag{D.5}$$

$$\hat{M}^{\downarrow\uparrow}_{\rm OE} = \left(\hat{M}^{\uparrow\downarrow}_{\rm EO}\right)^\dagger, \tag{D.6}$$

$$\hat{M}^{\downarrow\uparrow}_{\rm EO} = \frac{1}{2}\begin{pmatrix} \sqrt{3}\lambda_M & i\sqrt{3}\lambda_M & 0 & 0 & 0 \\ -\lambda_M & i\lambda_M & 0 & 0 & 0 \\ -i\lambda_M & -\lambda_M & 0 & 0 & 0 \\ 0 & 0 & 0 & 0 & -\lambda_X \\ 0 & 0 & 0 & 0 & -i\lambda_X \\ 0 & 0 & \lambda_X & i\lambda_X & 0 \end{pmatrix} \tag{D.7}$$

and

$$\hat{M}^{\uparrow\downarrow}_{\rm OE} = \left(\hat{M}^{\downarrow\uparrow}_{\rm EO}\right)^\dagger, \tag{D.8}$$

In the above matrices we have used the short notation λ_M for the SOC of the metal (Mo or W) and λ_X for the SOC of the chalcogen (S or Se).

Appendix E

Wyckoff symbols

In this Appendix we show the Wyckoff symbols that we need to generate the coordinates of the atoms for the modulated structure for the $P6_3/m$ and $P6_3/mmc$ groups of Section 5.2.3.5.

Position	**Coordinates**			
2a		$(0,0,\frac{1}{4})$	$(0,0,\frac{3}{4})$	
2c		$(\frac{1}{3},\frac{2}{3},\frac{1}{4})$	$(\frac{2}{3},\frac{1}{3},\frac{3}{4})$	
2d		$(\frac{2}{3},\frac{1}{3},\frac{1}{4})$	$(\frac{1}{3},\frac{2}{3},\frac{3}{4})$	
6h		$(x,y,\frac{1}{4})$	$(-y,x-y,\frac{1}{4})$	
	$(-x+y,-x,\frac{1}{4})$	$(-x,-y,\frac{3}{4})$	$(y,-x+y,\frac{3}{4})$	$(x-y,x,\frac{3}{4})$
12i	(x,y,z)	$(-y,x-y,z)$	$(-x+y,-x,z)$	$(-x,-y,z+\frac{1}{2})$
	$(y,-x+y,z+\frac{1}{2})$	$(x-y,x,z+\frac{1}{2})$	$(-x,-y,-z)$	$(y,-x+y,-z)$
	$(x-y,x,-z)$	$(x,y,-z+\frac{1}{2})$	$(-y,x-y,-z+\frac{1}{2})$	$(-x+y,-x,-z+\frac{1}{2})$

Table E.1: Wyckoff symbols for the $P6_3/m$ group.

Position	**Coordinates**			
2a		$(0,0,\frac{1}{2})$	$(0,0,\frac{1}{2})$	
2b		$(0,0,\frac{1}{4})$	$(0,0,\frac{3}{4})$	
2c		$(\frac{1}{3},\frac{2}{3},\frac{1}{4})$	$(\frac{2}{3},\frac{1}{3},\frac{3}{4})$	
2d		$(\frac{1}{3},\frac{2}{3},\frac{3}{4})$	$(\frac{2}{3},\frac{1}{3},\frac{1}{4})$	
4f	$(\frac{1}{3},\frac{2}{3},z)$	$(\frac{2}{3},\frac{1}{3},z+\frac{1}{2})$	$(\frac{2}{3},\frac{1}{3},-z)$	$(\frac{1}{3},\frac{2}{3},-z+\frac{1}{2})$
	$(x,y,\frac{1}{4})$	$(-y,x-y,\frac{1}{4})$	$(-x+y,-x,\frac{1}{4})$	$(-x,-y,\frac{3}{4})$
12j	$(y,-x+y,\frac{3}{4})$	$(x-y,x,\frac{3}{4})$	$(y,x,\frac{3}{4})$	$(x-y,-y,\frac{3}{4})$
	$(-x,-x+y,\frac{3}{4})$	$(-y,-x,\frac{1}{4})$	$(-x+y,y,\frac{1}{4})$	$(x,x-y,\frac{1}{4})$
	$(x,2x,z)$	$(-2x,x,z)$	$(x,-x,z)$	$(-x,-2x,z+\frac{1}{2})$
12k	$(2x,x,z+\frac{1}{2})$	$(-x,x,z+\frac{1}{2})$	$(2x,x,-z)$	$(-x,-2x,-z)$
	$(-x,x,-z)$	$(-2x,-x,-z+\frac{1}{2})$	$(x,2x,-z+\frac{1}{2})$	$(x,-x,-z+\frac{1}{2})$

Table E.2: Wyckoff symbols for the $P6_3/mmc$ group.

Bibliography

1. S. Z. Butler *et al. Progress, challenges, and opportunities in two-dimensional materials beyond graphene.* ACS Nano **7**, 2898 (2013).

2. K. S. Novoselov, A. K. Geim, S. V. Morozov, D. Jiang, Y. Zhang, S. V. Dubonos, I. V. Grigorieva and A. A. Firsov. *Electric field effect in atomically thin carbon films.* Science **306**, 666 (2004).

3. Q. H. Wang, K. Kalantar-Zadeh, A. Kis, J. N. Coleman and M. S. Strano. *Electronics and optoelectronics of two-dimensional transition metal dichalcogenides.* Nature Nanotechnology **7**, 699 (2012).

4. R. F. Frindt. *Single Crystals of MoS_2 Several Molecular Layers Thick.* Journal of Applied Physics **37**, 1928 (1966).

5. K. F. Mak, C. Lee, J. Hone, J. Shan and T. F. Heinz. *Atomically thin MoS_2: A new direct-gap semiconductor.* Physical Review Letters **105**, 136805 (2010).

6. H. Li, Z. Yin, Q. He, H. Li, X. Huang, G. Lu, D. W. H. Fam, A. I. Y. Tok, Q. Zhang and H. Zhang. *Fabrication of single- and multilayer MoS_2 film-based field-effect transistors for sensing NO at room temperature.* Small **8**, 63 (2012).

7. L. Britnell, R. V. Gorbachev, R. Jalil, B. D. Belle, F. Schedin, A. Mishchenko, T. Georgiou, M. I. Katsnelson, L. Eaves, S. V. Morozov, N. M. R. Peres, J. Leist, A. K. Geim, K. S. Novoselov and L. A. Ponomarenko. *Field-effect tunneling transistor based on vertical graphene heterostructures.* Science **335**, 947 (2012).

8. T. Georgiou, R. Jalil, B. D. Belle, L. Britnell, R. V. Gorbachev, S. V. Morozov, Y.-J. Kim, A. Gholinia, S. J. Haigh, O. Makarovsky, L. Eaves, L. A. Ponomarenko, A. K. Geim, K. S. Novoselov and A. Mishchenko. *Vertical field-effect transistor based on graphene–WS_2 heterostructures for flexible and transparent electronics.* Nature Nanotechnology **8**, 100 (2012).

9. H. Terrones, F. López-Urías and M. Terrones. *Novel hetero-layered materials with tunable direct band gaps by sandwiching different metal disulfides and diselenides.* Scientific Reports **3**, 1549 (2013).

10. R. M. Martin. *Electronic Structure: Basic Theory and Practical Methods* (Cambridge, 2004).

11. P. Hohenberg and W. Kohn. *Inhomogeneous electron gas.* Physical Review **136**, B864 (1964).

12. W. Kohn and L. J. Sham. *Self-consistent equations including exchange and correlation effects.* Physical Review **140**, A1133 (1965).

13. J. Junquera, O. Paz, D. Sánchez-Portal and E. Artacho. *Numerical atomic orbitals for linear-scaling calculations.* Physical Review B **64**, 235111 (2001).

14. E. Artacho, D. Sánchez-Portal, P. Ordejón, A. García and J. M. Soler. *Linear-scaling ab-initio calculations for large and complex systems.* Physica Status Solidi (b) **215**, 809 (1999).

15. J. C. Slater and G. F. Koster. *Simplified LCAO method for the periodic potential problem.* Physical Review **94**, 1498 (1954).

16. K. S. Novoselov, D. Jiang, F. Schedin, T. J. Booth, V. V. Khotkevich, S. V. Morozov and A. K. Geim. *Two-dimensional atomic crystals.* Proceedings of the National Academy of Sciences of the United States of America **102**, 10451 (2005).

17. Y. Zhang, Y.-W. Tan, H. L. Stormer and P. Kim. *Experimental observation of the quantum hall effect and Berry's phase in graphene.* Nature **438**, 201 (2005).

18. E. Cappelluti, R. Roldán, J. A. Silva-Guillén, P. Ordejón and F. Guinea. *Tight-binding model and direct-gap/indirect-gap transition in single-layer and multilayer MoS_2.* Physical Review B **88**, 075409 (2013).

19. J. Feng, X. Qian, C.-W. Huang and J. Li. *Strain-engineered artificial atom as a broad-spectrum solar energy funnel.* Nature Photonics **6**, 866 (2012).

20. P. Lu, X. Wu, W. Guo and X. C. Zeng. *Strain-dependent electronic and magnetic properties of MoS_2 monolayer, bilayer, nanoribbons and nanotubes.* Physical Chemistry Chemical Physics **14**, 13035 (2012).

21. H. Pan and Y.-W. Zhang. *Tuning the electronic and magnetic properties of MoS_2 nanoribbons by strain engineering.* The Journal of Physical Chemistry C **116**, 11752 (2012).

22. H. Peelaers and C. G. Van de Walle. *Effects of strain on band structure and effective masses in MoS_2.* Physical Review B **86**, 241401 (2012).

23. W. S. Yun, S. W. Han, S. C. Hong, I. G. Kim and J. D. Lee. *Thickness and strain effects on electronic structures of transition metal dichalcogenides: 2H–MX_2 semiconductors (M= Mo, W; X= S, Se, Te).* Physical Review B **85**, 033305 (2012).

24. E. Scalise, M. Houssa, G. Pourtois, V. Afanas'ev and A. Stesmans. *Strain-induced semiconductor to metal transition in the two-dimensional honeycomb structure of MoS_2.* Nano Research **5**, 43 (2012).

25. E. Scalise, M. Houssa, G. Pourtois, V. V. Afanas'ev and A. Stesmans. *First-principles study of strained 2D MoS_2.* Physica E: Low-dimensional Systems and Nanostructures **56**, 416 (2014).

26. Y. Li, Y.-L. Li, C. M. Araujo, W. Luo and R. Ahuja. *Single-layer MoS_2 as an efficient photocatalyst.* Catalysis Science & Technology **3**, 2214 (2013).

27. M. Ghorbani-Asl, S. Borini, A. Kuc and T. Heine. *Strain-dependent modulation of conductivity in single-layer transition-metal dichalcogenides.* Physical Review B **87**, 235434 (2013).

28. H. Shi, H. Pan, Y.-W. Zhang and B. I. Yakobson. *Quasiparticle band structures and optical properties of strained monolayer MoS_2 and WS_2.* Physical Review B **87**, 155304 (2013).

29. L. Hromadová, R. Martoňák and E. Tosatti. *Structure change, layer sliding, and metallization in high-pressure MoS_2.* Physical Review B **87**, 144105 (2013).

30. X. Xu, W. Yao, D. Xiao and T. F. Heinz. *Spin and pseudospins in layered transition metal dichalcogenides.* Nature Physics **10**, 343 (2014).

31. K. F. Mak, K. He, J. Shan and T. F. Heinz. *Control of valley polarization in monolayer MoS_2 by optical helicity.* Nature Nanotechnology **7**, 494 (2012).

32. K. F. Mak, K. He, C. Lee, G. H. Lee, J. Hone, T. F. Heinz and J. Shan. *Tightly bound trions in monolayer MoS_2.* Nature Materials **12**, 207 (2013).

33. T. Cao, G. Wang, W. Han, H. Ye, C. Zhu, J. Shi, Q. Niu, P. Tan, E. Wang, B. Liu and J. Feng. *Valley-selective circular dichroism of monolayer molybdenum disulphide.* Nature Communications **3**, 887 (2012).

34. G. Sallen, L. Bouet, X. Marie, G. Wang, C. R. Zhu, W. P. Han, Y. Lu, P. H. Tan, T. Amand, B. L. Liu and B. Urbaszek. *Robust optical emission polarization in MoS_2 monolayers through selective valley excitation.* Physical Review B **86**, 081301 (2012).

35. D. Xiao, G.-B. Liu, W. Feng, X. Xu and W. Yao. *Coupled spin and valley physics in monolayers of MoS_2 and other group-VI dichalcogenides.* Physical Review Letters **108**, 196802 (2012).

36. S. Wu, J. S. Ross, G.-B. Liu, G. Aivazian, A. Jones, Z. Fei, W. Zhu, D. Xiao, W. Yao, D. Cobden and X. Xu. *Electrical tuning of valley magnetic moment through symmetry control in bilayer MoS_2.* Nature Physics **9**, 149 (2013).

37. H. Zeng, J. Dai, W. Yao, D. Xiao and X. Cui. *Valley polarization in MoS_2 monolayers by optical pumping.* Nature Nanotechnology **7**, 490 (2012).

38. H. Ochoa and R. Roldán. *Spin-orbit-mediated spin relaxation in monolayer MoS_2.* Physical Review B **87**, 245421 (2013).

39. Z. Y. Zhu, Y. C. Cheng and U. Schwingenschlögl. *Giant spin-orbit-induced spin splitting in two-dimensional transition-metal dichalcogenide semiconductors.* Physical Review B **84**, 153402 (2011).

40. Q. Wang, S. Ge, X. Li, J. Qiu, Y. Ji, J. Feng and D. Sun. *Valley carrier dynamics in monolayer molybdenum disulfide from helicity-resolved ultrafast pump-probe spectroscopy.* ACS Nano **7**, 11087 (2013).

41. H. Zeng, G.-B. Liu, J. Dai, Y. Yan, B. Zhu, R. He, L. Xie, S. Xu, X. Chen, W. Yao and X. Cui. *Optical signature of symmetry variations and spin-valley coupling in atomically thin tungsten dichalcogenides.* Scientific Reports **3**, 1608 (2013).

42. W. Feng, Y. Yao, W. Zhu, J. Zhou, W. Yao and D. Xiao. *Intrinsic spin hall effect in monolayers of group-VI dichalcogenides: A first-principles study.* Physical Review B **86**, 165108 (2012).

43. W.-Y. Shan, H.-Z. Lu and D. Xiao. *Spin hall effect in spin-valley coupled monolayers of transition metal dichalcogenides.* Physical Review B **88**, 125301 (2013).

44. H. Rostami, A. G. Moghaddam and R. Asgari. *Effective lattice hamiltonian for monolayer MoS_2 : Tailoring electronic structure with perpendicular electric and magnetic fields.* Physical Review B **88**, 085440 (2013).

45. F. Rose, M. O. Goerbig and F. Piéchon. *Spin- and valley-dependent magneto-optical properties of MoS_2.* Physical Review B **88**, 125438 (2013).

46. G.-B. Liu, W.-Y. Shan, Y. Yao, W. Yao and D. Xiao. *Three-band tight-binding model for monolayers of group-VIB transition metal dichalcogenides.* Physical Review B **88**, 085433 (2013).

47. R. Roldán, M. P. López-Sancho, F. Guinea, E. Cappelluti, J. A. Silva-Guillén and P. Ordejón. *Momentum dependence of spin-orbit interaction effects in single-layer and multi-layer transition metal dichalcogenides.* 2D Materials **1**, 034003 (2014).

48. T. Li and G. Galli. *Electronic properties of MoS_2 nanoparticles.* The Journal of Physical Chemistry C **111**, 16192 (2007).

49. S. Lebègue and O. Eriksson. *Electronic structure of two-dimensional crystals from ab initio theory.* Physical Review B **79**, 115409 (2009).

50. A. Splendiani, L. Sun, Y. Zhang, T. Li, J. Kim, C.-Y. Chim, G. Galli and F. Wang. *Emerging photoluminescence in monolayer MoS_2.* Nano Letters **10**, 1271 (2010).

51. K. Kaasbjerg, K. S. Thygesen and K. W. Jacobsen. *Phonon-limited mobility in n-type single-layer MoS_2 from first principles.* Physical Review B **85**, 115317 (2012).

52. K. Kaasbjerg, K. S. Thygesen and A.-P. Jauho. *Acoustic phonon limited mobility in two-dimensional semiconductors: Deformation potential and piezoelectric scattering in monolayer MoS_2 from first principles.* Physical Review B **87**, 235312 (2013).

53. E. S. Kadantsev and P. Hawrylak. *Electronic structure of a single MoS_2 monolayer.* Solid State Communications **152**, 909 (2012).

54. K. Kośmider and J. Fernández-Rossier. *Electronic properties of the MoS_2-WS_2 heterojunction.* Physical Review B **87**, 075451 (2013).

55. N. Zibouche, A. Kuc and T. Heine. *From layers to nanotubes: Transition metal disulfides TMS_2.* The European Physical Journal B **85**, 49 (2012).

56. X. Li, J. T. Mullen, Z. Jin, K. M. Borysenko, M. Buongiorno Nardelli and K. W. Kim. *Intrinsic electrical transport properties of monolayer silicene and MoS_2 from first principles.* Physical Review B **87**, 115418 (2013).

57. R. A. Bromley, R. B. Murray and A. D. Yoffe. *The band structures of some transition metal dichalcogenides. III. group VIA: trigonal prism materials.* Journal of Physics C: Solid State Physics **5**, 759 (1972).

58. A. Kormányos, V. Zólyomi, N. D. Drummond, P. Rakyta, G. Burkard and V. I. Fal'ko. *Monolayer MoS_2: Trigonal warping, the Γ valley, and spin-orbit coupling effects.* Physical Review B **88**, 045416 (2013).

59. J. M. Soler, E. Artacho, J. D. Gale, A. García, J. Junquera, P. Ordejón and D. Sánchez-Portal. *The* SIESTA *method for ab initio order-N materials simulation.* Journal of Physics: Condensed Matter **14**, 2745 (2002).

60. E. Artacho, E. Anglada, O. Diéguez, J. D. Gale, A. García, J. Junquera, R. M. Martin, P. Ordejón, J. M. Pruneda, D. Sánchez-Portal and J. M. Soler. *The* SIESTA *method; developments and applicability.* Journal of Physics: Condensed Matter **20**, 064208 (2008).

61. M. S. Fuhrer, J. Nygård, L. Shih, M. Forero, Y.-G. Yoon, M. S. C. Mazzoni, H. J. Choi, J. Ihm, S. G. Louie, A. Zettl and P. L. McEuen. *Crossed nanotube junctions.* Science **288**, 494 (2000).

62. P. O. Lehtinen, A. S. Foster, Y. Ma, A. V. Krasheninnikov and R. M. Nieminen. *Irradiation-induced magnetism in graphite: A density functional study.* Physical Review Letters **93**, 187202 (2004).

63. F. D. Novaes, R. Rurali and P. Ordejón. *Electronic transport between graphene layers covalently connected by carbon nanotubes.* ACS Nano **4**, 7596 (2010).

64. B. Wang, M.-L. Bocquet, S. Marchini, S. Günther and J. Wintterlin. *Chemical origin of a graphene moirè overlayer on Ru(0001).* Physical Chemistry Chemical Physics **10**, 3530 (2008).

65. J. H. Ho, Y. H. Lai, Y. H. Chiu and M. F. Lin. *Modulation effects on Landau levels in a monolayer graphene.* Nanotechnology **19**, 035712 (2008).

66. J. J. Palacios, J. Fernández-Rossier and L. Brey. *Vacancy-induced magnetism in graphene and graphene ribbons.* Physical Review B **77**, 195428 (2008).

67. A. L. C. Pereira and P. A. Schulz. *Additional levels between Landau bands due to vacancies in graphene: Towards defect engineering.* Physical Review B **78**, 125402 (2008).

68. A. Carpio, L. L. Bonilla, F. d. Juan and M. A. H. Vozmediano. *Dislocations in graphene.* New Journal of Physics **10**, 053021 (2008).

69. M. P. López-Sancho, F. de Juan and M. A. H. Vozmediano. *Magnetic moments in the presence of topological defects in graphene.* Physical Review B **79**, 075413 (2009).

70. R. M. Ribeiro, V. M. Pereira, N. M. R. Peres, P. R. Briddon and A. H. C. Neto. *Strained graphene: tight-binding and density functional calculations.* New Journal of Physics **11**, 115002 (2009).

71. S. Yuan, R. Roldán and M. I. Katsnelson. *Excitation spectrum and high-energy plasmons in single-layer and multilayer graphene.* Physical Review B **84**, 035439 (2011).

72. S. Yuan, R. Roldán and M. I. Katsnelson. *Landau level spectrum of ABA- and ABC-stacked trilayer graphene.* Physical Review B **84**, 125455 (2011).

73. M. Neek-Amal, L. Covaci and F. M. Peeters. *Nanoengineered nonuniform strain in graphene using nanopillars.* Physical Review B **86**, 041405 (2012).

74. S. Yuan, R. Roldán, A.-P. Jauho and M. I. Katsnelson. *Electronic properties of disordered graphene antidot lattices.* Physical Review B **87**, 085430 (2013).

75. N. Leconte, J. Moser, P. Ordejón, H. Tao, A. Lherbier, A. Bachtold, F. Alsina, C. M. Sotomayor Torres, J.-C. Charlier and S. Roche. *Damaging graphene with ozone treatment: A chemically tunable metal–insulator transition.* ACS Nano **4**, 4033 (2010).

76. D. Soriano, N. Leconte, P. Ordejón, J.-C. Charlier, J.-J. Palacios and S. Roche. *Magnetoresistance and magnetic ordering fingerprints in hydrogenated graphene.* Physical Review Letters **107**, 016602 (2011).

77. N. Leconte, D. Soriano, S. Roche, P. Ordejon, J.-C. Charlier and J. J. Palacios. *Magnetism-dependent transport phenomena in hydrogenated graphene: From spin-splitting to localization effects.* ACS Nano **5**, 3987 (2011).

78. D. Van Tuan, A. Kumar, S. Roche, F. Ortmann, M. F. Thorpe and P. Ordejón. *Insulating behavior of an amorphous graphene membrane.* Physical Review B **86**, 121408 (2012).

79. H. Zheng, Z. F. Wang, T. Luo, Q. W. Shi and J. Chen. *Analytical study of electronic structure in armchair graphene nanoribbons.* Physical Review B **75**, 165414 (2007).

80. F. Guinea, M. I. Katsnelson and M. A. H. Vozmediano. *Midgap states and charge inhomogeneities in corrugated graphene.* Physical Review B **77**, 075422 (2008).

81. E. V. Castro, N. M. R. Peres and J. M. B. Lopes dos Santos. *Magnetic structure at zigzag edges of graphene bilayer ribbons.* arXiv: 0801.2788 (2008).

82. E. V. Castro, M. P. López-Sancho and M. A. H. Vozmediano. *Pinning and switching of magnetic moments in bilayer graphene.* New Journal of Physics **11**, 095017 (2009).

83. E. V. Castro, M. P. López-Sancho and M. A. H. Vozmediano. *New type of vacancy-induced localized states in multilayer graphene.* Physical Review Letters **104**, 036802 (2010).

84. E. V. Castro, M. P. López-Sancho and M. A. H. Vozmediano. *Effect of pressure on the magnetism of bilayer graphene.* Physical Review B **84**, 075432 (2011).

85. A. Cresti, N. Nemec, B. Biel, G. Niebler, F. Triozon, G. Cuniberti and S. Roche. *Charge transport in disordered graphene-based low dimensional materials.* Nano Research **1**, 361 (2008).

86. Y. C. Huang, C. P. Chang, W. S. Su and M. F. Lin. *Low-energy landau levels of bernal zigzag graphene ribbons.* Journal of Applied Physics **106**, 013711 (2009).

87. Y. O. Klymenko and O. Shevtsov. *Quantum transport in armchair graphene ribbons: analytical tight-binding solutions for propagation through step-like and barrier-like potentials.* The European Physical Journal B **69**, 383 (2009).

88. J. M. B. Lopes dos Santos, N. M. R. Peres and A. H. Castro Neto. *Graphene bilayer with a twist: Electronic structure.* Physical Review Letters **99**, 256802 (2007).

89. E. J. Mele. *Commensuration and interlayer coherence in twisted bilayer graphene.* Physical Review B **81**, 161405 (2010).

90. E. J. Mele. *Interlayer coupling in rotationally faulted multilayer graphenes.* Journal of Physics D: Applied Physics **45**, 154004 (2012).

91. S. Shallcross, S. Sharma, E. Kandelaki and O. A. Pankratov. *Electronic structure of turbostratic graphene.* Physical Review B **81**, 165105 (2010).

92. E. Suárez Morell, J. D. Correa, P. Vargas, M. Pacheco and Z. Barticevic. *Flat bands in slightly twisted bilayer graphene: Tight-binding calculations.* Physical Review B **82**, 121407 (2010).

93. R. de Gail, M. O. Goerbig, F. Guinea, G. Montambaux and A. H. Castro Neto. *Topologically protected zero modes in twisted bilayer graphene.* Physical Review B **84**, 045436 (2011).

94. R. Bistritzer and A. H. MacDonald. *Moirè bands in twisted double-layer graphene.* Proceedings of the National Academy of Sciences **108**, 12233 (2011).

95. E. Suárez Morell, P. Vargas, L. Chico and L. Brey. *Charge redistribution and interlayer coupling in twisted bilayer graphene under electric fields.* Physical Review B **84**, 195421 (2011).

96. P. Moon and M. Koshino. *Energy spectrum and quantum hall effect in twisted bilayer graphene.* Physical Review B **85**, 195458 (2012).

97. P. Moon and M. Koshino. *Optical absorption in twisted bilayer graphene.* Physical Review B **87**, 205404 (2013).

98. P. San-Jose, J. González and F. Guinea. *Non-abelian gauge potentials in graphene bilayers.* Physical Review Letters **108**, 216802 (2012).

99. C. J. Tabert and E. J. Nicol. *Optical conductivity of twisted bilayer graphene.* Physical Review B **87**, 121402 (2013).

100. N. J. Doran, D. J. Titterington, B. Ricco and G. Wexler. *A tight binding fit to the bandstructure of 2H-$NbSe_2$ and NbS_2.* Journal of Physics C: Solid State Physics **11**, 685 (1978).

101. W. H. Press, S. A. Teukolsky, W. T. Vetterling and B. P. Flannery. *Numerical Recipes* (Cambridge University Press, 1992).

102. F. Zahid, L. Liu, Y. Zhu, J. Wang and H. Guo. *A generic tight-binding model for monolayer, bilayer and bulk MoS_2.* AIP Advances **3**, 052111 (2013).

103. S. Gallego and M. C. Muñoz. *Spin-orbit effects in the surface electronic configuration of the $Pt_3Mn(111)$ and layered (2×2) $Pt/Pt_3Mn(111)$ compounds.* Surface Science **423**, 324 (1999).

104. L. Chico, M. P. López-Sancho and M. C. Muñoz. *Spin splitting induced by spin-orbit interaction in chiral nanotubes.* Physical Review Letters **93**, 176402 (2004).

105. D. Huertas-Hernando, F. Guinea and A. Brataas. *Spin-orbit coupling in curved graphene, fullerenes, nanotubes, and nanotube caps.* Physical Review B **74**, 155426 (2006).

106. K. Kośmider, J. W. González and J. Fernández-Rossier. *Large spin splitting in the conduction band of transition metal dichalcogenide monolayers.* Physical Review B **88**, 245436 (2013).

107. W. Jin, P.-C. Yeh, N. Zaki, D. Zhang, J. T. Sadowski, A. Al-Mahboob, A. M. van der Zande, D. A. Chenet, J. I. Dadap, I. P. Herman, P. Sutter, J. Hone and R. M. Osgood. *Direct measurement of the thickness-dependent electronic band structure of MoS_2 using angle-resolved photoemission spectroscopy.* Physical Review Letters **111**, 106801 (2013).

108. A. Kormányos, V. Zólyomi, N. D. Drummond and G. Burkard. *Spin-orbit coupling, quantum dots, and qubits in monolayer transition metal dichalcogenides.* Physical Review X **4**, 011034 (2014).

109. X. Li, F. Zhang and Q. Niu. *Unconventional quantum hall effect and tunable spin hall effect in Dirac materials: Application to an isolated MoS_2 trilayer.* Physical Review Letters **110**, 066803 (2013).

110. J. Klinovaja and D. Loss. *Spintronics in MoS_2 monolayer quantum wires.* Physical Review B **88**, 075404 (2013).

111. L. Wang and M. W. Wu. *Intrinsic electron spin relaxation due to the D'yakonov-Perel' mechanism in monolayer MoS_2.* Physics Letters A **378**, 1336 (2014).

112. M. Cazalilla, H. Ochoa and F. Guinea. *Quantum spin hall effect in two-dimensional crystals of transition-metal dichalcogenides.* Physical Review Letters **113**, 077201 (2014).

113. M. O. Goerbig, G. Montambaux and F. Piéchon. *Measure of diracness in two-dimensional semiconductors.* Europhysics Letters **105**, 57005 (2014).

114. N. Alidoust, G. Bian, S.-Y. Xu, R. Sankar, M. Neupane, C. Liu, I. Belopolski, D.-X. Qu, J. D. Denlinger, F.-C. Chou and M. Z. Hasan. *Observation of monolayer valence band spin-orbit effect and induced quantum well states in MoX_2.* Nature Communications **5**, 4673 (2014).

115. T. Cheiwchanchamnangij and W. R. L. Lambrecht. *Quasiparticle band structure calculation of monolayer, bilayer, and bulk MoS_2.* Physical Review B **85**, 205302 (2012).

116. H. Yuan, X. Wang, B. Lian, H. Zhang, X. Fang, B. Shen, G. Xu, Y. Xu, S.-C. Zhang, H. Y. Hwang and Y. Cui. *Generation and electric control of spin-valley-coupled circular photogalvanic current in WSe_2.* Nature Nanotechnology **9**, 851 (2014).

117. A. Castellanos-Gomez, R. Roldán, E. Cappelluti, M. Buscema, F. Guinea, H. S. J. van der Zant and G. A. Steele. *Local strain engineering in atomically thin MoS_2.* Nano Letters **13**, 5361 (2013).

118. L. Kleinman. *Relativistic norm-conserving pseudopotential.* Physical Review B **21**, 2630 (1980).

119. Z. Gong, G.-B. Liu, H. Yu, D. Xiao, X. Cui, X. Xu and W. Yao. *Magnetoelectric effects and valley-controlled spin quantum gates in transition metal dichalcogenide bilayers.* Nature Communications **4**, 2053 (2013).

120. M. Bokdam, P. A. Khomyakov, G. Brocks, Z. Zhong and P. J. Kelly. *Electrostatic doping of graphene through ultrathin hexagonal boron nitride films.* Nano Letters **11**, 4631 (2011).

121. K. Suenaga, C. Colliex, N. Demoncy, A. Loiseau, H. Pascard and F. Willaime. *Synthesis of nanoparticles and nanotubes with well-separated layers of boron nitride and carbon.* Science **278**, 653 (1997).

122. K. Watanabe, T. Taniguchi and H. Kanda. *Direct-bandgap properties and evidence for ultraviolet lasing of hexagonal boron nitride single crystal.* Nature Materials **3**, 404 (2004).

123. G. Giovannetti, P. A. Khomyakov, G. Brocks, P. J. Kelly and J. van den Brink. *Substrate-induced band gap in graphene on hexagonal boron nitride: Ab initio density functional calculations.* Physical Review B **76**, 073103 (2007).

124. J. Jung, A. M. DaSilva, A. H. MacDonald and S. Adam. *Origin of band gaps in graphene on hexagonal boron nitride.* Nature Communications **6**, 6308 (2015).

125. W. J. Schutte, J. L. De Boer and F. Jellinek. *Crystal structures of tungsten disulfide and diselenide.* Journal of Solid State Chemistry **70**, 207 (1987).

126. Y. Ma, Y. Dai, M. Guo, C. Niu and B. Huang. *Graphene adhesion on MoS_2 monolayer: An ab initio study.* Nanoscale **3**, 3883 (2011).

127. Y. Ma, Y. Dai, W. Wei, C. Niu, L. Yu and B. Huang. *First-Principles Study of the Graphene@$MoSe_2$ Heterobilayers.* Journal Physical Chemistry C **115**, 20237 (2011).

128. S. Grimme. *Semiempirical GGA-type density functional constructed with a long-range dispersion correction.* Journal of Computational Chemistry **27**, 1787 (2006).

129. M. Dion, H. Rydberg, E. Schröder, D. C. Langreth and B. I. Lundqvist. *Van der waals density functional for general geometries.* Physical Review Letters **92**, 246401 (2004).

130. P. A. Khomyakov, G. Giovannetti, P. C. Rusu, G. Brocks, J. van den Brink and P. J. Kelly. *First-principles study of the interaction and charge transfer between graphene and metals.* Physical Review B **79**, 195425 (2009).

131. S. Garcia-Gil. *Theoretical Characterization of Metallic and Semiconducting Nanostructures by means of DFT using Localized Basis Sets.* Ph.D. thesis, Universitat Autònoma de Barcelona (2011).

132. J. Bardeen, L. N. Cooper and J. R. Schrieffer. *Theory of superconductivity.* Physical Review **108**, 1175 (1957).

133. U. Rössler. *Solid State Theory: An Introduction* (Springer, 2009).

134. J. A. Manzanares. *Apuntes de "Física del Estado Sólido"* (Universidad de Valencia (Provided by the author), 2009).

135. H. Suhl, B. T. Matthias and L. R. Walker. *Bardeen-Cooper-Schrieffer theory of superconductivity in the case of overlapping bands.* Physical Review Letters **3**, 552 (1959).

136. Y. Noat, T. Cren, F. Debontridder, D. Roditchev, W. Sacks, P. Toulemonde and A. San Miguel. *Signatures of multigap superconductivity in tunneling spectroscopy.* Physical Review B **82**, 014531 (2010).

137. N. Schopohl and K. Scharnberg. *Tunneling density of states for the two-band model of superconductivity.* Solid State Communications **22**, 371 (1977).

138. D. Daghero and R. S. Gonnelli. *Probing multiband superconductivity by point-contact spectroscopy.* Superconductivity Science and Technology **23**, 043001 (2010).

139. W. L. McMillan. *Tunneling model of the superconducting proximity effect.* Physical Review **175**, 537 (1968).

140. G. Binnig, A. Baratoff, H. E. Hoenig and J. G. Bednorz. *Two-band superconductivity in Nb-doped $SrTiO_3$.* Physical Review Letters **45**, 1352 (1980).

141. J. Nagamatsu, N. Nakagawa, T. Muranaka, Y. Zenitani and J. Akimitsu. *Superconductivity at 39 K in magnesium diboride.* Nature **410**, 63 (2001).

142. M. Lüders, M. A. L. Marques, N. N. Lathiotakis, A. Floris, G. Profeta, L. Fast, A. Continenza, S. Massidda and E. K. U. Gross. *Ab initio theory of superconductivity. I. density functional formalism and approximate functionals.* Physical Review B **72**, 024545 (2005).

143. M. A. L. Marques, M. Lüders, N. N. Lathiotakis, G. Profeta, A. Floris, L. Fast, A. Continenza, E. K. U. Gross and S. Massidda. *Ab initio theory of superconductivity. II. application to elemental metals.* Physical Review B **72**, 024546 (2005).

144. M. E. Jones and R. E. Marsh. *The preparation and structure of magnesium boride, MgB_2.* Journal of the American Chemical Society **76**, 1434 (1954).

145. V. Russell, R. Hirst, F. A. Kanda and A. J. King. *An X-ray study of the magnesium borides.* Acta Crystallographica **6**, 870 (1953).

146. W. B. Pearson. *Crystal Chemistry and Physics of Metals and Alloys.* (Wiley, 1965).

147. J. M. An and W. E. Pickett. *Superconductivity of MgB_2: Covalent bonds driven metallic.* Physical Review Letters **86**, 4366 (2001).

148. A. Y. Liu, I. I. Mazin and J. Kortus. *Beyond eliashberg superconductivity in MgB_2: Anharmonicity, two-phonon scattering, and multiple gaps.* Physical Review Letters **87**, 087005 (2001).

149. F. Giubileo, D. Roditchev, W. Sacks, R. Lamy, D. X. Thanh, J. Klein, S. Miraglia, D. Fruchart, J. Marcus and P. Monod. *Two-gap state density in MgB_2: A true bulk property or a proximity effect?* Physical Review Letters **87**, 177008 (2001).

150. H. Schmidt, J. F. Zasadzinski, K. E. Gray and D. G. Hinks. *Evidence for two-band superconductivity from break-junction tunneling on MgB_2.* Physical Review Letters **88**, 127002 (2002).

151. P. Szabó, P. Samuely, J. Kačmarčík, T. Klein, J. Marcus, D. Fruchart, S. Miraglia, C. Marcenat and A. G. M. Jansen. *Evidence for two superconducting energy gaps in MgB_2 by point-contact spectroscopy.* Physical Review Letters **87**, 137005 (2001).

152. R. S. Gonnelli, D. Daghero, G. A. Ummarino, V. A. Stepanov, J. Jun, S. M. Kazakov and J. Karpinski. *Direct evidence for two-band superconductivity in MgB_2 single crystals from directional point-contact spectroscopy in magnetic fields.* Physical Review Letters **89**, 247004 (2002).

153. F. Bouquet, R. A. Fisher, N. E. Phillips, D. G. Hinks and J. D. Jorgensen. *Specific heat of $Mg^{11}B_2$: Evidence for a second energy gap.* Physical Review Letters **87**, 047001 (2001).

154. X. K. Chen, M. J. Konstantinović, J. C. Irwin, D. D. Lawrie and J. P. Franck. *Evidence for two superconducting gaps in MgB_2.* Physical Review Letters **87**, 157002 (2001).

155. M. Iavarone, G. Karapetrov, A. E. Koshelev, W. K. Kwok, G. W. Crabtree, D. G. Hinks, W. N. Kang, E.-M. Choi, H. J. Kim, H.-J. Kim and S. I. Lee. *Two-band superconductivity in MgB_2.* Physical Review Letters **89**, 187002 (2002).

156. D. Roditchev, F. Giubileo, F. Bobba, R. Lamy, E. M. Choi, H. J. Kim, W. N. Kang, S. Miraglia, J. Marcus, W. Sacks, J. Klein, A. M. Cucolo, S. I. Lee and D. Fruchart. *Two-gap interplay in MgB_2: a tunneling spectroscopy study.* Physica C: Superconductivity **408–410**, 768 (2004).

157. Z. Li, J. Yang, J. G. Hou and Q. Zhu. *First-principles study of MgB_2 (0001) surfaces.* Physical Review B **65**, 100507 (2002).

158. J. Kortus, I. I. Mazin, K. D. Belashchenko, V. P. Antropov and L. L. Boyer. *Superconductivity of metallic boron in MgB_2.* Physical Review Letters **86**, 4656 (2001).

159. R. Núñez González and A. Reyes Serrato. *Cálculos ab initio de la estructura electrónica del superconductor MgB_2.* Revista Mexicana de Física **48**, 391 (2002).

160. F. Bouquet, Y. Wang, R. A. Fisher, D. G. Hinks, J. D. Jorgensen, A. Junod and N. E. Phillips. *Phenomenological two-gap model for the specific heat of MgB_2.* Europhysics Letters **56**, 856 (2001).

161. G. Satta, G. Profeta, F. Bernardini, A. Continenza and S. Massidda. *Electronic and structural properties of superconducting MgB_2, $CaSi_2$, and related compounds.* Physical Review B **64**, 104507 (2001).

162. J. Tersoff and D. R. Hamann. *Theory of the scanning tunneling microscope.* Physical Review B **31**, 805 (1985).

163. E. Revolinsky, E. P. Lautenschlager and C. H. Armitage. *Layer structure superconductor.* Solid State Communications **1**, 59 (1963).

164. E. Revolinsky, G. A. Spiering and D. J. Beerntsen. *Superconductivity in the niobium-selenium system.* Journal of Physics and Chemistry of Solids **26**, 1029 (1965).

165. J. A. Wilson, F. J. DiSalvo and S. Mahajan. *Charge-density waves in metallic, layered, transition-metal dichalcogenides.* Physical Review Letters **32**, 882 (1974).

166. R. C. Morris and R. V. Coleman. *Tunneling measurement of the superconducting energy gap in $NbSe_2$.* Physics Letters A **43**, 11 (1973).

167. H. F. Hess, R. B. Robinson and J. V. Waszczak. *Vortex-core structure observed with a scanning tunneling microscope.* Physical Review Letters **64**, 2711 (1990).

168. L. F. Mattheiss. *Energy bands for 2H-$NbSe_2$ and 2H-MoS_2.* Physical Review Letters **30**, 784 (1973).

169. N. J. Doran, D. Titterington, B. Ricco, M. Schreiber and G. Wexler. *The electronic susceptibility and charge density waves in 2H layer compounds.* Journal of Physics C: Solid State Physics **11**, 699 (1978).

170. N. J. Doran. *A calculation of the electronic response function in 2H-$NbSe_2$ including electron-phonon matrix element effects.* Journal of Physics C: Solid State Physics **11**, L959 (1978).

171. J. Rodrigo and S. Vieira. *STM study of multiband superconductivity in $NbSe_2$ using a superconducting tip.* Physica C: Superconductivity **404**, 306 (2004).

172. T. Yokoya, T. Kiss, A. Chainani, S. Shin, M. Nohara and H. Takagi. *Fermi surface sheet-dependent superconductivity in 2H-$NbSe_2$.* Science **294**, 2518 (2001).

173. E. Boaknin, M. A. Tanatar, J. Paglione, D. Hawthorn, F. Ronning, R. W. Hill, M. Sutherland, L. Taillefer, J. Sonier, S. M. Hayden and J. W. Brill. *Heat conduction in the vortex state of $NbSe_2$: Evidence for multiband superconductivity.* Physical Review Letters **90**, 117003 (2003).

174. C. L. Huang, J.-Y. Lin, Y. T. Chang, C. P. Sun, H. Y. Shen, C. C. Chou, H. Berger, T. K. Lee and H. D. Yang. *Experimental evidence for a two-gap structure of superconducting 2H-$NbSe_2$: A specific-heat study in external magnetic fields.* Physical Review B **76**, 212504 (2007).

175. Y. Jing, S. Lei, W. Yue, X. Zhi-Li and W. Hai-Hu. *Quasiparticle density of states of 2H-$NbSe_2$ single crystals revealed by low-temperature specific heat measurements according to a two-component model.* Chinese Physics B **17**, 2229 (2008).

176. J. D. Fletcher, A. Carrington, P. Diener, P. Rodière, J. P. Brison, R. Prozorov, T. Olheiser and R. W. Giannetta. *Penetration depth study of superconducting gap structure of 2H-$NbSe_2$.* Physical Review Letters **98**, 057003 (2007).

177. R. Corcoran, P. Meeson, Y. Onuki, P.-A. Probst, M. Springford, K. Takita, H. Harima, G. Y. Guo and B. L. Gyorffy. *Quantum oscillations in the mixed state of the type II superconductor 2H-$NbSe_2$.* Journal of Physics: Condensed Matter **6**, 4479 (1994).

178. K. Rossnagel, O. Seifarth, L. Kipp, M. Skibowski, D. Voß, P. Krüger, A. Mazur and J. Pollmann. *Fermi surface of 2H-$NbSe_2$ and its implications on the charge-density-wave mechanism.* Physical Review B **64**, 235119 (2001).

179. A. Meerschaut and C. Deudon. *Crystal structure studies of the 3R-$Nb_{1.09}S_2$ and the 2H-$NbSe_2$ compounds: correlation between nonstoichiometry and stacking type (= polytypism).* Materials Research Bulletin **36**, 1721 (2001).

180. M. Marezio, P. D. Dernier, A. Menth and G. W. Hull Jr. *The crystal structure of $NbSe_2$ at 15K.* Journal of Solid State Chemistry **4**, 425 (1972).

181. J. Wilson, F. DiSalvo and S. Mahajan. *Charge-density waves and superlattices in the metallic layered transition metal dichalcogenides.* Advances in Physics **24**, 117 (1975).

182. M. H. Whangbo and E. Canadell. *Analogies between the concepts of molecular chemistry and solid-state physics concerning structural instabilities. electronic origin of the structural modulations in layered transition metal dichalcogenides.* Journal of the American Chemical Society **114**, 9587 (1992).

183. M. D. Johannes, I. I. Mazin and C. A. Howells. *Fermi-surface nesting and the origin of the charge-density wave in 2H-$NbSe_2$.* Physical Review B **73**, 205102 (2006).

184. T. M. Rice and G. K. Scott. *New mechanism for a charge-density-wave instability.* Physical Review Letters **35**, 120 (1975).

185. M. Calandra, I. I. Mazin and F. Mauri. *Effect of dimensionality on the charge-density wave in few-layer 2H-$NbSe_2$.* Physical Review B **80**, 241108(R) (2009).

186. F. Weber, S. Rosenkranz, J.-P. Castellan, R. Osborn, R. Hott, R. Heid, K.-P. Bohnen, T. Egami, A. H. Said and D. Reznik. *Extended phonon collapse and the origin of the charge-density wave in 2H-$NbSe_2$.* Physical Review Letters **107**, 107403 (2011).

187. D. E. Moncton, J. D. Axe and F. J. DiSalvo. *Neutron scattering study of the charge-density wave transitions in 2H-$TaSe_2$ and 2H-$NbSe_2$.* Physical Review B **16**, 801 (1977).

188. R. Brouwer and F. Jellinek. *The low-temperature superstructures of 1T-$TaSe_2$ and 2H-$TaSe_2$.* Physica B+C **99**, 51 (1980).

189. C. D. Malliakas and M. G. Kanatzidis. *Nb-Nb interactions define the charge density wave structure of 2H-$NbSe_2$.* Journal of the American Chemical Society **135**, 1719 (2013).

190. D. Sanchez, A. Junod, J. Muller, H. Berger and F. Lévy. *Specific heat of 2H-$NbSe_2$ in high magnetic fields.* Physica B: Condensed Matter **204**, 167 (1995).

191. M. Nohara, M. Isshiki, F. Sakai and H. Takagi. *Quasiparticle density of states of clean and dirty s-wave superconductors in the vortex state.* Journal of the Physical Society of Japan **68**, 1078 (1999).

192. T. Hanaguri, A. Koizumi, K. Takaki, M. Nohara, H. Takagi and K. Kitazawa. *Anomaly of quasi-particle density of states in the vortex state of $NbSe_2$.* Physica B: Condensed Matter **329–333, Part 2**, 1355 (2003).

193. T. Kiss, T. Yokoya, A. Chainani, S. Shin, M. Nohara and H. Takagi. *Fermi surface and superconducting gap of 2H-$NbSe_2$ using low-temperature ultrahigh-resolution angle-resolved photoemission spectroscopy.* Physica B: Condensed Matter **312–313**, 666 (2002).

194. T. Valla, A. V. Fedorov, P. D. Johnson, P.-A. Glans, C. McGuinness, K. E. Smith, E. Y. Andrei and H. Berger. *Quasiparticle spectra, charge-density waves, superconductivity, and electron-phonon coupling in 2H-$NbSe_2$.* Physical Review Letters **92**, 086401 (2004).

195. T. Kiss, T. Yokoya, A. Chainani, S. Shin, T. Hanaguri, M. Nohara and H. Takagi. *Charge-order-maximized momentum-dependent superconductivity.* Nature Physics **3**, 720 (2007).

196. S. V. Borisenko, A. A. Kordyuk, V. B. Zabolotnyy, D. S. Inosov, D. Evtushinsky, B. Büchner, A. N. Yaresko, A. Varykhalov, R. Follath, W. Eberhardt, L. Patthey and H. Berger. *Two energy gaps and fermi-surface "Arcs" in $NbSe_2$.* Physical Review Letters **102**, 166402 (2009).

197. D. J. Rahn, S. Hellmann, M. Kalläne, C. Sohrt, T. K. Kim, L. Kipp and K. Rossnagel. *Gaps and kinks in the electronic structure of the superconductor 2H-$NbSe_2$ from angle-resolved photoemission at 1 K.* Physical Review B **85**, 224532 (2012).

198. H. Schmidt, J. F. Zasadzinski, K. E. Gray and D. G. Hinks. *Evidence for two-band superconductivity from break-junction tunneling on MgB_2.* Physical Review Letters **88**, 127002 (2002).

199. H. Schmidt, J. Zasadzinski, K. Gray and D. Hinks. *Break-junction tunneling on MgB_2.* Physica C: Superconductivity **385**, 221 (2003).

200. G. Karapetrov, M. Iavarone, A. Koshelev, W. Kwok, G. Crabtree, D. Hinks and S. Lee. *Momentum-dependent scanning tunneling spectroscopy in MgB_2.* Physica C: Superconductivity **388–389**, 141–142 (2003). Proceedings of the 23rd International Conference on Low Temperature Physics (LT23).

201. M. Iavarone, G. Karapetrov, A. E. Koshelev, W. K. Kwok, G. W. Crabtree, D. G. Hinks, W. N. Kang, E.-M. Choi, H. J. Kim, H.-J. Kim and S. I. Lee. *Two-band superconductivity in MgB_2.* Physical Review Letters **89**, 187002 (2002).

202. F. Giubileo, D. Roditchev, W. Sacks, R. Lamy, D. X. Thanh, J. Klein, S. Miraglia, D. Fruchart, J. Marcus and P. Monod. *Two-gap state density in MgB_2: A true bulk property or a proximity effect?* Physical Review Letters **87**, 177008 (2001).

203. J. Kortus, O. V. Dolgov, R. K. Kremer and A. A. Golubov. *Band filling and interband scattering effects in MgB_2: Carbon versus aluminum doping.* Physical Review Letters **94**, 027002 (2005).

204. H. J. Choi, D. Roundy, H. Sun, M. L. Cohen and S. G. Louie. *The origin of the anomalous superconducting properties of MgB_2.* Nature **418**, 758 (2002).

205. G. Wexler and A. M. Woolley. *Fermi surfaces and band structures of the 2H metallic transition-metal dichalcogenides.* Journal of Physics C: Solid State Physics **9**, 1185 (1976).

206. T. Straub, T. Finteis, R. Claessen, P. Steiner, S. Hüfner, P. Blaha, C. S. Oglesby and E. Bucher. *Charge-density-wave mechanism in 2H-$NbSe_2$: Photoemission results.* Physical review letters **82**, 4504 (1999).

207. J. R. Long, S. P. Bowen and N. E. Lewis. *Anomalous resistivity of iodine-free 2H-$NbSe_2$.* Solid State Communications **22**, 363 (1977).

208. J. M. E. Harper, T. H. Geballe and F. J. DiSalvo. *Heat capacity of 2H-$NbSe_2$ at the charge density wave transition.* Physics Letters A **54**, 27 (1975).

209. C. J. Arguello, S. P. Chockalingam, E. P. Rosenthal, L. Zhao, C. Gutiérrez, J. H. Kang, W. C. Chung, R. M. Fernandes, S. Jia, A. J. Millis, R. J. Cava and A. N. Pasupathy. *Visualizing the charge density wave transition in 2H-$NbSe_2$ in real space.* Physical Review B **89**, 235115 (2014).

210. P. Mallet, W. Sacks, D. Roditchev, D. Défourneau and J. Klein. *Spatial and energy variation of the local density of states in the charge density wave phase of 2H-$NbSe_2$.* Journal of Vacuum Science & Technology B **14**, 1070 (1996).

211. I. Guillamón, H. Suderow, S. Vieira, L. Cario, P. Diener and P. Rodière. *Superconducting density of states and vortex cores of 2H-NbS_2.* Physical Review Letters **101**, 166407 (2008).

212. Y. Hamaue and R. Aoki. *Effects of organic intercalation on lattice vibrations and superconducting properties of 2H-NbS_2.* Journal of the Physical Society of Japan **55**, 1327 (1986).

213. D. M. Ceperley and B. J. Alder. *Ground state of the electron gas by a stochastic method.* Physical Review Letters **45**, 566 (1980).

214. J. P. Perdew and A. Zunger. *Self-interaction correction to density-functional approximations for many-electron systems.* Physical Review B **23**, 5048 (1981).

215. S. G. Louie, S. Froyen and M. L. Cohen. *Nonlinear ionic pseudopotentials in spin-density-functional calculations.* Physical Review B **26**, 1738 (1982).

216. H. J. Monkhorst and J. D. Pack. *Special points for Brillouin-zone integrations.* Physical Review B **13**, 5188 (1976).

217. Kumar, A. and Ahluwalia, P.K. *Electronic structure of transition metal dichalcogenides monolayers 1H-MX_2 (M = Mo, W; X = S, Se, Te) from ab-initio theory: new direct band gap semiconductors.* European Physical Journal B **85**, 186 (2012).

218. L. Fernández-Seivane, M. A. Oliveira, S. Sanvito and J. Ferrer. *On-site approximation for spin–orbit coupling in linear combination of atomic orbitals density functional methods.* Journal of Physics: Condensed Matter **18**, 7999 (2006).

219. N. Troullier and J. L. Martins. *Efficient pseudopotentials for plane-wave calculations.* Physical Review B **43**, 1993 (1991).

220. L. Kleinman and D. M. Bylander. *Efficacious form for model pseudopotentials.* Physical Review Letters **48**, 1425 (1982).

221. J. P. Perdew, K. Burke and M. Ernzerhof. *Generalized gradient approximation made simple.* Physical Review Letters **77**, 3865 (1996).

222. F. Jellinek, G. Brauer and H. Müller. *Molybdenum and niobium sulphides.* Nature **185**, 376 (1960).

223. S. García-Gil, A. García, N. Lorente and P. Ordejón. *Optimal strictly localized basis sets for noble metal surfaces.* Physical Review B **79**, 075441 (2009).